Modelling Cosmic Ray Ground Level Enhancements

by

Jennifer Louise Cramp, B.Sc.(Hons.)

Submitted in fulfilment of the requirements
for the Degree of
Doctor of Philosophy

University of Tasmania
Hobart

February 1996

Declaration

This thesis contains no material which has been accepted for the award of any other higher degree or graduate diploma in any tertiary institution. To the best of my knowledge and belief, this thesis contains no material previously published or written by another person, except where due reference has been made in the text of the thesis.

Jennifer Louise Cramp

Jennifer Louise Cramp

Abstract

Analyses of seven cosmic ray ground level enhancements (GLE) are presented. The first four events were part of the unprecedented sequence of relativistic solar proton events which occurred during 1989. Three of the larger events of the 21st solar cycle have also been modelled. In each case, analysis is based on data from the world-wide network of neutron monitors. Surface muon telescope data has also been used for of the 29 September 1989 event.

A sophisticated model has been developed from that of Smart *et al.* (1979). Modifications include the calculation of asymptotic directions using a geomagnetic field model which accounts for distortion of the field during geomagnetic disturbances, and the use of a least squares method for determining the best fit parameters. An exponential function used to describe the pitch angle distribution has been further developed to allow bi-directional particle flow and rigidity dependence. The form of the particle spectrum used in most of the analyses was a modified power law in rigidity. An approximation of the Ellison and Ramaty (1985) shock acceleration spectrum has recently been included in the model.

A rigidity dependent pitch angle distribution was required to model the GLE on 29 September 1989 and indicates that, initially, the anisotropy of the particle distribution decreased with increasing rigidity. Significant back-scattering of particles resulted in the observation of a late peak at stations viewing in the anti-sun direction and two peaks at some other stations.

The three GLEs which occurred during October 1989 have been modelled with particular emphasis on the initial spikes seen at some stations for both the 19 and 22 October events. In the case of 19 October 1989, a further spike later in the event appears to have been produced by the same mechanism as the initial spike, which had a significantly different particle distribution and spectrum to that of the main event. Enhancement of the pitch angle distributions in the anti-sun direction during the 22 October event is probably due to scattering by a disturbed plasma region beyond the Earth. The 24 October 1989 event was best modelled using a modified form of the Ellison and Ramaty shock acceleration spectrum. A rigidity dependent pitch angle distribution resulted in only marginal improvement in the fit to the observed data.

The 12 October 1981 GLE has been modelled with a bi-directional pitch angle distribution. This is found to be consistent with results at lower energies and is further evidence for the presence of a looped structure in the interplanetary magnetic field. Further complexity in the interplanetary medium was present during the 7-8 December 1982 GLE. Interplanetary magnetic field data are consistent

with a magnetic cloud-like feature situated just beyond the Earth. Observed neutron monitor increases were satisfactorily reproduced by a model with an elliptical deficit region to account for the scattering which impeded some particles approaching the Earth. The derived particle arrival direction for the 16 February 1984 GLE was $\sim 40^{\circ}$ from the measured interplanetary magnetic field direction. This could not be satisfactorily explained, however it is found to be consistent with the results of previous studies.

Acknowledgements

I wish to express my sincere thanks to the people who have helped me in the course of my studies. In particular, my supervisors Dr. John Humble (University of Tasmania) and Dr. Marc Duldig (Australian Antarctic Division) for their guidance and encouragement throughout.

I would like to thank Drs. Damian Hall and Chris Baker, former cosmic ray physics PhD students, for their interest in my work and helpful discussions from time to time. Thanks also for the fun and friendship we have shared while occupying adjoining offices. Special thanks to Dr. Edward King for his valued friendship, untiring investigation of computing problems and the many encouraging words. I would also like to thank Dr. Hilary Cane for useful discussions and insights into features of solar events and the interplanetary medium.

The work presented in this thesis would not have been possible without access to the GLE database which is held at the Geophysics Directorate, Phillips Laboratory, Boston. Special thanks to M.A. Shea and L.C. Gentile who are responsible for the maintenance of this facility. Thanks also to the principal investigators who contributed to the database.

I am grateful to the Australian Antarctic Division for giving me the opportunity to spend several weeks at Mawson base assisting with a computing upgrade in the cosmic ray observatory. Thanks also to the cosmic ray section for access to computing and photocopying facilities.

I have been in receipt of an ARC-linked Australian Postgraduate Award for most of my candidature, for which I am extremely grateful. Thanks also to the Australian Institute of Physics, Astronomical Society of Australia, Donovan Astronomical Trust and Australian Federation of University Women - South Australian Branch for financial support to attend several conferences. I was particularly pleased for the opportunity to attend the 24th International Cosmic Ray conference held in Rome during 1995. Following this conference it was my privilege to spend two weeks in Bern, Switzerland meeting with Drs. Erwin Flückiger, Peggy Shea, Don Smart, Marc Duldig and John Humble during which time I participated in many useful discussions. Particular thanks to Erwin and Rosmarie Flückiger for their hospitality during this time.

I have made many good friends during my time in the Physics Department and would particularly like to thank Edward, Damian, Chris, Simon, Kristi, Chris and Lisa for their friendship and many lively social occasions. In particular, thanks to Edward and Chris for the times spent enjoying our lovely wilderness. Thanks also to Tammy, Judy and Lou for their friendly interest in my progress.

I am indebted to my family for their love and support throughout the years.

Thankyou to my parents for their encouragement to pursue whatever studies I chose and for giving me such a broad range of experiences during my childhood and early adult years.

Finally, thanks to my husband, Jim Lovell, for his love and encouragement and for being there to 'pick up the pieces' in times of need. I hope I can do the same for you.

Contents

Chapter 1

Introduction

1.1 Early observations and interpretations

The first observation of solar accelerated particles with cosmic ray detectors was on 28 February 1942, however the analysis and interpretation of the data was delayed due to uncertainties in the interpretation as well as difficulties in publication associated with World War II. A second event occurred on 7 March 1942 and a third on 25 July 1946. These three increases in cosmic ray intensity were reported by Forbush (1946). He noted that each event coincided with the observation of a solar flare or radio fadeout indicating a solar flare (the flare associated with the March 1942 event was just behind the west limb of the Sun so could not be identified visually). Another indirect observation of the effects of solar accelerated particles was the jamming of British anti-aircraft radar systems on 27 and 28 February 1942 (Lovell, 1987). It was observed that the jamming was confined to daylight hours with a maximum effect in the direction of the Sun. The Royal Greenwich Observatory confirmed that on 28 February a large sunspot group was on the solar central meridian, and this lead to the conclusion that the radar jamming was caused by radio emission associated with the sunspots. The report of this was classified secret and only released after the war. The classification of this report as well as the delay in publication by Forbush meant that the details of these first solar particle events were not known for some time after their occurrence.

Forbush (1946) reported increases recorded in ionisation chamber data worldwide for each of the events in 1942 and 1946. He discussed mechanisms by which these could have been produced. An enhancement in the geomagnetic diurnal variation occurred during one of the events, but this could not have produced cosmic ray enhancement simultaneously on the night and day sides of the Earth. Another suggested mechanism was a change in the Sun's magnetic moment. This too was rejected as it should produce effects independent of the orientation of the Sun with respect to the Earth, but each of the observed increases occurred when a particularly active region of the Sun was oriented towards the Earth. Forbush was lead to the conclusion that the cosmic ray enhancements were caused by charged particles emitted from the Sun.

A fourth sudden increase occurred on 19 November 1949 and was the first solar event to be recorded by a high altitude cosmic ray monitor. Forbush *et al.*

(1950) used the relative responses at Climax (altitude ~3500 m) and Cheltenham (~70 m) to calculate an atmospheric absorption coefficient for the particles. This value was found to be quite different from the absorption coefficient for galactic cosmic rays. Forbush *et al.* also observed an obvious latitude effect with smaller increases observed at equatorial latitudes. These two facts lead Forbush *et al.* to the conclusion that the particles were not 'ordinary mesons', but were the nucleonic component produced by relatively low energy primary particles.

The largest recorded solar particle event occurred on 23 February 1956 and has been widely studied. A variety of instruments recorded increases during this event including muon detectors, neutron pile monitors (developed specifically to study lower energy particles) and a balloon borne neutron detector. Meyer *et al.* (1956) compared the responses of different instruments and deduced that the particle spectrum was steeper than that of galactic cosmic rays. They found that particles up to energies of 20–30 GeV were present early in the event, but that the intensity at high energies dropped off more quickly that at lower energies.

The cosmic ray intensity exhibited a sharp rise over a period of approximately 20 minutes to reach a peak at more than 40 times the background. Meyer *et al.* interpreted such a short rise-time as indicative of relatively uncomplicated particle transport from the Sun to the Earth. They also noted that the cosmic ray enhancement lasted much longer than the radio emission from the flare site and deduced that there must have been scattering regions present, trapping the particles in the vicinity of the Earth for up to 15 hours. A power law was found to fit the decay phase of the particle intensity, however this broke down at high energies and at later times. Meyer *et al.* explored the physical conditions which could explain these observations and extended a model which had been developed to interpret previous events. The main features of this model were:

- A magnetic field-free region within ~1.4 AU;
- A boundary beyond 1.4 AU which scatters particles back towards the Earth leading to an isotropic distribution of particles in the field-free region.

The slow decline in particle intensity indicated that the boundary region must prevent the escape of particles from the field-free region. The power law nature of the decline indicated a thick continuous barrier through which the particles would diffuse. Departure from the power law at high energies and later times indicated a finite thickness. The physical conditions required by this model were thought to be a result of gas continually escaping from the Sun and pushing out the galactic magnetic field. Meyer *et al.* thought that this would produce a field-free region in the inner solar system surrounded by a region of field irregularities which would act as scattering centres for charged particles. One consequence of the model described by Meyer *et al.* is that particles accelerated from a site on the invisible solar disc could still result in an increase in cosmic ray intensity at Earth. This would have a slower rise but should reach a significant intensity due to the reflection of particles by the barrier beyond the Earth. Meyer *et al.* dismissed the lack of observation of such an event on the basis of statistics and the short period over which neutron monitor observations had been made.

Lüst and Simpson (1957) also studied the 23 February 1956 solar particle event. Their analysis indicated that lower energy particles arrived at the Earth later than those of higher energies. The time delay was considerably larger than the difference in particle speeds would produce. One possibility was that the high energy particles were released first from the acceleration site. Lüst and Simpson investigated a diffusion model for the energy dependent escape of particles from magnetic fields in the source region. This was also explored by Piddington (1958), however the model was very simplistic and it was thought that other effects may reduce the efficiency of the mechanism. The only alternative to explain the delay in arrival times was scattering in the medium through which the particles travelled. Lüst and Simpson believed that this could not be explained by the presence of a uniform magnetic field between the Sun and the Earth and suggested that there may be a combination of field irregularities and radially stretched magnetic fields. Piddington rejected this hypothesis, suggesting instead a radial field which rotated with the Sun out to a certain distance and then ceased to be radial. This point was thought to be within 1 AU. Under these field conditions, particles accelerated at the Sun would spiral along the field lines and if these intersected the Earth, an increase in cosmic ray intensity would be observed. Particles travelling in a purely radial field should become collimated and arrive at Earth in a parallel beam. The observations on 23 February 1956 indicated some scattering, therefore there must have been some irregularities in the field. Piddington proposed that scattering by magnetic irregularities would produce energy-dependent arrival times at Earth. He also suggested that the outer, non-radial parts of the field could reflect particles back towards the Earth and hence maintain cosmic ray intensities above the background level for some hours.

McCracken and Palmeira (1960) reported a small cosmic ray enhancement which took place on 17 July 1959. This event occurred during the recovery phase of a Forbush decrease. McCracken and Palmeira compared the features of this event with those of the six previous events. They summarised the main features of the first six events by the following:

- Cosmic ray intensity increases rapidly to a maximum within ~15–100 minutes of the observation of electromagnetic radiation from the flare site. The smooth decline to pre-increase intensity has a much longer timescale than the rapid rise.
- The particle spectrum is steep.
- Small differences (up to ~10 minutes) in onset times at different sites are explained by energy dependent arrival times with the high energy particles initially restricted to a small solid angle.

These characteristics were found to be common to each of the first six solar particle events, however the event of 17 July 1959 did not fulfil the first condition. The rise-time for this event was 6–8 hours and this caused some controversy over whether it should be interpreted in the same way as the other events. McCracken and Palmeira explained the atypical rise-time in terms of disordered magnetic fields between the Sun and the Earth. They considered the effect of plasma emitted

by the Sun carrying magnetic fields out through the largely radial interplanetary magnetic field. This was based on the model of Piddington (1958) and was expected to result in areas of disordered magnetic field surrounding the Sun due to remnants of ejected plasma. Clearly the position of these disordered fields with respect to the flare site and the Earth would determine their effect on the transport of solar accelerated particles to Earth. Three hypotheses were derived to account for different situations.

The first scenario was that an active group had passed central meridian some days prior to the particle event and was situated near the west limb. Plasma emissions that occurred while this group was near central meridian resulted in field lines connected to the active group and also enveloping the Earth as the plasma had already moved out beyond the Earth. These field lines would provide a path for any cosmic rays emitted during a solar flare to gain almost immediate access to the Earth. Small irregularities in the field would create some dispersion, the first particles travelling parallel to the field, and scattered particles arriving later in a roughly isotropic distribution.

The second scenario proposed by McCracken and Palmeira was the case of an active group within 40° of central meridian. Plasma emitted from this group would have produced a radial field, but this would not envelop the Earth. Cosmic ray particles emitted under such conditions would tend to follow the radial field lines, but some would diffuse through the (possibly disordered) field to the Earth. The arrival of such particles would be later than in the first case and isotropy would be reached sooner.

The third scenario was similar to the second with an active group within 40° of central meridian; however, in this case McCracken and Palmeira considered the effect of matter ejected 1–2 days earlier. This matter would envelop the Earth, depressing the galactic cosmic ray intensity in the early stages of a Forbush decrease. If accelerated particles were then emitted from the same solar region, they would have an easy pathway to the vicinity of the Earth but would then have to diffuse through the strong, disordered fields associated with the Forbush decrease. This would result in a long rise-time and isotropy would be reached rapidly. This interpretation was applied to the 17 July 1959 event.

McCracken and Palmeira classified the seven solar particle events into three categories according to the flare site and cosmic ray conditions over the preceeding days. They found that events in each of the three categories displayed the features expected from the scenarios outlined above. Those classified into the first category rose rapidly to maximum intensity, the second group had slightly longer rise-times and the third category exhibited a much slower rise.

Steljes *et al.* (1961) studied two solar particle events which occurred on 12 and 15 November 1960. They considered the models proposed by McCracken and Palmeira to see if they could explain the features of these later events. A combination of the second and third scenario described by McCracken and Palmeira was applied for the 12 November event. Steljes *et al.* suggested that looped field lines caused by a previous outburst were adjacent to the Earth, but not enveloping it. Some of the accelerated particles were assumed to travel along the looped field lines and become trapped inside the magnetic bottle. Others were thought

to diffuse through the magnetic fields surrounding the bottle region and produce a slow rise to maximum intensity at Earth. After reaching a peak, the cosmic ray intensity began to decline. During this time the magnetic bottle region was rotating with the Sun and sweeping round towards the Earth. As it intersected the Earth, the cosmic ray intensity increased at low energies (due to the trapped particles) reaching a second peak about 4 hours after the first. At the same time, the intensity of high energy cosmic rays decreased due to the exclusion of galactic cosmic rays from the magnetic bottle. Gradually equilibrium was regained due to diffusion of the solar particles outwards and the galactic cosmic rays inwards. Steljes *et al.* found this to be quite a satisfactory explanation of the two peaks observed in the cosmic ray intensity. The second event they studied occurred on 15 November 1960 while the effects of the Forbush decrease continued at high energies. Steljes *et al.* interpreted this to mean that the Earth was still inside the looped field structure which blocked the passage of galactic cosmic rays. The solar particle event produced a very fast rise in cosmic ray intensity and this was explained by collimation of accelerated particles into a focused beam along the looped field lines which provided fast access to the Earth. Some of the cosmic ray data for this event displayed pulsations in intensity. Steljes *et al.* suggested that this could be caused by particles continuing along the looped field lines and being reflected back by a magnetic mirror near the Sun. In this way the particles could oscillate back and forth along the field lines and produce pulsations in the intensity observed at Earth.

The analysis of cosmic ray data for all these events was based on paths through the geomagnetic field determined using a dipole representation of the field. The development of more sophisticated geomagnetic field representations allowed more detailed analysis of the response of Earth-based instruments and led to mathematical modelling of the spectrum and distribution of the solar accelerated particles. These advances are discussed in the next two chapters.

1.2 Solar flares and associated emission

Metric radio emissions give the greatest information about solar particle acceleration and release. This type of emission is divided into five classes according to spectral characteristics. Types II and IV are most significant in events which produce ground level enhancements (GLEs). Figure 1.1 shows radio emission frequency plotted against time after the start of the solar flare. The five types of metric radio emission (labelled Type I to Type V) occupy different regions of this plot. Individual events vary greatly and not all types of emission will be observed for every flare. Descriptions of types II, III and IV are given below.

1.2.1 Type II

Type II or slow-drift bursts begin between 5 and 20 minutes after the start of the solar flare, usually at the time of the flare maximum. The duration of type II bursts is approximately 10 minutes. The spectrum exhibits a slow, systematic drift of the

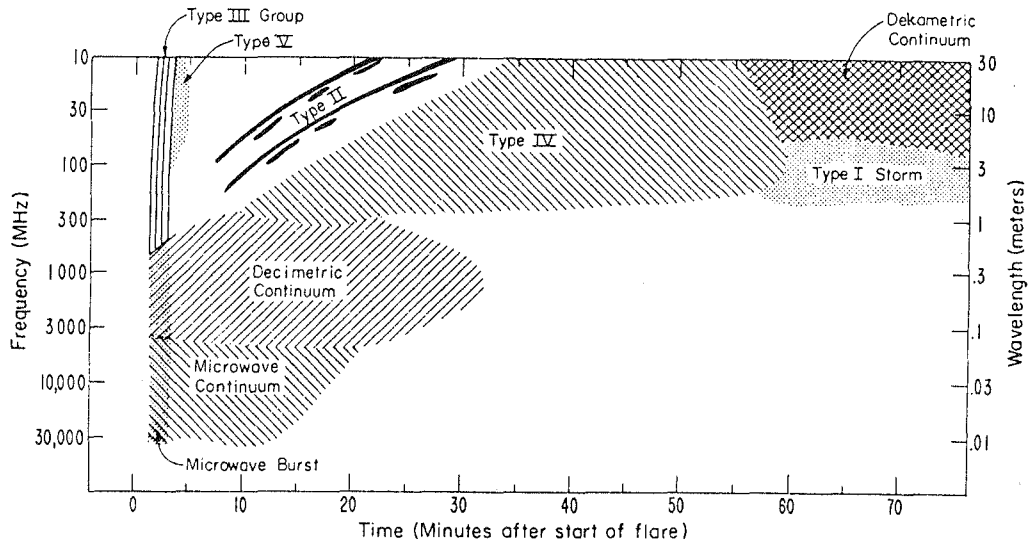

Figure 1.1: Plot of radio frequency of emission against time after start of flare. Metric bursts are labelled Type I to Type V. From Solar-Geophysical Data vol. 515 (suppl) p. 28, July 1987.

main features from high to low frequencies at about 1 MHz per second. Spectral features are sharp and often duplicated at twice the frequency, indicating emission of fundamental and second harmonics. The fundamental frequency rarely exceeds 150 MHz and the polarisation is random.

Type II bursts are very good indicators of shocks moving out through the corona (Dulk, 1985). Details of the emission mechanism are not known, but the emission frequencies are the fundamental and harmonics of the local plasma frequency.

1.2.2 Type III

Type III bursts are very common and often occur in the absence of flares. When the emission is associated with a flare, it usually occurs in a group of bursts at the start of the flare. Classical type III bursts begin at a frequency of a few hundred MHz and rapidly drift to lower frequencies. The emission is caused by high energy electron streams travelling outward at 0.1c to 0.5c which generate Langmuir waves which, in turn, are partly converted into radio waves (Dulk, 1985).

1.2.3 Type IV

The term spectral type IV is used to describe any form of continuum radio emission following a flare. This includes any persistent, smooth emission over a broad band of frequencies. Slow variations may occur and the emission may not be entirely free of bursts. Type IV events are relatively rare at metre wavelengths. They begin during the latter part of large flares, last for hours or days and are almost always preceeded by a type II burst. The time delay in the start of type IV emission after the start of type II bursts generally ranges from zero to about 30 minutes.

Occasionally the type IV emission may begin slightly before the type II burst.

Type IV emission actually encompasses at least three different phenomena. The so-called *early flare continuum* is related to type III bursts. The second variety is termed *moving*, as the source of this emission travels outwards from the region of the flare. These bursts typically last for a few tens of minutes, but durations as long as two hours have been observed. The emission usually exhibits partial circular polarisation. In a review of moving type IV emission, Stewart (1985) concluded that the most likely mechanism was a hybrid model including second harmonic plasma emission and gyro-synchrotron emission. A third kind of type IV emission is known as *stationary* and includes long-lived continuum storms which may last up to a day or more and sometimes develop into type I noise storms. The cone of emission is narrow and is rarely observed when the flare is near the limb. The emission is strongly circularly polarised and usually begins at ~300 MHz and drifts to lower frequencies. The emission mechanism is thought to be fundamental plasma radiation (Dulk, 1985). Both moving and stationary type IV emission have been shown to be associated with coronal mass ejections (Cane and Reames, 1988).

1.2.4 Particle acceleration

Solar flares are sometimes divided into two categories (known as impulsive and long-duration) according to the duration of soft X-ray emission and the types of electromagnetic radiation emitted. Cane, McGuire and von Rosenvinge (1986) summarised the differences between the two flare types. In brief, impulsive flares have smaller volumes, higher energy densities and do not appear to be associated with coronal mass ejections. The characteristics of associated particle events are also different from those of long-duration flares. The distinction between the types of particle events is due to the acceleration processes involved.

Kahler (1994) used the terms impulsive and gradual injection phases to identify the two acceleration processes. The impulsive phase may occur in both impulsive and long duration flares, but the gradual injection phase will only occur in the latter. The impulsive acceleration phase is a gyro-synchronous process which results in accelerated ions and electrons with enhanced $^3He/^4He$ and Fe/O ratios. This process is closely associated with type III bursts (Cane and Reames, 1988).

Kahler (1993) noted that nearly all large-flux solar energetic particle events (including GLEs) are produced during the gradual injection phase of long-duration flares. These are also associated with fast coronal mass ejections, so type IV emission is usually observed. The elemental abundances of the accelerated particles are the same as the ambient coronal material. It is generally accepted that shock acceleration is involved in these events (the presence of a shock is indicated by type II emission) (Lee and Ryan, 1986), however there is some dispute over whether the acceleration is carried out in a single coronal shock, or by two shocks, one in the corona and the other in the interplanetary medium.

Kahler (1994) investigated the role of the impulsive and gradual phases in high energy solar particle events (including some GLEs). Gamma ray observations indicate that protons can be accelerated to energies of greater than 1 GeV during the

impulsive phase (Mandzhavidze *et al.*, 1993), however, Kahler notes that the only GLE particles clearly associated with impulsive phase acceleration are neutrons.

The second question addressed by Kahler (1994) was whether one or two shocks were involved in gradual phase acceleration. Cane, von Rosenvinge and McGuire (1990) argued for a two-component model, finding two distinct features in the profiles of a number of events. Others, including Kahler, found no evidence for two shocks involved in the acceleration. Kahler concluded that the accelerated particles in GLEs are produced in coronal shocks. The two component events studied by Cane, von Rosenvinge and McGuire were observed at quite low energies and it is likely that in most cases, interplanetary shock acceleration would not be sufficient to produce a second component at ground level.

A further question related to coronal shock acceleration is whether particle injection is a delta-like process or takes place over a longer period of time. This argument stems from a desire to explain the duration and time profiles of solar energetic particle events. Reid (1964) explored instantaneous injection and coronal diffusion and found that this was satisfactory when accompanied by a trapping mechanism in the interplanetary medium. Bieber *et al.* (1986) further developed this idea, using coronal diffusion coupled with interplanetary focussed transport and found good agreement with observations. On the other hand, Debrunner *et al.* (1988) studied the same event as Bieber *et al.* and concluded that the acceleration process was probably not delta-like. They found some features of the event to be consistent with the extended injection models of Lee and Ryan (1986) who used different values of diffusion coefficients and time dependence of the injection rate to generate a variety of different time profiles. Clearly this question is still open to debate.

1.3 Thesis outline

The purpose of this work is to deduce features of solar particle acceleration and interplanetary propagation from modelled particle spectra and arrival distributions at Earth. This thesis describes the analysis and modelling of seven ground level enhancements. The historical development of GLE modelling is reviewed in Chapter 2 which also includes a description of the method for calculating asymptotic viewing directions. The procedure for dealing with neutron monitor data obtained at different atmospheric depths is also described. The iterative modelling procedure used by Smart *et al.* (1979) is outlined in Chapter 3 along with the improvements which have been made to this model for the work presented in this thesis. These include the incorporation of asymptotic directions calculated using a complex geomagnetic field model and the use of a least squares method to determine the best fit parameters. A review of geomagnetic field models is included, culminating with the Tsyganenko (1987; 1989) models which were employed by Kobel (1989) for calculation of asymptotic directions. Several different forms of pitch angle distribution are also described in Chapter 3.

Chapters 4 to 6 present the results of the GLE modelling. The responses of neutron monitors and surface muon telescopes during the 29 September 1989 GLE

have been modelled and these results are reported in Chapter 4. The incorporation of muon data into the modelling procedure is discussed, including the yield functions and geometric factors of the muon telescopes.

Three events which occurred in October 1989 are discussed in Chapter 5. The 19 October GLE exhibited a small spike in the onset at some stations. A similar spike was recorded later in the event. Modelling has been performed for the times of both spikes and during the main event. Mechanisms for producing the spikes and the main event are discussed. The 22 October event has been modelled extensively. The mechanism responsible for a highly anisotropic spike at the start of the event is discussed as well as the significant contribution later in the event from particles arriving from the anti-sun direction. The analysis of the 24 October GLE has been used to test rigidity dependence in the pitch angle distribution and three different functional forms for the particle spectrum.

The results of modelling three earlier events are presented in Chapter 6. The 12 October 1981 GLE was modelled with a bi-directional pitch angle distribution to investigate a possible looped structure in the interplanetary magnetic field. The probable presence of a magnetic cloud-like structure beyond the Earth during the 7–8 December 1982 GLE has been modelled by including an elliptical deficit region to account for the particles which encountered this feature while propagating towards the Earth. The 16 February 1984 GLE was a short-lived, anisotropic event. The pitch angle distributions derived are compared with the degree of anisotropy and scattering mean free path determined in previous analyses.

The results presented in Chapters 4 to 6 are discussed in Chapter 7. This includes comparison of scattering mean free paths and spectra. Possible improvements to the model and further work are also discussed.

Chapter 2

The Development of GLE Modelling

This chapter outlines the historical development of GLE modelling and sets into context the form of model used in the investigations reported in this thesis. Following the work of Forbush and others who established the solar origin of the particles responsible for GLEs, the next step concerns understanding the propagation of the particles from the Sun and the mechanisms which produce the anisotropies observed by ground-based instruments. Clearly this involves knowledge of both interplanetary and geomagnetic conditions. Only once these are satisfactorily accounted for can we concentrate on the actual form of the spectrum and spatial distribution of the arriving particles. The first part of this chapter presents the developments in understanding of the interplanetary magnetic field and its role in the transport of energetic particles from the Sun to the Earth. Following that, geomagnetic effects and the tracing of the paths of cosmic ray particles through the geomagnetic field are described. This leads to the definition of several terms related to cutoff rigidities which are used throughout the thesis. Finally, different GLE modelling techniques are discussed.

2.1 Interplanetary magnetic field

Since the first Earth-based observation of solar cosmic rays on 28 February 1942, attempts have been made to understand the transport mechanisms involved with solar accelerated particles travelling to Earth. Initially this was hampered by lack of knowledge of the intervening magnetic field structure. It was not until the advent of satellite observations that direct measurement of the interplanetary magnetic field (IMF) could take place, so the early ideas were entirely theoretical. For instance the method of calculating particle trajectories originated by Störmer and used by various other investigators was based on the assumption that particles initially move along a line parallel to the Sun-Earth line. Parker (1963) gave a historical overview of the progression of ideas relating to interplanetary phenomena. Cosmic ray variations provided indications of the changing IMF and were used to test many theories about its configuration. Of particular interest were the anti-correlation of galactic cosmic ray intensity with solar activity and

the cosmic ray decreases observed during geomagnetic storms following some solar flares. These observations were first made by Forbush (1954) and many theories attempted to explain them. One popular idea, dispelled by Parker, was that a static dipole field could exclude particles from the inner solar system, resulting in the observed variations when changes in the field strength occurred. Parker demonstrated that even slight irregularities in such a field would allow particles to 'leak' in and establish equal cosmic ray density inside and outside the field.

A major step in the understanding of cosmic ray variations and the IMF came with the idea of 'solar corpuscular radiation', clouds of plasma emitted by the Sun carrying magnetic fields out into interplanetary space. Morrison (1956) applied this idea in modelling the galactic cosmic ray modulation. He used Alfvén's theory of electric fields generated by ionised matter ejected from the Sun. It was suggested that the presence of plasma clouds and associated fields would shield the Earth from the galactic cosmic rays coming into the solar system. The increased occurrence of the solar corpuscular radiation with solar activity was used to explain the anti-correlation with galactic cosmic ray intensity.

Biermann (1951, 1952, 1953, 1957 as cited by Parker, 1963) proposed that the solar ejection of particles was a continuing process and not limited to individual eruptions associated with solar flares. This theory was based on observations of the acceleration of comet tails away from the Sun regardless of the orbital inclination of the comet. Greater acceleration was observed at times of high solar activity. Biermann's theory was that the acceleration was caused by a general streaming of particles outward from the Sun. He attempted to estimate the quiet-day flux of solar corpuscular radiation and combined this with estimates of the electron density near the Earth to achieve a solar corpuscular velocity of a few hundred km/s. Further investigations by Biermann and others (including Parker) concluded that the 'quiet time' corpuscular radiation was due to the normal dynamical processes occurring in the Sun. Parker postulated that the plasma in interplanetary space is a supersonic extension of the expanding solar corona and introduced the term 'solar wind'. He concluded that the result was an overall IMF with kinks and irregularities due to increased solar wind speed and magnetic variations associated with solar flares and other active regions. Parker went on to show that the IMF would take the form of an Archimedean spiral due to the rotation of the Sun. For an undisturbed field this resulted in an angle of about 60° between the lines of force and the radial direction at the orbit of Earth, based on a solar wind speed of about 300 km/s. It is now known that the average solar wind speed is more like 400 km/s which produces an angle of $\sim 45°$ between the magnetic lines of force and the Sun-Earth line. Parker (1961) also demonstrated that this field configuration could be distorted quite significantly by the presence of fast solar wind streams and other phenomena. He associated fast solar wind streams with solar flares; however, it is now accepted that the likely cause is most often a coronal mass ejection.

Parker's theories could not be tested until direct measurements of the IMF strength and direction were made by instruments on board satellites and other spacecraft. Observations made by Pioneer V and Explorer X confirmed that there was a spiral structure to the IMF (Piddington, 1962). Later, IMP1 enabled more

detailed data to be obtained. Ness *et al.* (1964) reported that the direction of the IMF was approximately along the calculated streaming angle with the field strength usually between 4 and 7 nT but sometimes as low as 1 nT or as high as 10 nT. Parker (1965) noted that the irregularities in the IMF measured by IMP1 were transported rigidly in the solar wind and were of similar scale to the gyroradii of some energetic particles. He questioned whether the irregularities were unrelated to each other, or were localised waves as this would relate to their effectiveness in scattering high energy particles.

Ness *et al.* noted a sudden reversal in the IMF direction during which the field strength passed through zero. Further observations revealed a long-lived sector structure which co-rotated with the Sun. Wilcox *et al.* (1980) interpreted such observations as the presence of a wavy neutral sheet separating the two hemispheres of opposite polarity. This neutral sheet has been found to affect the transport of energetic particles in the heliosphere.

Until recently, direct measurements of the IMF were limited to heliospheric latitudes within about 20–30° of the ecliptic. However the Ulysses spacecraft has now made measurements more than 80° from the ecliptic. Other craft are probing the outer reaches of the heliosphere and helping develop a full picture of the dynamics of the interplanetary region. Near-Earth satellites such as IMP8 enable measurement of the local IMF direction. This is essential if we are to fully understand the processes by which solar particles are transported to Earth.

2.2 Geomagnetic field effects

Understanding the IMF is only the first step towards modelling the propagation of solar particles to Earth. Once the particles reach the vicinity of the Earth their motion becomes governed by the geomagnetic field. Models of the geomagnetic field began as early as the mid 19th century with Gauss. He developed an analytical representation of the main dipole field using data from a ground-based network of observatories to determine numerical values of the coefficients. Later models incorporated high-degree spherical harmonics to better approximate the field (Rao *et al.*, 1963).

The first attempts at calculating the trajectories of solar particles through the geomagnetic field involved assumptions about arrival directions from the Sun that did not take into account the IMF as we know it today. By assuming that particles approached the Earth along a line parallel to the Sun-Earth line, the trajectory calculations resulted in *forbidden zones* near the poles of the Earth (Schlüter as cited by Firor, 1954). This is contrary to observation and reflects the inadequacy of the original assumption.

Various methods for calculating the trajectories of solar particles through the geomagnetic field were devised. Some were based on computations of the paths of negatively charged particles projected vertically away from the Earth, others involved model experiments where electrons were projected away from uniformly magnetised spheres. Assuming a point source for the solar particles, these calculations result in *impact points* for particles arriving at Earth. The effect of using

a finite source is to produce *impact zones*. Firor (1954) studied the events of 19 November 1949 and 28 February 1942 using the impact zone theory. He assumed a source which was isotropic over a finite area (*e.g.* $\sim 15°$ disc for 19 November 1949) and zero outside that area. His results were fairly consistent with the observed increases except that several high latitude stations outside the calculated impact zones recorded significant increases. This result was not surprising given the simplistic nature of the assumed source geometry. Incorporating a more complex source could not be justified as the detectors were of different types and therefore not directly comparable (McCracken, 1962). The introduction in 1956 and 1957 of standard neutron monitors for the International Geophysical Year[1] (IGY) made it possible to have directly comparable data from a world-wide network of detectors. Despite this, McCracken (1962) rejected the possibility of using a 'trial and error' method to improve the source function in Firor's analysis as this would be too time consuming.

McCracken also recognised that the centred dipole approximation to the geomagnetic field was inadequate. McCracken *et al.* (1962) calculated *asymptotic cones of acceptance*, the solid angle containing all the asymptotic directions of approach that contribute to the counting rate of a detector. The *asymptotic direction of approach* is defined as the direction of a particle's velocity vector before entry into the geomagnetic field (the boundary of the field was assumed to be spherical with a radius of 25 Earth radii). In order to accurately determine the asymptotic directions of particles their trajectories must be traced through the geomagnetic field.

For a spherical coordinate system the equations of motion for a charged particle in a magnetic field are

$$\left.\begin{aligned}
\frac{dv_r}{dt} &= \frac{e}{mc}\left(v_\theta B_\phi - v_\phi B_\theta\right) + \frac{v_\theta^2}{r} + \frac{v_\phi^2}{r} \\
\frac{dv_\theta}{dt} &= \frac{e}{mc}\left(v_\phi B_r - v_r B_\phi\right) - \frac{v_r v_\theta}{r} + \frac{v_\phi^2}{r tan\theta} \\
\frac{dv_\phi}{dt} &= \frac{e}{mc}\left(v_r B_\theta - v_\theta B_r\right) - \frac{v_r v_\phi}{r} - \frac{v_\theta v_\phi}{r tan\theta} \\
\frac{dr}{dt} &= v_r \\
\frac{d\theta}{dt} &= \frac{v_\theta}{r} \\
\frac{d\phi}{dt} &= \frac{v_\phi}{r sin\theta}
\end{aligned}\right\} \qquad (2.1)$$

where v_r, v_θ, v_ϕ are the velocity components, B_r, B_θ, B_ϕ are the magnetic field components, c is the speed of light, e and m are respectively the charge and mass of the particle and r is the radial distance from the centre of the Earth. This system of simultaneous differential equations can be integrated numerically if the components of the magnetic field B_r, B_θ, B_ϕ are known as explicit functions of r, θ, ϕ. McCracken *et al.* (1962) used the Finch and Leaton (1957, as cited by McCracken 1962) 6th degree spherical harmonic expansion, however any other

[1] An 18 month period from July 1957 to December 1958.

model can be substituted. The Finch and Leaton model was the most sophisticated available in the early 1960's.

Clearly, particles of different energies will follow different paths through the geomagnetic field. Rather than considering energy, it is useful to define particle rigidity as the relativistic momentum divided by charge. The units of rigidity are volts. Particles with equal rigidity will follow identical paths through the magnetic field. A cosmic ray particle travelling towards the Earth will follow the same path as a particle with opposite charge (but the same rigidity) travelling away from the Earth anti-parallel to the cosmic ray arrival direction. It is therefore useful to trace the trajectory of negative particles from points of interest on the Earth. The altitude for the starting point of the trajectory is taken as 20 km. Most cosmic ray particles undergo nuclear interactions at about this height and the secondary particles produced in these interactions will continue essentially undeflected by the geomagnetic field.

Given the position and velocity vectors of one point on a trajectory the equations of motion (2.1) can be used to give the coordinates of a subsequent point of the trajectory. Repeated applications produce a step by step determination of the trajectory. McCracken *et al.* (1962) used a modified Runge-Kutta integration method to do this. After each step, the value of the radial distance, r corresponding to the new point was examined. If this was less than one Earth radius (R_E), the trajectory had intersected the Earth and integration was terminated. The fact that a calculated trajectory re-enters the Earth indicates that the particular combination of rigidity and arrival direction associated with the trajectory is not accessible from outside the geomagnetic field. At a number of predetermined values of r, McCracken *et al.* compared the magnitude of the velocity with that of the initial velocity. Any discrepancy is indicative of systematic errors in the integration procedure. The magnitude of these errors is very sensitive to the step length in the Runge-Kutta process, so by reducing the step length it is possible to reduce the errors to an insignificant level. Integration was continued until r > 25.0 R_E. At this point, the position and velocity vectors are known and the direction of the velocity vector in geographic coordinates can be calculated:

$$tan(\Lambda) = \frac{-v_\theta sin\theta + v_r cos\theta}{\sqrt{v_\phi^2 + (v_\theta cos\theta + v_r sin\theta)^2}}$$

$$\Psi = \phi + \arctan \frac{v_\phi}{v_\theta cos\theta + v_r sin\theta}$$

where Λ and Ψ are the asymptotic latitude and longitude respectively.

McCracken *et al.* (1962) assumed that the asymptotic directions were invariant with respect to time, unless the geomagnetic field was significantly disturbed. Calculations were performed for trajectories of particles which had arrival directions at Earth at 16° and 32° from the zenith (azimuths of 0°, 90°, 180° and 270°) as well as those arriving vertically. These nine directions were chosen to represent regions which contribute approximately equally to the counting rate of the neutron monitor. This is justified by the work of Rao *et al.* (1963) who determined theoretically that the counting rate of a neutron monitor as a function of zenith angle (θ) is roughly in the ratio 1:4:4 for the annuli $0° < \theta < 8°$, $8° < \theta < 24°$ and $24° < \theta < 40°$.

Thus by dividing each of the outer two regions into four sections, nine regions are obtained each contributing equally to the count rate. Phillips and Parsons (1962) obtained experimental results which suggested a greater contribution from higher zenith angles. These results may have been contaminated and so were not conclusive. The use of the nine directions is considered satisfactory for neutron monitors, but not for instruments with higher mean energy of response. McCracken (1962) used the vertical and 32° zenith asymptotic directions determined by McCracken *et al.* to calculate mean viewing directions. He noted that the incorporation of a ring current into the magnetic field approximation may change some asymptotic directions by up to 15°, however it was not practicable at the time of McCracken's analysis to incorporate such corrections.

Current methods for calculating asymptotic directions are essentially the same as that of McCracken *et al.* except for the incorporation of different geomagnetic field models. Recent developments in this area are discussed in the next chapter and have been employed in modelling results presented in Chapters 4 to 6.

2.3 Cutoff rigidity terminology

The path of a cosmic ray particle through the geomagnetic field is dependent upon its rigidity and direction of motion. As a consequence of this there are minimum rigidities below which particles do not have access to particular sites on the surface of the Earth. These are known as *geomagnetic cutoff rigidities.* The cutoff at the geomagnetic equator is ~17 GV and decreases to almost zero at the poles. In order to determine geomagnetic cutoffs it is necessary to systematically calculate the trajectories of arriving particles as a function of rigidity.

Re-entrant trajectories have been described above as combinations of rigidity and arrival direction which are not accessible from outside the geomagnetic field. Considering one arrival direction at some point on the Earth and calculating a set of trajectories at decreasing rigidities there comes a point where the first re-entrant trajectory is encountered. The rigidity at which this transition occurs is known as the *upper cutoff rigidity*, P_U. At rigidities less than P_U there may be some re-entrant and some allowed trajectories until, below a certain rigidity (the *lower cutoff rigidity*, P_L), all trajectories are re-entrant. The rigidity region between P_U and P_L is called the *penumbra.* Some authors use the term penumbra to indicate the solid angle containing the set of arrival directions at a given rigidity within which re-entrant and allowed trajectories alternate. The former definition will apply throughout this thesis. Some stations, particularly those at low latitudes, do not exhibit a penumbral region in their asymptotic cones of view. In this case P_U is equal to P_L. The term P_U is often used to denote the upper limiting rigidity of an anisotropy. This is a completely different usage a will not be referred to in this thesis.

For those stations which do have a penumbral region it is useful to define the *effective geomagnetic cutoff rigidity*, P_c. P_c is defined such that if all trajectories above this rigidity were allowed and all trajectories below it were re-entrant, the resulting count rate of a cosmic ray detector would equal the actual count rate.

Theoretical values of P_c may be calculated from a linear average of the allowed rigidity intervals in the penumbra, or from functions weighted by the particle spectrum and detector response. In the case of a linear average, the effective cutoff rigidity, P_c, is given by

$$P_c = P_U - \sum_{P_L}^{P_U} \Delta P(allowed)$$

where trajectory calculations were performed at rigidity intervals of ΔP and only allowed trajectories are included in the summation. This definition of P_c will apply throughout this thesis and will often be referred to as simply the geomagnetic cutoff. The above definitions of P_U, P_c and P_L follow the conventions set down by Cooke *et al.* (1991).

The cutoff rigidities P_U, P_c and P_L for a particular site depend on the zenith and azimuth of the arrival direction, however it is commonly accepted that cutoffs for vertically incident particles may be quoted as typical of a particular site. All geomagnetic cutoffs stated in this thesis are for vertical incidence unless indicated otherwise.

Some sites have effectively zero geomagnetic cutoff. At such sites, atmospheric interactions determine the threshold rigidity for access. As particles propagate through the Earth's atmosphere their kinetic energy is reduced by interactions with atmospheric nuclei. In order to generate a response at an Earth-based instrument, particles must have sufficient energy to penetrate the atmosphere and undergo interactions to produce secondary particles. Individual particles will not lose equal amounts of energy while propagating through the atmosphere, therefore the minimum required energy to penetrate to sea-level is statistical in nature. The *effective atmospheric cutoff* is defined as the energy (or rigidity, P_{atm}) below which particles do not make a significant contribution to the count rate of a detector. This will depend upon the spectrum of arriving particles, but is usually thought to be about 450 MeV which corresponds to ~1 GV in rigidity. The actual value of the atmospheric cutoff is only of importance at sites where it exceeds the geomagnetic cutoff *i.e.* those at high magnetic latitudes. Clearly P_{atm} depends on altitude and is somewhat lower at sites such as South Pole (altitude 2820 m) than at sea level. This is an important consideration when modelling the response of cosmic ray detectors at such sites and is discussed further in Chapter 7.

2.4 GLE modelling

The particles which contribute most to the the increased counting rate during a GLE have rigidities between the effective atmospheric cutoff and about 3 GV. Significant contributions from higher rigidity particles may occur in GLEs with harder than average spectra or with a sufficiently large particle flux. Plots of asymptotic directions of approach for low rigidity particles calculated by McCracken (1962) showed that for most neutron monitors the asymptotic cone of acceptance is quite small compared with the total 4π of the celestial sphere (the extent in latitude and longitude being about 25° and 15° respectively). McCracken therefore used a

mean asymptotic direction of view to represent each detector in his GLE analysis. This assumption can be grossly wrong particularly for stations such as Hobart and others in equatorial regions (see Figure 5.7).

McCracken postulated that for detectors with identical response functions and small asymptotic cones of acceptance, the difference between counting rates must be due to different cosmic ray fluxes arriving from the various mean viewing directions. Since the IGY monitors were identical, a source function could be derived from the response of several detectors with small asymptotic cones of view and similar cutoff rigidities. McCracken also realised that if the solar particles were distributed isotropically the rigidity spectrum could be determined by comparison of the response at identical instruments with different cutoff rigidities. However, the distribution of the particles is often anisotropic, so he had to devise a more general method for spectral calculation. In fact he proposed two methods. The first involved having a neutron monitor and a muon telescope with small, overlapping cones of view (*i.e.* the same mean direction of view). Because the two types of monitor sample different rigidity ranges, a spectral exponent could be determined providing appropriate response functions were known for the two instruments. This method can only be used when both instruments record significant increases in count rate. Since the muon telescope response is dominated by high rigidity particles, a significant increase in count rate will only occur during the most energetic GLEs. The second method avoided using two different types of detectors and was based on the assumption that although the particle distribution may be anisotropic, the spectrum of particles would be the same in all directions. Detectors with small asymptotic cones of view were used to determine the directional dependence of the particle flux and this function was then used to compare the response of two detectors with larger viewing cones and differing cutoff rigidities enabling the calculation of the spectral exponent.

Calculations such as those performed by McCracken (1962) rely on a knowledge of the response of instruments to incoming particles. McCracken stated that the enhancement ΔC in counting rate at time t produced by solar cosmic rays is given by

$$\Delta C = \sum_z \int_{P=0}^{\infty} \oint J(P, \mathbf{A}(P,\theta,\phi), t) S_z(P,\theta,\phi) d\Omega dP$$

where $\mathbf{A}$ is the unit vector describing the asymptotic direction of approach of a particle of rigidity P, (θ, ϕ) specifies the arrival direction of the particle, J is the source function, S_z is the specific yield function and $d\Omega$ is an infinitesimally small solid angle, integration over Ω covering the hemisphere above the horizon.

The specific yield functions of neutron monitors give their response to particles arriving at the top of the atmosphere. This may be determined from latitude surveys or by simulation of the nucleonic cascade in the atmosphere (Lockwood *et al.*, 1974). The yield function used by McCracken was calculated from a latitude survey. This method uses the variation of cutoff rigidity with latitude to determine the response at different rigidities. The yield function must therefore be extrapolated above about 17 GV (the geomagnetic cutoff rigidity at the magnetic equator), however particles with rigidity above this level make little or no contribution to events such as those studied by McCracken. Many modifications

have been made to the specific yield functions for neutron monitors since the time of McCracken's work. One such function generally accepted as the best for use in the modelling of enhancements of solar origin was calculated by Debrunner *et al.* (1982). This is significantly different to that used by McCracken in the low rigidity range in which most solar accelerated particles fall. McCracken's results may have been improved by the use of a more appropriate yield function, however using more sophisticated representations of the geomagnetic field in calculation of the asymptotic directions of approach would seem to be of greater significance.

During the mid 1960's it became clear that the solar wind caused distortion of the geomagnetic field, compressing the field lines on the dayside and producing a tail on the nightside (Ness *et al.*, 1964). Clearly this asymmetry, as well as the effects of currents in the magnetopause and the neutral sheet of the geomagnetic tail, results in variations in the asymptotic viewing directions of the cosmic ray detectors as the Earth rotates (Ahluwalia and McCracken, 1965; Gall, 1968; Gall *et al.*, 1969). Once this was recognised, attempts to analyse GLEs used asymptotic directions calculated for the specific time for which they were modelling (eg. Smart *et al.* 1971, Duggal *et al.* 1971). While this represented a significant improvement in the accuracy of the calculated asymptotic directions, it still did not take into account the changes in the various currents and solar wind speed with time. The geomagnetic field models used by Smart *et al.* (1971), Duggal *et al.* (1971) and others only represented the undisturbed field so could not account for the increased distortion at times of greater geomagnetic disturbance, however they did take into account the time of day.

After calculating the asymptotic viewing directions of detectors, it is necessary to convolve these with a source function. This is generally assumed to be symmetric about the 'garden hose' field line which connects the Earth to the Sun. Under average conditions, this field line has a 'footpoint' on the Sun approximately 60° from central meridian and intersects the Earth at about 45° to the Sun-Earth line as shown schematically in Figure 2.1. The shape of this field line can vary considerably due to changes in the solar wind speed and other interplanetary phenomena. The propagation of charged particles in the IMF results in a distribution of pitch angles. In order to model this distribution it must be described in a functional form. The early source functions were very simple and did not reflect the complexity of propagation through the interplanetary medium. Duggal *et al.* (1971) were the first to suggest a cosine function for the pitch angle distribution. They used a geomagnetic field model which incorporated the effects of external field sources and calculated a mean viewing direction for each detector as an approximation to the asymptotic cone of view. This enabled them to calculate the particle spectrum and the position of the axis of symmetry of the pitch angle distribution. The method involved an iterative process, choosing different positions for the axis of symmetry and finding the best fit coefficients m and C for the pitch angle distribution $\mathrm{I}_i = m\cos\delta_i + C$, where I_i is the normalised intensity and δ_i the angle between the axis of symmetry and the mean asymptotic direction for the ith detector. C represents the intensity of particles arriving from directions which subtend an angle of 90° with respect to the source. The particle spectrum was assumed to be a power law in rigidity and was determined by normalising

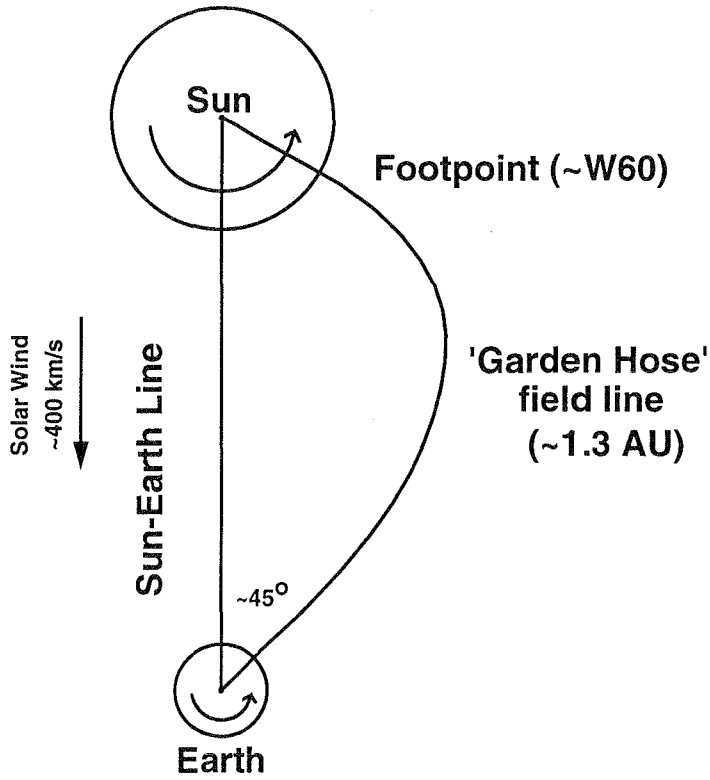

Figure 2.1: Schematic representation of the 'garden hose' field line (from Duldig, 1994).

the response at each station using the derived pitch angle distribution. Duggal *et al.* admitted that there may be quite a degree of uncertainty in the resulting spectrum due to the yield function for neutron monitors being poorly defined at rigidities less than about 1.5 GV.

Smart *et al.* (1971) analysed the same event as Duggal *et al.* (1971) but instead of approximating the asymptotic viewing direction of each station by one mean direction, they incorporated into their model the individual viewing directions at selected rigidities. Some assumptions involved in the model were that the interplanetary magnetic field has an average direction defined by the solar wind and that the direction of the particle anisotropy is along the interplanetary field direction. The *average* particle motion was also assumed to be along the interplanetary magnetic field direction, but the actual particle pitch angle distribution was defined by a function, symmetric about this direction. The aim of the analysis was to choose appropriate spectra and anisotropy functions such that when these were multiplied by the neutron monitor specific yield function, the observed cosmic ray increases at Earth were reproduced. An iterative process was used to test many different combinations of variables until a satisfactory solution was obtained. The analysis was performed for each two minute interval throughout the event. The derived particle pitch angle distribution was of gaussian form. This form was used

because of its compatability with diffusive propagation models and other stochastic processes. Furthermore, no other function (including a cosine relationship) was found to give as good a fit to the observed data. This method of analysis is outlined by Smart *et al.* (1979) in their description of the analysis of the 7 May 1978 GLE. Once again the gaussian pitch angle distribution was found to give the best fit to the observed cosmic ray increases, however increases at some stations viewing in the anti-sun direction were significantly under-estimated by the model. It was suggested that the increases at these stations may be supplemented by particle scattering occurring beyond the Earth. The investigators were unable to find a pitch angle function which could adequately model the increases at these stations. Another instance of 'reverse' particle propagation was found in the event of 7-8 December 1982 as modelled by Smart *et al.* (1987). In this case they chose to derive a separate 'reverse flux pitch angle distribution' as well as the normal 'forward flux distribution', again using a gaussian form for the distributions. Further quantitative improvements in GLE modelling occurred with the introduction of an exponential form for the pitch angle distribution (Smart and Shea, 1990). In modelling the 23 February 1956 GLE they found the exponential form to be superior to the gaussian distribution.

2.5 Atmospheric corrections

The GLE modelling methods outlined above rely upon the observed increases at each station being directly comparable. This is not true if stations have significantly different atmospheric pressures *e.g.* stations at different altitudes and polar locations compared with those near the equator. Ideally a yield function which depends upon the atmospheric depth should be used, however it is possible to get a similar result by applying suitable pressure corrections to the data. We can define an attenuation length to represent the absorption of particles by the atmosphere. This depends upon the spectrum of the particles, therefore the attenuation lengths of solar and galactic cosmic rays are not the same. Since both galactic and solar particles are present during a GLE a method which incorporates the attenuation lengths of both populations is required.

Attenuation lengths for galactic cosmic rays have been determined for most neutron monitor stations and are routinely used to correct data to standard atmospheric pressures. The attenuation length for the solar particles observed during a GLE (the flare attenuation length) must be calculated for that particular time as each GLE will have a different particle spectrum. The flare attenuation length may be calculated by comparing the response at two stations at different altitudes but with essentially the same viewing directions. Examples of such pairs of neutron monitor stations are Mt. Wellington and Hobart, Mt. Washington and Durham, Jungfraujoch and Bern. Wilson *et al.* (1967) demonstrated the procedure by which this calculation is made.

Since both galactic and solar particles are exponentially absorbed by the atmosphere, the relationship between intensities at sea level and altitude are

$$I_s(SL) = I_s(alt) \exp(-\alpha \Delta p)$$

$$I_g(SL) = I_g(alt) \exp(-\beta \Delta p)$$

where I_s and I_g are the intensities of solar and galactic particles, SL and alt represent stations at sea level and altitude respectively, α and β are the pressure coefficients for solar and galactic particles and Δp is the pressure difference between the stations. These relationships lead to

$$\frac{\Delta I_s(alt)}{\Delta I_s(SL)} = \exp\left[(\alpha - \beta)\, \Delta p\right] \tag{2.2}$$

where ΔI_s, the percentage increase observed is defined as

$$\Delta I_s = \frac{I_0 - I_g}{I_0} \times 100$$

and I_0 is the total measured intensity. If β is known, then α may be calculated from Equation 2.2.

McCracken (1962) states that the fractional increase in counting rate corrected to standard pressure is

$$F = \left\{ \frac{C_E}{C_0} \exp\left(\frac{\delta P}{\lambda_f}\right) - \exp\left(\frac{\delta P}{\lambda}\right) \right\} \exp\left(\frac{P_0 - P}{\lambda}\right) \tag{2.3}$$

where C_0 and P_0 are the mean counting rate and pressure prior to the GLE increase, C_E and $P_0 + \delta P$ are the counting rate and pressure at some time during the event, P is the standard pressure, λ_f is the flare attenuation length (α^{-1}) and λ is the attenuation length derived from α and β by the relationship

$$\lambda = \frac{1}{\alpha - \beta}$$

Equation 2.3 can be used to correct the fractional increase observed at an altitude station to sea level pressure. In this case the equation becomes

$$\Delta N(SL) = \Delta N \exp\left(\frac{P - P_{SL}}{\lambda}\right)$$

where ΔN and $\Delta N(SL)$ are the increases at altitude and sea level respectively, P and P_{SL} are the corresponding atmospheric pressures and λ is the attenuation length as defined above. The value of P_{SL} is the atmospheric pressure at equatorial sea level, *i.e.* a standard atmosphere.

2.6 Summary

The historical development outlined in this chapter sets into context the form of GLE model used in the investigations presented in this thesis. The modelling procedure outlined by Smart *et al.* (1979) incorporated the best available geomagnetic field model and used the full asymptotic cones of view rather than discarding information by approximating these by effective viewing directions. Atmospheric correction by the two attenuation length method described in Section 2.5 is used

in all analyses presented here. The modelling method used in this thesis is based on that of Smart *et al.* Significant modifications are described in the next chapter including the use of a geomagnetic field model which incorporates disturbance of the field as well as the introduction of a least squares method to determine the fit parameters. These two modifications have enabled the introduction of more complex functional forms to describe other elements of the model such as the pitch angle distribution. The development of functional forms of the pitch angle distribution is also discussed in the next chapter.

Chapter 3

Improvements to the Model

The model used in this thesis is based on that of Smart *et al.* (1979). This chapter discusses the improvements made to that model. The first of these is the use, for calculation of asymptotic directions, of a geomagnetic field model which accounts for distortion of the field during times of geomagnetic disturbance. Secondly, a least squares method for determining the best fit parameters was incorporated. The combined effect of these two modifications is to allow more complexity to be introduced in other parts of the model. By using a better representation of the geomagnetic field, the accuracy of the calculated viewing directions is improved, allowing a more realistic determination of the predicted response of cosmic ray detectors to the incident particles. The use of a least squares method eliminates the 'trial and error' of adjusting parameters 'by hand' and more parameters can be incorporated without making the problem too cumbersome. This has enabled experimentation with different functional forms for the pitch angle distribution. It has been noted that several events have a significant contribution from particles reflected from beyond the Earth (Smart *et al.*, 1979; Smart *et al.*, 1987; Humble *et al.*, 1991) so that the pitch angle distribution may in fact have two peaks, one centred on the local interplanetary magnetic field line and the other 180° away. This effect has been modelled with a pitch angle distribution which is the sum of two distributions, one centred on the 'forward' direction and the other on the 'reverse'. The rigidity dependence of the pitch angle distribution has also been investigated.

Most other GLE models have considered the neutron monitor response to particles with vertical incidence. In all the models presented here, the full viewing cone has been approximated by nine approach directions at the neutron monitor. This has been found to be important for highly anisotropic events (Cramp *et al.*, 1995).

3.1 Geomagnetic field

The geomagnetic field in undisturbed form has an underlying dipolar configuration, but is compressed on the dayside and expanded on the nightside as a result of interaction with the solar wind which produces various current systems on the boundaries and within the magnetosphere. The internal component of the field

may be represented by centred or eccentric dipole models, but a more accurate spherical harmonic series is usually employed.

The International Geomagnetic Reference Field (IGRF) is a series of models of the main geomagnetic field, each consisting of a set of spherical harmonic coefficients (Kodama, 1992) for a series expansion of the geomagnetic potential, V. This is of the form

$$V = a \sum_{n=1}^{N} \sum_{m=0}^{n} \left(\frac{a}{r}\right)^{n+1} \mid g_n^m \cos m\phi + h_n^m \sin m\phi \mid P_n^m(\cos\theta)$$

where the g's and h's are the IGRF coefficients, a is the mean radius of the Earth, r is the radial distance from the centre of the Earth, ϕ is the east longitude measured from Greenwich, θ is the geocentric colatitude and $P_n^m(\cos\theta)$ is the associated Schmidt normalised Legendre function of degree n and order m (Cain *et al.*, 1967). In principle N should be infinite, but the available data do not justify values of N greater than 10 for most epochs (Kodama, 1992).

IGRF coefficients are found by least squares fitting of the model to databases obtained from ground, marine, air and satellite measurements (Tsyganenko, 1990). A set of coefficients has been calculated for each five year period from 1945. The most recent IGRF available at the time of this work was a predictive model for 1990-95 based on the secular variation of the parameters and measurements taken no later than one or two years prior to the epoch. Once data for this period have been collected, the coefficients will be revised and the new model will become the Definitive Geomagnetic Reference Field (DGRF) for that epoch. DGRF models are currently available for 1945 to 1985. The 1990 model is not yet classified as a DGRF. Linear interpolation between coefficients for the different epochs and extrapolation from the most recent IGRF allows determination of the model for any given time.

The IGRF gives a good representation of the component of the geomagnetic field due to the Earth's core, however additional external magnetic field models are needed to account for the effects of the various current systems flowing within the magnetosphere. The major current systems are the magnetopause current, tail current, neutral sheet current, field aligned (Birkeland) currents and the ring current, illustrated in Figure 3.1. These current systems result in diurnal and seasonal variations in the field (Tsyganenko, 1990).

The magnetopause current results from the deflection of solar wind plasma by the dayside magnetosphere. This is a Lorentz force effect, so protons and electrons are affected oppositely resulting in a current in the dawn to dusk direction. The magnetopause current is 'closed' either by the tail current or field aligned currents through the dayside high latitude ionosphere.

The tail currents are due to a Lorentz force produced as the solar wind flows across the open field lines in the magnetotail. The currents are confined to the outer reaches of the tail as it is only there that a component of the magnetic field is perpendicular to the direction of flow of the solar wind plasma. The tail currents result in a dawn to dusk electric field across the magnetotail, effectively creating a magnetohydrodynamic generator which extracts kinetic energy from the solar wind. The J×B force resulting from the tail currents confines the tail

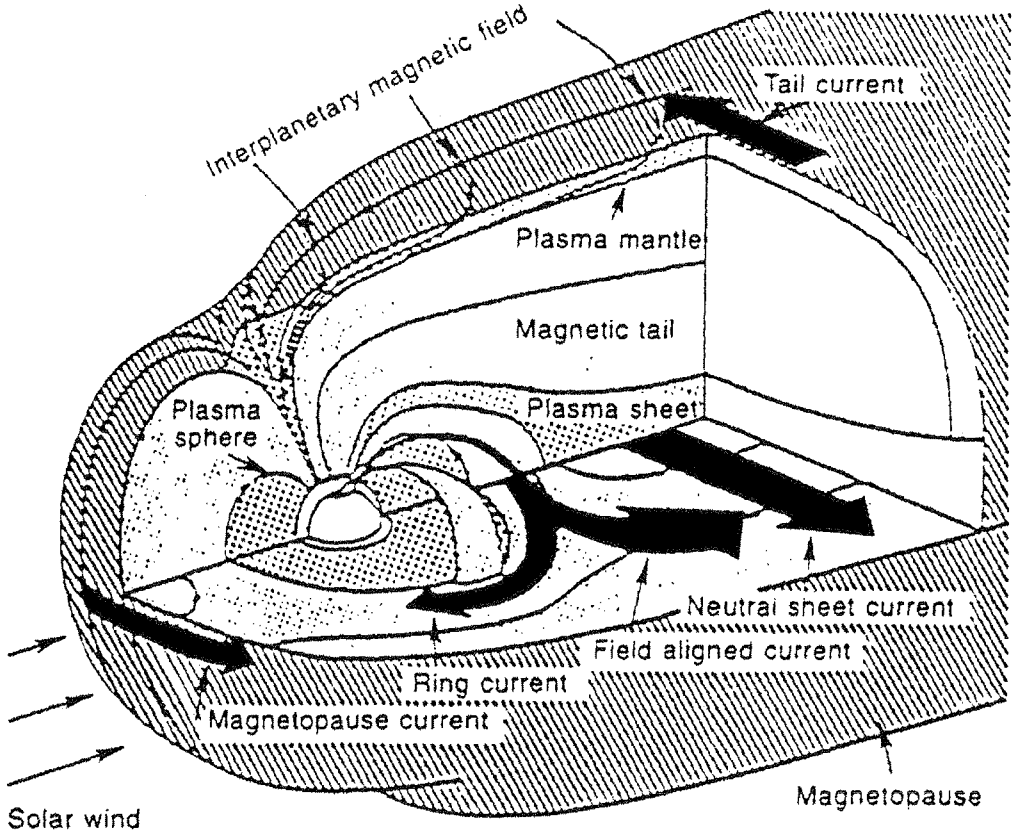

Figure 3.1: Schematic representation of the current systems flowing in the magnetosphere. From Potemra (1984).

plasma to a sheet. It is across this sheet that the neutral sheet current flows as a discharge of the dawn to dusk electric field across the tail. This electric field can also drive a field aligned current through the auroral oval due to the enhanced conductivity of this region associated with the increased ionisation resulting from auroral precipitation.

The ring current is a gradient drift effect. The magnetic field is strongest close to the Earth, so as particles gyrate along field lines from one hemisphere to the other they encounter a gradient in the magnetic field. This gradient causes the particles to flow around the Earth with protons and electrons moving in opposite directions thus producing a clockwise current as viewed from the north.

These currents all contribute to the external magnetic field. Since the field strength due to the core decreases as r^{-3}, beyond about 10 R_E the field is dominated by the external components (Tsyganenko, 1990). The outer regions of the magnetosphere are also the most variable since the strength of the currents is closely connected with the highly variable solar wind conditions. It is therefore important to generate a model which can account for these variations as satisfactorily as possible given the available data. Tsyganenko (1990) outlines the effect of the current systems and the attempts to account for them in many magnetospheric

models. Such models are fitted to sets of field measurements divided up according to the level of field distortion. One measure of distortion which is often used is the Kp index. This index is determined by the amplitude ranges of two horizontal geomagnetic components measured over 3-hour intervals. Measurements are made at eleven observatories and standardised to eliminate local time effects. The Kp index follows a quasi-logarithmic scale. The values of Kp range from 0 to 9 with intermediate levels sub-divided into three ranges for each integer value *i.e.* 0, 0+, 1−, 1, 1+ ...9−, 9. Descriptions of the measurement and calculation of Kp and other planetary indices can be found in Menvielle and Berthelier (1991).

3.1.1 Modelling magnetospheric current systems

Magnetopause current

The magnetopause current sustains the balance between the external pressure due to the solar wind plasma and the internal magnetic pressure of the magnetosphere. Early models of its effect were based on numerical treatment of the pressure balance equation (Tsyganenko, 1990). These models were restricted to the case of zero geodipole tilt and resulted in separate representations of the field in the quasi-dipole and tail regions of the field.

Instruments on board satellites and space probes have provided a considerable body of experimental evidence on the actual location of the magnetopause. This has resulted in alternative approaches in which the shape of the magnetopause is specified by an appropriate function incorporating a parametric dependence on solar wind pressure. One major advantage of this method is that it is possible to incorporate the geodipole tilt. Several investigators have used a paraboloid to specify the shape of the magnetopause. This can be described by two parameters which depend on the solar wind pressure. A similarity factor can be determined to avoid re-calculation of the model for each new pair of parameters. These models have produced satisfactory agreement in the near Earth regions, but not beyond ~20 R_E tailwards (Tsyganenko, 1990). A better functional shape for the magnetopause is an ellipsoid. Models employing this shape are satisfactory to ~40-50 R_E into the magnetotail (Tsyganenko, 1990). Composite shapes such as a semi-infinite cylinder capped by a hemisphere on the dayside have also been employed, but some mathematical complications arise due to the composite form of the function. Alternatively, numerical methods can be used to determine currents, thus allowing the incorporation of boundaries with a more general shape. This has the advantage of not forcing the model magnetopause to take on a predefined shape, but it can be difficult to find a simple analytical approximation for the magnetic field corresponding to the numerical form of the current system.

A third major type of model of the field associated with the magnetopause current system is based on the formal adjustment of appropriate fictitious magnetic field sources. While this may yield a reasonable distribution within the modelling region, the models are generally not satisfactory beyond this and usually do not properly simulate the geodipole tilt effects (Tsyganenko, 1990).

Magnetotail currents

Modelling the field due to the magnetotail currents has been approached on many occasions via the 'inverse problem' (Tsyganenko, 1990) using assumed forms of the current systems to generate models of the magnetic field. This is a problematic approach as there are no experimental data to suggest the correct form for the current systems, while there are experimental measurements of the magnetic fields. Over-simplification of the model current can lead to a considerable loss of information potentially present in the magnetic field data sets, while comparatively high levels of noise in the data impose upper limits on the reasonable number of degrees of freedom and hence the complexity of the current system models.

Mead and Fairfield (1975) proposed a simple model which incorporated the fields from the current sheet and magnetopause in a single set of analytical expressions containing polynomials in solar magnetic coordinates. They also included a linear dependence on geodipole tilt. The model has 14 free parameters and is divided into four subsets according to different levels of Kp. This model reflects only the most general features of the real magnetosphere and does not reproduce the sheet-like structure of the tail current (Tsyganenko, 1990). Similar methods with different functional forms have been employed by others (*e.g.* Kosik, 1984), but without any clear physical interpretation for the choice of function.

Another popular form of modelling involved the use of mathematical transforms to stretch the tail field. Such a model proposed by Voigt (1984) provides good agreement with the observed field line structure, however simplifying assumptions lead to a zero current density along the x_{GSM} axis resulting in inadequate modelling of the near tail magnetic structure. A different approach was taken by Tsyganenko (1989) who considered the modification of an appropriate vector potential. This model incorporated the effect of warping in the current sheet and is described in more detail later in this chapter.

Field aligned current systems

The field aligned current systems play an important role in the transfer of energy from the solar wind to the ionosphere, but there is still only limited understanding of the physical mechanisms responsible for their generation (Tsyganenko, 1990). The field aligned currents in different parts of the magnetosphere have vastly different spatial scale thus a common scale length cannot be defined for the purposes of modelling. In the remote regions of the magnetosphere, the field aligned currents may be distributed over a volume on the scale of tens of R_E while at ionospheric heights their dimensions do not exceed a few hundreds of kilometres in latitude and a few thousands of kilometres in longitude.

Modelling of these current systems requires a special choice of vector potential. A representation of the magnetic vector as the sum of toroidal and poloidal components has been successful in producing a rather crude model. This provides sufficiently good results only in the near Earth region, $R \lesssim$ 5-7 R_E (Tsyganenko 1990 and references therein).

Ring current

Tsyganenko (1990) discussed the progression of models for the ring current beginning in the early 1960's just after the discovery of the radiation belts. These models involved many simplifying assumptions which are no longer thought to be valid. Most of the models generate axially symmetric ring currents, however experimental data suggest a continuous merging of the tail current sheet with the ring current on the nightside. Tsyganenko and Usmanov (1982) addressed this problem by the incorporation of the partial ring current. This was also included in the later Tsyganenko models (Tsyganenko, 1987; Tsyganenko, 1989) which are discussed in the next section.

3.1.2 Tsyganenko magnetospheric models

The Tsyganenko models are described in Tsyganenko (1987) and Tsyganenko (1989), hereafter referred to as T87 and T89 respectively.

The T87 model represents external magnetospheric sources by three terms: (i) ring current; (ii) magnetotail current system including the plasma sheet current and return currents; (iii) remaining external sources including magnetopause currents and an averaged contribution from the large-scale field-aligned current systems.

The ring current is assumed to be aligned with the dipole equatorial plane. The magnitude of the field depression produced at the centre of the ring current is represented by one linear parameter. The second parameter in this term is non-linear and defines the scale size of the current distribution.

The tail current system is represented as the result of integration over a continuous distribution of axially symmetric diffuse current filaments. The function has three linear and two non-linear parameters. The return current system is simulated by a pair of current sheets parallel to the central one and located about 30 R_E above and below the equatorial plane. The distance of 30 R_E is used because it is of the order of the asymptotic tail radius. In order to restrict the current sheet width in the dawn-dusk direction, the field components are multiplied by an even function which tends to zero as $y \rightarrow \pm\infty$. This allows a smooth, continuous transition in the current flow line distribution from the ring current to the plasma sheet. The magnetotail cross-section forms two closed loops encircling the tail lobes.

The remainder of the external field (including the field of magnetopause currents and an averaged contribution from the large-scale system of field-aligned currents) is represented by polynomials in y and z (GSM coordinates) which also contain an exponential term in x and the sine and cosine of the geodipole tilt angle. There are two different scales of exponential, the second with half the scale length of the first. This allows resolution of finer details from the large scale background.

The complete model has 26 linear parameters (of which 20 are independent) and 10 non-linear parameters, three of the non-linear parameters are fixed to constant values and one is not independent. The resulting 20 linear and six non-linear parameters were determined from fits to six sets of data corresponding to different levels of Kp. The Kp sub-ranges were merged to produce statistically

significant data sets (*e.g.* 1–, 1 and 1+ are merged to form a single set labelled 1). The sixth data set includes all Kp values above 5. The data sets were obtained from the IMP and HEOS satellite measurements of the field.

T87 also includes a 'truncated' version of the model. This model is based upon data points with $x_{GSM} \geq -25$ R_E and includes several simplifications which decrease the number of parameters required to describe the model. A more detailed division of the Kp index scale was also used in sorting the data into subsets. One significant difference is the omission of the larger of the two scale lengths in the third term described above. As a result, the 'truncated' model gives better results for the dawn to dusk sectors of the near magnetotail region at high Kp levels. The truncated model is therefore recommended for use in the region $x_{GSM} \gtrsim -30$ R_E.

Fairfield (1991) compared the results of T87 with observations looking for any systematic deficiencies. He found that on the dayside in the high-latitude cusp region the model frequently predicts too large a field strength. This is thought to be due to the inability of the models to account for the diamagnetic currents associated with the relatively dense plasmas of this region. There are also large spatial gradients and a tendency for the cusp position to change in response to solar wind conditions and magnetospheric activity. Fairfield also notes that the effects of solar wind pressure are only partially removed by Kp-dependent models, this is important in determining the tail lobe field strength. The T87 model is shown to produce a tail configuration which is not as stretched as the observed field. This lack of field line stretching is also evident in the dawn and dusk meridians.

A major difference between the T87 and T89 models is the introduction of warping of the tail current sheet in T89. For non-zero tilt angle, Ψ, the current sheet undergoes two dimensional warping. Near the midnight meridian plane the warping results in a gradual departure of the current sheet from the dipole equatorial plane towards the plane parallel to the solar wind stream. For $\Psi > 0$ this is accompanied by a bending of the sheet which results in the current surface being raised above the equatorial plane in the central tail region, whereas it is depressed below the plane near the flanks (vice-versa for $\Psi < 0$). No effects of current sheet warping were included in T87, instead the current sheet as a whole was shifted along the z_{GSM} axis.

In T87, modelling of the current sheet was based on analytic solutions for an infinitely thin disc in the $z_{GSM} = 0$ plane. In the T89 model, the discontinuity in B_x at $z_{GSM} = 0$ was removed to achieve a characteristic half-thickness scale, D. This produces a non-zero current in the whole space, but the current density goes rapidly to zero for $z_{GSM} > D$. By adding a dependence of D on x_{GSM} and y_{GSM}, current sheet warping can be modelled.

It is assumed that the ring current and tail current form a united sheet-like system in the near nightside magnetosphere. At relatively small geocentric distances the current sheet nearly coincides with the dipole equatorial plane and gradually departs from it at larger distances, approaching asymptotically a plane parallel to that of the solar magnetospheric equator. The model is based on the vector potential for the warped current disc matched with the dipole equatorial plane near the Earth.

The function describing the nightside current sheet contains two free parameters related to (i) the characteristic distance to a region where the current sheet warps and (ii) the degree of transverse bending of the sheet. The axis-symmetric disc generated by the model extends over all local times, therefore some modification is necessary to redistribute the current from the dayside and confine the main current sheet to the tail region. This is done in two ways, firstly the function D(x,y) for current sheet thickness is chosen such that the sheet becomes thicker on the dayside and the flanks of the tail. Secondly, the vector potential of the disc is multiplied by a 'truncation' factor which equals unity in the central tail region, but smoothly drops off to zero towards the magnetopause region as well as for $|y| \rightarrow \infty$. The result is that the total current is depressed through the dayside magnetosphere and is localised within a thin, warped sheet on the nightside.

The remainder of the ring current is represented by a similar current disc with possible effects of day-night asymmetry incorporated by allowing the thickness of the sheet to vary (as in the tail sheet model). Eleven free parameters are obtained for the ring and tail current sheet models including radial scale lengths to maxima in the current, scale lengths and position of steepest descent for the 'truncation factor', increments of current sheet thickness between dayside and nightside and parameters which describe the shape of the warped current sheet. T89 indicates that fine detail in the near Earth tail cannot be successfully modelled due to the relatively high level of noise in the data and the low density of data points.

The return currents closing the central tail current across the high latitude magnetopause regions are simulated by a pair of planar current sheets parallel to the GSM equatorial plane. The current is assumed to consist of two components, symmetric and anti-symmetric with respect to the dipole tilt angle. The four non-linear parameters in the model were fixed at values chosen from *a priori* considerations and test runs. Two linear parameters were fitted.

The contribution from magnetopause currents and that from other sources (including field aligned currents) were modelled in the same way as in the 'truncated' T87 model. Major improvements of the model concern the nightside part of the ring current. The main result here is that a significantly depressed field and hence more stretched force line pattern is obtained in the near magnetotail region.

There are conflicting opinions regarding modelling of the magnetotail by the T87 and T89 models. As mentioned above, Fairfield (1991) concluded that T87 lacked sufficient tailward stretching and therefore predicted the B_z component to be larger than measured values. Kayser and Fairfield (1991, cited by Peredo *et al.*, 1993) reached similar conclusion concerning the T89 model. On the other hand, several others (Peredo *et al.*, 1993 and references therein) found that both T87 and T89 underestimated B_z in the region x_{GSM} = -10 to -22 R_E and thus exhibited too much stretching in the near-tail region. The key to this conflict appears to be the different data sets used to compare the measured field with that predicted by the models. Flaring of the tail field lines results in a decrease in B_z with increasing distance z from the middle of the of the tail current sheet. Since most IMP and HEOS tail data have large values of z, their measured B_z values are relatively small, while those measured by ISEE may include some larger values as the orbit of this satellite gives much better coverage of the near-Earth equatorial

plasma sheet region. Fairfield (1991) used IMP and HEOS data for comparisons with the T87 model and therefore came up with the conclusion that the model overestimated B_z, however Peredo *et al.* (1993) compared the T87 and T89 models with field data from ISEE. It was these data that revealed that the models in fact underestimate B_z. This is probably because the models were based on data from IMP and HEOS and were biased by the small B_z values in the outer part of the tail.

Peredo *et al.* (1993) used the ISEE data along with that from IMP and HEOS to compute a modified version of the T87 model, incorporating tail warping effects in the same way as in the T89 model. This model predicts B_z values which are much closer to the observed values. There is however a significant scatter in measured values of B_z, the reason for which is unknown. Until this scatter can be explained and accounted for in the models, there will continue to be large uncertainties in the predicted B_z values.

3.1.3 Asymptotic directions calculated with the Tsyganenko field model

The method of calculation of asymptotic directions is essentially unchanged from that of McCracken (1962). This method can be applied to any geomagnetic field model. The software employed to calculate the asymptotic directions used in this thesis was developed at the University of Bern by E. Kobel (Kobel, 1989; Flückiger and Kobel, 1990). The internal geomagnetic field is represented by the appropriate IGRF and the external field by Tsyganenko's 1989 model (Tsyganenko, 1989). This model is considered valid within a magnetopause described by the composite shape of a rotational paraboloid and a cylinder. The axis of symmetry of the paraboloid lies in the $x_{GSM} - z_{GSM}$ plane and passes through the origin of the coordinate system. The angle of the axis of symmetry with respect to the x_{GSM} axis depends on the tilt of the dipole axis and the geomagnetic activity. The tail-side magnetopause is modelled by a cylinder of radius 30 R_E centred on the x_{GSM} axis. The maximum tailwards extent of the valid model is set to 70 R_E.

The cosmic ray trajectories are traced through the magnetic field by numerical integration of the differential equation describing the path of a charged particle in a magnetic field (Equations 2.1). The integration method used is that of Stoer and Bulirsch (1980) which was found to be faster than the usual Runge-Kutta method. Input parameters required are date, time, level of geomagnetic activity (Kp), location on Earth and arrival direction at or near the Earth. From this information the direction of approach and the entry point at the magnetopause can be calculated. Cutoff rigidities are obtained by performing trajectory calculations systematically through the rigidity spectrum.

Asymptotic directions calculated for use in GLE modelling must give a good approximation to the full cone of view of each monitor. Many researchers only perform calculations for those particles arriving vertically above the neutron monitor. In the analyses presented in this thesis, the full cone of view has been approximated by considering nine approach directions. These directions represent

nine regions which have approximately equal contribution to the neutron monitor count rate (see discussion in Section 2.2). A range of rigidity values must be used and the separation in rigidity between subsequent calculations depends upon the change in asymptotic direction. Calculations begin at 20 GV (or higher for particularly energetic events) with rigidity step-size dependent upon the particular station and decreasing to a minimum of 0.1 GV as the geomagnetic cutoff is approached. For stations with geomagnetic cutoff above the atmospheric cutoff ($\sim$ 1 GV) calculations continue through the penumbral region to the point below which all trajectories are forbidden. This is often termed the Störmer cutoff rigidity. Calculations are terminated at 1 GV for stations with Störmer cutoffs below this rigidity.

3.1.4 Error in trajectory-tracing software

The software used for the calculation of viewing directions in the analyses presented in this thesis was provided by the University of Bern. This was described in Section 3.1.3. In April 1995, after most of the analyses were completed, it was discovered that there was an error in this software which resulted in incorrect viewing directions for some arrival directions. The calculated viewing directions for vertically incident particles were correct, as were those for particles arriving with azimuths of 0° and 180°. Viewing directions calculated for particles arriving with any other azimuth were incorrect and the effect was greater at high zenith angles. Comparison of the results with and without the error indicated that the discrepancies were largest at high rigidities ($>\sim$20 GV) and at rigidities near the geomagnetic cut-off. It is at these low rigidities where the error is most significant in the modelling of GLEs. As a test of this effect, the viewing directions for 1805 UT on 22 October 1989 were recalculated and the GLE analysis repeated with the corrected viewing directions. This event was extremely anisotropic, so the modelling should be most sensitive to changes in viewing direction. The spectrum was also quite steep, placing greater emphasis on the low rigidity viewing directions than in an event with a flatter spectrum. The results of this analysis are presented in Section 5.2.1 and show a slight difference in fitted spectrum compared with the original analysis. The other parameters of the model were not significantly changed. Since the effect of this error on the analysis of this highly anisotropic event was only marginal, it was thought to be unnecessary to repeat the analyses for the other events presented in this thesis. While the fitted parameters may change very slightly if the corrected viewing directions were used, the overall result and interpretations would be unchanged.

3.2 GLE modelling procedure

The current modelling software was developed from a program written by Don Smart. The operation of the original program is described in this section and modifications are described in the following sections. The aim of this software is to calculate the expected response of cosmic ray detectors given certain input parameters defining the spectrum and spatial distribution of solar particles in a

GLE. The calculated responses may then be compared with the recorded data to assess the validity of the chosen input parameters. The parameters are refined iteratively until satisfactory results are achieved.

3.2.1 Input

The calculation of asymptotic viewing directions has been described in the previous sections. These calculations must be performed for a set of rigidity values for each station to be modelled and stored for use by the modelling software. The range of rigidities is usually 1–20 GV for neutron monitors as this is the range over which they are most sensitive to solar accelerated particles. The most energetic GLEs may include contributions from particles with rigidity greater than 20 GV and be detected by surface muon telescopes. Muon telescopes respond to vertically incident particles with rigidities greater than about 4 GV. If muon telescopes are included in the models, the asymptotic directions for these instruments should be calculated up to at least 25 GV. The rigidity intervals are chosen so that straight-line interpolation between the calculated viewing directions provides a satisfactory approximation of the viewing directions at intermediate rigidities. Large steps (up to ~5 GV) are satisfactory at high rigidities, but the step size decreases to a minimum of 0.1 GV towards the station's cutoff. Asymptotic viewing directions for non-vertical arrival at Earth can be included. For neutron monitors it is usual to split the volume above the detector into nine sections and represent each of these by the central arrival direction. These nine directions are: vertical (zenith angle 0°, azimuth 0°) and azimuths of 0°, 90°, 180° and 270° at zenith angles of 16° and 32°. The justification for using these nine directions was described in Section 2.2.

The rigidity spectrum of solar particles is specified by a functional form. One or two parameters are required depending on the form chosen. This is described in more detail in the next section.

The particle pitch angle distribution also has a functional form. The axis of symmetry of the distribution is specified by a latitude and longitude in extended Earth coordinates. The number of parameters required to specify the shape of the pitch angle distribution depends on its functional form. This is described in Section 3.4.

The original software allowed for spectra and pitch angle distribution arrays to be read in from files, thus allowing shapes other than the usual functional forms. This feature has been disabled in order to allow the incorporation of least squares methods for determination of parameters (see Section 3.3).

The procedure outlined in the next section must be applied to each new set of parameters.

3.2.2 Main procedure

Preliminary calculations

The pitch angle weighting function is calculated for pitch angles from 0° to 180° in steps of 1°. This function is normalised to one particle per steradian over the

forward steradian (pitch angles from 0° to ~33°).

The differential rigidity spectrum of galactic cosmic rays is used to determine the number of galactic cosmic rays at each rigidity. Since the galactic cosmic ray intensity varies with the solar cycle, this calculation involves a factor known as the cosmic ray modulation parameter. A plot of this parameter with respect to time can be found in Badhwar and O'Neill (1995). The cosmic ray modulation parameter is determined from the count rate of a calibrated neutron monitor (Climax in the case of Badhwar and O'Neill).

The differential rigidity spectrum of the solar particles may be represented as a power law, a shock acceleration spectrum (Ellison and Ramaty, 1985) or a modified version of the Ellison and Ramaty spectrum. The shock acceleration spectrum is the theoretically determined result of a shock of infinite size interacting with the particles for infinite time. Non-infinite extent or time will result in a spectrum that falls off more rapidly with increasing rigidity. The modified Ellison and Ramaty spectrum is an attempt to model this. The Ellison and Ramaty type spectra are recent inclusions by Don Smart and hence have not been available for the majority of the work presented in this thesis. Prior to the introduction of these spectral forms, a similar effect was obtained by modification of the power law spectrum. An additional parameter was included to model the change in power law exponent as a function of rigidity. This produces a spectrum which steepens with rigidity in a similar way to the pure and modified forms of the Ellison and Ramaty spectrum.

Major calculations

If non-vertical contributions are included, each set of viewing directions calculated for different arrival directions at one station is treated as a separate station for the main part of the calculation. The contributions at each station are averaged towards the end of the process. The main calculations take place within two loops. The outer loop steps through each station (or each set of viewing directions if non-vertical arrival directions are included) and the inner loop steps in rigidity.

The rigidity values of the calculated viewing directions are treated as mid-points of rigidity intervals. When the latitude and longitude of the viewing direction is read in, the angular distance, α, from the axis of symmetry of the pitch angle distribution is calculated according to the equation

$$\alpha = \cos^{-1}\left[\cos(90-\theta_a)\cos(90-\theta_v) + \sin(90-\theta_a)\sin(90-\theta_v)\cos(\Delta\phi)\right]$$

where θ_a and θ_v are the latitudes of the axis of symmetry and the viewing direction respectively and $\Delta\phi$ is the longitude difference (within $\pm 180°$) of the axis of symmetry and the viewing direction. The angular distance, α, is required for the determination of the pitch angle weighting of the response at this viewing direction.

The differential rigidity spectra are used to calculate the number of galactic and solar particles present in the rigidity range and these are multiplied by the value of the yield function at the central rigidity. There are several yield function options available. The analyses presented in this thesis have been performed using the Debrunner *et al.* (1982) neutron monitor yield function. This yield function

was calculated theoretically but normalised to agree with experimental results. It is regarded as the most satisfactory at low rigidities (private communication D.F. Smart and M.A. Shea). There are three other neutron monitor yield functions included in the software. The first is based on that of Lockwood *et al.* (1974), but incorporates the work of Wainio *et al.* (1968) below 1.3 GV. The second is a preliminary version of the Lockwood *et al.* yield function (private communication to M.A. Shea, 1973) and the third is based on the work of Webber and Quenby (1959). These three yield functions are quite similar and only differ significantly from the Debrunner *et al.* function at low rigidities ($\lesssim 3$ GV). The muon yield function determined by Webber and Quenby (1959) has been used in the past, but recently another function (Murakami *et al.*, 1979) has been incorporated and used in the modelling of the 29 September 1989 GLE (see Chapter 4).

The number of particles resulting from the solar particle spectrum times yield must be multiplied by the value of the pitch angle weighting function at α. This is the end of the inner loop which steps through rigidity. These calculations are repeated for all rigidity values for which viewing directions were not re-entrant. Further calculations involving all approach directions must be made before moving on to the next station.

The galactic spectrum times yield is normalised to 100 particles (cm^2 ster s GV)$^{-1}$ at 15 GV. The number of particles in this normalised spectrum is then summed over the whole rigidity range to determine the background cosmic ray intensity. The number of solar particles times yield times the pitch angle weighting function is also summed over the rigidity range and a percentage increase above background is calculated based on the test flare spectrum (normalised to an arbitrary flux).

This is the end of the outer loop through all stations (or all arrival directions at each station). If non-vertical contributions have been included, the average over all arrival directions for each station is calculated. This averaging procedure is based on the assumption that the galactic contribution from each of the arrival directions are equal. It is important to choose appropriate arrival directions to ensure that this is a valid assumption. For some stations, the geomagnetic cutoff may vary between arrival directions and result in slightly different galactic contributions, however this effect is not significant.

In order to calculate the absolute flux of solar particles, it is necessary to select one station to be used in normalisation. It is usual to choose a station with one of the highest observed increases, however it is unwise to select a polar station as uncertainties in the yield functions at very low rigidities have a more significant impact for such stations. The flux constant in the forward steradian ($J_{||}$) is equal to the ratio of actual to calculated percentage increase at the selected station, divided by the assumed flux constant of the test spectrum (100 particles (cm^2 ster s GV)$^{-1}$). The calculated percentage increase at all other stations must be multiplied by $J_{||}$. The flux average over 4π steradians is calculated by dividing $J_{||}$ by a quantity representing the anisotropy of the pitch angle distribution. This quantity is the sum of the pitch angle weighting function over the forward steradian divided by its sum over 4π steradians.

The calculated percentage increases can be compared to the recorded increases

to assess the quality of the model fit. If necessary, the calculated increase at each station can be broken down into the contribution from each rigidity range. This allows the calculation of the rigidity of 50% response. This is analogous to the median rigidity of the detector for the galactic particle spectrum.

The modelling procedure described above has been summarised by Smart *et al.* (1979) as follows:

1. Assume a direction of maximum particle flux (axis of symmetry of the pitch angle distribution).

2. Select a pitch angle distribution *i.e.* choose the value of parameters in a pre-defined function describing the pitch angle distribution.

3. Select a particle spectrum *i.e.* choose the value of parameters in the chosen spectral function.

4. For each selected rigidity, calculate the angle between the asymptotic direction and the direction of the maximum particle flux. This is the same as the pitch angle.

5. The number of particles at a specific rigidity and pitch angle is determined from the rigidity spectrum and pitch angle distribution and multiplied by the neutron monitor specific yield function to determine the neutron monitor response at that rigidity.

Steps 4 and 5 are repeated for the full set of allowed rigidities for each station. The sum over all rigidities gives the calculated response of the neutron monitor to the anisotropic flux of solar cosmic rays given the input parameters chosen in steps 1-3. The calculated response of each neutron monitor is compared with the actual observation and input parameters varied accordingly.

When following this procedure, it may be necessary to perform the calculations over a full grid in parameter space in order to ensure that the best solution is obtained and to estimate the confidence limits of the parameters. Without doing this it is very difficult to tell if the solution is just a 'local minimum' in the difference between calculated and observed increases. Given that there are at least 4–6 parameters (latitude and longitude of the direction of maximum flux, 1 or 2 parameters for the pitch angle distribution function, 1 or 2 parameters for the spectrum) depending upon the functional forms chosen, the task of obtaining a solution is very time consuming. Some simplification can be achieved by assuming fixed values for some parameters *e.g.* the direction of maximum particle flux may be fixed to the interplanetary magnetic field direction if this is known. However, the additional information required to choose reasonable values at which to fix parameters is often unavailable. Fixing parameters also limits the interpretation of the final fit parameters. If all parameters are allowed to vary, then the solution is more general and potentially provides more information about the interplanetary transport of the solar accelerated particles. In order to remove the 'trial and error' element from this modelling procedure, a non-linear least squares method has been incorporated to determine the best fit parameters. This procedure is described in the next section.

3.3 Least squares determination of parameters

The chosen least squares package, *gaushaus*, was written at the University of Wisconsin Computing Centre and released in their Supplementary Program Series No.603 in 1966. An iterative technique combining the Gauss (Taylor series) method and the method of steepest descent is used to obtain the final parameters from a set of initial guesses. The least squares method involves minimising the sum of squares of differences between observed data and values calculated with the model function. This is commonly called the sum of squares and has the form

$$S = \sum_{k=1}^{n} [Y_k - f(\underline{\theta}, \xi_k)]^2 \tag{3.1}$$

where Y_k is the kth observed data point, f is the model function, $\underline{\theta}$ is the set of parameters and ξ_k is a set of constants appropriate to the kth observation. For each iteration a new set of parameters $\underline{\theta}$ are derived with the aim of decreasing the value of S. The method of steepest descent usually works well on initial iterations, but is progressively slower as the minimum is approached. On the other hand, the Gauss method works well when the minimum is near, but can be slow over the initial iterations. A combination of these two methods should converge rapidly to the solution.

Gaushaus has three options for the termination of calculations. A maximum number of iterations must be set and if this is reached, calculations are terminated even though convergence may not have been achieved. The other two criteria for termination are (i) sum of squares convergence and (ii) parameter convergence. If the sum of squares convergence criterion is set to ϵ_1, calculations will terminate when

$$\left| \frac{S(\underline{\theta}^i) - S(\underline{\theta}^{i-1})}{S(\underline{\theta}^{i-1})} \right| < \epsilon_1$$

where S is defined as above, $\underline{\theta}$ is the set of parameter values and i, $i-1$ represent consecutive iterations. If the parameter convergence criterion is set to ϵ_2, calculations will terminate when

$$\left| \frac{\theta_j^i - \theta_j^{i-1}}{\theta_j^{i-1}} \right| < \epsilon_2, \text{ for all } \theta_j$$

where θ_j is the jth parameter, j ranging from one to the number of parameters and i, $i-1$ represent consecutive iterations. If both ϵ_1 and ϵ_2 are set, calculations will terminate when either of these criteria are satisfied.

An array of constants may be set to indicate an *a priori* sign restriction on any of the parameters. In this case, the parameter will retain the sign of the initial guess throughout the least squares procedure. It is not possible to restrict parameters to a range of values (*e.g.* latitude between –90° and 90° or longitude between 0° and 360°) however it is a simple matter to test, within the subroutine which evaluates the model, whether these are out of range and apply appropriate corrections (*e.g.* a longitude of 450° would be interpreted as 90°). The final parameter values must be tested and corrected in the same manner.

The output from gaushaus includes the final function values, final parameter values and individual confidence limits for each parameter. These confidence limits are based on a linear hypothesis in the region of each parameter. In the linear case they represent approximate 95% confidence limits for each parameter when all other parameters are ignored. Clearly the relevance of these limits depends not only on the extent of non-linearity of the model, but also on the independence of the parameters. This is discussed in Chapter 7.

The observed data points are the percentage increases at the neutron monitors. Clearly it is necessary to have at least as many stations as parameters, however it is not necessary for all of the stations to have observed an increase. In particular, stations with high geomagnetic cutoffs which did not record an increase provide valuable spectral information. Similarly, bounds can be set on the width of the pitch angle distribution by including stations which did not record an increase. It is just as important for the model to predict zero responses at these stations as to reproduce the observed increases at other stations.

The use of a least squares technique to determine parameter values does not eliminate the possibility of finding a local minimum in the sum of squares. This can be avoided by using several sets of initial parameter guesses and confirming that, in each case, convergence to the same final parameter values is achieved. If the initial guesses are well separated in parameter space, this process ensures that the derived parameters represent the best fit.

3.3.1 Weighted least squares

In many problems solved by least squares methods, the errors in the observed values may not be equal and hence the observations should not be treated equally in the minimisation of S. In such cases it is usual to minimise a weighted sum of squares, S_w. The sum of squares (Eq. 3.1) is then replaced by

$$S_w = \sum_{k=1}^{n} w_k \left[Y_k - f(\underline{\theta}, \xi_k)\right]^2 \tag{3.2}$$

where w_k is the weight assigned to the kth observation, Y_k. The way in which this is achieved with gaushaus is for the user to supply as the set of observed values, the actual observations multiplied by the square root of their weight. The calculated function values must also be multiplied by this value. It is easy to see that the result of replacing Y_k by $\sqrt{w_k}Y_k$ and $f(\underline{\theta}, \xi_k)$ by $\sqrt{w_k}f(\underline{\theta}, \xi_k)$ in Equation 3.1 is to produce Equation 3.2, thus a weighted sum of squares can be minimised.

In the specific application of the weighted least squares method in GLE modelling, the observed data values, Y_k, are the actual percentage increases in count rate. The calculated function values, $f(\underline{\theta}, \xi)$, are the calculated increases from the model, given the input parameters $\underline{\theta}$. The weight applied to each observed increase is defined as

$$\sigma = \frac{\sqrt{background + increase}}{background} \times 100$$

where *background* is the average count rate prior to the GLE and *increase* is the increase in count rate above this background level. The value of *background* is

usually obtained from an average over one hour of data, but must be scaled to the same time interval over which *increase* is recorded.

3.4 Pitch angle distribution

Many functions have been used to describe particle pitch angle distributions when modelling GLEs. Probably the most widely used distributions have been cosine relationships and gaussians. Smart and Shea (1990) found that significantly better results could be obtained with an exponential function of the form

$$G(\alpha) = \exp\left[\frac{0.5(\alpha - \sin\alpha\cos\alpha)}{A}\right] \tag{3.3}$$

where α is the pitch angle and A is a variable parameter. This function results from a simplification of the work by Beeck and Wibberenz (1986) who considered theoretically the scattering properties of the interplanetary medium. The function describes an anisotropy which is not strictly applicable during the rapid evolution of some GLEs.

Humble *et al.* (1991) used a composite of two forms of Equation 3.3, one to describe the anisotropic flux in the 'forward' direction (pitch angles less than 90°) and another to describe the flux in the 'reverse' direction (pitch angles greater than 90°). The resulting function was the average of the two forms weighted by the cosine of the pitch angle and can be expressed as

$$G(\alpha) = \exp\left[\frac{0.5(\alpha - \sin\alpha\cos\alpha)}{A - 0.5(A-B)(1-\cos\alpha)}\right] \tag{3.4}$$

An example of a pitch angle distribution generated from this function is shown in Figure 3.2. The particles propagating in the 'reverse' direction are due to scattering in the interplanetary medium beyond the Earth. This form of pitch angle distribution is the function used in many of the analyses presented in this thesis and is the basis of the more complex forms discussed in the next two sections.

3.4.1 Reverse particle propagation

The pitch angle distribution described by Equation 3.4 has been found to be a satisfactory model for times when particles undergo scattering beyond the Earth which produces only minimal reverse particle propagation. During some events, stations with viewing directions $\sim 180°$ away from the direction of maximum flux record significant increases while other stations (such as those viewing $\sim 90°$ or $\sim 270°$ from maximum) do not. Under normal field conditions, the only possible explanation for this is that particles are being efficiently scattered back towards the Earth by some structure in the magnetic field beyond the Earth. In order to model such a situation, forward and reverse pitch angle distributions both described by Equation 3.4 have been added together with the height of the reverse distribution being a fitted parameter in the model. The resulting function is

$$G'(\alpha) = G(\alpha) + C \times G(\alpha') \tag{3.5}$$

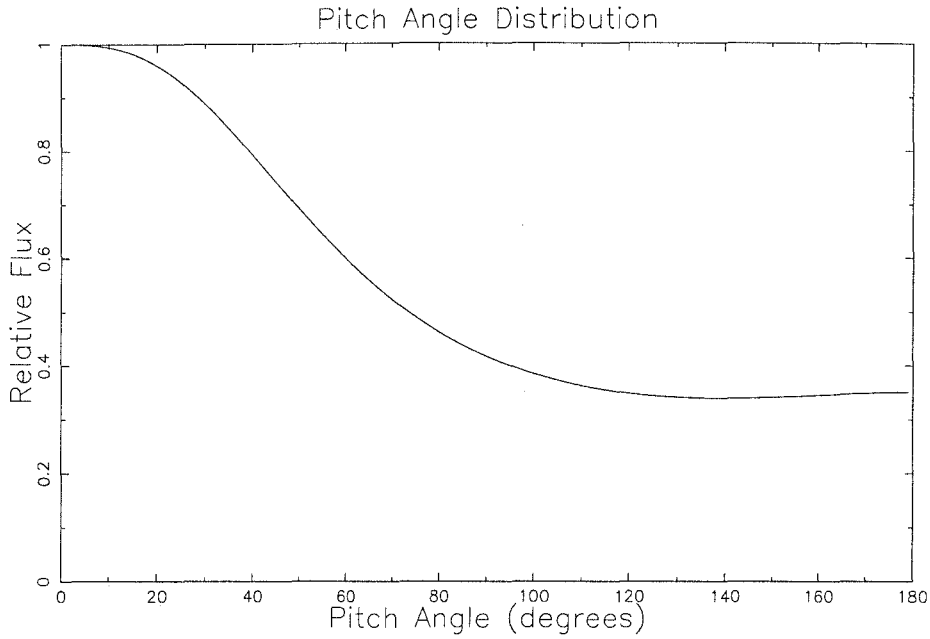

Figure 3.2: Pitch angle distribution generated from Equation 3.4

where G is defined by Equation 3.4, $\alpha' = 180 - \alpha$ and C is a number between 0 and 1 which determines the ratio of fluxes at pitch angles of 180° and 0°. An example of a possible pitch angle distribution generated from Equation 3.5 is shown in Figure 3.3.

3.4.2 Rigidity dependence

Beeck and Wibberenz (1986) discussed an approximate solution of the Fokker-Planck equation which has contributions from pitch angle scattering and adiabatic focusing. These effects determine the shape of the pitch angle distribution of solar particles arriving at Earth and are dependent upon the mean free path, focusing length and pitch angle diffusion coefficient. Palmer (1982) reviewed predictions of the values of these quantities, but the rigidity dependence was unclear. This has in general lead to the assumption that any dependence upon rigidity is insignificant. If any of these quantities do depend on rigidity then the particle pitch angle distributions should also vary in shape with rigidity. With this possibility in mind, rigidity dependence has been introduced into the parameters A and B in Equation 3.4 in order to generate rigidity dependent pitch angle distributions. A simple linear variation of A and B with rigidity does not produce satisfactory results due to the exponential form of Equation 3.4. Various forms were tried and the most suitable was

$$A(P) = A_0 - \Delta A \left(1 - \frac{1}{exp(P/2)}\right)$$

where P is rigidity in GV, A_0 and ΔA are parameters of the model. A similar relationship is used for the rigidity dependence of B. The parameters ΔA and ΔB

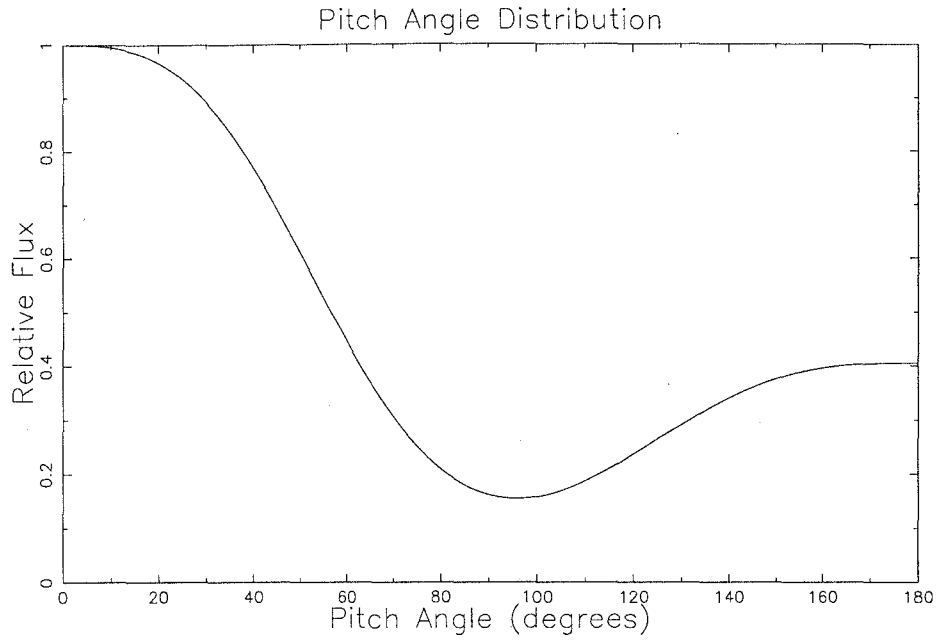

Figure 3.3: Pitch angle distribution generated from Equation 3.5

may be either positive or negative, thus producing pitch angle distributions which increase or decrease in anisotropy with rigidity. Examples of possible rigidity dependent pitch angle distributions are shown in Figure 3.4.

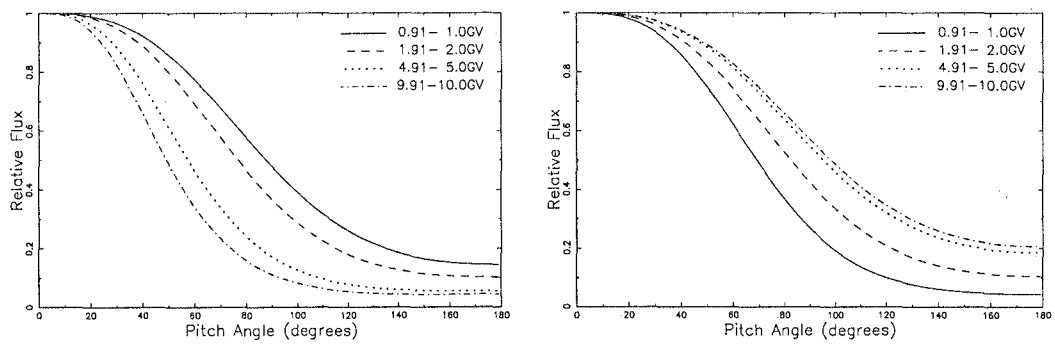

Figure 3.4: Rigidity dependent pitch angle distributions, anisotropy increasing (left) or decreasing (right) with rigidity.

Rigidity dependence may also be applied to the composite pitch angle distribution (Eq. 3.5). In this case the rigidity dependent distribution is defined by six parameters: A, ΔA, B, ΔB, A', $\Delta A'$, B', $\Delta B'$, C, ΔC where the primed parameters define the 'reverse' particle distribution. Examples of rigidity dependent pitch angle distributions of this form are shown in Figure 3.5.

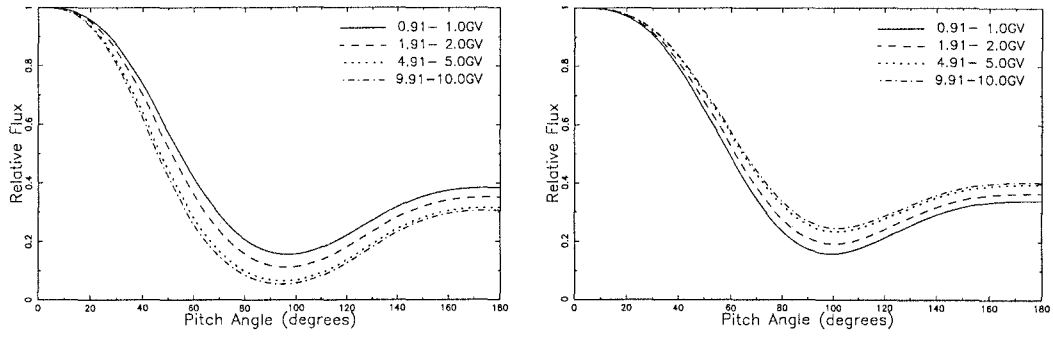

Figure 3.5: Composite rigidity dependent pitch angle distributions

3.5 Summary

The model of Smart *et al.* (1979) has been improved by the incorporation of asymptotic directions calculated with a recent geomagnetic field model, the use of a least squares package to determine the best fit parameters and more complex pitch angle distribution functions to model different propagation characteristics of the interplanetary medium.

Disturbance of the geomagnetic field can now be accounted for by the use of Tsyganenko's (Tsyganenko, 1989) magnetospheric model. This has been incorporated into the calculation of asymptotic directions of cosmic ray particles by E. Kobel, University of Bern. Kobel's software allows calculation of viewing directions at any location on the Earth with any approach angle for all times covered by IGRF models. Six geomagnetic disturbance levels are covered from Kp=0 to Kp$\geq$5. Viewing directions calculated with this software are used throughout the analyses presented in this thesis.

A least squares method for determining best fit parameters of the model has eliminated the time consuming iterative process described by Smart *et al.* (1979). As well as making the modelling process quicker, this has given more confidence that the final parameters represent the best fit solution and allowed the introduction of more complex functional forms without making the problem too cumbersome. It is important to include as many observations as possible, including null observations which are still valid data points.

Various functional forms have been introduced to model the particle pitch angle distribution. The shape of the pitch angle distribution is determined by the propagation characteristics of the interplanetary medium through which the particles travel, therefore the best fit distributions should give information about these characteristics. This is discussed further in the interpretation of specific results particularly in Chapters 4 to 6.

The next three chapters present the results of modelling seven GLEs. The first four of these occurred as part of the unprecedented sequence of relativistic solar particle events in 1989. The 29 September 1989 GLE has been modelled using data from neutron monitors and surface muon telescopes. These results are presented in Chapter 4. Both the 19 and 22 October 1989 GLEs (discussed in Chapter 5) had unusual time profiles. Initial spikes are investigated in both these

events as well as a later spike in the 19 October event. Results for the 24 October event are also presented in Chapter 5. Chapter 6 contains the results of modelling the 12 October 1981, 7–8 December 1982 and 16 February 1984 GLEs. The first two of these events took place during times of unusual interplanetary magnetic field configurations. The effect of these has been explored in the modelling.

Chapter 4

29 September 1989

4.1 Introduction

The GLE which occurred on 29 September 1989 was the largest recorded since 1956 and was observed by neutron monitors all over the world. The highest recorded neutron monitor increase was 404% at Calgary. Neutron monitor increases were observed even at equatorial stations such as Darwin, indicating the presence of particles of at least 14 GV. Surface muon detectors at several sites also recorded the event. Swinson and Shea (1990) reported an increase at the Embudo underground muon telescope which has a threshold rigidity of ~19 GV. Data from underground muon telescopes at Mawson and Hobart (threshold ~30 GV) showed no evidence of the event. These observations are consistent with an upper rigidity of ~25 GV for particles in this event. It is very unusual for solar accelerated particles of such high rigidity to be present in significant numbers.

Figure 4.1 shows the intensity time profiles from several neutron monitors and surface muon telescopes. It is clear from this figure that there were two distinct peaks in intensity. Some stations observed both peaks while others recorded only one. The increases at muon telescopes all reached maximum intensity at the time of the first neutron monitor peak. This suggests that the particle spectrum softened between the first and second peaks.

Hα records do not indicate the presence of a flare on the visible solar disc at the time of this GLE, however 'behind the limb' flare activity was seen from ~1230 UT. Swinson and Shea (1990) published photographs of this activity, including a looped prominence which was visible from before 1326 UT until after 2315 UT. Intense radio emission of types II, III and IV was observed. The Type II emission occurred between 1125 and 1157 UT while the Type IV emission started at the same time and continued until 1217 UT. Type III emission was observed between 1124 and 1128 UT. Soft X-rays were also observed, commencing at 1047 UT and peaking with intensity X9.8 at 1133 UT. It is believed that these emissions were associated with a solar flare located at ~25°S, 98± 5°W in NOAA region 5698.

Cliver *et al.* (1993) reported observations of gamma-ray line (GRL) emission from the visible disc, even though the flare site was behind the limb. They believe that there was a shock driven by a coronal mass ejection (CME) which was broad enough to encompass the 'front-side' regions and noted that the timing of the

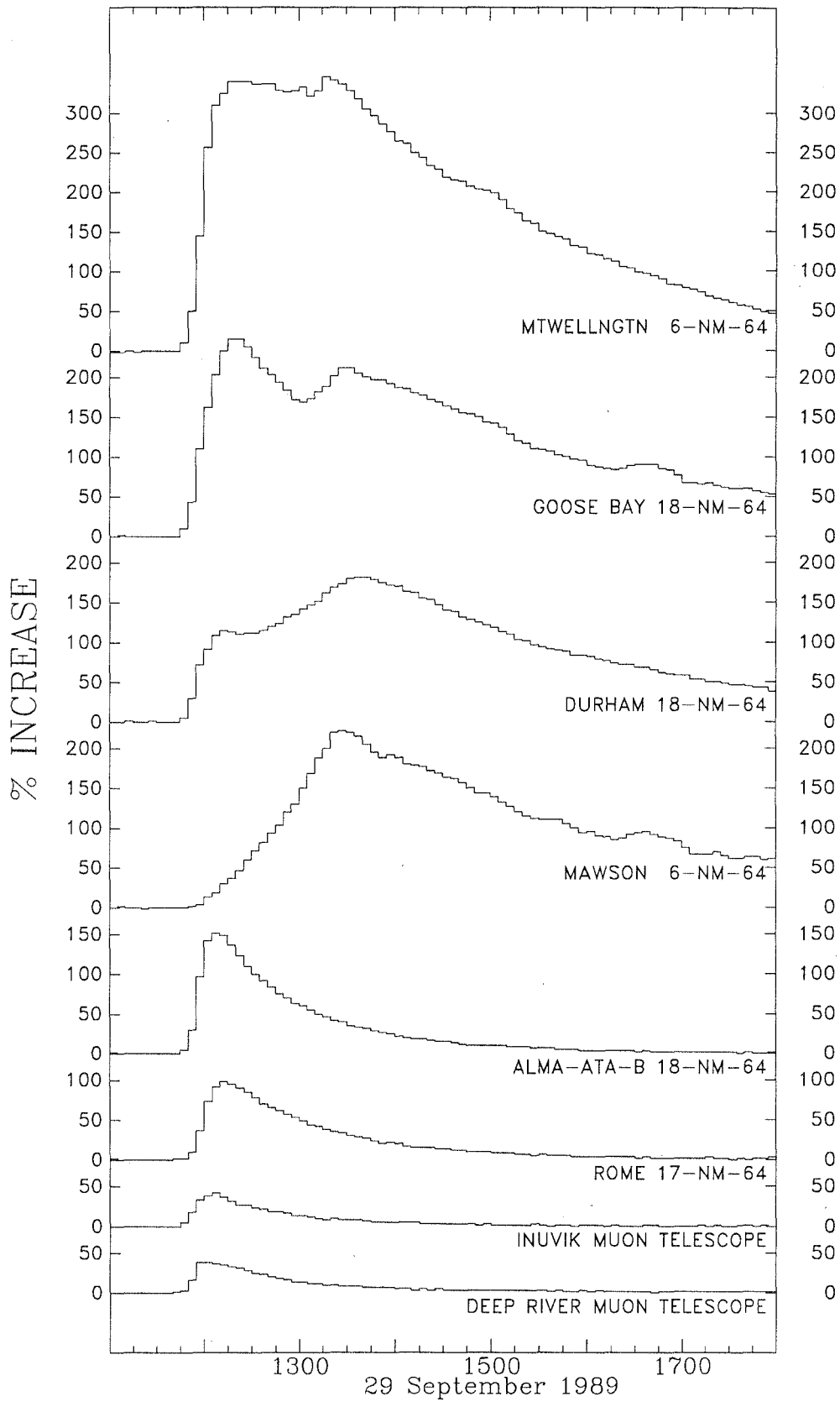

Figure 4.1: Cosmic ray increases at Mt. Wellington, Goose Bay, Durham, Mawson, Alma-Ata and Rome neutron monitors and Inuvik and Deep River surface muon telescopes between 1100 and 1800 UT on 29 September 1989.

type II and III radio emission was consistent with a CME-driven shock. Such a shock could accelerate particles, some of which may travel to Earth and produce the GLE. Other accelerated particles may 'precipitate' to the Sun and produce GRL emission. Cliver *et al.* estimated that $\sim$ 3–30% of protons accelerated to energies greater than 30 MeV must have precipitated. Acceleration of particles by a shock extending from the flare site to the visible disc of the Sun provides a plausible mechanism for transport of the particles to the interplanetary magnetic field line connected to the Earth.

4.2 Analysis

4.2.1 Muon telescope geometric factor

In order to account for the non-vertical contribution to the muon increase it is necessary to determine the appropriate arrival directions for which to calculate asymptotic viewing directions. For neutron monitors these were determined by summing the percentage of counting rate over all zenith angles and determining the annuli with contributions in the ratio 1:4:4 (Rao *et al.*, 1963). The equation for the dependence of counting rate on zenith angle, due to atmospheric absorption is

$$Z(\theta,\phi) = Aexp\left(\frac{-x}{\lambda cos\theta}\right)\left[B + \frac{x}{\lambda cos\theta}\right] \tag{4.1}$$

where A is a constant, x is the atmospheric depth in g cm^{-2}, λ is the interaction mean free path and B is 1 or 2. Rao *et al.* chose the value of B according to assumptions about the zenith angle dependence of the neutron monitor count rate in a parallel beam of high energy nucleons. This choice has very little effect on the form of Z.

The muon telescopes used in this analysis consisted of two layers of detectors. Arriving particles must pass through both trays to be detected. In order to determine the zenith angle response of such an instrument, a geometrical factor must be included in Equation 4.1. Sullivan (1971) derived functions for the projected overlap of trays 'seen' by particles arriving from arbitrary directions. For rectangular trays of length a, width b and separation l, the projected overlap for a particle with zenith θ and azimuth ϕ is

$$A(\theta,\phi) = X\,H(X)\,Y\,H(Y)$$

where

$$\begin{aligned} X &= a - \xi H(\xi) + \psi H(-\xi) \\ Y &= b - \eta H(\eta) + \eta H(-\eta) \\ \xi &= -l\,tan\theta cos\phi \\ \eta &= -l\,tan\theta sin\phi \\ H(k) &= 1 \text{ for } k > 0 \\ H(k) &= 0 \text{ for } k \leq 0 \end{aligned}$$

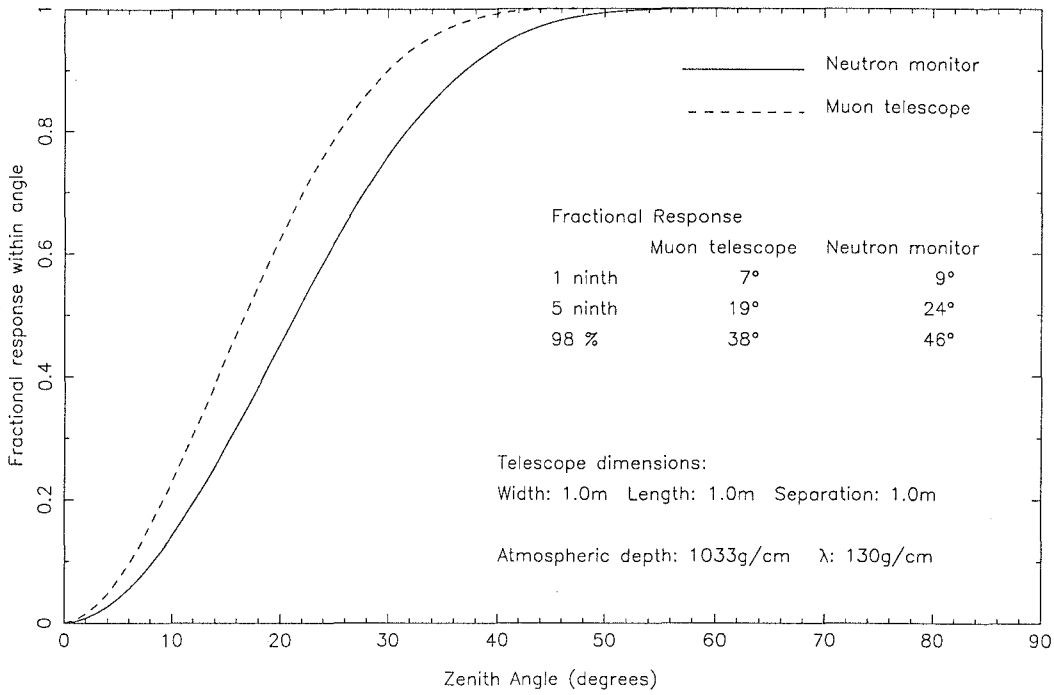

Figure 4.2: Fractional response against zenith angle for a cubic muon telescope compared with that for a neutron monitor.

Table 4.1: Dimensions of muon telescopes and arrival directions for which asymptotic directions were calculated. Fluxes are in units of particles $(cm^2\ s\ ster\ GV)^{-1}$.

Telescope	Length	Width	Separation	Zeniths			Azimuths			
Deep River	1.0	1.0	1.0	0	13	28	5	95	185	275
Goose Bay	1.0	1.0	1.0	0	13	28	59	149	239	329
Inuvik	1.0	1.0	1.0	0	13	28	77	167	257	347
Moscow	1.0	1.0	1.0	0	13	28	0	90	180	270
Mt. Norikura	1.0	1.0	1.73	0	10	21	45	135	225	315
Nagoya	1.0	1.0	1.73	0	10	21	45	135	225	315

The projected area may be summed over all azimuths to produce a zenith angle dependence which must then be multiplied by Equation 4.1. Figure 4.2 shows the resulting zenith angle dependence of a cubic muon telescope compared with that of a neutron monitor. This muon telescope zenith angle dependence may be summed over all angles to find the annuli which respond in the ratios 1:4:4 in order to choose the appropriate nine arrival directions for calculating viewing directions. In the case of a cubic detector, the annuli required are $0° < \theta < 7°$, $7° < \theta < 19°$ and $19° < \theta < 38°$, so asymptotic viewing directions should be calculated for zenith angles of 0°, 13° and 28°. The dimensions of muon telescopes used in this analysis are shown in Table 4.1 along with the zeniths and azimuths for which asymptotic directions were calculated. The azimuths were chosen to be aligned with the corners of the detectors except for Moscow as the orientation of this telescope was not known.

4.2.2 Yield functions

Fujimoto *et al.* (1977) produced functions to describe the response of muon telescopes from numerical fits to the curves later published by Murakami *et al.* (1979). These functions take into account the zenith angle of viewing as well as the atmospheric depth of the instrument and rock depth for underground detectors. The yield functions for the muon telescopes can be obtained by dividing the response functions by the primary cosmic ray spectrum.

Neutron monitor yield functions are defined so that the response to galactic cosmic rays is 100 particles $(cm^2\ s\ ster\ GV)^{-1}$ above 15 GV. This is a somewhat arbitrary figure, so the muon yield function needs to be scaled so that it is equivalent. This has been done by an approximate method, however the rigidity dependence of the function should still be valid. As a result, the derived particle distributions can be determined with reasonable confidence, however there may be some additional errors in the spectral determination.

The rigidity dependent response of a surface muon telescope to galactic cosmic rays was calculated using the Fujimoto *et al.* yield function, but substituting the appropriate modulated cosmic ray spectrum for the standard spectrum used in their function. The muon yield function was then incorporated into the GLE model so that the response at neutron monitors was determined using the Debrunner *et al.* (1982) yield function and that at muon telescopes was calculated with the scaled muon yield function. A first attempt at modelling was made for one time near the peak of the GLE. The results were examined to determine and approximate scaling factor for the muon yield function. This was applied and the least squares modelling was then repeated. This iterative procedure was performed a few times until a satisfactory result was obtained. The scaling factor determined by this method was found to be satisfactory for the other times modelled.

The Fujimoto *et al.* numerical fits to the Murakami *et al.* response functions are very convenient to use, however there is some doubt as to their accuracy at low rigidities. Murakami *et al.* believe their functions to be superior to others for rigidities above 10 GV. Below this rigidity some discrepancy was noted between derived and observed muon fluxes. These functions were designed for use in studies of galactic cosmic ray modulation and are quite sufficient for that purpose. They are also satisfactory for modelling the background cosmic ray intensity during a GLE, however they are not ideal for use with a solar particle spectrum. It may have been possible to use a different yield function for the solar particles, but the simultaneous use of two different muon yield functions would probably have introduced larger errors. The general theme of the results presented here should not be significantly affected by the deficiencies in the muon yield function.

4.2.3 Results

Modelling was performed for three times during the GLE using the Debrunner *et al.* (1982) neutron monitor yield function and the Fujimoto *et al.* (1977) muon yield function as described above. The first two modelling times were chosen as the major peaks in the neutron monitor data. The third was during the decay phase. Five minute data were used for the intervals beginning 1215, 1325 and

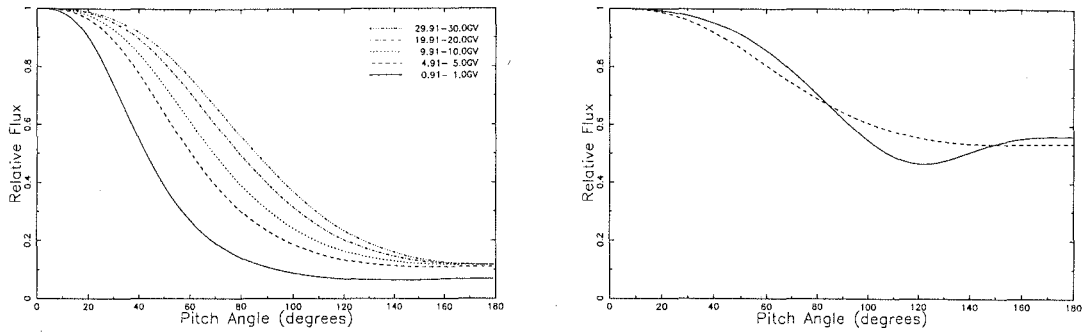

Figure 4.3: Rigidity dependent pitch angle distribution derived for 1215 UT on 29 September 1989 (left). Rigidity independent pitch angle distributions derived for 1325 UT (solid line) and 1600 UT (dashed line) during the same GLE (right).

1600 UT. The geographic latitude and longitude of the apparent particle arrival directions are shown in Table 4.2 along with the derived spectral parameters. The spectral form was a modified power law in rigidity. The two parameters quoted are the power law exponent (γ) and the change of γ per GV ($\delta\gamma$). A positive value of $\delta\gamma$ results in a spectrum which steepens with increasing rigidity. The fluxes shown in Table 4.2 are $J_{||}$, the flux in the forward steradian and J_{av}, the flux averaged over 4π steradians.

Table 4.2: Apparent particle arrival directions and spectral parameters during the 29 September 1989 GLE. Fluxes in units of particles $(cm^2\ s\ ster\ GV)^{-1}$.

	γ	$\delta\gamma$	$J_{\|\|}$	J_{av}	Latitude	Longitude	Ψ
1215 UT	–2.1	0.3	15.4	5.9	40°	253°	100°
1325 UT	–4.6	0.1	190.0	129.0	25°	263°	57°
1600 UT	–6.0	0.0	285.7	199.0	–42°	250°	26°

The pitch angle distribution at 1215 UT was found to be rigidity dependent. Figure 4.3 (left) shows the distribution at selected rigidities. The small isotropic component was approximately equal at all rigidities but the 'forward' part of the distribution was broader at high rigidities. The derived pitch angle distributions for 1325 and 1600 UT are also shown in Figure 4.3 (right). No rigidity dependence was found at these times. The small depression at ~120° in the distribution derived for 1325 UT is of only marginal significance. This indicates that there may have been preferential scattering from a region beyond the Earth, but there was fairly strong scattering from all directions, creating a significant isotropic component. There was no evidence of preferential back-scattering at 1600 UT.

The derived rigidity spectra are shown in Figure 4.4. The change of slope with increasing rigidity was much more significant early in the event. Later the spectra were very close to pure power laws. These spectra may have larger uncertainties than those derived for other events due to the scaling process used for the muon

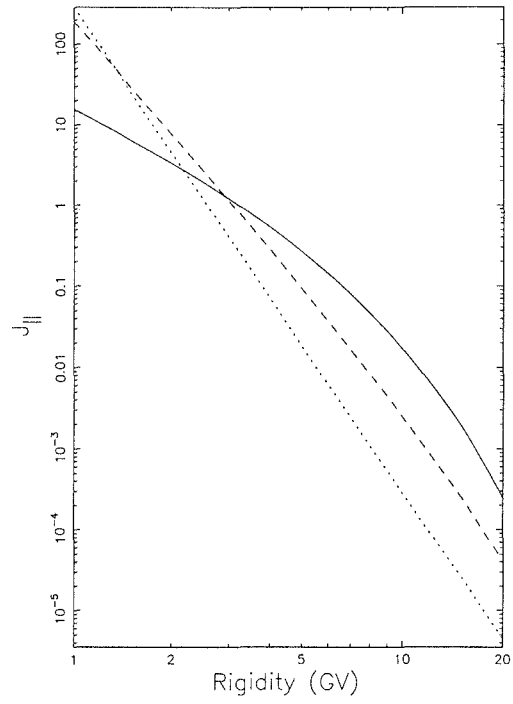

Figure 4.4: Derived rigidity spectra for 1215 UT (solid line), 1325 UT (dashed line) and 1600 UT (dotted line) during the 29 September 1989 GLE.

yield function. This will be most significant at high rigidities, but the inclusion of neutron monitors with geomagnetic cutoffs up to ~14 GV helps to minimise the errors.

The calculated percentage increases for each of the modelled times are shown in Tables 4.3, 4.4 and 4.5 along with the actual increases (with poisson errors) and the increases corrected to sea level atmospheric pressure by the two attenuation length method described in Section 2.5. A flare attenuation length of 120 g cm^{-2} was used in the correction. It should be noted that the actual errors in neutron monitor data are ~1.5 times the poisson error, due to multiplicity and scintillation (Hatton, 1971). The Σ variance values at the bottom of the tables are the sums of squares of differences between the calculated and corrected percentage increases.

4.3 Interpretation

The apparent particle arrival directions cannot be compared with measured interplanetary magnetic field directions as no field data are available between 0300 UT on 26 September 1989 and 2200 UT on 1 October. A rapid change in latitude of the arrival direction occurred during the event, however this is no greater than the change in latitude of the hourly average field directions between 1700 and 2100 UT on 25 September (a similar length of time to that covered by the modelling). The derived pitch angle distribution for 1600 UT was quite broad, so it seems likely that a change in the axis of symmetry of ~20–30° may have little effect on the

Table 4.3: Increases at 1215 UT, 29 September 1989 normalised to Hobart.

Station	Actual %	Corrected %	Calculated %
Alma Ata	136.9±0.4	86.2	91.6
Apatity	110.3±0.8	105.9	121.0
Bern	97.3±1.5	88.5	72.0
Brisbane	73.5±1.8	73.5	78.6
Calgary	301.8±0.7	271.6	290.9
Campo Imperatore	115.6±0.8	83.2	65.2
Cape Schmidt	338.9±1.3	325.3	299.0
Climax	179.9±0.7	111.5	158.7
Darwin	11.7±1.1	11.7	10.0
Deep River	233.4±0.5	228.7	186.9
Durham	113.6±0.9	113.6	139.6
Goose Bay	248.3±1.0	248.3	188.6
Hermanus	96.2±1.0	96.2	98.6
Hobart	301.3±1.4	301.3	301.3
Inuvik	305.4±1.0	305.4	349.7
Irkutsk	209.3±0.9	194.6	184.9
Jungfraujoch	134.3±0.5	80.6	71.3
Kerguelen Island	146.4±0.8	144.9	93.2
Kiel	106.2±0.8	105.1	87.2
Kiev	113.9±0.9	111.6	103.6
Lomnicky Stit	158.9±0.4	108.1	92.8
Magadan	292.9±1.0	278.3	266.8
Mawson	36.9±1.0	34.3	47.3
McMurdo	166.7±0.7	160.0	134.4
Mexico City	43.6±1.4	31.0	32.0
Mirny	44.4±1.1	42.6	41.6
Moscow	126.7±0.8	122.9	100.4
Mt Norikura	26.8±0.2	14.2	20.8
Mt Wellington	337.9±1.2	304.1	301.6
Newark	97.8±1.1	97.8	129.4
Novosibirsk	132.4±0.8	127.1	172.5
Oulu	104.2±1.0	102.1	106.3
Potchefstroom	98.0±1.2	83.3	62.3
Rome	94.8±0.8	94.8	59.5
Samarkand	60.8±0.8	53.5	109.1
Sanae	64.0±1.5	62.1	57.9
South Pole	191.9±0.5	134.3	108.8
Tblisi	102.6±0.8	92.3	75.8
Terre Adelie	73.1±0.9	69.4	120.2
Thule	345.5±1.3	342.0	340.7
Tixie Bay	208.0±1.0	199.7	249.9
Tokyo	22.5±0.7	22.5	23.1
Tsumeb	52.0±0.4	42.6	37.4
Deep River muon	33.6±0.7	33.6	27.9
Goose Bay muon	33.2±0.7	33.2	26.9
Inuvik muon	32.1±0.8	32.1	33.7
Moscow muon	23.1±0.6	23.1	12.0
Mt. Norikura muon	14.5±0.3	14.5	15.0
Nagoya muon	10.0±0.3	10.0	13.9
Σ variances from corrected %			30024.6

Table 4.4: Increases at 1325 UT, 29 September 1989 normalised to Hobart.

Station	Actual %	Corrected %	Calculated %
Alma Ata	38.3±0.4	24.7	26.4
Apatity	186.2±0.9	179.9	191.3
Bern	77.2±1.4	70.7	51.6
Brisbane	25.5±1.7	25.5	23.9
Calgary	362.4±0.8	327.8	315.2
Campo Imperatore	49.8±0.7	37.3	24.8
Cape Schmidt	334.2±1.3	322.9	304.5
Climax	178.3±0.7	113.8	114.9
Darwin	0.0±1.1	0.0	1.9
Deep River	221.6±0.5	217.4	224.5
Durham	173.3±0.9	173.3	186.4
Goose Bay	210.9±0.9	206.0	220.5
Hermanus	69.8±0.9	69.8	43.2
Hobart	286.6±1.4	286.6	286.6
Inuvik	371.8±1.1	370.8	365.2
Irkutsk	126.4±0.8	118.1	109.8
Jungfraujoch	92.3±0.5	56.7	46.4
Kerguelen Island	260.9±0.9	257.6	199.8
Kiel	147.8±0.9	146.6	145.3
Kiev	108.1±0.9	106.1	87.4
Lomnicky Stit	132.3±0.4	91.5	74.0
Magadan	276.7±1.0	262.6	251.0
Mawson	221.9±1.3	216.3	202.3
McMurdo	267.3±0.8	256.3	244.1
Mexico City	13.4±1.3	9.0	8.4
Mirny	206.4±1.4	198.5	206.1
Moscow	181.3±0.9	176.3	149.6
Mt Norikura	4.9±0.2	2.7	4.5
Mt Wellington	337.3±1.2	306.9	290.3
Newark	155.7±1.2	155.7	144.5
Novosibirsk	169.9±0.8	165.9	149.4
Oulu	169.8±1.1	167.4	196.5
Potchefstroom	29.5±1.0	25.4	18.4
Rome	33.6±0.7	33.6	22.3
Samarkand	14.1±0.8	12.5	13.7
Sanae	182.6±1.9	177.0	183.3
South Pole	360.9±0.6	258.6	217.4
Tblisi	27.2±0.7	25.0	22.3
Terre Adelie	237.7±1.1	231.1	216.5
Thule	337.1±1.3	334.3	351.6
Tixie Bay	231.3±1.0	223.0	222.4
Tokyo	2.5±0.6	2.5	4.2
Tsumeb	13.3±0.4	10.9	8.4
Deep River muon	8.8±0.6	8.8	8.9
Goose Bay muon	8.5±0.7	8.5	8.2
Inuvik muon	8.9±0.7	8.9	10.4
Moscow muon	10.8±0.6	10.8	5.6
Mt. Norikura muon	2.8±0.3	2.8	3.1
Nagoya muon	0.8±0.3	0.8	2.7
Σ variances from corrected %			11752.8

Table 4.5: Increases at 1600 UT, 29 September 1989 normalised to Hobart.

Station	Actual %	Corrected %	Calculated %
Alma Ata	3.8±0.3	2.4	4.1
Apatity	108.1±0.8	104.3	98.0
Bern	9.9±1.2	9.1	11.2
Calgary	164.1±0.6	148.4	144.4
Cape Schmidt	147.4±1.0	142.6	150.5
Climax	54.2±0.6	34.6	32.0
Darwin	0.0±1.1	0.0	0.3
Deep River	101.7±0.4	99.8	112.5
Durham	81.4±0.8	81.4	86.2
Goose Bay	88.4±0.8	86.3	108.3
Hermanus	11.4±0.8	11.4	10.3
Hobart	104.3±1.1	104.2	104.3
Inuvik	149.7±0.8	149.3	148.1
Irkutsk	27.8±0.7	26.0	24.6
Jungfraujoch	15.7±0.4	9.4	9.8
Kerguelen Island	136.1±0.8	134.4	107.3
Kiel	60.5±0.8	60.0	52.2
Kiev	27.4±0.8	26.9	24.1
Lomnicky Stit	30.3±0.3	22.2	17.1
Magadan	95.3±0.8	90.4	93.1
Mawson	95.3±1.1	93.0	105.0
McMurdo	176.0±0.7	166.6	178.6
Mirny	98.9±1.2	94.5	119.9
Moscow	70.5±0.8	68.4	56.0
Mt Norikura	0.0±0.2	0.0	0.7
Mt Wellington	122.5±0.9	111.4	110.0
Newark	64.3±1.0	64.3	55.8
Novosibirsk	48.8±0.7	47.7	46.9
Oulu	101.5±1.0	100.0	99.0
Potchefstroom	5.3±1.0	4.5	3.6
Rome	3.2±0.7	3.2	4.2
Samarkand	0.0±0.7	0.0	2.1
Sanae	107.0±1.7	105.9	99.8
South Pole	259.5±0.5	186.0	149.1
Tblisi	2.8±0.6	2.5	3.9
Terre Adelie	172.4±1.1	167.6	152.5
Thule	107.1±1.0	106.2	102.7
Tixie Bay	129.1±0.9	124.5	115.3
Tokyo	0.0±0.6	0.0	0.5
Tsumeb	0.6±0.4	0.5	1.4
Deep River muon	1.5±0.6	1.5	1.2
Goose Bay muon	0.9±0.6	0.9	1.0
Inuvik muon	2.2±0.7	2.2	1.3
Moscow muon	1.6±0.2	1.6	0.9
Mt. Norikura muon	0.0±0.6	0.0	0.5
Nagoya muon	0.0±0.3	0.0	0.5
Σ variances from corrected %			4076.3

calculated increases. It seems reasonable that the change in latitude of the apparent particle arrival directions was due to movement of the local interplanetary magnetic field line.

The geographic longitude of the apparent particle arrival direction remained fairly constant. This implies a changing 'garden hose' angle due to the rotation of the Earth. The angles between the longitudes of the arrival directions and the Sun-Earth line (Ψ) are shown in the final column of Table 4.2. The value of Ψ at 1215 UT (100°) was significantly larger than the nominal 45° of the Archimedean spiral field. Examination of the measured field direction on 2 October 1989 reveals many hours when the average field direction was ~100° west of the Sun-Earth line. While there is no evidence to suggest that this field direction was constant from 29 September until 2 October, the data show that such a field direction is possible. Results for the later two times indicate that the field direction was closer to its nominal position, however the errors on these are expected to be larger because of the broadness of the derived pitch angle distributions. The solar wind speed on 25 and 26 September was low (down to ~280 km/s). This may have continued until close to the time of the GLE and would lead to a larger 'garden hose' angle than normal. Such slow solar wind speeds would also result in the footpoint of the 'garden hose' field line being closer to the western limb of the Sun and would help to explain the access of particles from a flare site beyond the limb.

It may be expected that low rigidity particles would be more affected by scattering in the interplanetary medium. This could result in rigidity dependent pitch angle distributions which were broader at low rigidities. The rigidity dependence of the pitch angle distribution at 1215 UT was in the opposite sense to this. The presence of high rigidity particles at larger pitch angles than those of lower rigidity may be due to the relative sizes of their gyroradii. Particle gyroradii increase with rigidity as the particles are more loosely bound to the magnetic field. The flare site was clearly some distance from the footpoint of the 'garden hose' field line (even given the low solar wind speed). Cliver *et al.* (1993) suggested that shock acceleration may have been responsible for the particles gaining access to this field line. They proposed that the shock was driven by a coronal mass ejection. This shock would expand rapidly to encompass field lines originating on the visible disc. Early in the event, it is possible that the shock may not have expanded sufficiently to provide a good connection to the 'garden hose' field line. In such circumstances, particles with large gyroradii (*i.e.* higher rigidity) would be more easily captured on to the field line and would propagate to Earth with large pitch angles. The speed of these particles along the field line would be some fraction of their total speed, so the dominance of high rigidities at large pitch angles may persist for some time. This could explain the derived distribution and may also account for the flattening of the particle spectrum at low rigidities, as the particles with small gyroradii may not have gained access to the field line until later in the event.

The pitch angle distribution derived for 1325 UT gives a slight indication of preferential back-scattering of particles from beyond the Earth resulting an enhancement at pitch angles near 180°. The distance to such a scattering region can be estimated by assuming that the particle population responsible for the first peak in the neutron monitor data resulted in the second peak when reflected

back. The time difference between the two peaks was ~70 minutes which means a travel time of ~35 minutes to the reflection point. This places the scattering region ~3.5–4 AU beyond the Earth. Particles travelling such a long distance through the interplanetary medium are highly likely to be scattered. If an efficient scattering region resulted in reflection at this distance from Earth, the pitch angle distribution of the returning particles would be very broad. This is consistent with the derived pitch angle distribution, but the estimated confidence limits are such that the enhancement at 180° pitch angle may not be real. The rigidity spectrum of any reflected particles may not be the same as that of the particles arriving directly from the Sun. This would depend on the rigidity dependence of the scattering efficiency. A model allowing different spectra for the two distributions may produce a more conclusive result.

4.4 Summary

The response of neutron monitors and surface muon telescopes has been modelled for three times during this large GLE. This is the first time a self-consistent model has included neutron monitor and muon telescope data simultaneously. Difficulties associated with matching the neutron and muon yield functions indicate that further work is required to improve the accuracy of the yield functions.

Rigidity dependence was found in the pitch angle distribution at 1215 UT. High rigidity particles were present at larger pitch angles than lower rigidity particles. This is contrary to the anticipated form of rigidity dependence caused by greater scattering at lower rigidities. The presence of high rigidity particles at large pitch angles indicates that these may have had easier access to the 'garden hose' field line early in the event. This is also consistent with the spectral evolution. Pitch angle distributions later in the event did not show any dependence on rigidity, confirming that the rigidity dependence at 1215 UT is probably related to particle access to the 'garden hose' field line rather than propagation characteristics of the interplanetary medium.

The change in apparent particle arrival direction during this event is thought to be due to movement of the local interplanetary magnetic field line although no IMF measurements are available to confirm this. There is some indication of preferential back-scattering from a region beyond the Earth, however this cannot be shown conclusively due to the high degree of scattering from all directions.

Chapter 5

October 1989 Events

Three GLEs were recorded during the month of October 1989, the solar particle fluence recorded at Earth exceeding in one month the total recorded in either of the previous two solar cycles (Shea, 1990). Figure 5.1 shows the Mt. Wellington neutron monitor data between 17 and 27 October 1989. The three GLEs are clearly visible on 19, 22 and 24 October.

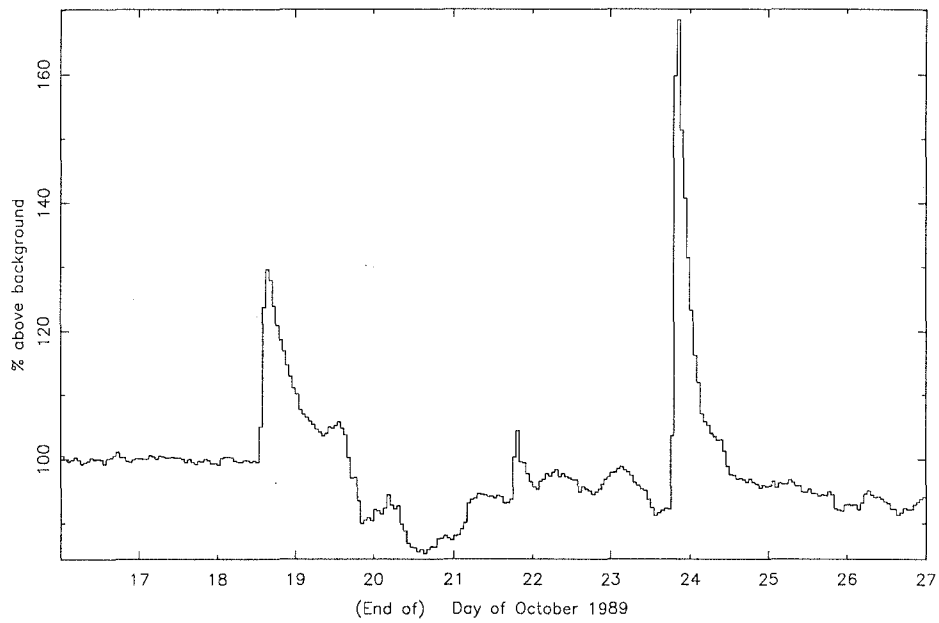

Figure 5.1: Mt. Wellington neutron monitor data during October 1989. Three GLEs can be seen on 19, 22 and 24 October.

Each of the three October 1989 GLEs resulted from flares in solar active region 5747. The first two events displayed some interesting fine structure which is discussed in detail in the following sections. Both of these events had very anisotropic onsets, the most notable being an intense spike observed at six neutron monitors on 22 October 1989. The spike at the onset of the 19 October event was much smaller, but was followed by a similar feature superimposed upon the main event ~100 minutes later. Mechanisms for producing such highly anisotropic initial onsets are discussed.

The third event discussed in this chapter showed almost classical form, despite the disturbance in the interplanetary medium due to the activity over the preceeding days. The neutron monitor response has been modelled using a rigidity dependent pitch angle distribution. A comparison of different spectral forms is also presented.

5.1 19 October 1989

The 19 October 1989 GLE reached a maximum intensity of 92% above the background at the South Pole neutron monitor. Figure 5.2 shows the cosmic ray profiles recorded at eight neutron monitors. Of particular interest is the small spike observed at several sites (*e.g.* Calgary, South Pole) shortly after 1300 UT. This has been associated with the decay products of solar neutrons (Shea *et al.*, 1991a; Shea *et al.*, 1991b). A similar spike can be seen at many of the same stations, peaking in the five minute interval from 1445 UT. The particle spectra and distributions have been modelled for both spikes and are discussed in conjunction with the neutron decay hypothesis and other possible mechanisms.

The location of the solar flare associated with this GLE was S25°, E9° on the solar disc. Hα emission began at 1229 UT, peaked with importance 3B at 1239 UT and ended at 2149 UT. The observed X-ray intensity of the flare was X13.0 and gamma-ray emission was recorded from 1257 UT (the start of the observations), reaching a maximum at 1258 UT and ending at 1325 UT. Metric radio emission of types I, II, III and IV were recorded. The type II emission occurred between 1250 and 1313 UT while pulsating type IV emission was observed from 1335 until 1452 UT.

The interplanetary magnetic field direction measured at IMP8 was within $\sim$10° of the Sun-Earth line throughout this GLE. The geomagnetic field was moderately disturbed at the start of the event with the Kp index falling from 4– to 2– towards the end of the event. A storm sudden commencement at 0916 UT on 20 October 1989 marked the passage of a shock. Cane and Richardson (1995) also reported a possible shock passing the Earth at $\sim$1700 UT on 20 October 1989, however this did not produce a sudden commencement. They associated the second shock with the solar flare which produced the GLE. Cane and Richardson noted Hα and X-ray activity in active region 5747 during October 18 and 19, but could not find a definite association with the first shock. Bavassano *et al.* (1994) did not report a second shock and attributed the first to activity associated with the flare on 19 October.

5.1.1 Interpretation of the neutron monitor response

Shea *et al.* (1991a) proposed a neutron decay hypothesis to explain the early onset at several stations. This mechanism involves solar neutrons produced by the "knock-on" process as accelerated protons interact in the lower chromosphere. The neutrons propagate radially away from the flare site and at some point decay, producing protons, electrons and neutrinos. Some fraction of the protons may be

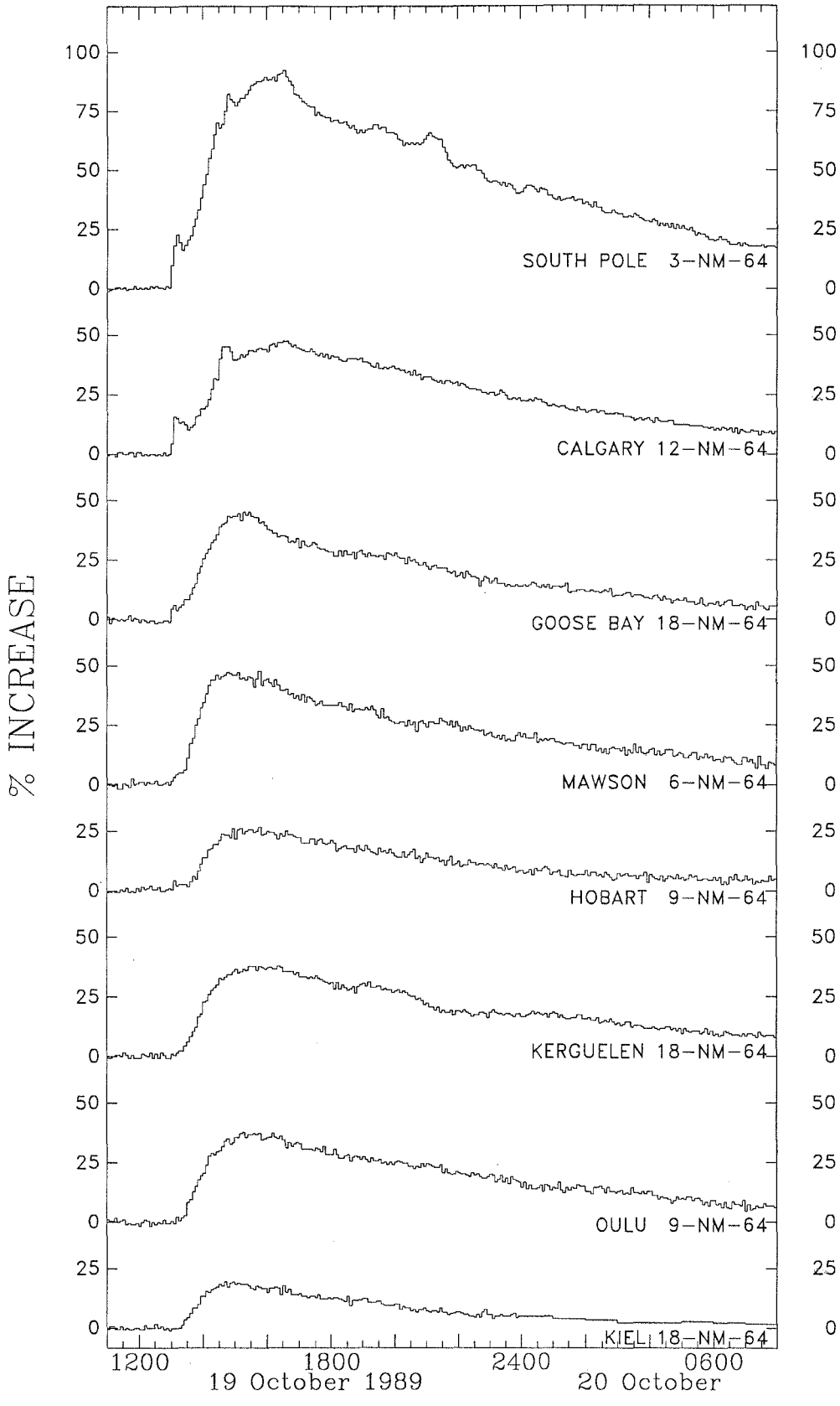

Figure 5.2: Cosmic ray increases at South Pole, Calgary, Goose Bay, Mawson, Hobart, Kerguelen Island, Oulu and Kiel neutron monitors between 1100 UT on 19 October 1989 and 0800 UT on 20 October 1989.

produced in the vicinity of the field line connected to Earth. These will propagate along the field line, arriving earlier than the solar flare protons which must propagate diffusively and follow the full length of the field line from the Sun to the Earth. Shea *et al.* determined that the spectrum of particles in the initial spike was deficient at rigidities greater than 3 GV. They stated that neutrons within the energy range 1–3 GeV have a reasonable probability of decay within 1 AU, so this spectrum is consistent with the neutron decay theory. A hardening of the spectrum was noted following the initial spike. The pitch angle distributions derived by Shea *et al.* (1991b) indicate that the particle distribution was deficient at pitch angles less than 28°. They believe that this is also consistent with neutron decay, as the position of the flare site and the probable interplanetary magnetic field line are such that the decay protons have a low probability of moving in the exact direction of the field line.

The results presented by Shea *et al.* (1991a; 1991b) are indeed consistent with the neutron decay hypothesis, however, they make no mention of the second spike recorded by many of the same neutron monitors around 1445 UT. The appearance of both spikes at the same stations indicates that the particles arrived from approximately the same direction in space. It is likely that the same mechanism was responsible for both spikes. This would eliminate the neutron decay hypothesis for the early spike as this mechanism could not produce the later one. Shea *et al.* and Bieber and Evenson (1991) both reported spectral differences between the early spike and the main GLE. There are also clear differences in anisotropy between the spikes and the main event. A full analysis for the times of both spikes as well as the main event is required to determine the characteristics of the two mechanisms.

Modelling

Analysis of the initial spike was performed for the five minute interval beginning at 1305 UT. This included the peak of the spike at most stations. In order to ensure that the results were not affected by any contribution from the mechanism responsible for the main event, the observed response at those stations without a spike was set to zero in the least squares analysis. Some of these stations recorded intensities slightly above background at this time, however the smooth rise to the main event indicates that this was unrelated to the spike at other stations. The percentage increases entered as the 'observed' increases in the least squares analysis are shown in the fourth column (labelled Input) of Table 5.1. The preceeding columns show the actual increases (with poisson errors) and the altitude corrected responses (corrected to sea level by the two attenuation length method using a flare attenuation length of 101 g cm^{-2}). The derived particle pitch angle distribution is shown in Figure 5.3. The axis of symmetry of this distribution was S3°, E322° in extended Earth coordinates. The exponent of the power law spectrum was –6.5. The flux at 1 GV over the forward steradian was 54.1 particles (cm ^{2} s ster GV)$^{-1}$ while the flux averaged over 4π steradians was 5.6 particles (cm ^{2} s ster GV)$^{-1}$. The calculated increases using these parameters are shown in Table 5.1, normalised to the response at the Calgary neutron monitor.

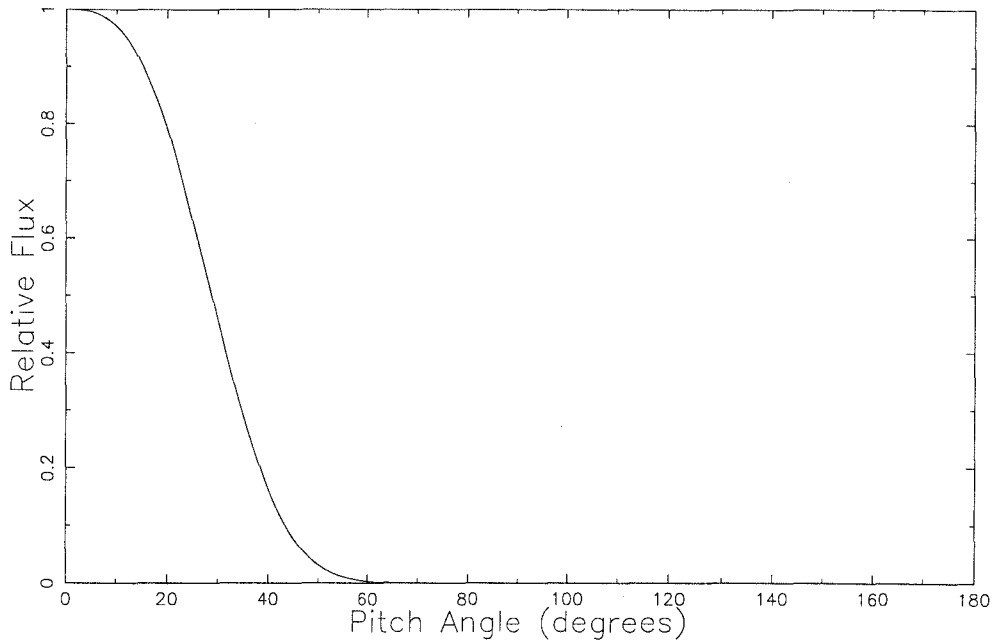

Figure 5.3: Derived pitch angle distribution at 1305 UT, 19 October 1989 during the initial spike.

The Σ variance values shown at the bottom of the table are the sums of squares of differences between calculated and corrected percentage increases. This definition applies in all other tables showing calculated increases and Σ variances.

The derived particle arrival direction at 1305 UT was $\sim$19° west of the Sun-Earth line and within 15° of the hourly averaged interplanetary magnetic field direction. The pitch angle distribution was very anisotropic and did not exhibit the deficit at small pitch angles shown by Shea *et al.* (1991b). While these features are not inconsistent with the neutron decay hypothesis, they could also be produced by scatter free propagation of solar protons along the 'garden hose' field line. The derived particle spectrum is steeper than that determined by Shea *et al.* for low rigidities ($<$ 3 GV), however, their spectrum steepened with increasing rigidity.

Investigation of the later spike is more difficult as the recorded increases are due to the combined effects of two mechanisms. If the two spikes were produced by the same mechanism, the particles should arrive from the same direction in space. To determine the expected arrival direction at 1445 UT from that derived for 1305 UT, the rotation of the Earth must be taken into account. The resulting arrival direction is S3°, E297° in extended Earth coordinates. The size of the spikes at Calgary and South Pole were estimated for the five minute interval from 1445 UT and compared with those at 1305 UT. The spikes at 1445 UT were $\sim$0.6 times those at 1305 UT. The expected increases at all stations were calculated using the same pitch angle distribution and spectrum as that derived for 1305 UT, but with the arrival direction appropriate for 1445 UT. The results were normalised to 0.6 times the increase at Calgary at 1305 UT. It is possible that the pitch angle distribution at 1445 UT was broader than that at 1305 UT and that the spectrum may also have changed, however, the same parameters were

Table 5.1: Increases at 1305 UT and 1445 UT, 19 October 1989

	1305 UT				1445 UT			
Station	Actual %	Corrected %	Input	Calculated %	Actual %	Corrected %	Input	Calculated %
Bern	0.0±1.1	0.0	0.0	0.1	3.1±1.1	2.5	2.4	3.2
Calgary	15.6±0.4	11.5	11.5	11.5	45.1±0.4	33.4	26.5	31.7
Climax	2.5±0.3	0.9	0.0	1.2	22.6±0.3	8.4	8.0	9.8
Deep River	6.7±0.4	6.4	6.4	5.9	41.9±0.4	39.8	38.8	38.3
Durham	1.2±0.7	1.2	1.2	2.3	29.8±0.8	29.8	28.5	29.1
Goose Bay	6.3±0.7	6.2	6.2	5.9	43.4±0.7	43.0	42.9	40.7
Hermanus	1.8±0.8	1.8	1.8	0.1	4.9±0.8	4.9	4.8	2.9
Hobart	4.5±0.9	4.5	4.5	3.7	23.6±1.0	23.6	20.1	22.6
Huancayo	0.3±0.5	0.1	0.0	0.0	0.0±0.5	0.0	0.0	0.1
Inuvik	0.0±0.6	0.0	0.0	0.0	29.2±0.7	28.9	28.9	27.8
Jungfraujoch	1.3±0.2	0.4	0.0	0.1	4.8±0.2	1.6	1.5	3.0
Kerguelen Island	0.5±0.6	0.5	0.0	0.9	34.6±0.6	33.6	33.5	33.4
Kiel	0.0±0.7	0.0	0.0	1.2	17.4±0.7	17.1	16.7	15.1
Lomnicky Stit	0.9±0.2	0.5	0.0	0.2	8.8±0.2	5.1	5.0	4.6
Mawson	3.2±0.9	3.0	0.0	0.0	47.3±1.0	44.5	44.5	42.9
McMurdo	1.5±0.5	1.4	0.0	0.0	35.6±0.5	32.0	32.0	28.6
Mt Washington	8.1±0.8	4.8	4.8	3.0	57.8±0.9	34.1	32.8	32.5
Mt Wellington	3.7±0.6	2.9	2.9	4.7	29.8±0.7	23.5	19.6	22.1
Newark	0.0±0.9	0.0	0.0	1.5	23.9±1.0	23.9	23.1	19.9
Novosibirsk	0.0±0.6	0.0	0.0	0.6	12.8±0.6	12.2	11.7	10.7
Oulu	0.0±0.8	0.0	0.0	0.0	35.2±0.9	34.1	34.1	39.9
Potchefstroom	2.6±0.8	1.8	0.0	0.1	3.7±0.8	2.5	2.4	0.8
Rome	0.3±0.7	0.3	0.0	0.0	0.9±0.7	0.9	0.9	1.1
Sanae	5.4±1.3	5.0	2.3	0.4	47.0±1.5	43.7	43.7	41.8
South Pole	18.4±0.2	7.7	7.7	8.0	82.1±0.3	34.5	34.1	33.6
Terre Adelie	0.0±0.8	0.0	0.0	0.0				
Thule	0.9±0.8	0.9	0.0	0.0	32.0±0.9	31.4	31.4	29.9
Σ variances from corrected %				21.5				126.0

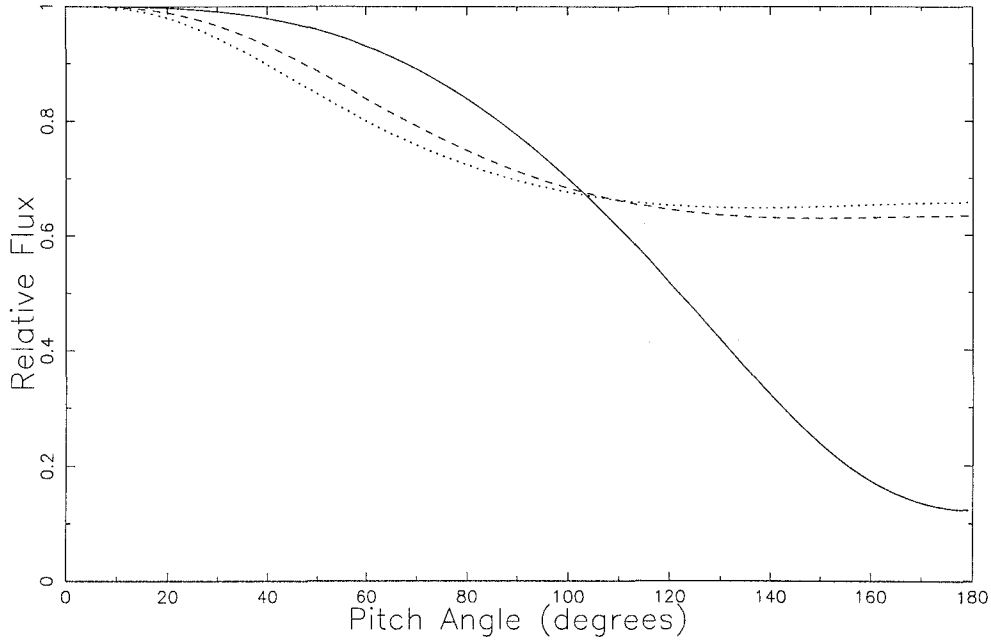

Figure 5.4: Derived pitch angle distributions at 1330 UT (solid line), 1445 UT (dashed line) and 1500 UT (dotted line), 19 October 1989.

used as a first approximation. The calculated responses from this model were consistent with the stations which showed evidence of a spike at 1445 UT. The increase calculated for South Pole was somewhat lower than observed, however this was found to increase significantly with a slight broadening of the pitch angle distribution. The calculated responses were subtracted from the observed increases at 1445 UT (corrected to sea level atmospheric pressure) to produce the figures in the seventh column of Table 5.1. These numbers were used as the 'observed' increases in the least squares analysis to investigate the main GLE. No data has been entered for Terre Adelie, as a possible step in the data from this station just after 1425 UT which is inconsistent with other data makes the actual increases beyond this point difficult to determine. The derived pitch angle distribution is shown as the dashed line in Figure 5.4. The other traces in this figure are described below. The axis of symmetry of the pitch angle distribution was S1°, E46° which is ~90° east of the Sun-Earth line. The exponent of the power law spectrum was −6.0. The mild anisotropy of the pitch angle distribution indicates significant scattering during the propagation of the particles. The unusual arrival direction almost perpendicular to the local interplanetary magnetic field direction is very strange and must be considered in the context of the rest of the event.

The neutron monitor responses were also analysed for the five minute intervals beginning 1330, 1500 and 1825 UT. The actual, altitude corrected and calculated percentage increases for these times are shown in Table 5.2. The particle pitch angle distributions derived for 1330 and 1500 UT are shown as the solid and dotted lines respectively in Figure 5.4. The derived pitch angle distribution for 1825 UT was essentially isotropic, so is not shown in the figure. The axes of symmetry of the pitch angle distributions and the spectral parameters are tabulated in Table 5.3

Table 5.2: Increases at 1330 UT, 1500 UT and 1825 UT, 19 October 1989.

	1330 UT			1500 UT			1825 UT		
Station	Actual %	Corrected %	Calculated %	Actual %	Corrected %	Calculated %	Actual %	Corrected %	Calculated %
Bern	0.0±1.1	0.0	0.8	6.8±1.1	5.6	3.4	1.7±1.1	1.4	1.2
Calgary	10.2±0.4	7.5	6.2	39.2±0.4	29.0	33.1	38.9±0.4	28.8	28.4
Climax	5.2±0.3	1.9	2.6	21.2±0.3	7.8	10.2	10.2±0.3	3.8	4.8
Deep River	9.5±0.4	9.0	7.9	41.7±0.4	39.6	38.9	27.8±0.4	26.4	27.7
Durham	6.3±0.7	6.3	6.3	30.8±0.8	30.8	30.0	17.2±0.7	17.2	19.0
Goose Bay	8.3±0.7	8.2	8.3	43.6±0.7	43.2	40.7	28.8±0.7	28.5	28.6
Hermanus	0.7±0.8	0.7	0.8	2.6±0.8	2.6	3.1	2.6±0.8	2.6	1.2
Hobart	1.9±0.9	1.9	3.2	21.5±1.0	21.5	24.4	18.7±1.0	18.7	17.8
Huancayo	1.1±0.5	0.4	0.0	0.0±0.5	0.0	0.1	0.0±0.5	0.0	0.0
Inuvik	1.5±0.7	1.5	1.9	33.0±0.7	32.7	30.4	24.1±0.7	23.9	29.4
Jungfraujoch	1.6±0.2	0.5	0.8	4.4±0.2	1.5	3.1	2.9±0.2	1.0	1.2
Kerguelen Island	6.1±0.6	5.9	6.9	36.4±0.6	35.3	35.3	28.9±0.6	28.0	28.7
Kiel	4.7±0.7	4.6	3.7	18.2±0.7	17.8	15.8	10.9±0.7	10.7	9.6
Lomnicky Stit	3.1±0.2	1.8	1.2	8.4±0.2	4.9	4.9	No data		
Mawson	11.3±1.0	10.6	8.8	46.0±1.0	43.2	41.9	33.0±1.0	31.0	28.4
McMurdo	3.8±0.5	3.4	6.8	35.7±0.5	32.1	30.3	32.3±0.5	29.1	29.0
Mt Washington	12.0±0.9	7.1	7.0	No Data			36.4±0.9	21.5	23.4
Mt Wellington	4.5±0.7	3.6	3.2	31.0±0.7	24.5	23.9	20.8±0.7	16.4	16.4
Newark	4.5±0.9	4.5	4.4	24.2±1.0	24.2	20.8	12.6±0.9	12.6	11.3
Novosibirsk	2.9±0.6	2.8	2.0	13.1±0.6	12.4	11.7	7.8±0.6	7.4	6.7
Oulu	8.2±0.9	8.0	8.5	35.3±0.9	34.2	40.9	27.8±0.9	27.0	28.5
Potchefstroom	0.0±0.8	0.0	0.2	0.4±0.8	0.3	0.9	3.9±0.8	2.7	0.2
Rome	0.1±0.7	0.1	0.3	1.6±0.7	1.6	1.1	0.6±0.7	0.6	0.3
Sanae	8.5±1.4	7.9	8.3	48.3±1.5	44.9	44.4	31.9±1.4	29.7	28.4
South Pole	20.3±0.2	8.5	8.1	77.2±0.3	32.4	33.0	70.4±0.3	29.6	28.6
Terre Adelie	9.5±0.8	8.8	6.0						
Thule	3.5±0.8	3.4	3.5	32.8±0.9	32.1	33.1	34.8±0.9	34.1	29.0
Σ variances from corrected %			32.7			119.1			89.7

along with those determined for 1445 UT as described above. The final column of Table 5.3 gives the angle in longitude between the axis of symmetry and the Sun-Earth line. The apparent particle arrival directions determined for each of these times was east of the Sun-Earth line and approximately perpendicular to the local interplanetary magnetic field direction. The increases recorded at 1305 UT by those stations which did not observe the spike are also consistent with an eastern arrival direction, however the intensities were too small for detailed modelling to be performed.

Table 5.3: Spectral parameters and apparent particle arrival directions for 1330 UT, 1445 UT, 1500 UT and 1825 UT, 19 October 1989. Fluxes in units of particles $(cm^2\ s\ ster\ GV)^{-1}$.

	γ	$J_{\|\|}$	J_{av}	Latitude	Longitude	Ψ
1330 UT	–5.7	10.8	7.5	–30	54	E77°
1445 UT	–6.0	68.4	51.6	–1	46	E91°
1500 UT	–6.0	71.0	53.4	14	45	E97°
1825 UT	–6.8	83.1	80.8	Isotropic distribution		

Comparison of the parameters in Table 5.3 with those derived for 1305 UT clearly indicates that two mechanisms were responsible for the observed particle increases. The first, which produced the spikes at 1305 and 1445 UT was a focused transport of particles along the 'garden hose' field line. The second mechanism resulted in a particle arrival direction almost perpendicular to the local interplanetary magnetic field direction. These particles arrived with mild anisotropy from east of the Sun-Earth line. The rigidity spectrum of the particles also differed between the two mechanisms. Those which produced the spike at 1305 UT had a significantly softer spectrum (–6.5) than that derived for 1330 UT (–5.7). The spectrum of particles involved in the main event (eastern arrival) gradually softened as isotropy was approached.

5.1.2 Discussion

The interplanetary magnetic field direction at Earth at the time of this GLE was very close to the Sun-Earth line. This direction was maintained for some hours, indicating a region where the field lines were nearly radial. This lack of curvature for at least part of the 'garden hose' field line means that the footpoint of the field line was probably east of its nominal location (W57°). It is therefore quite likely that some of the accelerated particles from the flare at E9° gained relatively easy access to this field line and propagated to Earth. The length of the 'garden hose' field line may have been less than the nominal 1.3 AU due to the almost radial section, thus decreasing the propagation time and the degree of scattering. This situation would explain both the prompt onset and the anisotropic pitch angle distribution derived for the early part of the event.

The association of an observed interplanetary shock with this solar event is in dispute. There is some doubt as to whether the second solar wind signature

reported by Cane and Richardson (1995) was a shock since it did not produce a storm sudden commencement; however association of the first shock (0916 UT, 20 October) with the same flare activity as the GLE results in a very fast shock transit speed which may be inconsistent with other evidence. Both possibilities must be considered. The two scenarios are (i) the shock which passed Earth at 0916 UT on 20 October 1989 originated from the same flare activity as the GLE; or (ii) the second feature at ~1700 UT was a shock and was associated with the GLE flare. In this case, the first shock was associated with previous activity and was somewhere between the Sun and the Earth at the time of the GLE. The above interpretation of the early spike is independent of these two scenarios, providing the presence of a shock in the interplanetary medium did not impede the passage of particles along the 'garden hose' field line. This depends on the location and extent of the shock.

If the first shock was associated with the same solar eruption as the GLE, its average propagation speed was ~2000 km/s. The speed of the shock as it left the Sun would have been much greater than this. Such fast shocks are very rare, in fact only one has previously been observed to have an average speed faster than this (H. Cane, private communication). The second scenario links the second, less intense shock with the GLE flare and the first shock with previous, as yet unidentified solar activity. On the surface, these may appear to be strange associations, as an eruption large enough to produce a GLE would be expected to produce a significant interplanetary shock. Furthermore, the strength of the first shock is such that a definite association with solar activity may be expected. However, it is possible for a coronal mass ejection, which would drive such a shock, to be produced without the presence of a solar flare. Secondly, examination of the flow speed behind the two shocks suggests that the second was travelling faster than the first. While only a loose correlation exists between flow speed and shock transit speed (Cliver *et al.*, 1990), this evidence indicates that the first shock was not travelling at sufficient speed to be associated with the GLE flare.

Particles accelerated in the flare eruption would propagate along many field lines. The IMF distortion evident from the small 'garden hose' angle may indicate a region of compressed field near the Earth, so field lines with footpoints some distance from that of the 'garden hose' field line may pass quite close to the Earth. Particles propagating along these field lines may diffuse towards the Earth. The broad pitch angle distributions derived for the main part of the event are consistent with this theory. The harder spectrum at 1330 UT (compared with that of the early spike) is also compatible with this idea as the lower rigidity particles would be less likely to diffuse across field lines. Diffusion of particles from nearby field lines is possible under either of the two scenarios outlined above, however it seems more likely in the presence of an interplanetary shock. Without such a discontinuity, it is probable that the field lines near the 'garden hose' field line would provide similarly scatter-free propagation paths. Under such conditions it is unlikely that a significant number of particles would diffuse across field lines and propagate to Earth. An interplanetary shock and associated magnetic field turbulence would cause particles to be scattered. This would lead to a fairly isotropic flow of particles, some of which may reach the Earth. The edge of the

interplanetary shock must have been near but not intersecting the 'garden hose' field line. A CME on the eastern side of the solar disc could produce such a shock.

The second spike in the neutron monitor data began at ~1430 UT, nearly 80 minutes after the end of the metric type II emission. This emission is associated with the propagation of a shock through the corona. Thus, at the time of the second spike, the shock had propagated into interplanetary space. In the absence of another shock further out in the interplanetary medium, the only obvious mechanism by which a second energetic particle population could find access to the 'garden hose' field line is by acceleration at the shock front. Stochastic shock acceleration by an interplanetary shock is unlikely to accelerate particles to sufficient energies to penetrate the Earth's atmosphere. Diffusive scattering across the shock provides a more efficient acceleration mechanism, but there must be adequate scattering both upstream and downstream of the shock. If this requirement is satisfied, acceleration to ~1 GeV is possible in tens of minutes (Lee and Ryan, 1986). If conditions were suitable for acceleration of particles to energies greater than the atmospheric threshold, the acceleration process may be expected to be continuous. This is contrary to the observation of two distinct spikes arriving along the 'garden hose' field line.

In the case of two shocks in the interplanetary medium, the particle interactions with the turbulent magnetic region behind the outer shock would result in scattering as discussed above. Some particles may travel back towards the Sun. The second shock emerging from the corona would also scatter particles allowing some to gain access to the 'garden hose' field line. Propagation of these particles to Earth would produce a second anisotropic increase. Scattering at the rearward shock is expected to be fairly efficient due to the speed and strength of the shock soon after leaving the corona and the converging magnetic field lines through which the particles must propagate as they approach it.

Interplanetary shock acceleration or scattering at interplanetary shocks would result in a much softer particle spectrum than that of the first spike. It is not possible to accurately model the spectrum of the second spike as the neutron monitor responses would have to be estimated by assuming a smooth response to the particles arriving from the east. The low response modelled for South Pole may indicate that the applied spectrum (the same as that derived for the first spike) was deficient at low rigidities.

It is difficult to interpret the modelled particle distributions if the shock which passed Earth at 0916 UT on 20 October was the only shock present in the interplanetary medium at the time of the GLE. This indicates that the disturbance which passed Earth at ~1700 UT on 20 October was a shock and was associated with the same solar activity as the GLE. The shock observed at 0916 UT must have been produced in an earlier solar event.

The two spikes observed in neutron monitor data during this GLE can be explained by focussed transport along the 'garden hose' field line of (i) particles gaining direct access by acceleration in the flare eruption and (ii) particles reflected between two interplanetary shocks to gain access to the field line. The results presented here do not completely rule out the neutron decay hypothesis for the first spike, but focused transport is sufficient to produce the observed features and

is a simpler concept. This also allows for the focussed transport path to remain in place for the propagation of the particles which produced the second spike.

5.2 22 October 1989

The second GLE of the October 1989 sequence occurred on 22 October. The cosmic ray profile was unusual and varied significantly between stations. Six neutron monitor stations observed a very narrow (< 20 minute) spike preceeding the main event. In the case of McMurdo, the intensity of the spike was nearly five times the maximum intensity of the main GLE. Figure 5.5 shows the cosmic ray profiles of the stations which observed the spike. The peak of the main event did not occur at the same time at all stations. Most reached their maximum within the half hour from 1830 UT to 1900 UT, with some exhibiting two distinct maxima. Data from some stations which did not observed the spike are shown in Figure 5.6. The timescale is the same as for Figure 5.5.

The location of the solar flare associated with this GLE was S27°, W32° on the solar disc. Hα emission began at 1708 UT, peaked at 1757 UT with importance 2B and ended at 2108 UT. A loop-type prominence was observed. A coincident X-ray event began at 1708 UT and peaked with intensity X2.9 at 1757 UT. Metric type II bursts were observed between 1745 UT and 1759 UT and type IV emission occurred between 1744 UT and 1842 UT. Both the type II and type IV emissions were of importance 3. A coronal mass ejection occurred at about 1800 UT (Kahler, 1993); the exact time that the CME began is unknown due to a gap in observations. The earliest cosmic ray onset was at South Pole neutron monitor in the two minute interval beginning at 1758 UT.

5.2.1 Modelling

Data from 25 neutron monitors were used in modelling this event. In all cases the five-minute cosmic ray data were used. The times chosen for the analysis were the peak of the spike (1805 UT–1810 UT) and eight other times spread through the event (1820 UT, 1830 UT, 1840 UT, 1850 UT, 1900 UT, 1910 UT, 1920 UT and 2300 UT where each of these times indicates the start of a five minute period).

The geomagnetic field was disturbed at the time of this event, as evidenced by a Kp value of 5+ throughout. Under such conditions the viewing directions of the neutron monitors can be quite different from the viewing directions at geomagnetically quiet times. The use of the Tsyganenko magnetospheric model allows the calculation of asymptotic viewing directions appropriate to the disturbance. Figure 5.7 is a comparison of the viewing directions of several stations calculated for quiet (Kp=0) and disturbed (Kp=5) geomagnetic conditions at the time of the event. The viewing directions are plotted in extended geographic coordinates (latitude and longitude). For each station, consecutive points (representing the viewing directions at different rigidities) are joined until the penumbral region is encountered. For rigidities within the penumbra, the allowed viewing directions are plotted as individual points. Markers indicate the viewing directions at 1, 5 and 10 GV for each station.

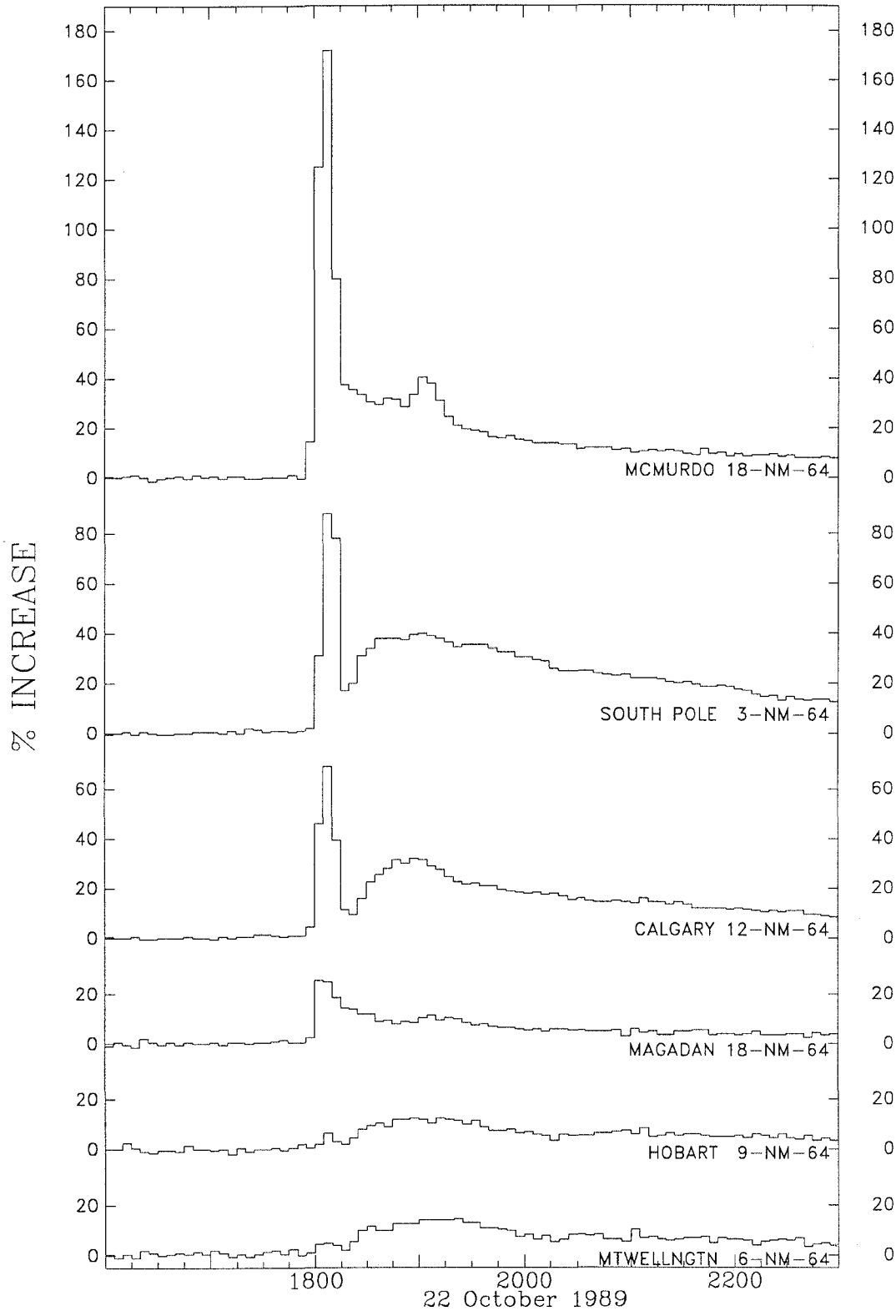

Figure 5.5: Cosmic ray increases at McMurdo, South Pole, Calgary, Magadan, Hobart and Mt. Wellington neutron monitors between 1600 and 2300 UT on 22 October 1989.

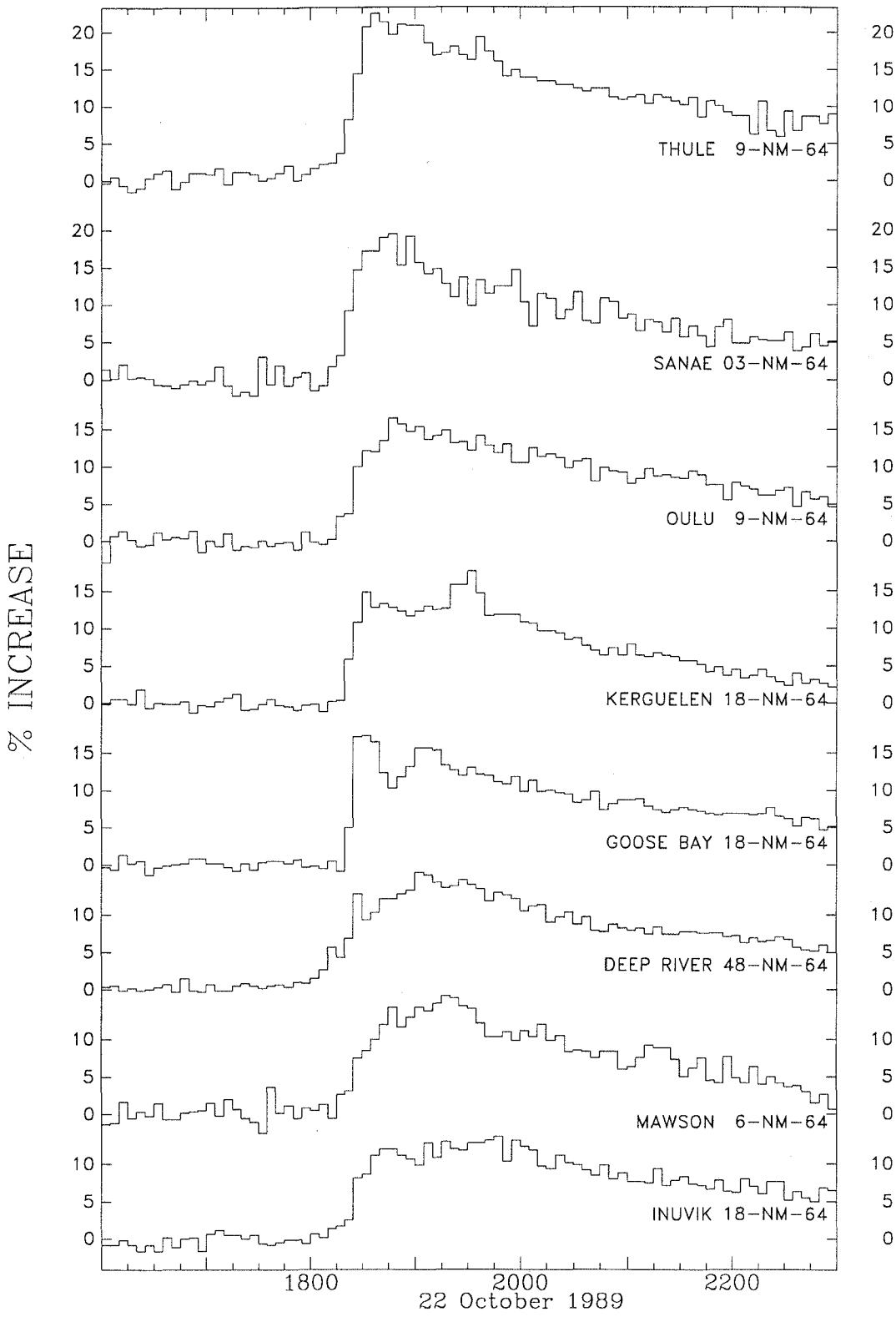

Figure 5.6: Cosmic ray increases at Thule, Sanae, Oulu, Kerguelen Island, Goose Bay, Deep River, Mawson and Inuvik neutron monitors between 1600 and 2300 UT on 22 October 1989.

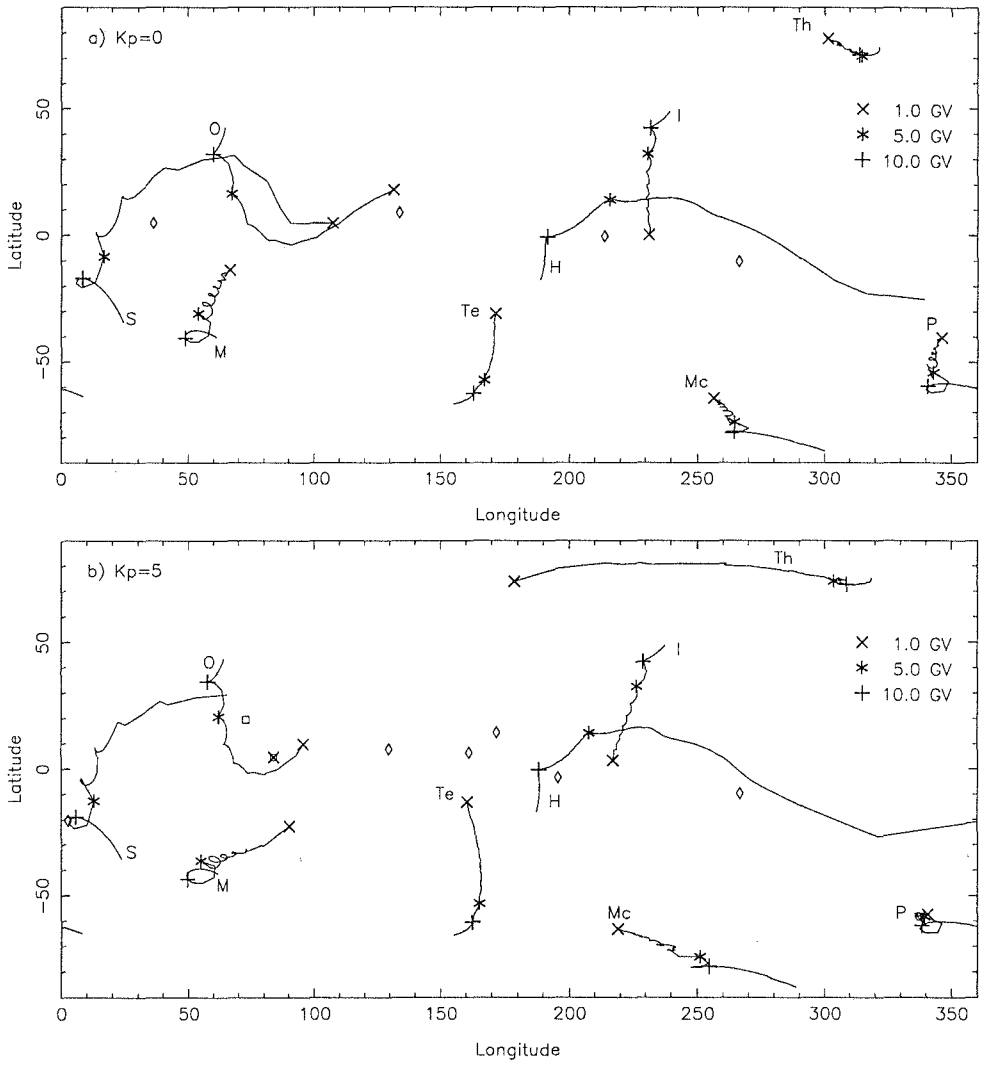

Figure 5.7: Viewing directions at 1805 UT on 22 October 1989 under a) quiet (Kp=0) and b) disturbed (Kp=5) geomagnetic conditions. Sanae S and □; Mawson M; Oulu O; Terre Adelie Te; Hobart H and ◇; Inuvik I; McMurdo Mc; Thule Th; South Pole P. The viewing directions at 1, 5 and 10 GV are indicated by ×, ∗ and + respectively.

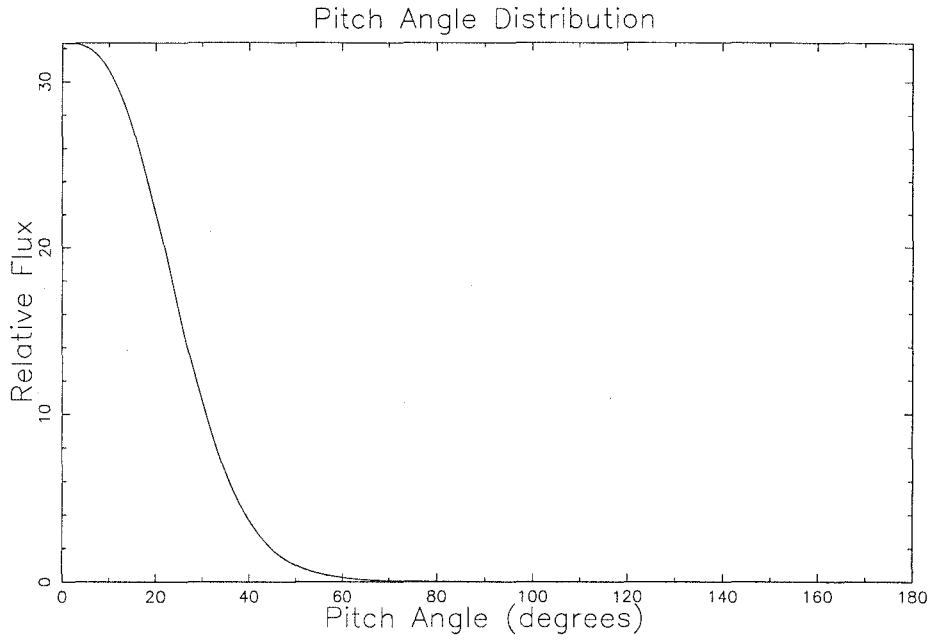

Figure 5.8: Derived pitch angle distribution at 1805 UT, 22 October 1989 during the initial spike.

Modelling the spike

Examination of 10-second data from the South Pole neutron monitor reveals two distinct peaks within the spike (Bieber *et al.*, 1990). The results presented here are for the period 1805 UT to 1810 UT which includes the first of the peaks in the South Pole data. The pitch angle distribution found to give the best fit to the observed increases is shown in Figure 5.8. The axis of symmetry of this distribution was S50°, E264°in extended Earth coordinates which is very close to the Sun-Earth line. This pitch angle distribution reflects a very high degree of anisotropy in the arriving particles. The original analysis of this data resulted in a fitted power-law spectrum with a slope of –6.3. When the errors in the trajectory tracing code (refer Section 3.1.4) were corrected, this analysis was repeated to see how much effect the changes would make. Changes in the pitch angle distribution and particle arrival direction were insignificant, however the spectral exponent was found to be –5.8. The flux at 1 GV over the forward steradian ($J_{||}$) was 230.4 particles (cm^2 s ster GV)$^{-1}$ and the average over 4π steradians was 24.5 particles (cm^2 s ster GV)$^{-1}$. The percentage increases calculated from the model are shown in Table 5.4 along with the observed percentage increases (and their poisson errors) and the increases corrected to sea level atmospheric pressure according to the two attenuation length method described in Section 2.5. The flare attenuation length was assumed to be 100 g cm^{-2}. The calculated increases were normalised to the response at McMurdo.

Table 5.4: Increases at 1805 UT, 22 October 1989 normalised to McMurdo.

Station	Actual %	Corrected %	Calculated %
Bern	4.6±1.1	3.8	0.7
Calgary	69.1±0.4	47.0	47.3
Climax	5.9±0.3	2.2	2.9
Deep River	3.0±0.4	2.8	1.6
Durham	1.3±0.7	1.3	1.8
Goose Bay	0.0±0.7	0.0	0.2
Hermanus	0.0±0.8	0.0	0.5
Hobart	6.4±1.0	6.4	6.8
Inuvik	1.0±0.7	1.0	0.5
Jungfraujoch	0.0±0.2	0.0	0.3
Kerguelen Island	0.0±0.6	0.0	0.0
Kiel	3.5±0.7	3.4	1.6
Lomnicky Stit	1.5±0.2	0.9	0.8
Magadan	25.2±0.7	22.9	20.9
Mawson	1.4±1.0	1.3	0.1
McMurdo	172.0±0.7	153.1	153.1
Mt Washington	2.6±0.8	1.4	1.3
Mt Wellington	5.3±0.7	4.2	6.3
Newark	0.4±0.9	0.4	1.8
Oulu	0.0±0.9	0.0	0.0
Potchefstroom	1.2±0.8	0.8	0.1
Rome	0.9±0.7	0.9	0.1
Sanae	0.0±1.3	0.0	0.1
South Pole	88.0±0.2	33.4	33.4
Terre Adelie	1.4±0.8	1.3	2.6
Thule	2.1±0.8	2.1	0.0
Σ variances from corrected %			35.3

Modelling the main event

The second phase of the GLE was modelled at seven times each separated by ten minutes and one other time later in the event. In each case a five minute average was used for the percentage increases recorded by the neutron monitors. The latitude and longitude of the axes of symmetry of these distributions are listed in Table 5.5 along with the spectral parameters. The fitted spectra were modified power laws. The two parameters quoted are the power law exponent (γ) and the change of γ per GV ($\delta\gamma$). A positive value of $\delta\gamma$ results in a spectrum which steepens with increasing rigidity. The values of $\delta\gamma$ in the spectra fitted for this event result in very little bending of the spectrum. Plots of the spectrum for four of the modelling times are shown in Figure 5.9. It can be seen that the spectrum softened during the event. The flux in the forward steradian ($J_{||}$) was averaged over 4π steradians to obtain J_{av}. These values are also shown in Table 5.5. The fitted pitch angle distributions are shown in Figures 5.10 and 5.11. The distributions are scaled according to the flux in the forward steradian determined in the model. It can be seen from these figures that the particle intensity in the anti-sun direction was enhanced. The reason for this is discussed in the next section. The calculated percentage increases at each station are listed in Tables 5.6, 5.7 and 5.8 along with the observed percentage increases (and their poisson errors) and the increases corrected to sea level atmospheric pressure according to the two attenuation length method described previously.

Table 5.5: Derived source positions and spectral parameters for the main part of the 22 October 1989 GLE. Fluxes in units of particles $(cm^2\ s\ ster\ GV)^{-1}$.

Time	1820	1830	1840	1850	1900	1910	1920	2300
Latitude	−53	−48	−45	−40	−40	−35	−31	-22
Longitude	239	233	229	225	222	218	214	271
γ	−5.4	−5.8	−6.2	−6.6	−6.7	−6.7	−6.8	−6.5
$\delta\gamma$	0.1	0.1	0.1	0.0	0.0	0.1	0.05	0.0
$J_{||}$	30.6	42.3	60.8	74.5	115.1	97.9	69.9	15.3
J_{av}	8.7	20.5	32.9	40.2	54.9	49.2	44.5	12.6

5.2.2 Discussion

This event displays a remarkable evolution in the pitch angle distribution. The anisotropy of particles arriving at Earth is determined by the diffusion and scattering that takes place during propagation through the interplanetary medium. Interpretation of this event must explain how the propagation conditions could evolve so rapidly. Suggested hypotheses are discussed below.

The fitted pitch angle distributions for the main event show significant enhancement in the number of particles arriving from the anti-sun direction. This enhancement became progressively more pronounced up to the peak of the event (at about 1850 UT) until the increasing isotropy due to scattering flattened the

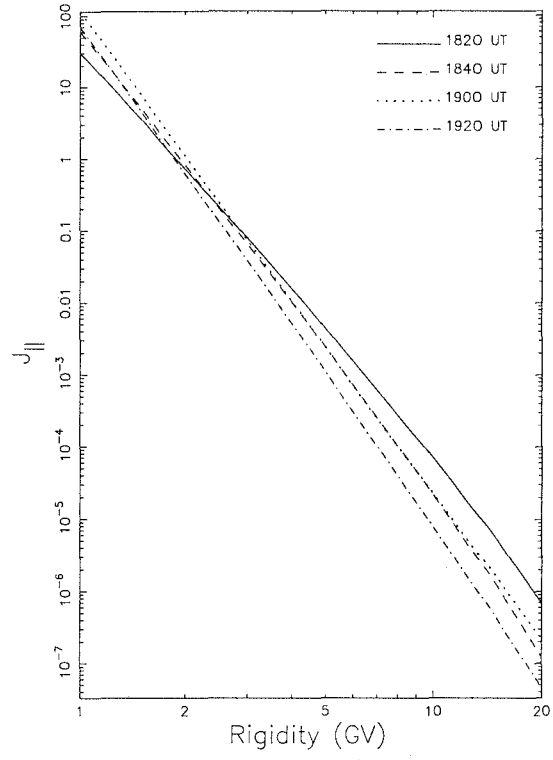

Figure 5.9: Fitted spectra at 1820, 1840, 1900 and 1920 UT, 22 October 1989.

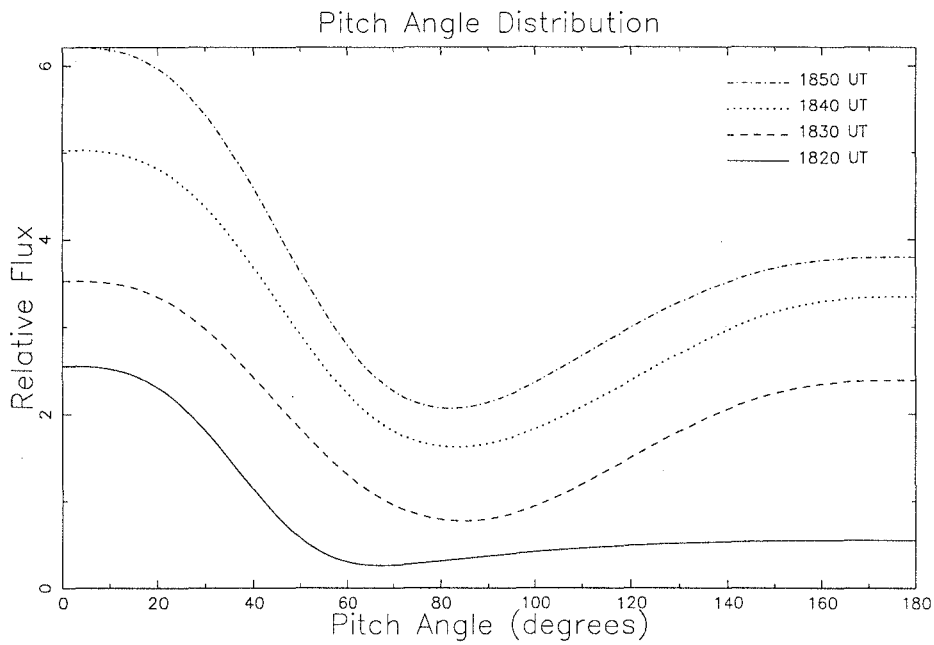

Figure 5.10: Derived pitch angle distributions for 1820, 1830, 1840 and 1850 UT during the 22 October 1989 GLE.

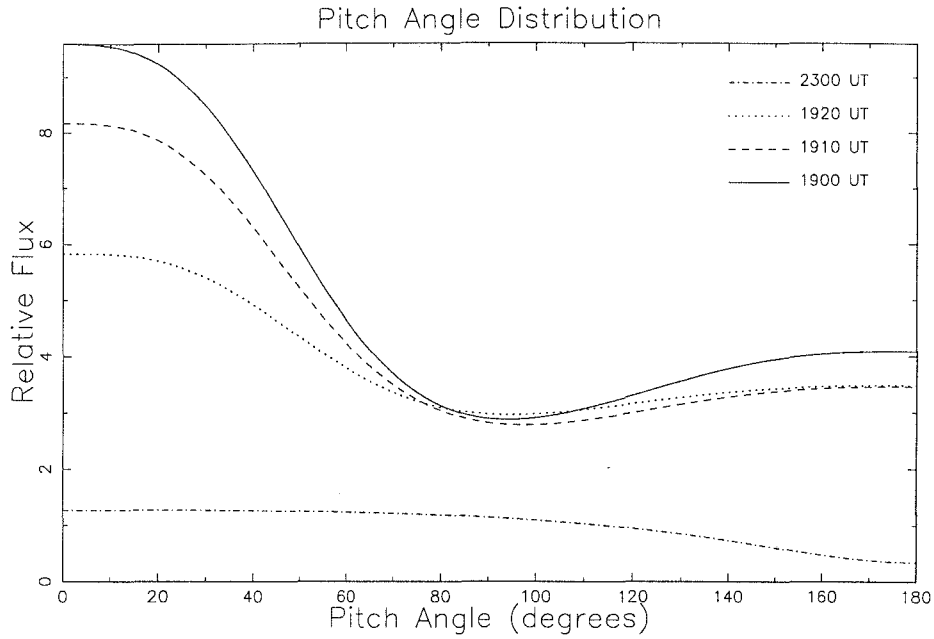

Figure 5.11: Derived pitch angle distributions for 1900, 1910, 1920 and 2300 UT during the 22 October 1989 GLE.

pitch angle distribution. After 1910 UT the particle intensity was constant for pitch angles beyond ~80°. The reason for the enhancement in the anti-sun direction is discussed later in this section.

In seeking to understand the mechanism by which the spike observed at the start of this event could be produced, it is necessary to consider both the early arrival compared to the second part of the event and the difference in anisotropy between the two parts. Clearly the lack of scattering (as evidenced by the extreme anisotropy) results in a much shorter average pathlength for these particles and hence an earlier arrival time, so if a satisfactory explanation can be found for the scatter-free transport, this should also explain the early arrival.

Bieber *et al.* (1990) used the time of arrival and the time of acceleration (indicated by solar radio emission) to determine that the distance travelled by the particles would be ~5 AU if they were released immediately. This is in conflict with the observed lack of scattering, therefore Bieber *et al.* inferred a delay of ~40 minutes due to some process occurring in the corona. These calculations are based on acceleration occurring at 1733 UT, however the first metric type II burst was not observed until 1745 UT. Metric type II bursts are the defining radio emission type for particle acceleration in gradual flares (see Section 1.2). If we conclude that the acceleration took place at 1745 UT then the confinement in the corona is reduced to ~20 minutes. There is no evidence for two separate particle injections in the solar signatures (*e.g.* metric type II/IV or soft X-rays). This suggests that the differences between features of the spike and main part of the event must be due to propagation effects or continued coronal shock acceleration of the particles after the initial pulse.

Table 5.6: Increases at 1820 UT and 1830 UT, 22 October 1989 normalised to McMurdo.

	1820 UT			1830 UT		
Station	Actual %	Corrected %	Calculated %	Actual %	Corrected %	Calculated %
Bern	4.1±1.1	3.1	1.0	3.0±1.1	2.5	1.0
Calgary	9.5±0.4	6.5	7.5	22.7±0.4	15.4	12.2
Climax	8.3±0.3	3.1	2.2	10.7±0.3	4.0	3.5
Deep River	6.7±0.4	6.4	5.3	9.1±0.4	8.6	9.5
Durham	6.8±0.7	6.8	5.8	12.3±0.7	12.3	10.6
Goose Bay	5.0±0.7	5.0	5.7	17.3±0.7	17.1	8.8
Hermanus	0.0±0.8	0.0	0.9	0.0±0.8	0.0	1.1
Hobart	4.3±1.0	4.3	4.1	9.3±1.0	9.3	9.4
Inuvik	3.4±0.7	3.4	4.0	9.6±0.7	9.5	8.5
Jungfraujoch	1.5±0.2	0.5	0.8	1.5±0.2	0.5	0.9
Kerguelen Island	5.8±0.6	5.6	6.9	14.8±0.6	14.2	14.2
Kiel	5.5±0.7	5.4	4.5	7.0±0.7	6.9	7.2
Lomnicky Stit	0.0±0.2	0.0	1.4	0.7±0.2	0.4	1.7
Magadan	14.0±0.7	12.7	10.4	12.2±0.7	11.1	13.4
Mawson	3.2±1.0	3.0	5.3	8.5±1.0	8.0	7.5
McMurdo	35.6±0.6	31.7	31.7	30.5±0.5	21.1	27.1
Mt Washington	12.6±0.8	6.9	6.0	21.5±0.8	11.8	11.2
Mt Wellington	5.0±0.7	4.0	3.9	11.5±0.7	9.1	8.8
Newark	6.2±0.9	6.2	4.6	7.2±1.0	7.2	7.8
Oulu	3.7±0.9	3.6	7.0	12.1±0.9	11.6	15.7
Potchefstroom	0.0±0.8	0.0	0.3	0.0±0.8	0.0	0.3
Rome	1.5±0.7	1.5	0.3	0.2±0.7	0.2	0.3
Sanae	9.2±1.4	8.6	6.6	17.1±1.4	15.9	14.8
South Pole	20.2±0.2	7.7	7.1	33.0±0.2	12.5	12.0
Terre Adelie	6.2±0.8	5.8	8.0	16.1±0.8	15.0	15.2
Thule	8.1±0.8	7.9	7.1	20.6±0.9	20.2	15.1
Σ variances from corrected %			53.5			140.0

Table 5.7: Increases at 1840 UT, 1850 UT and 1900 UT, 22 October 1989 normalised to McMurdo.

	1840 UT			1850 UT			1900 UT		
Station	Actual %	Corrected %	Calculated %	Actual %	Corrected %	Calculated %	Actual %	Corrected %	Calculated %
Bern	0.0±1.1	0.0	1.0	0.0±1.1	0.0	0.9	2.1±1.1	1.7	1.0
Calgary	27.9±0.4	19.0	14.5	30.0±0.4	20.4	13.0	31.5±0.4	21.4	17.5
Climax	9.9±0.3	3.7	4.0	9.1±0.3	3.4	3.4	8.3±0.3	3.1	3.3
Deep River	11.8±0.4	11.2	13.6	12.7±0.4	12.1	13.5	16.1±0.4	15.3	14.7
Durham	12.6±0.7	12.6	13.5	11.0±0.7	11.0	13.0	12.2±0.7	12.2	14.2
Goose Bay	12.3±0.7	12.2	13.1	11.8±0.7	11.8	13.4	15.6±0.7	15.4	14.1
Hermanus	0.0±0.8	0.0	1.0	0.0±0.8	0.0	0.8	0.0±0.8	0.0	0.9
Hobart	8.8±1.0	8.8	12.7	11.9±1.0	11.9	12.2	12.0±1.0	12.0	16.7
Inuvik	13.0±0.7	12.9	13.1	12.0±0.7	12.0	13.7	10.8±0.7	10.7	20.8
Jungfraujoch	0.2±0.2	0.1	0.8	0.7±0.2	0.2	0.7	0.2±0.2	0.1	0.8
Kerguelen Island	13.3±0.6	12.8	15.9	12.3±0.6	11.8	14.4	12.3±0.6	11.8	14.7
Kiel	6.3±0.7	6.2	8.6	5.5±0.7	5.4	7.8	5.3±0.7	5.2	8.2
Lomnicky Stit	0.2±0.2	0.1	1.9	0.0±0.2	0.0	1.6	0.0±0.2	0.0	1.9
Magadan	9.3±0.7	8.5	14.8	9.1±0.7	8.3	13.6	10.5±0.7	9.6	18.2
Mawson	12.0±1.0	11.2	12.1	11.7±1.0	11.0	12.2	14.4±1.0	13.5	13.4
McMurdo	31.8±0.5	28.3	28.3	28.4±0.5	25.3	25.3	40.7±0.6	36.3	36.3
Mt Washington	24.6±0.8	13.5	14.3	26.6±0.8	14.6	13.8	25.7±0.8	14.1	15.0
Mt Wellington	10.1±0.7	8.0	12.8	12.1±0.7	9.6	12.3	14.1±0.7	11.1	16.9
Newark	10.0±1.0	10.0	9.0	6.4±0.9	6.4	8.1	6.6±0.9	6.6	9.5
Oulu	13.5±0.9	13.0	17.9	15.6±0.9	15.0	16.2	15.4±0.9	14.8	16.1
Potchefstroom	0.0±0.8	0.0	0.2	2.8±0.8	1.9	0.2	0.0±0.8	0.0	0.3
Rome	0.6±0.7	0.6	0.3	0.0±0.7	0.0	0.2	0.0±0.7	0.0	0.2
Sanae	19.0±1.4	17.7	17.9	15.4±1.4	14.3	16.6	15.7±1.4	14.6	16.7
South Pole	37.8±0.2	14.4	13.1	37.7±0.2	14.3	11.1	39.9±0.2	15.2	16.4
Terre Adelie	17.1±0.8	15.9	18.6	15.3±0.8	14.2	18.0	19.1±0.8	17.8	28.0
Thule	21.3±0.9	20.9	16.6	21.0±0.9	20.6	14.9	20.8±0.9	20.3	15.2
Σ variances from corrected %			173.9			191.7			419.6

Table 5.8: Increases at 1910 UT, 1920 UT and 2300 UT, 22 October 1989 normalised to McMurdo.

	1910 UT			1920 UT			2300 UT		
Station	Actual %	Corrected %	Calculated %	Actual %	Corrected %	Calculated %	Actual %	Corrected %	Calculated %
Bern	0.0±1.1	0.0	0.7	3.8±1.1	3.1	0.6	0.0±1.1	0.0	0.3
Calgary	27.6±0.4	18.8	14.5	22.6±0.4	15.4	12.7	10.3±0.4	7.0	6.3
Climax	10.6±0.3	3.9	2.7	7.7±0.3	2.8	2.7	5.2±0.3	1.9	1.2
Deep River	14.6±0.4	13.9	13.0	13.5±0.4	12.8	12.7	4.5±0.4	4.3	5.4
Durham	10.4±0.7	10.4	12.6	9.3±0.7	9.3	11.9	3.3±0.7	3.3	3.6
Goose Bay	15.3±0.7	15.1	12.7	12.7±0.7	12.6	12.6	4.6±0.7	4.6	6.1
Hermanus	0.1±0.8	0.1	0.7	0.5±0.8	0.5	0.7	0.0±0.8	0.0	0.3
Hobart	12.4±1.0	12.4	14.7	11.7±1.0	11.7	12.2	3.6±1.0	3.6	3.8
Inuvik	11.8±0.7	11.7	20.1	13.0±0.7	12.9	16.8	4.6±0.7	4.6	6.5
Jungfraujoch	0.0±0.2	0.0	0.5	2.2±0.2	0.7	0.6	0.0±0.2	0.0	0.3
Kerguelen Island	12.5±0.6	12.0	12.6	15.9±0.6	15.3	12.2	1.5±0.6	1.4	3.0
Kiel	4.4±0.7	4.3	7.2	3.3±0.7	3.2	6.5	0.4±0.7	0.4	1.9
Lomnicky Stit	0.7±0.2	0.4	1.5	1.1±0.2	0.6	1.3	0.0±0.2	0.0	0.5
Magadan	9.3±0.7	8.5	15.3	10.0±0.7	9.1	10.7	2.9±0.7	2.6	3.2
Mawson	14.9±1.0	14.0	12.1	15.5±1.0	14.6	12.2	3.7±1.0	3.5	5.0
McMurdo	31.1±0.5	27.7	27.7	21.0±0.5	18.7	18.7	7.3±0.5	6.5	6.5
Mt Washington	22.5±0.8	12.4	13.3	26.0±0.8	14.3	12.8	9.7±0.8	5.3	4.2
Mt Wellington	13.3±0.7	10.5	14.9	13.9±0.7	11.0	12.1	4.9±0.7	3.9	3.7
Newark	7.1±1.0	7.1	8.1	7.4±1.0	7.4	7.3	1.0±0.9	1.0	2.4
Oulu	14.1±0.9	13.5	13.6	13.2±0.9	12.7	13.0	4.9±0.9	4.7	2.7
Potchefstroom	0.3±0.8	0.2	0.2	0.0±0.8	0.0	0.1	0.0±0.8	0.0	0.1
Rome	0.0±0.7	0.0	0.2	0.0±0.7	0.0	0.2	0.0±0.7	0.0	0.1
Sanae	14.9±1.4	13.9	14.0	11.0±1.4	10.2	13.4	5.7±1.4	5.3	5.5
South Pole	38.1±0.2	13.9	13.4	34.7±0.2	13.2	11.9	13.8±0.2	5.2	6.3
Terre Adelie	17.4±0.8	16.2	23.9	21.3±0.8	19.8	18.2	7.9±0.8	7.3	6.0
Thule	16.8±0.9	16.5	12.6	18.1±0.9	17.7	12.3	7.2±0.8	7.1	4.8
Σ variances from corrected %			266.3			111.0			30.8

Nemzek *et al.* (1994) discussed two theories for the production of the highly anisotropic spike. They note that a narrow time profile is usually taken as evidence of non-diffusive propagation through interplanetary space. This requires that the pitch angle focussing of the diverging solar magnetic field dominates over diffusion. The other possibility discussed by Nemzek *et al.* is that the particles may be the decay products of solar neutrons (as described in the interpretation of 19 October 1989 GLE in Section 5.1.1). This is thought to be less likely than the focussed transport mechanism. There are several problems with associating the spike with decayed neutrons, not the least of which is the high particle intensity. This event is many orders of magnitude larger than the only other event observed at ground level for which neutron decay has been suggested as a possible mechanism. Furthermore, Nemzek *et al.* comment that the persistence of the spike down to low energies (as measured by instruments on board spacecraft) cannot be explained by the decayed neutrons since at these energies the decay would have to have taken place very close to the Sun and the particles would therefore have a propagation path similar to the primary protons. There was some dispute over whether the spike in the low energy data was in fact produced by the same particle population as that responsible for the cosmic ray spike. The reason for doubt is that the satellite instruments may not have been viewing the correct interplanetary region to observe the extreme anisotropy. If this were the case, the spike and the pulse in the satellite data would both be associated with the main event in ground-based instruments. Nemzek *et al.* defend their interpretation which was based on the remarkable similarities in the satellite and neutron monitor data. Both datasets exhibited a distinct spike followed by a slower pulse and the double peaked nature of the spike is also correlated between the two datasets. They also point out that the extreme anisotropy at neutron monitor energies may not be present at the much lower energies of the satellite observations. Furthermore, Nemzek *et al.* maintain that since there were four space-based measuring platforms in operation and the two from which their data were obtained viewed almost an entire unit sphere around them, a large zone of interplanetary pitch angles were sampled and it is expected that any anisotropy would be recorded by at least one instrument. This conclusion therefore adds further weight to the argument that the spike was not caused by the decay products of solar neutrons. Perhaps the most important fact which eliminates neutron decay as the mechanism for the spike is that there were no direct observations of solar neutrons. If neutrons were present in sufficient numbers to produce enough protons to generate the observed response at Earth, there must have been some which survived without decaying before reaching the Earth. These would have been expected at Huancayo neutron monitor (Bieber and Evenson, 1991) but there was no evidence of an increase, so it seems impossible that the spike was caused by the decay products of solar neutrons. Furthermore, the significant depression in the intensity-time profiles after the spike is not consistent with a neutron decay mechanism.

Having rejected mechanisms by which the spike could have been produced as an additional particle flux on top of a more 'normal' GLE, it remains to discuss mechanisms by which one particle population could be observed in two such different phases. The main difference between the two phases is the degree of anisotropy in

the pitch angle distributions. The distributions during the main part of the event were broader than for the spike and also displayed a significant contribution from particles arriving from the anti-sun direction. This effect was noticeable within the first five minutes of the main event.

It can be seen from the pitch angle distributions shown in Figures 5.10 and 5.11 that the enhancement around 180° pitch angle was first pronounced in the distribution at 1830 UT and reached a peak around 1850 UT after which the general scattering of particles caused the distribution to flatten out. It seems likely that the enhancement in the anti-sun direction was due to particles moving beyond the Earth and being reflected back along the same interplanetary magnetic field line. In order to assess the feasibility of this scenario it is necessary to determine the probable distance travelled by these particles and investigate the possibility of a reflecting region in the interplanetary magnetic field.

It is probable that the reflected particles were (at least initially) from the population that was responsible for the spike. The time delay between the spike and the first observation of particles from the anti-sun direction results in a distance travelled of the order of 1.5–2 AU. This must be the return distance between the Earth and the scattering region and implies that the particles were reflected somewhere between 1.8 and 2 AU from the Sun. Flückiger *et al.* (1993) reported interplanetary magnetic field data from the Galileo spacecraft which reveals that a high field strength (~30 nT) perturbed plasma domain passed the Earth between ~1000 UT on October 19 and ~13 UT on October 20. It is estimated that at the time of the 22 October GLE, this region would extend from 1.8 to 3 AU. The back-scatter efficiency of the region can be estimated if it is assumed that the back-scatter contribution to the pitch angle distribution for 1820 UT results from the population responsible for the spike. The ratio of the number of particles in each of these populations can be estimated by the ratio of the integrals of the pitch angle distributions over all pitch angles, multiplied by the spectral constant (to obtain the number of particles at 1GV). The resulting back-scatter efficiency is ~8%. This is clearly a very approximate value and does not take into account differences in the particle spectrum between the two times, but indicates that the required back-scatter efficiency is not unreasonable. The shape of the distribution centred on 180° pitch angle is broader than that centered on 0°. This is also consistent with the back-scatter theory as the particles being reflected back from beyond the Earth have travelled further through the interplanetary medium and encountered more scattering regions. The reflection of the particles also may not be simple reversals of direction, but may have taken place through multiple scatterings.

Another difference between the spike and the world-wide GLE was the particle arrival direction. The axis of symmetry of the pitch angle distribution derived for the spike was very close to the Sun-Earth line, while later the particles arrived from a direction closer to the nominal 'garden hose' field line. Two possible explanations for this are (i) that the particles followed two different paths in the IMF; or (ii) that the field direction changed during the event. The first of these hypotheses seems attractive as this could easily account for changes in anisotropy, however it is inconsistent with the early observation of back-scattered particles. The timing of

these observations indicates that the initial reflected particles were those associated with the spike. In fact a weak signature of the spike can be seen in some reverse viewing stations (*e.g.* see in Figure 5.6 a spike in the Deep River data coincident with a sharp increase at Mawson). This could not occur if the particles had travelled along different field lines. It seems likely that the change in arrival direction must have been due to changes in the direction of the IMF. This requires a change in longitude of ~25° within ~15 minutes. It should be noted that the field prior to and after the data gap at the time of this GLE was quite variable. The hourly average field vectors exhibited changes of up to 100° in longitude on several occasions.

The most logical explanation for the other features of this complex event appears to be an initial particle injection followed by continuous shock acceleration over an extended period of time. This interpretation is consistent with the intensity-time profiles and the slight steepening of the spectrum after the spike. The persistent anisotropy in the forward direction results from continued scatter-free propagation of particles accelerated by the expanding coronal shock. A delta-like injection followed by interplanetary diffusion would result in less anisotropy.

In summary, the GLE of 22 October 1989 exhibited extreme anisotropy produced by particle propagation through a scatter-free region where dominated by adiabatic focussing. Isotropy was approached gradually, however some anisotropy can still be seen to be present as late as 2300 UT. Changes in the apparent particle arrival direction indicate that the direction of the local interplanetary magnetic field changed during the event. Shock acceleration during the gradual phase of the flare (as indicated by type II emission) may have continued over an extended period, however coronal diffusion could also extend the injection time. A significant contribution was made by particles scattered back from beyond the Earth. A high field, turbulent plasma region is thought to be responsible for the scattering.

5.3 24 October 1989

The GLE which occurred on 24 October 1989 was recorded by at least 31 neutron monitors with geomagnetic cutoff rigidities up to ~4.5 GV. The largest increase was 199% at South Pole in the two minute interval beginning at 2058 UT. The earliest onsets were Inuvik, in the five minute interval from 1815 UT and South Pole, in the two minute interval from 1818 UT. The rate of rise was quite slow and the enhancement persisted for more than 12 hours. Intensity time profiles from several stations are shown in Figure 5.12.

The solar flare associated with this GLE was located at S20°, W57° on the solar disc. Hα emission began at 1739 UT, peaked with importance 3B at 1813 UT and continued until after 2359 UT. A high speed dark filament was also observed. Soft X-ray emission began and reached maximum intensity prior to 1736 UT when the importance was X5.7. Intense metric type II emission was observed between 1800 and 1801 UT and weaker emission occurred from 1806 to 1810 UT. Type V emission was also observed between 1801 and 1816 UT. The geomagnetic field was not highly disturbed during the event, with Kp values of 4- and 3+.

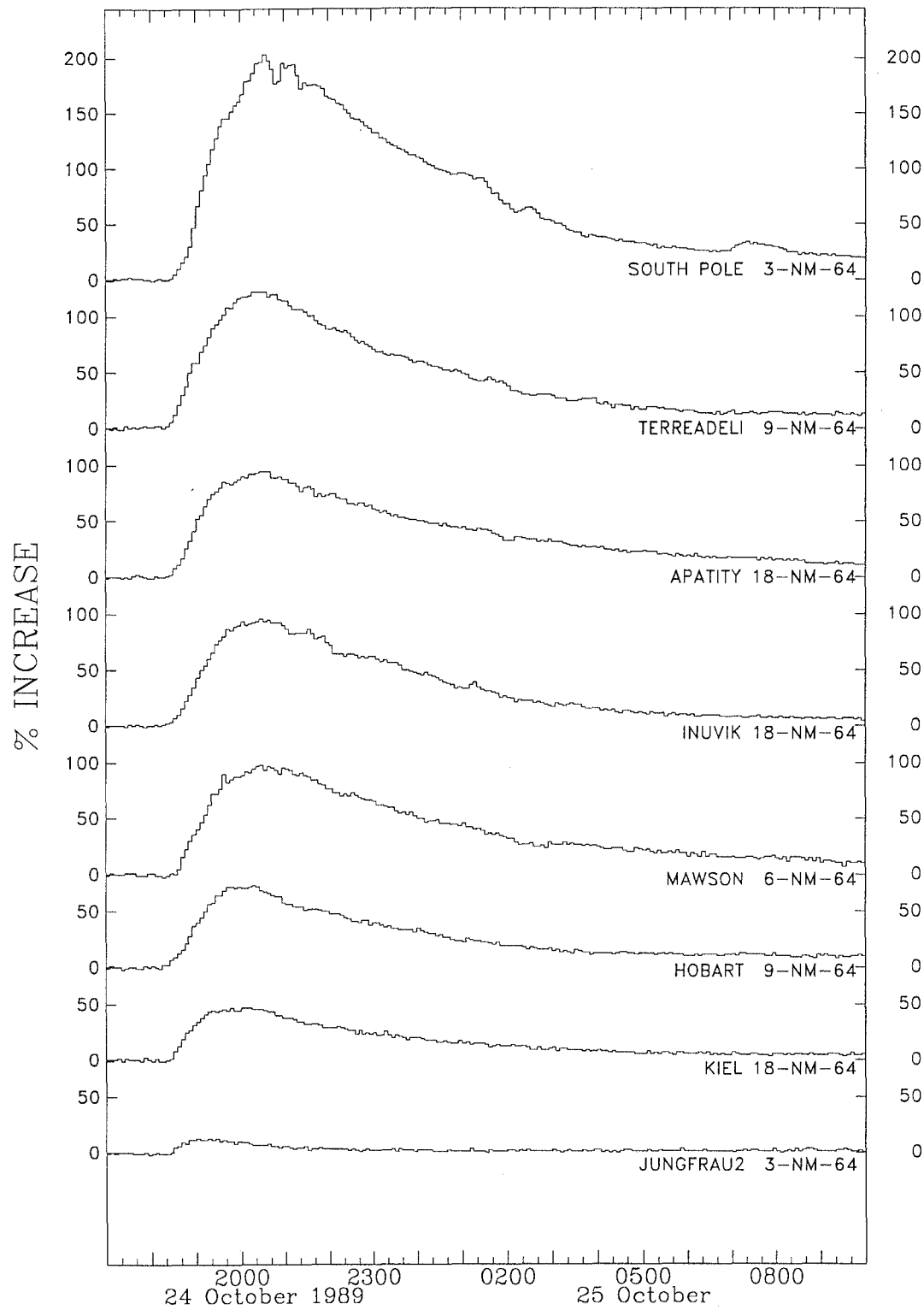

Figure 5.12: Cosmic ray increases at South Pole, Terre Adelie, Apatity, Inuvik, Mawson, Hobart, Kiel and Jungfraujoch neutron monitors between 1700 UT on 24 October 1989 and 1000 UT on 25 October 1989.

This GLE exhibited no particularly unusual features, but was of significant intensity and recorded at a large number of neutron monitors. The size of the enhancement and availability of data make this event a good candidate for detailed analysis. This event has been chosen as a test for the different types of spectral form now available in the GLE model. Most other work presented in this thesis has employed a modified power law spectrum, but recent developments have included a shock acceleration spectrum (Ellison and Ramaty, 1985) and modification of this. The results of using these spectral forms are compared with those derived from power law spectra. This event has also been modelled with a rigidity dependent pitch angle distribution. Terre Adelie was used as the normalisation station in all models.

5.3.1 Spectral form

Three different spectral forms have been tested in the models for this event. The tests were performed for three times, one during the rising phase and two near the maximum neutron monitor intensity. The spectral forms were: power law in rigidity; Ellison and Ramaty shock acceleration spectrum (Ellison and Ramaty, 1985); and a modification of the Ellison and Ramaty spectrum. An approximation to the Ellison and Ramaty spectrum has been used in order to vary its shape with one parameter. The form of this spectrum is a power law in rigidity with exponent $-\gamma - (1 - \beta^2)$ where β is the ratio of particle speed to the speed of light and γ is a variable in the least squares analysis. This approximation produces a spectrum very close to that of Ellison and Ramaty (D.F. Smart, private communication). The theoretically determined spectrum is the result of a shock of infinite extent interacting with the particles for an infinite time. In reality the spectrum may steepen more rapidly with increasing rigidity since the extent of the shock and the interaction time will not be infinite. A further modification of the spectral form has been introduced to model this. In this case, the exponent of the power law is $-\gamma - (1 - \beta^2)(1 + \delta\gamma)$ where $\delta\gamma$ is an additional parameter in the model.

Parameters of the model were determined by least squares analysis for the five minute intervals beginning 1900, 2010 and 2025 UT using each of the three spectral forms. A simple pitch angle distribution (Equation 3.4) was used. The effects of a rigidity dependent pitch angle distribution are discussed in the following section. Table 5.9 shows the sum of squares of differences between calculated and recorded percentage increases for each of the models. These sums are not normalised, so cannot be compared between the different times for which the models were calculated, however they do provide a relative measure of the 'goodness of fit' of the different models for any particular time.

It is clear from the numbers shown in Table 5.9 that in each case the model with the modified Ellison and Ramaty spectral form gives the best fit to the observed data. For each of the modelled times, the parameters describing the shape and axis of symmetry of the pitch angle distributions were almost identical irrespective of the spectral form. Thus comparison between the spectral forms has not been biased by any differences in the other parameters. The spectra fitted for 1900 UT are shown in Figure 5.13. The Ellison and Ramaty spectrum does not

Table 5.9: Comparison of fits with models using different spectral forms

Spectral Type	1900	2010	2025
Power Law	208.5	554.4	731.2
Ellison and Ramaty	199.9	523.2	719.2
Modified Ellison and Ramaty	176.0	460.3	655.9

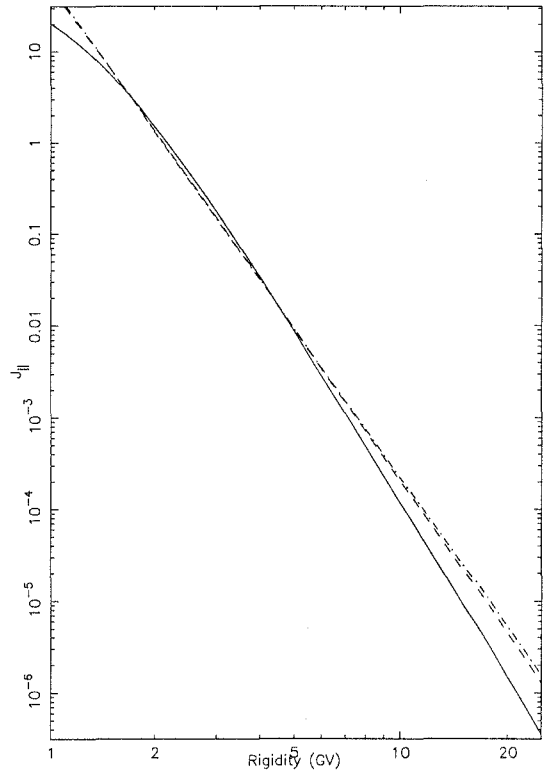

Figure 5.13: Fitted spectra for 1900 UT: Modified Ellison and Ramaty (solid line); Ellison and Ramaty (dashed line); and Power Law (dot-dash line).

differ significantly from the pure power law over the range of rigidities plotted, however the amount of bending in the modified Ellison and Ramaty spectrum is much more noticeable. The modified Ellison and Ramaty spectra fitted for 2010 and 2025 UT do not steepen as much as that shown in Figure 5.13.

5.3.2 Pitch angle distributions

The models for 1900, 2010 and 2025 UT were also tested for rigidity dependence of the pitch angle distributions. The modified Ellison and Ramaty spectral form was chosen and a simple pitch angle distribution (Equation 3.4) was compared with a rigidity dependent distribution of the same form as those shown in Figure 3.4. The sums of variances (as previously defined) for these models are shown in Table 5.10.

The fitted pitch angle distributions for 1900 UT are shown in Figure 5.14. A distribution similar to that on the left of this figure can be reproduced from

Table 5.10: Comparison of fits with models using different pitch angle distributions.

Pitch angle distribution	1900	2010	2025
Simple	176.0	460.3	655.9
Rigidity dependent	155.8	459.8	598.8

the parameters of the rigidity dependent distribution using a rigidity of 2.7 GV. This is not surprising since most of the stations had median rigidities of response between 2 and 3 GV. The rigidity dependence shows that the higher rigidity particles were less affected by scattering during the propagation to Earth. The sums of variances listed in Table 5.10 indicate that for 1900 and 2025 UT, a slightly better fit to the observed data was obtained using the rigidity dependent pitch angle distributions. While the improvement in the sum of variances may appear to be significant, this represents only a ~10% change in the calculated increases at the stations for which the effect was most significant. Changes in most of the calculated increases were insignificant. While it is possible to find a suggestion of rigidity dependence in the pitch angle distributions, this is not a significant effect and the minor improvements do not justify the introduction of two extra parameters into the model. The full results presented in the next section do not include rigidity dependence in the pitch angle distributions.

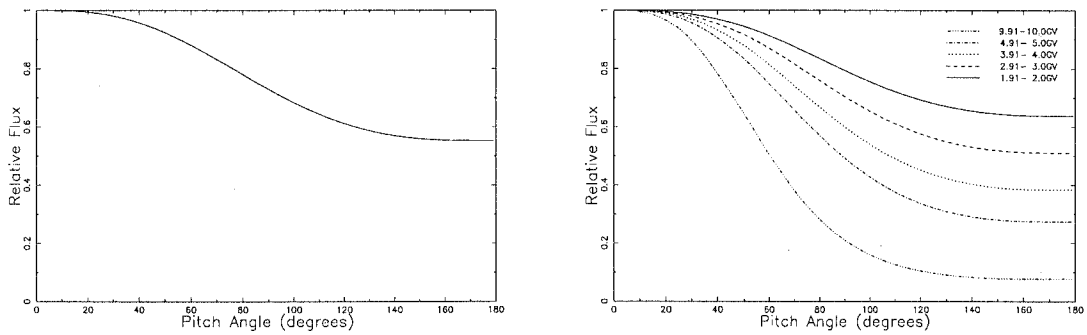

Figure 5.14: Derived pitch angle distributions for 24 October 1989 GLE at 1900 UT. Rigidity dependent distribution (right) gives a slightly better fit to observations.

5.3.3 Results

The outcome of the comparisons between spectral forms and pitch angle distributions was to model this GLE using modified Ellison and Ramaty spectra and pitch angle distributions independent of rigidity. The times chosen for modelling were five minute periods beginning 1900, 2010, 2025, 2100, 2130 UT on 24 October and 0000 UT on 25 October. The derived spectral parameters and axes of symmetry of the pitch angle distributions are shown in Table 5.11. The derived pitch angle distributions and spectra are plotted in Figures 5.15 and 5.16 respectively.

Table 5.11: Derived source positions and spectral parameters for 24 October 1989 GLE. Fluxes in units of particles $(cm^2\ s\ ster\ GV)^{-1}$.

Time	1900	2010	2025	2100	2130	0000
Latitude	−5	−33	−32	−42	−36	−40
Longitude	158	175	170	160	185	172
γ	−2.6	−4.2	−5.4	−5.7	−4.7	−4.4
$\delta\gamma$	7.0	5.3	2.0	1.5	5.2	6.6
$J_{\|\|}$	19.7	110.1	166.5	176.1	127.6	69.8
J_{av}	14.7	86.8	132.4	142.5	109.3	60.4

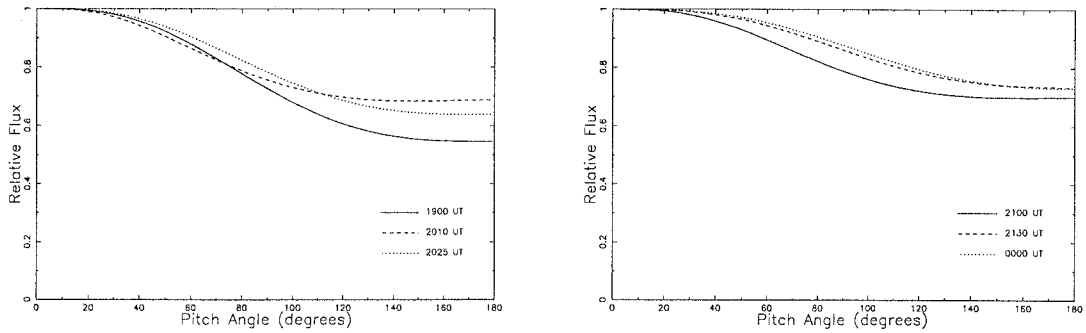

Figure 5.15: Derived particle pitch angle distributions for the 24 October 1989 GLE at times as labelled.

The calculated increases at each station obtained from these models are shown in Tables 5.12 and 5.13 along with the actual increases (with poisson errors) and the increases corrected to sea level atmospheric depth. This correction was performed by the two attenuation length method, using a calculated flare attenuation length of 106 g cm^{-2}. The sums of variances between calculated and corrected increases are also shown in these tables.

The derived pitch angle distributions are noteworthy for the small anisotropy, even during the rising phase of the event. This indicates significant scattering of the particles during propagation through the interplanetary medium. This may be unexpected given the location of the associated solar flare right at the nominal footpoint of the 'garden hose' field line, however it is likely that the medium was quite disturbed due to effects associated with the preceding two GLEs. There are no interplanetary magnetic field or plasma data available for this period. The degree of isotropy in the pitch angle distributions means that the uncertainties in the derived latitude and longitude of the axes of symmetry are quite large. These axes could be altered by up to ~30° without large changes in the quality of the fit to observed data. It is difficult to comment on the derived axes of symmetry of the pitch angle distributions without measurements of the IMF direction. The latitudes of the arrival directions are more southerly than

Table 5.12: Increases at 1900 UT, 2010 UT and 2025 UT, 24 October 1989, normalised to Terre Adelie.

	1900 UT			2010 UT			2025 UT		
Station	Actual %	Corrected %	Calculated %	Actual %	Corrected %	Calculated %	Actual %	Corrected %	Calculated %
Alma-Ata	2.4±0.1	1.1	2.2	1.8±0.1	0.8	1.2	2.1±0.1	0.9	1.5
Apatity	51.8±0.7	47.8	43.4	92.0±0.7	84.8	80.7	94.4±0.7	87.0	86.0
Bern	10.0±0.9	6.2	7.3	8.7±0.9	5.4	5.5	2.2±0.9	1.4	6.0
Calgary	47.8±0.5	47.8	34.7	105.4±0.5	82.4	81.2	104.3±0.5	81.6	83.9
Climax	35.2±0.4	15.3	16.0	40.2±0.4	17.9	20.1	38.2±0.4	16.6	18.1
Deep River	32.2±0.4	31.0	34.8	73.8±0.4	71.0	77.1	76.5±0.4	73.6	75.6
Durham	34.2±0.8	34.2	36.1	60.9±0.8	60.9	67.3	54.8±0.8	54.8	63.1
Goose Bay	36.7±0.7	36.5	32.3	73.3±0.8	72.9	77.5	69.8±0.8	69.5	77.6
Hermanus	6.7±0.8	6.7	7.2	7.0±0.8	7.0	6.3	4.5±0.8	4.5	6.0
Hobart	39.7±1.1	39.7	37.9	72.4±1.1	72.3	65.1	68.7±1.1	68.6	63.2
Inuvik	43.1±0.7	42.8	48.1	91.3±0.7	90.8	92.0	96.1±0.7	95.5	97.9
Irkutsk	16.6±0.7	14.9	12.7	17.2±0.8	15.5	14.3	14.8±0.8	13.3	13.5
Jungfraujoch	10.6±0.3	4.3	6.5	8.0±0.3	3.2	5.3	7.1±0.3	2.9	5.9
Kerguelen Island	51.8±0.7	50.4	51.0	85.6±0.7	83.3	89.3	87.6±0.7	85.2	94.0
Kiel	34.1±0.8	33.6	36.0	46.4±0.8	45.7	44.3	45.9±0.8	45.2	42.5
Kiev	16.7±0.8	16.4	14.7	16.5±0.8	15.8	15.1	15.4±0.8	14.8	15.1
Lomnicky Stit	19.3±0.3	12.8	11.9	17.3±0.3	11.5	10.6	15.4±0.3	10.2	10.8
Magadan	39.9±0.8	36.7	35.2	60.5±0.8	55.7	60.9	56.1±0.8	51.6	56.7
Mawson	41.0±1.1	39.0	42.1	90.9±1.2	86.4	82.4	97.6±1.2	92.7	86.9
McMurdo	52.2±0.6	48.0	44.2	105.4±0.7	96.7	101.5	108.4±0.7	99.4	107.8
Moscow	40.2±0.7	36.3	37.6	54.1±0.7	48.8	47.8	54.9±0.7	49.5	47.3
Mt Wellington	47.3±0.8	39.1	38.2	89.1±0.8	73.7	66.0	85.5±0.8	70.7	63.5
Newark	29.2±1.0	29.2	30.4	43.7±1.0	43.7	44.7	41.2±1.0	41.2	39.4
Novisibirsk	28.5±0.7	27.3	26.1	33.0±0.7	31.6	32.9	33.3±0.7	31.9	31.1
Oulu	46.5±1.0	45.1	43.4	91.9±1.1	89.2	81.8	93.5±1.1	90.8	86.8
Potchefstroom	3.9±0.9	2.9	2.8	2.5±0.9	1.8	1.1	2.4±0.9	1.8	1.5
Rome	2.0±0.7	2.0	2.6	0.0±0.7	0.0	1.6	1.6±0.7	1.6	1.9
Sanae	40.0±1.5	37.7	33.7	85.0±1.6	80.1	77.2	83.2±1.6	78.4	76.3
South Pole	66.6±0.3	32.8	35.7	179.6±0.4	88.5	85.2	196.8±0.4	97.0	90.5
Terre Adelie	59.1±0.9	55.5	55.5	119.2±1.0	112.1	112.1	122.5±1.0	115.5	115.5
Thule	40.3±0.9	39.6	39.2	84.3±1.0	82.9	77.5	90.3±1.0	88.8	78.1
Σ variances from corrected %			176.0			460.3			169.8

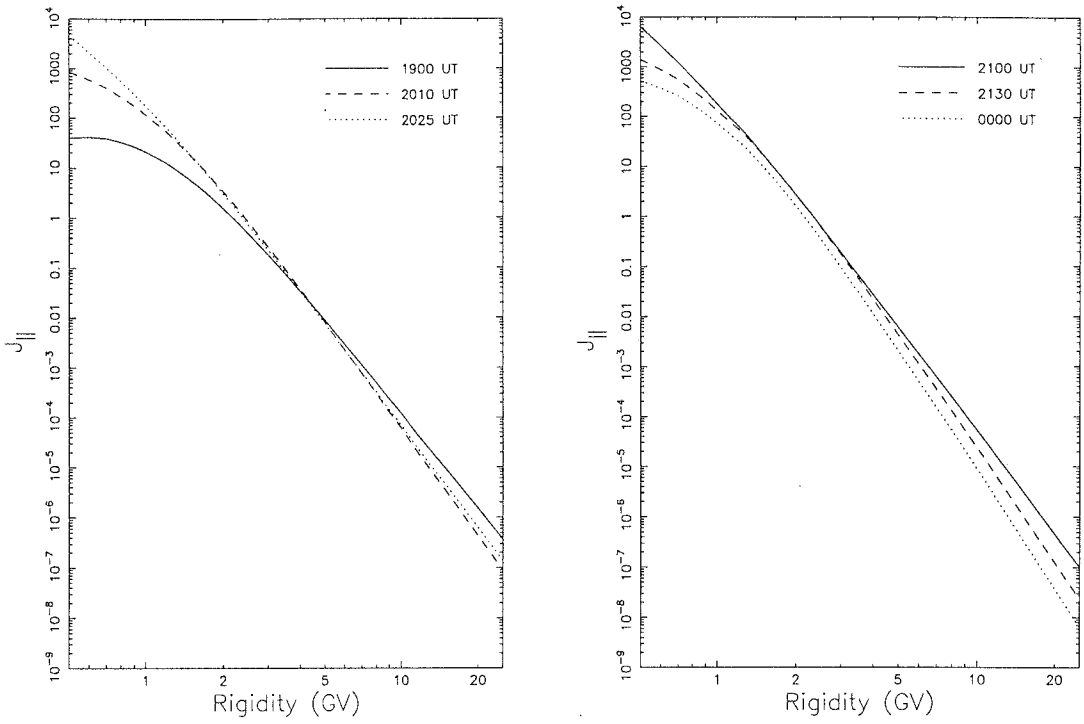

Figure 5.16: Derived particle spectra for the 24 October 1989 GLE at times as labelled.

for most GLEs, but are consistent with those derived for the GLE of 22 October 1989 (just two days earlier). It should also be noted that the IMF direction on 21 October was measured to be as far south as –85° (GSE) and quite variable. The changes in the derived geographic longitudes of the axes of symmetry between 2010, 2025 and 2100 UT reflect the Earth's rotation. These axes correspond to a nominal 'garden hose' angle of about 45° west of the Sun-Earth line. The derived longitudes for 1900 and 2130 UT do not follow the same sequence, but the movement of the axis of symmetry between modelled times is small enough that it could be explained by changes in the IMF direction. The measured IMF directions at IMP8 on the following days (25–26 October) were highly variable, swinging by up to 70° between hourly average values. It is quite possible that similar variations could have been taking place at the time of this event. The field variability combined with the large uncertainties in the derived latitude and longitude are sufficient to explain the unexpected changes of the particle arrival direction during this event.

Bieber and Evenson (1991) estimated spectral indices by comparing the response of the South Pole neutron monitor with an unshielded monitor at the same site. This method exploits the different response functions of the two monitors and is assumed to be independent of particle anisotropy since the monitors are located at the same site. In reality, since the two monitors have slightly different rigidity dependent responses, their viewing directions may be slightly different, but this would not be a large effect. The spectrum of the 24 October 1989 GLE

Table 5.13: Increases at 2100 UT and 2130 UT, 24 October 1989 and 0000 UT, 25 October 1989, normalised to Terre Adelie.

	2100 UT			2130 UT			0000 UT		
Station	Actual %	Corrected %	Calculated %	Actual %	Corrected %	Calculated %	Actual %	Corrected %	Calculated %
Alma-Ata	1.9±0.3	0.8	1.1	2.0±0.1	0.9	0.6	1.4±0.1	0.6	0.3
Apatity	88.3±0.7	81.4	83.7	81.4±0.7	75.1	76.8	50.5±0.7	46.5	47.8
Bern	1.2±0.9	1.2	4.8	6.4±0.9	4.0	3.2	0.0±0.9	0.0	1.7
Calgary	97.2±0.5	76.0	79.0	97.8±0.5	76.5	77.4	55.2±0.5	43.1	46.1
Climax	30.3±0.4	13.2	17.3	26.4±0.4	11.5	13.9	14.3±0.4	6.3	8.0
Deep River	73.9±0.4	71.1	74.5	71.1±0.4	68.4	71.5	39.1±0.4	37.5	44.0
Durham	53.8±0.8	53.8	59.5	49.9±0.8	49.9	57.2	28.4±0.8	28.4	35.3
Goose Bay	73.2±0.8	72.8	77.5	71.5±0.8	71.1	72.6	41.4±0.7	41.4	44.2
Hermanus	4.9±0.8	4.9	4.6	1.8±0.8	1.8	3.1	0.0±0.8	0.0	1.7
Hobart	56.6±1.1	56.5	53.0	51.9±1.1	51.8	51.5	34.3±1.0	34.3	30.8
Inuvik	86.7±0.8	86.2	85.1	86.5±0.6	85.9	87.2	46.7±0.7	46.2	51.0
Irkutsk	10.8±0.6	9.7	9.9	10.0±0.7	9.0	8.0	6.3±0.6	5.7	4.4
Jungfraujoch	4.3±0.3	1.7	4.3	3.3±0.3	1.3	3.0	1.9±0.3	0.8	1.6
Kerguelen Island	89.4±0.7	87.0	88.1	84.4±0.7	82.1	82.7	54.0±0.7	52.4	50.5
Kiel	38.1±0.8	37.5	34.8	32.5±0.7	32.0	33.3	19.5±0.7	19.1	20.0
Kiev	12.5±0.8	12.0	12.7	9.2±0.7	8.8	10.0	5.6±0.7	5.4	5.6
Lomnicky Stit	11.5±0.3	7.6	8.5	9.9±0.3	6.6	6.4	5.4±0.3	3.6	3.5
Magadan	48.8±0.8	44.9	42.5	45.3±0.8	41.7	41.9	26.9±0.7	24.7	24.9
Mawson	94.6±1.2	89.9	82.7	87.7±1.2	83.3	74.7	50.4±1.1	47.9	46.4
McMurdo	99.1±0.6	90.9	99.9	86.0±0.6	78.9	91.4	53.9±0.6	49.6	54.8
Moscow	45.7±0.7	41.2	35.6	37.8±0.7	34.0	33.4	20.9±0.6	18.8	19.8
Mt Wellington	66.1±0.8	54.7	54.9	62.8±1.0	51.9	49.9	40.1±0.9	40.1	29.7
Newark	36.6±1.0	36.6	38.6	34.2±1.0	34.2	34.6	17.4±1.0	17.4	20.9
Novisibirsk	24.3±0.7	23.3	23.9	20.7±0.7	19.8	20.7	10.8±0.7	10.4	11.9
Oulu	86.3±1.0	83.8	84.8	79.3±1.0	77.0	77.6	50.2±1.0	48.7	48.4
Potchefstroom	0.9±0.9	0.7	1.0	1.7±0.9	1.2	0.6	2.8±0.9	2.0	0.3
Rome	0.9±0.7	0.9	1.4	0.3±0.4	0.3	0.8	0.0±1.4	0.0	0.4
Sanae	87.3±1.6	82.2	76.8	78.2±1.6	73.7	71.2	45.1±1.5	42.4	42.9
South Pole	191.1±0.4	94.2	87.1	175.7±0.4	86.6	81.4	109.6±0.3	53.7	50.2
Terre Adelie	113.9±1.0	107.3	107.3	100.9±1.0	94.8	94.8	59.9±0.9	56.3	56.3
Thule	81.7±1.0	80.3	75.5	75.4±0.9	68.1	72.1	43.6±0.9	42.7	42.9
Σ variances from corrected %			408.5			512.6			327.7

was estimated at two times. The first was during the "twenty minute interval beginning eight minutes (to suppress dispersion effect) after the start of the first two minute reading in which both ... [monitors] observed an increase significant at the three sigma level". The second time for which the spectral index was determined was chosen to be "one hour of data late in the decay phase of the event, but before the fluxes were too low to permit an accurate determination". The spectral form used by Bieber and Evenson was a power law in momentum with a sharp cutoff at 10 GV. They estimated the spectral index to be –3.37 and –4.97 for their early and late times respectively. No absolute flux values were given. In order to compare these with the spectra determined with the full neutron monitor model, the closest modelled times have been chosen (1900 and 0000 UT) and the fluxes have been assumed to be equal at 1 GV. These spectra are plotted in Figure 5.17. It can be seen that there is good agreement between the spectra determined by the different methods for rigidities between 1 and 2 GV. This is not surprising, since it is at the low rigidities where the difference in the response of the standard and unshielded monitors will be most significant. The divergence of the spectra above ~2 GV demonstrates the value of the full model determination of spectra over the single site method employed by Bieber and Evenson.

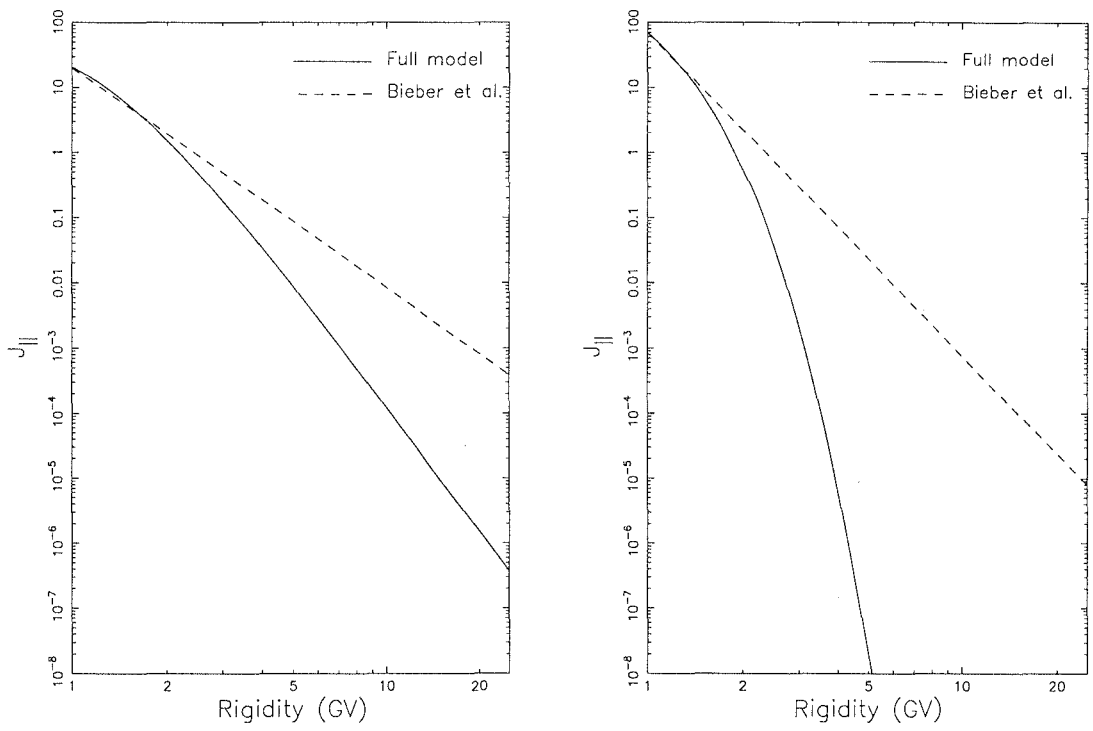

Figure 5.17: Comparison of spectra determined from the full neutron monitor model with those estimated by Bieber and Evenson from the responses of the standard and unshielded neutron monitors at South Pole. The left-hand plot shows the spectrum determined for 1900 UT and the early time of Bieber and Evenson, while the right-hand plot compares the spectrum at 0000 UT with the late time of Bieber and Evenson.

5.4 Summary

The results presented in this chapter have highlighted the contrasting anisotropies observed in different GLEs. The first two events exhibited highly anisotropic onsets, observed as spikes at a few stations. The anisotropy of these as well as a second spike during the 19 October event have been interpreted as the result of transport along a path where adiabatic focussing dominated over diffusion. This is an alternative to the neutron decay hypothesis (Shea *et al.*, 1991a; Shea *et al.*, 1991b) for the early spike. The particle arrival direction for the spikes during the 19 October event was found to be consistent with the measured interplanetary magnetic field direction. No field data were available for 22 October.

The main part of the 19 October GLE was in stark contrast to the two spikes. The particles arrived with very mild anisotropy from east of the Sun-Earth line. This has been interpreted as diffusive propagation from field lines passing close to, but not intersecting the Earth.

The contrast in anisotropy between the spike and the main event on 22 October was not as great. A change in the particle arrival direction has been attributed to movement of the local interplanetary magnetic field line, although no data are available to confirm this. The direction and variability of the particle arrival direction throughout the event is consistent with the data from 19 and 26 October (on either side of the data gap). A significant contribution to the neutron monitor response was made by particles arriving from the anti-sun direction. This has been interpreted as back-scattering from a high field strength, disturbed plasma region situated $\sim$1 AU beyond the Earth. The overall scenario suggested for this event is either extended shock acceleration or diffusion in the corona, accompanied by back-scattering of particles from beyond the Earth.

The 24 October GLE, unlike the two previous events, had a fairly smooth time profile. This event was dominated by scattering in the interplanetary medium which resulted in a mild anisotropy. A rigidity dependent pitch angle distribution gave a slight, but not significant, improvement to the fit of the calculated increases to the observed data. The form of the distribution gave some indication that scattering may have been less significant at higher rigidities. The modified Ellison and Ramaty spectral form was found to give better results than either a power law or the pure Ellison and Ramaty form. This implies acceleration by a finite shock for a finite time. The Ellison and Ramaty spectrum and its modified form are discussed further in Section 7.2.

Chapter 6

Earlier Events

The GLEs discussed in this chapter were three of the largest to occur in the 21st solar cycle (the largest, which occurred on 7 May 1978 is not discussed here). The 12 October 1981 solar proton event has previously been studied by Richardson *et al.* (1991). They analysed data from satellite-based instruments and were motivated by a desire to explain the unusually prompt arrival of particles from an eastern solar flare. The conclusion of their study was that the interplanetary magnetic field was distorted from the normal Archimedean spiral and the presence of closed or looped field structures enabled propagation to the Earth from the east of the Sun. The results presented here are for higher energy particles, but are consistent with these findings.

The GLE which commenced late on 7 December 1982 was observed as a gamma-ray event as well as a solar proton event. This has led to extensive study by many investigators (*e.g.* Rieger *et al.*, 1987; Flückiger *et al.*, 1990). Modelling this event with the improved technique described earlier in this thesis has revealed some problems with fitting to the observed increases at early times in the event. Further enhancement of the model was required to account for a deficit region associated with a structure thought to be a magnetic cloud, just beyond the Earth.

The final event discussed in this chapter occurred on 16 February 1984. Previous studies have concentrated on mechanisms by which the accelerated particles could have gained access to the 'garden hose' field line from a probable flare site $\sim 40^\circ$ behind the west limb of the Sun (Belov *et al.*, 1985; Bieber *et al.*, 1986; Debrunner *et al.*, 1988; Filippov and Noskovskikh, 1990). The results presented here reveal an unusual arrival direction at Earth, $\sim 40^\circ$ away from the measured interplanetary magnetic field direction. This is found to be consistent with previous studies, however no satisfactory explanation could be found.

Analysis of these events has revealed interesting features of particle propagation through the interplanetary magnetic field. In each case the particle arrival directions have not been fixed to the measured field directions, but remained as free parameters in the least squares fits. This minimises the number of assumptions in the model and produces general solutions which can then be compared with other data to reveal unexpected features of the interplanetary particle transport.

6.1 12 October 1981

The GLE which commenced at about 0730 UT on 12 October 1981 produced increases of ~15% above the pre-event background at several neutron monitor stations. At least twelve of the world-wide network of neutron monitors detected the GLE. Typical increases are shown in Figure 6.1. The geomagnetic field was moderately disturbed; the 3-hourly Kp index was 5+ between 0600 and 0900 UT, dropping to 4– in the following three hour period. The GLE was associated with a solar flare located at S18°, E31°. Hα emission commenced at 0622 UT, peaked with importance 2B at 0628 UT and ended at 0756 UT. This was accompanied by an X3 X-ray event which commenced at ~0615 UT. Type IV radio emission was observed between 0624 and 1032 UT.

It is unusual for a GLE to result from activity on the eastern side of the solar disc, simply because the usual interplanetary magnetic field connection between the Sun and the Earth has its footpoint around W60° on the solar disc. Under nominal field conditions, energetic charged particles associated with eastern flares may propagate in the corona to regions further west in order to gain access to field lines connected with the Earth. Such events are not usually observed by ground-based instruments and typically have delays in arrival and gradual, long-lived increases (Richardson *et al.*, 1991). Alternatively, Cane *et al.* (1988) suggest that particles associated with eastern flare events may be accelerated by shocks onto field lines far removed from the flare site. This scenario also results in delayed arrival times due to properties of the shock and the magnetic connection between the shock and the observing instrument.

The event of 12 October 1981 does not display the usual features of a particle event originating with an eastern flare. The particle increase observed by satellite-based instruments had a rapid onset and rise to maximum intensity, and an inferred travel distance of 3–4 AU (Richardson *et al.*, 1991). The event was also observed with ground-based neutron monitors. Richardson *et al.* noted that a bi-directional solar wind heat flux, indicative of closed- or looped-field plasma structures, occurred between 0000 and 2200 UT on 11 October. After these observations, the Earth entered a region of enhanced plasma density with a slightly depressed magnetic field strength and rotating magnetic field direction. The magnetic field rotation suggests the presence of a magnetic cloud. This would explain the presence of unusual field structure, however Richardson *et al.* point out that the identification is not certain since depressed field strength and enhanced plasma density are not considered typical features of magnetic clouds. The ISEE-3 ion anisotropies presented by Richardson *et al.* provide further evidence of an interplanetary magnetic field which was distorted from the nominal Archimedean spiral. The 1 to 4 MeV nucleon intensity first showed evidence of the solar particles in the period 1300–1400 UT and these ions arrived from east of the Sun. Richardson *et al.* also noted that bi-directional ion streaming occurred prior to that time, commencing at ~1000 UT and continuing until about 1800 UT. This may indicate that ISEE-3 entered a region of closed or looped magnetic field lines. This interpretation would explain the prompt arrival of the solar particles if the magnetic field loop were connected to the Sun near the eastern flare site, providing a

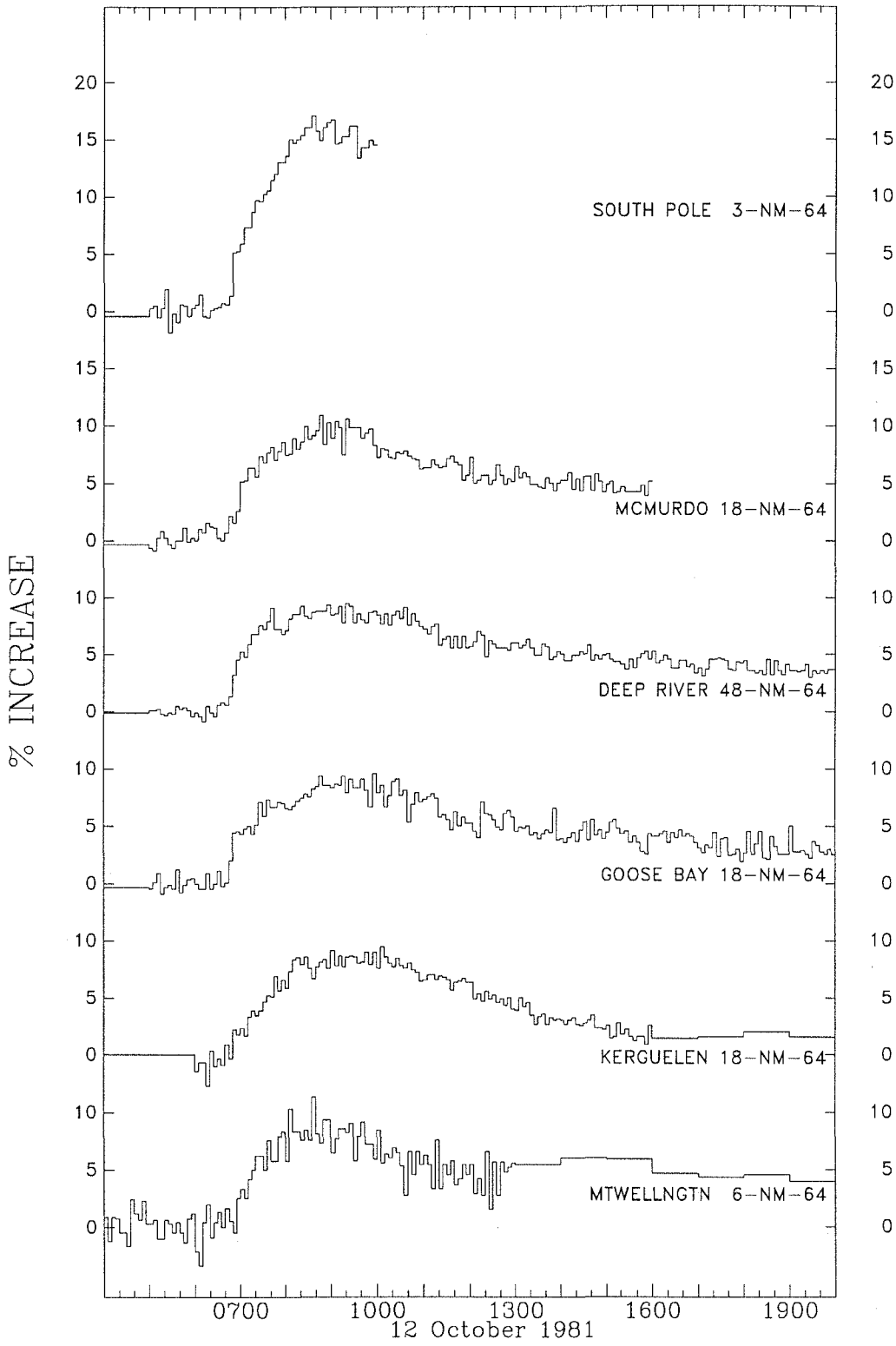

Figure 6.1: Cosmic ray increases at South Pole, McMurdo, Deep River, Goose Bay, Kerguelen Island and Mt. Wellington neutron monitors between 0400 and 2000 UT on 12 October 1981.

well-connected path for the propagation of charged particles. A field configuration such as this would also affect the arrival direction of the GLE particles at Earth. This has been investigated and is discussed in the following section.

6.1.1 Modelling the neutron monitor response

Data from thirteen neutron monitors were used in the model. Analysis was performed for eight times between 0715 UT and 1000 UT. Interplanetary magnetic field directions measured at IMP8 were available, however the axes of symmetry of the pitch angle distributions were not fixed to these directions, remaining as free parameters in the least squares analysis. If the field structure was a closed loop, the particles could flow in either direction along the field lines. Fixing the arrival direction parameters to the measured field direction gives preference to one direction over the other. By allowing all parameters to vary within the least squares analysis, a more general solution was obtained. The arrival directions and pitch angle distributions were compared with the measured field directions to obtain further information about the overall field structure and particle propagation.

The pitch angle distribution function used to model the neutron monitor response allowed for particle flow in two directions separated by 180° in pitch angle *i.e.* particles travelling in opposite directions along the same field line. The spectral form was a power law in rigidity.

The calculated percentage increases at each station are shown in Tables 6.1 and 6.2, along with the actual increases (with their Poisson errors) and the increases corrected to sea level pressure by the two attenuation length method. The flare attenuation length was assumed to be 100 g cm^{-2}. The Σ variances values listed in these tables are the sums of squares of differences between calculated and actual (corrected) increases.

The latitude and longitude of the axes of symmetry of the pitch angle distributions determined for this event are listed in Table 6.3 along with the derived spectral parameters. The fitted pitch angle distributions are shown in Figure 6.2. The first four distributions (0715 – 0840 UT) are approximately centred on the interplanetary magnetic field direction measured at IMP8, while the later distributions are centred on the reverse of this direction. Arrows at the top of each plot indicate the orientation of the measured field direction with respect to the pitch angle distribution. The direction of the arrows shows alignment with the forward or reverse direction of the field. The measured field directions and particle arrival directions (axes of symmetry) are plotted in Figure 6.3. The fitted arrival directions are linked with either the measured field direction or the reverse direction, depending on which was closest. There are some gaps in the IMP8 data, so the measurements closest to the modelled times have been plotted. From this plot, it is clear that the direction of maximum flux reversed between 0840 and 0850 UT. Examination of the pitch angle distributions at these and earlier times shows bi-directional particle flow. The measured field direction throughout this event was ~100°–180° west of the Sun-Earth line. This is consistent with a looped field structure such as that shown schematically in Figure 6.4. The initial particle arrival direction was along the path west of the Sun-Earth line and approached

Table 6.1: Increases at 0715 UT, 0750 UT, 0820 UT and 0840 UT, 12 October 1981 normalised to Deep River response.

	0715 UT			0750 UT		
Station	Actual %	Corrected %	Calculated %	Actual %	Corrected %	Calculated %
Alert	2.9±0.6	2.9	2.3	6.1±0.6	6.1	5.9
Apatity	3.7±0.6	3.3	3.2	6.1±0.6	5.4	7.0
Deep River	6.8±0.4	6.8	6.8	7.2±0.4	7.2	7.2
Goose Bay	4.3±0.7	4.3	3.9	7.1±0.7	7.1	6.5
Inuvik	3.7±0.6	3.6	3.5	6.3±0.6	6.2	5.7
Jungfraujoch	1.5±0.3	0.6	1.5	2.5±0.3	1.0	1.6
Kerguelen Island	3.9±0.5	3.5	3.5	5.7±0.5	5.1	7.2
Leeds	4.2±0.6	3.9	3.0	5.2±0.6	4.9	5.3
Mawson	1.7±2.6	1.6	2.8	11.0±2.6	10.1	6.4
McMurdo	6.3±0.5	5.8	5.2	7.8±0.5	7.2	5.9
Mt Wellington	5.0±0.7	4.1	4.9	7.9±0.7	6.4	6.3
South Pole	8.7±0.2	3.7	4.2	13.0±0.2	5.6	5.9
Thule	2.8±0.8	2.7	2.9	8.1±0.8	7.9	7.8
Σ variances from corrected %			5.0			23.5
	0820 UT			0840 UT		
Station	Actual %	Corrected %	Calculated %	Actual %	Corrected %	Calculated %
Alert	7.5±0.6	7.5	5.9	6.1±0.6	6.1	6.2
Apatity	7.6±0.6	6.8	6.1	7.0±0.6	6.2	6.0
Deep River	9.2±0.4	9.2	9.2	8.8±0.4	8.8	8.8
Goose Bay	7.4±0.7	7.4	7.8	8.4±0.7	8.4	7.9
Inuvik	6.5±0.6	6.4	5.8	7.0±0.6	6.9	6.4
Jungfraujoch	2.1±0.3	0.9	1.7	2.3±0.3	0.9	1.8
Kerguelen Island	7.9±0.5	7.1	6.3	7.7±0.5	6.9	6.4
Leeds	7.1±0.6	6.7	5.0	4.7±0.6	4.4	5.0
Mawson	4.5±2.6	4.1	5.7	6.1±2.6	5.6	5.5
McMurdo	8.5±0.5	7.8	6.7	9.5±0.5	8.7	7.3
Mt Wellington	7.6±0.7	6.2	7.0	8.1±0.7	6.6	6.7
South Pole	15.4±0.2	6.6	7.2	15.7±0.2	6.8	7.8
Thule	7.1±0.8	6.9	7.4	6.2±0.8	6.0	7.2
Σ variances from corrected %			13.0			6.4

Table 6.2: Increases at 0850 UT, 0900 UT, 0930 UT and 1000 UT, 12 October 1981 normalised to Deep River response.

	0850 UT			0900 UT		
Station	Actual %	Corrected %	Calculated %	Actual %	Corrected %	Calculated %
Alert	5.9±0.6	5.9	6.9	6.8±0.6	6.8	6.7
Apatity	8.1±0.6	7.2	7.7	9.5±0.6	8.5	9.0
Deep River	8.8±0.4	8.8	8.8	8.4±0.4	8.4	8.4
Goose Bay	8.5±0.7	8.5	9.3	8.3±0.7	8.3	8.5
Inuvik	8.2±0.6	8.0	8.5	7.9±0.6	7.7	6.8
Jungfraujoch	2.5±0.3	1.0	1.4	2.2±0.3	0.9	1.1
Kerguelen Island	8.3±0.5	7.5	7.3	9.1±0.5	8.2	7.4
Leeds	6.3±0.6	5.9	5.2	6.1±0.6	5.7	4.7
Mawson	11.0±2.6	10.1	11.0	9.3±2.6	8.6	10.0
McMurdo	8.3±0.5	7.6	7.1	8.9±0.5	8.2	6.8
Mt Wellington	9.3±0.7	7.5	7.3	6.4±0.7	5.2	6.0
South Pole	16.0±0.2	6.9	7.0	16.6±0.2	7.1	7.5
Thule	7.4±0.8	7.2	6.9	6.6±0.8	6.3	6.7
Σ variances from corrected %			4.0			8.1
	0930 UT			1000 UT		
Station	Actual %	Corrected %	Calculated %	Actual %	Corrected %	Calculated %
Alert	5.3±0.6	5.3	6.2	6.7±0.6	6.7	7.8
Apatity	7.8±0.6	6.9	8.2	8.7±0.6	7.7	8.5
Deep River	7.8±0.4	7.8	7.8	8.4±0.4	8.4	8.4
Goose Bay	8.3±0.7	8.3	7.9	7.9±0.7	7.9	8.6
Inuvik	7.4±0.6	7.3	6.1	7.1±0.6	7.0	6.7
Jungfraujoch	2.2±0.3	0.9	1.3	2.5±0.3	1.0	1.0
Kerguelen Island	8.6±0.5	7.7	7.0	7.6±0.5	6.8	7.6
Leeds	6.8±0.6	6.4	4.8	4.4±0.6	4.1	4.6
Mawson	11.5±2.6	10.6	9.0	12.5±2.6	11.5	8.8
McMurdo	9.8±0.5	9.0	6.7	7.3±0.5	6.7	7.0
Mt Wellington	5.8±0.7	4.7	5.6	8.4±0.7	6.7	6.1
South Pole	16.1±0.2	6.9	7.4		No Data	
Thule	6.1±0.8	5.9	6.2	10.1±0.8	9.8	7.8
Σ variances from corrected %			16.7			8.9

the Earth from the anti-sunward direction.

The fitted particle arrival directions shown in Figure 6.3 are all reasonably close to the measured field directions. The confidence limits on the derived latitude and longitude depend on the degree of anisotropy in the pitch angle distribution. For relatively isotropic distributions such as those modelled late in this event, moving the axis of symmetry through quite large angles makes very little difference to the calculated responses, resulting in a shallow minimum in the sum of variances. In such cases the apparent particle arrival direction cannot be determined precisely. The separation of the measured and implied field directions for the times from 0900–1000 UT are considered to be within the expected confidence limits.

Table 6.3: Apparent particle arrival directions and spectral parameters derived for the GLE of 12 October 1981. Fluxes in units of particles $(cm^2\ s\ ster\ GV)^{-1}$.

	Latitude	Longitude	γ	$J_{\|\|}$	J_{av}
0715 UT	−7	284	−4.2	3.1	1.1
0750 UT	13	299	−5.0	7.4	4.5
0820 UT	4	302	−4.9	7.9	4.1
0840 UT	−1	301	−4.8	5.9	3.6
0850 UT	−5	31	−5.2	9.6	6.8
0900 UT	−15	48	−5.5	10.9	8.2
0930 UT	−24	50	−5.3	8.2	6.4
1000 UT	10	35	−5.6	10.8	9.2

The largest discrepancy between measured field direction and calculated particle arrival direction was for 0715 UT. It should be noted that the observed neutron monitor increases at this time were small (up to ~7%), so the errors were more significant than at later times. While the model parameters presented here produce a very good fit to the data, it is quite possible that a model with the particle arrival direction closer to the measured field could predict increases within the errors of the recorded increases. The field direction was quite variable at this time, moving by almost 20° in the following five minute interval. This reduces the validity of the average field direction and may account for part of the discrepancy. The derived particle spectrum is also of interest in this case. The stations with most influence in determining the spectrum were Jungfraujoch (magnetic cutoff $P_c \sim 4$ GV) and Leeds ($P_c \sim 2$ GV). It is interesting to note that the predicted increase at Leeds was low, while at Jungfraujoch it was high. One possible reason for this is that the atmospheric depth correction is highly significant for Jungfraujoch (altitude 3550 m), so an error in this correction could affect the result. Another possibility is that the power law spectrum is inadequate to reproduce the observed responses. A spectrum which steepens with increasing rigidity may eliminate the apparent contradiction of the predictions for Leeds and Jungfraujoch. This may also affect the other parameters of the model, however it is thought that the significance of the recorded increases is not great enough to justify further complications in the model.

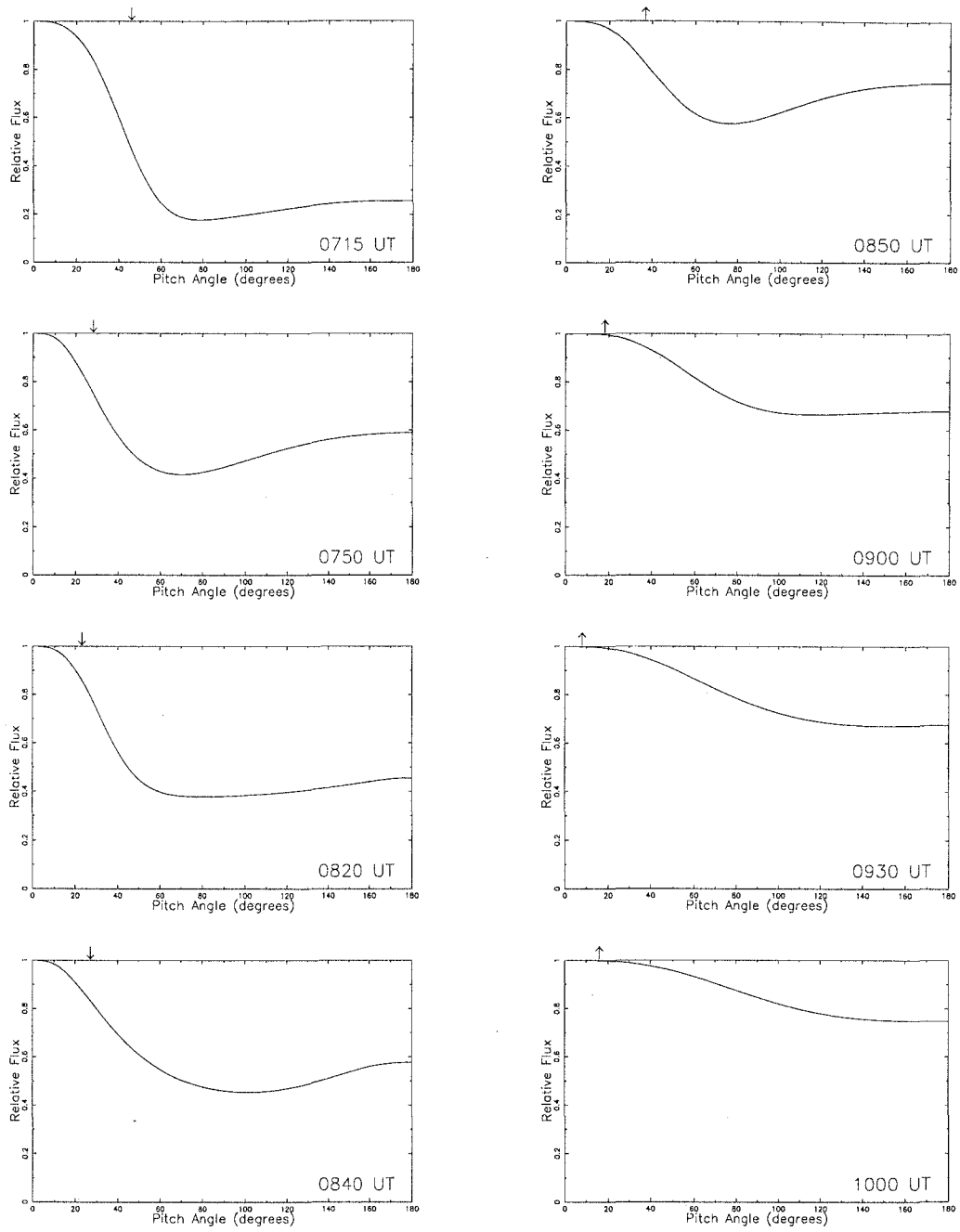

Figure 6.2: Fitted pitch angle distributions for the GLE of 12 October 1981 at the labelled times. The arrow at the top of each plot indicates the measured interplanetary magnetic field direction.

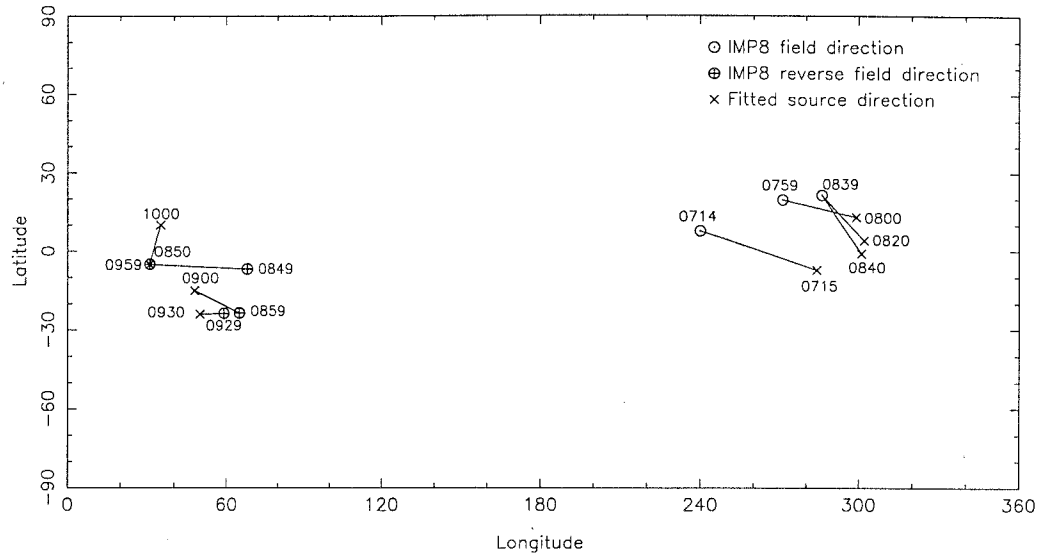

Figure 6.3: Fitted particle arrival directions for 12 October 1981 linked to measured IMF directions (as labelled). Coordinates are expanded Earth latitude and longitude.

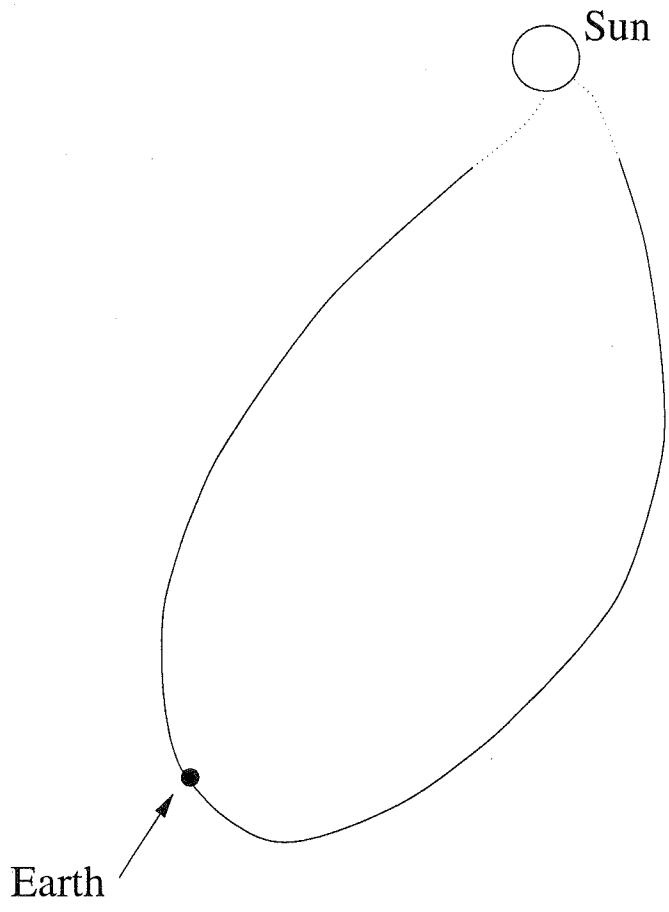

Figure 6.4: Schematic diagram of possible interplanetary magnetic field structure on 12 October 1981 with the Earth located on the eastern side of a loop.

The separation between apparent particle arrival directions and the measured field directions for times between 0750 and 0850 UT, while smaller than that for 0715 UT, are somewhat larger than may be expected given the narrow pitch angle distributions. In the case of 0820 UT, the closest available field measurement was at 0839 UT. It is possible that the field direction may have been quite different at 0820 UT, however interpolation between the field directions at 0759 and 0839 UT does not provide any closer agreement. Without additional data it is not possible to say whether interpolation is reasonable. There appears to be a smooth progression of the field direction from 0719 to 0759 and 0839 UT, but it is difficult to infer much from only three data points.

The pitch angle distributions between 0750 and 0850 UT all exhibit bidirectional flow. The flow directions in the model were forced to be separated by 180°. If this is not a true representation of the particle flow, it could introduce significant errors in the derived particle arrival directions at these times. A further consideration is that the spectrum of particles arriving along the two pathways was assumed to be the same. This is not necessarily true and may have added to the errors on the other parameters. Since the viewing directions of neutron monitors depend on rigidity, a change in the spectrum may result in a significant change in either the shape of the pitch angle distribution or its axis of symmetry. The effect of this should also be considered for the model at 0715 UT when there was a significant isotropic background which may have been composed of a different particle population. In order to model two particle populations with different spectra, each would need to be described by independent spectral and particle distribution parameters. This would introduce several extra parameters in the model and is not feasible with the small number of stations for which data are available. Taking into account all these considerations, the fitted particle arrival directions are largely consistent with the measured interplanetary magnetic field directions.

The particle spectrum softened during the event as is seen in most GLEs. It is possible, however that this was partly due to the change in arrival direction. Once particles began arriving from both directions (at 0750 UT), the spectrum steepened significantly. This may indicate that access to the western arrival direction was easier for the high rigidity particles. This could only be resolved by more detailed modelling as described above.

The most striking feature that has been shown by the modelling of this GLE is the particle propagation in both directions along the local interplanetary magnetic field line. A closed or looped field structure was suggested in the work of Richardson *et al.* (1991), but they were unable to confirm this with certainty. The initial particle flow was from the west and access to this field line may have been easier for high rigidity particles. Later in the event, the arrival direction changed as the particles propagated along a field line connected to the east of the Sun. The flow along this path was less focused. The flow of these particles began earlier than the arrival from the east noted by Richardson *et al.* however this is probably due to the different energy regimes of the two analyses. Richardson *et al.* noted velocity dispersion at the onset of the event. The scattering during propagation may also have been more significant at lower energies. The results presented here

are therefore considered to be consistent with those of Richardson *et al.* and in fact strengthen the proposition that there was a loop structure in the interplanetary magnetic field.

6.2 7-8 December 1982

A GLE began around 2350 UT on 7 December 1982 and reached maximum intensity of about 55% above the background at the Kerguelen Island neutron monitor within 10 minutes. The response at other neutron monitors peaked at various times between 0000 UT and 0030 UT. It can be seen from the data plotted in Figure 6.5 that some stations (such as Kerguelen and Alert) recorded a very rapid increase with a narrow peak while other stations (such as Deep River and Goose Bay) recorded similarly fast onsets but slower decays. A third group of stations (such as Oulu, Inuvik and Apatity) displayed a slower rise to maximum intensity, peaking 15–30 minutes after those with the rapid onset. The time profiles from these stations show a variety of shapes, some with sharp peaks, others with fairly flat tops.

The solar flare which has been associated with this event was in NOAA/USAF region 4022 and located at S19°, W86° on the solar disc. The Hα flare began at 2346 UT, peaked at 2351 UT with importance 1B and ended at 0008 UT. An X-ray event peaked with importance X2.8 at 2354 UT. Type II radio bursts were observed between 2343 and 0023 UT and type IV between 0000 and 0030 UT. Radio bursts of types III and V were observed as well as the type II and IV. The type III emission was intermittent and occurred between 0003 and 0625 UT while the type V emission was observed from 0421 to 0424 UT. Strong gamma-ray emissions were also observed by instruments on board the Solar Maximum Mission satellite. It is unusual for gamma-ray emission to be associated with an event which resulted in particles observed at ground level. Evenson *et al.* (1990) associated gamma-ray events with a particular class of solar particle events which have high electron to proton ratios. They believe that this is due to the direction of propagation of the shock responsible for acceleration of the particles in the solar flare. If the shock is directed down into the Sun, the accelerated particles have to escape through the shock in order to propagate into interplanetary space. Evenson *et al.* claim that in such circumstances, only a few particles (predominantly electrons) will escape and the remainder will be stopped by the solar atmosphere, producing gamma-rays. They believe that the two populations of particles (those escaping into interplanetary space and those producing the gamma-rays) must be viewed as separate even though they may have had the same source originally. Rieger *et al.* (1987) examined the gamma-ray spectrum of the 7–8 December event in conjunction with energetic particle data and concluded that the particles released into space and those responsible for generating the gamma rays could only originate from the same acceleration process if the propagation and escape of the particles was energy dependent. If this was not so, then different acceleration processes are required to explain features of the data.

A moderate geomagnetic storm (Kp = 6+) occurred during 7 December, but

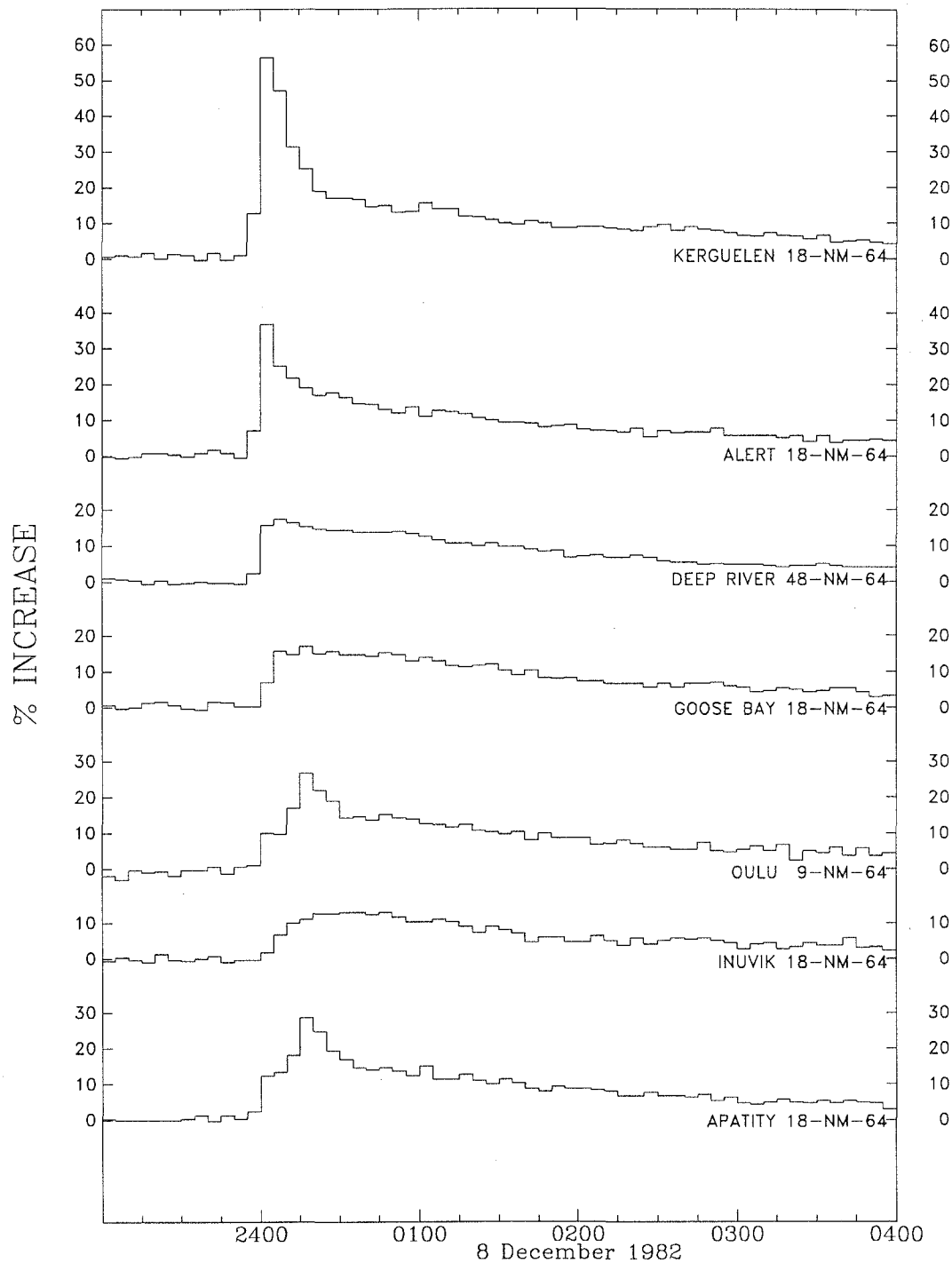

Figure 6.5: Cosmic ray increases at Kerguelen Island, Alert, Deep River, Goose Bay, Oulu, Inuvik and Apatity neutron monitors between 2300 UT on 7 December 1982 and 0400 UT on 8 December 1982.

the Kp index had reduced to 4 by the time the GLE began. This is within the range of Kp values included in the Tsyganenko magnetospheric models. The interplanetary magnetic field direction measured at IMP8 was ~110° west of the Sun-Earth line. This means that the field was either looped back towards the Sun or kinked from its nominal position and locally approaching from ~70° east of the Sun-Earth line. The hourly average IMF magnitude, latitude and longitude in GSE coordinates and five minute average measurements of the plasma density for 7 and 8 December 1982 are plotted in Figure 6.6. This shows a smooth rotation of the field latitude between ~5 and 23 UT on 7 December. At the same time, the field strength was high (~20 nT), the longitude showed a small oscillation and the plasma density was low. High field strength accompanied by a rotation in the field direction and low plasma temperatures indicate the presence of a magnetic cloud (Burlaga, 1991). Plasma temperature data are not available for this time, but the sudden depression of plasma density suggests a discontinuous plasma regime which could be a magnetic cloud. The geomagnetic disturbance which occurred during this day also indicates the presence of a disturbed plasma region moving past the Earth. Particle data recorded at both IMP8 and ISEE3 showed evidence of some bi-directional flow associated with this region (I. Richardson, private communication to H. Cane). It seems reasonable to assume that a magnetic cloud-like structure was just beyond the Earth at the time of this GLE. The propagation of this magnetic feature from the Sun is probably the cause of the unusual field direction observed at the time of the GLE and must be considered when interpreting the particle event. This is particularly important early in the event when the cloud was still very close to the Earth.

Figure 6.7 shows a possible field configuration which could have produced the observed field direction at Earth. The shaded area represents the magnetic cloud. The radial dimension of this feature has been estimated from the solar wind speed and the length of time it took to pass the Earth. The timing also indicates that the cloud was ~0.01 AU beyond the Earth at the start of the GLE. The likely shape of the magnetic cloud is unclear. It has been suggested that most plasma emissions from the Sun will form 'tear-drop' shapes as they propagate outwards (H. Cane, private communication), however, in this case the shape drawn in Figure 6.7 seems more likely given the observed magnetic field direction. The hatched region behind the cloud is a region of turbulent magnetic fields. Some possible field lines have been drawn in this region (dashed lines). These would produce the observed field direction which persisted for some time at the Earth. The data plotted in Figure 6.6 show that the field longitude did not return to its nominal position ~45° west of the Sun-Earth line until after 12 UT on 8 December. The field direction continued to vary throughout 9 December. This indicates that the turbulent region behind the cloud had a radial size of between ~0.1 AU and ~0.3 AU.

6.2.1 Modelling the neutron monitor response

Modelling the neutron monitor response to this event has been undertaken at the times when stations reached peak intensity (0000, 0015 and 0020 UT) and also during the decay phase (0050 UT). Some difficulty was experienced in reproducing

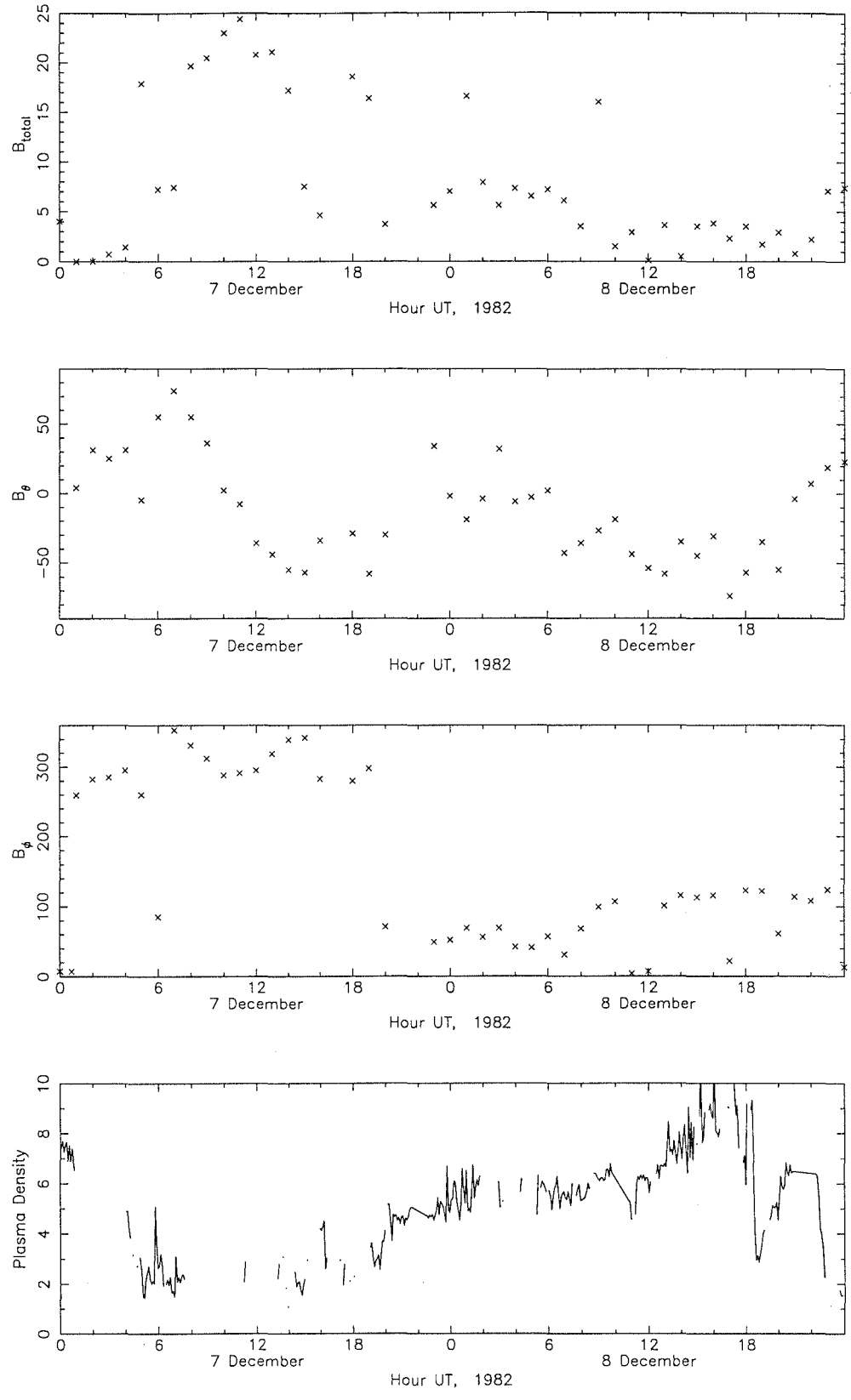

Figure 6.6: Interplanetary magnetic field magnitude (top panel), latitude (second panel), longitude (third panel) in GSE coordinates and plasma density (bottom panel) for 7 and 8 December 1982.

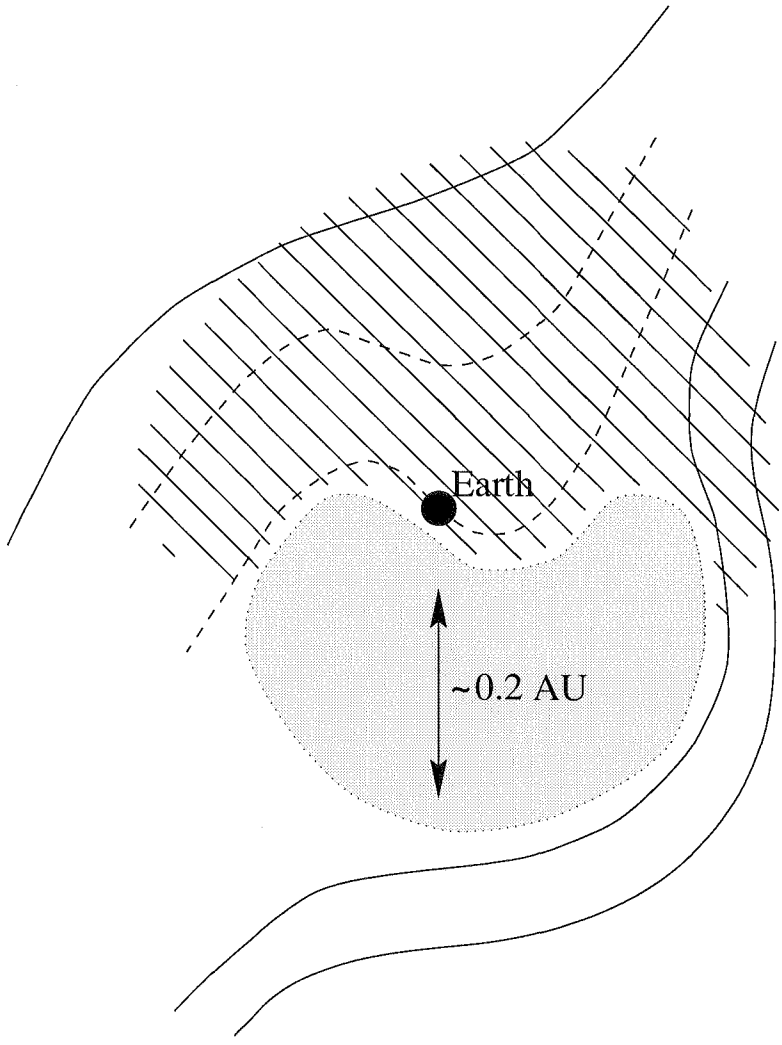

Figure 6.7: Possible field configuration at the time of the 7-8 December 1982 GLE. The shaded region is a magnetic cloud and the hatched area represents the turbulent magnetic field region behind the cloud. Possible field lines have been drawn with dashed lines to produce the observed field direction ~110° west of the Sun-Earth line.

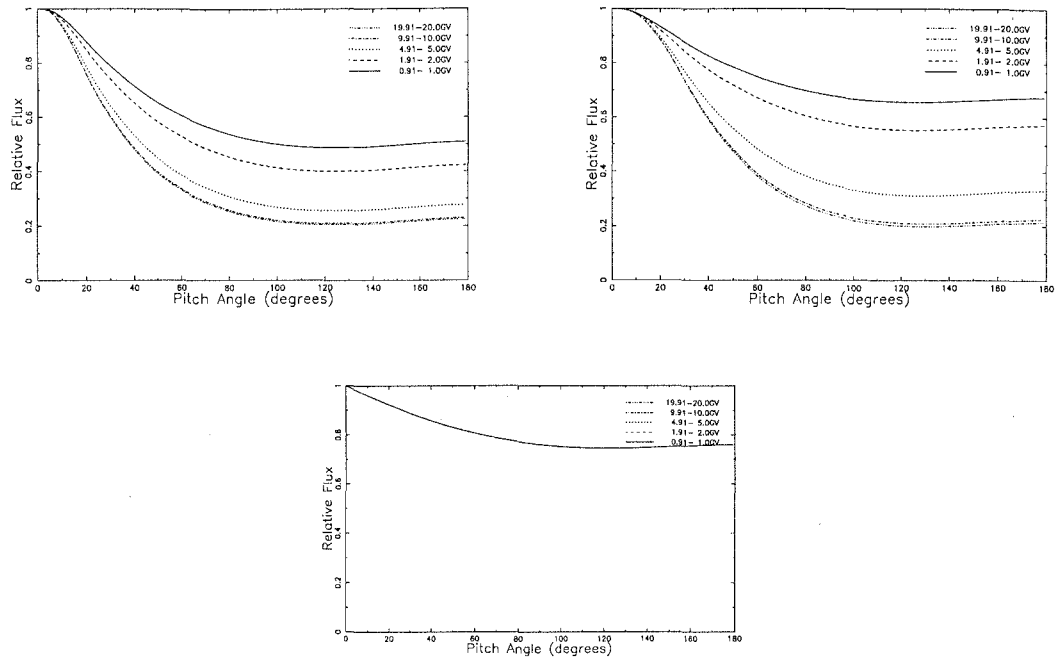

Figure 6.8: Pitch angle distributions at 0015 UT (top left), 0020 UT (top right) and 0050 UT (bottom) during the GLE of 7–8 December 1982.

the observed increases at 0000 UT using the usual model. Further complexities were introduced and the results are discussed at the end of this section.

A rigidity dependent pitch angle distribution was used in the model, however the improvement in the fit compared with a model without rigidity dependence was not significant. The fitted pitch angle distributions for 0015, 0020 and 0050 UT are shown in Figure 6.8. These indicate that the degree of anisotropy decreased fairly rapidly. This is consistent with the high likelihood of scattering near the magnetic cloud and in the turbulent region surrounding the Earth. The axes of symmetry of the pitch angle distributions are listed in Table 6.4 with the measured interplanetary magnetic field direction (converted to geographic coordinates). The measured field direction for 0015 and 0020 UT is the average direction for 0012–0031 UT quoted by Flückiger *et al.* (1990). No measured field direction is stated for 0050 UT as the data listed by Flückiger *et al.* do not extend to this time. The hourly average data are available, but are not appropriate for comparison with the model since the field direction was changing very rapidly. The fitted particle arrival direction for 0015 UT is very close to the measured field direction, but the agreement is not as good for 0020 UT. It should be noted that the measured field direction changed from N50°, E45° (geographic) to N40°, E80° within a few minutes, so there were clearly rapid changes in direction which could lead to discrepancies between the model and the measured field.

The spectral form used in the model was a modified power law with the parameter $\delta\gamma$ representing the change in the exponent (γ) per GV. This functional form allows the spectrum to steepen with increasing rigidity. The fitted parameters γ

Table 6.4: Apparent particle arrival directions and measured field directions for the GLE of 7–8 December 1982.

	Fitted		Measured	
	Latitude	Longitude	Latitude	Longitude
0015 UT	32	76	25	81
0020 UT	27	57	25	80
0050 UT	−18	30	-	-

and $\delta\gamma$ are listed in Table 6.5 along with the calculated particle fluxes. The fitted spectra are plotted in Figure 6.9. It would appear from this plot that the spectrum became harder between 0015 and 0020 UT and then softened towards the end of the event. The spectra at 0015 and 0020 UT are in fact very similar between 1 and 10 GV and since there was very little contribution from the particles above 10 GV it is hard to determine the spectrum accurately at higher rigidities. It is therefore reasonable to conclude that the spectrum did not change much between 0015 and 0020 UT.

Table 6.5: Spectral parameters and calculated particle fluxes during the GLE of 7–8 December 1982. Fluxes in units of particles $(cm^2\ s\ ster\ GV)^{-1}$.

	γ	$\delta\gamma$	$J_{\|\|}$	J_{av}
0015 UT	−3.6	0.7	9.8	6.4
0020 UT	−5.0	0.0	16.3	12.5
0050 UT	−5.4	0.0	15.2	12.8

The calculated percentage increases at 0015, 0020 and 0050 UT are shown in Table 6.6 along with the actual increases (and Poisson errors) and increases corrected to sea level pressure by the two attenuation length method. The flare attenuation length used in these corrections was 110 g cm^{-2}. The sum of variances values at the bottom of the table are the sums of squares of differences between the calculated increases and the observed increases corrected to sea level. These values are less than five percent lower than the corresponding values for the model without the rigidity dependent pitch angle distribution.

The neutron monitor responses at 0000 UT were first modelled using a power law spectrum and a non-rigidity dependent pitch angle distribution. The calculated percentage increases are shown in the fourth column (Model 1) of Table 6.7 along with the observed increases (with Poisson errors) and increases corrected to sea level pressure. The fitted pitch angle distribution is shown in Figure 6.10. The axis of symmetry of this distribution was N48°, E108°, some distance from the measured field direction of N25°, E80°. The slope of the fitted spectrum was −5.1. The calculated parallel flux at 1 GV was 53.7 particles $(cm^2\ ster\ sec\ GV)^{-1}$ while the average flux at 1 GV was 10.7 particles $(cm^2\ ster\ sec\ GV)^{-1}$ over 4π steradians.

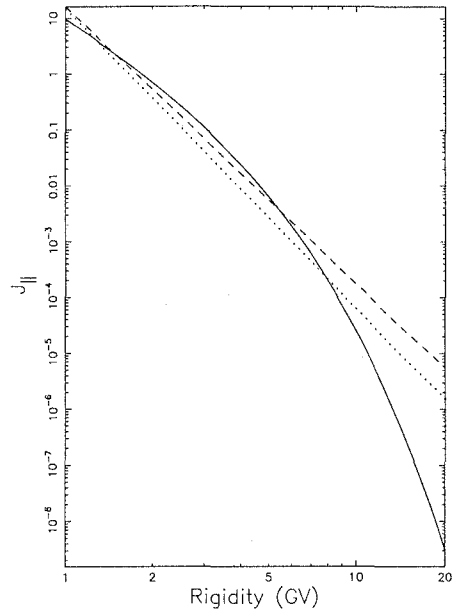

Figure 6.9: Spectra at 0015 (solid line), 0020 (dashed line) and 0050 UT (dotted line) for the 7–8 December 1982 GLE.

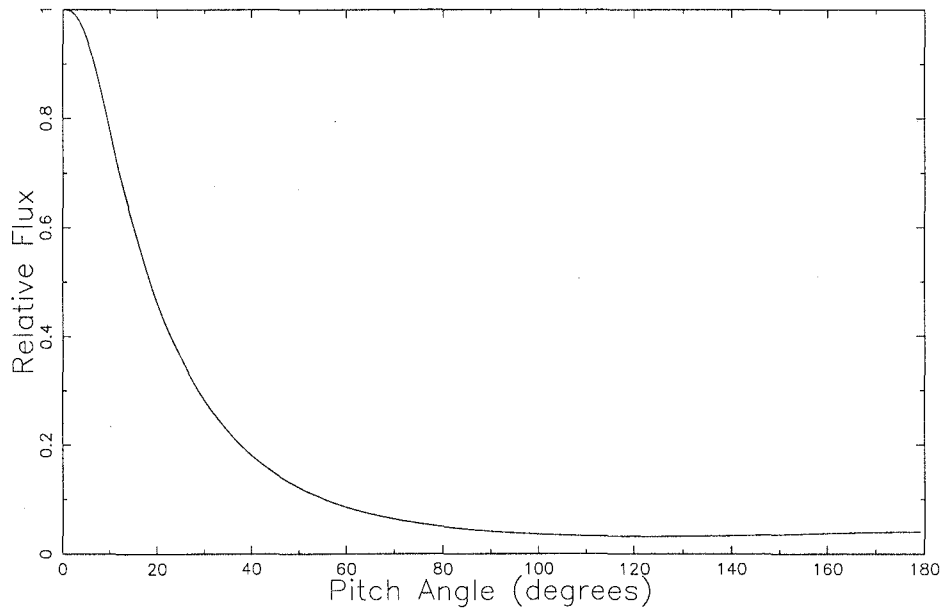

Figure 6.10: Fitted pitch angle distribution for 0000 UT, 8 December 1982 (Model 1).

Table 6.6: Increases at 0015, 0020 and 0050 UT, 8 December 1982 normalised to Kerguelen Island response.

Station	Actual %	Corrected %	Calculated %	Actual %	Corrected %	Calculated %	Actual %	Corrected %	Calculated %
Alma Ata	0.8±0.1	0.4	0.3	0.9±0.1	0.4	0.7	1.1±0.1	0.5	0.8
Alert	19.1±0.6	18.7	20.5	17.0±0.6	16.7	18.2	12.1±0.6	11.9	12.6
Apatity	28.6±0.7	28.0	28.6	24.6±0.7	24.1	23.9	13.6±0.7	13.3	13.5
Cape Schmidt	10.0±0.6	10.0	11.9	9.0±0.6	9.0	12.1	7.7±0.6	7.7	12.3
Deep River	15.4±0.4	14.9	14.6	14.5±0.4	14.1	15.3	14.1±0.4	13.7	13.9
Durham	16.9±0.7	16.9	17.7	19.4±0.7	19.4	16.5	11.9±0.7	11.9	12.8
Goose Bay	17.0±0.7	17.0	13.6	15.0±0.7	15.0	14.8	14.6±0.7	14.6	14.0
Hobart	10.0±3.1	10.0	11.4	10.7±3.1	10.7	10.3	13.4±3.1	13.4	10.3
Inuvik	10.9±0.7	10.8	11.9	12.7±0.7	12.6	12.0	11.8±0.7	11.7	12.3
Irkutsk	2.5±0.6	2.3	3.5	2.9±0.6	2.6	3.5	2.9±0.6	2.6	3.4
Jungfraujoch	1.1±0.3	0.5	2.2	2.7±0.3	1.2	3.0	0.0±0.3	0.0	2.1
Kerguelen Island	25.3±0.6	24.8	24.8	19.1±0.6	18.7	18.7	12.9±0.6	12.6	12.6
Khabarovsk	0.3±1.0	0.3	0.8	1.2±1.0	1.2	1.2	0.0±1.0	0.0	1.3
Kiel	14.3±0.7	14.2	12.8	12.0±0.7	11.9	11.7	9.0±0.7	8.9	7.9
Kiev	5.3±0.7	5.1	4.7	4.6±0.7	4.5	4.7	2.3±0.7	2.2	4.1
Leeds	15.2±0.7	15.0	13.9	5.1±0.7	14.9	12.6	9.1±0.7	9.0	8.7
Lomnicky Stit	5.5±0.3	4.1	3.4	7.3±0.3	5.5	3.9	2.6±0.3	1.9	3.1
Magadan	11.5±0.7	10.8	10.2	11.7±0.7	11.0	9.1	8.7±0.7	8.2	9.1
Mawson	19.5±2.7	18.7	20.2	18.4±2.7	17.7	20.1	14.1±2.7	13.5	14.6
Moscow	12.5±0.7	12.1	11.3	10.2±0.7	9.9	10.2	9.2±0.7	8.9	7.5
Mt. Washington	26.9±1.0	18.6	17.2	26.3±1.0	18.1	16.8	21.3±1.0	14.7	13.4
Mt. Wellington	10.4±0.7	8.8	11.5	11.2±0.7	9.5	10.6	13.8±0.7	11.7	10.3
Newark	14.8±0.9	14.8	15.4	15.0±0.9	15.0	13.4	9.4±0.9	9.4	9.9
Novosibirsk	8.1±0.8	7.9	6.8	6.3±0.8	6.2	6.1	4.1±0.8	4.0	5.7
Oulu	26.7±0.9	26.2	26.4	22.0±0.9	21.6	23.3	14.3±0.9	14.0	13.6
Rome	2.1±0.8	2.1	0.5	0.0±0.8	0.0	1.1	0.0±0.8	0.0	1.0
South Pole	30.0±0.3	16.5	12.5	30.2±0.3	16.6	13.3	25.2±0.3	13.9	12.4
Terre Adelie	10.8±0.8	10.3	12.0	13.0±0.8	12.3	12.0	14.1±0.8	13.4	12.4
Thule	19.2±0.8	19.0	18.1	17.5±0.8	17.3	17.3	12.6±0.8	12.5	12.8
Tixie Bay	8.3±0.8	8.2	13.9	8.6±0.8	8.5	12.7	8.6±0.8	8.5	12.2
Tsumeb	0.0±0.4	0.0	0.1	0.0±0.4	0.0	0.5	0.0±0.4	0.0	0.4
Σ variances from corrected %			100.9			82.3			73.1

Table 6.7: Increases at 0000 UT, 8 December 1982 normalised to Kerguelen Island response.

Station	Actual %	Corrected %	Model 1 Calculated %	Model 2 Calculated %
Alma Ata	1.6±0.1	0.8	0.7	0.8
Alert	36.6±0.6	35.9	34.7	36.8
Apatity	12.2±0.7	11.8	23.2	9.0
Cape Schmidt	4.0±0.6	4.0	6.8	4.8
Deep River	15.5±0.4	15.0	7.1	15.7
Durham	1.8±0.7	1.8	13.5	9.0
Goose Bay	6.9±0.7	6.9	5.5	11.3
Hobart	3.7±3.1	3.7	8.0	7.0
Inuvik	1.8±0.7	1.8	6.9	4.8
Irkutsk	2.5±0.6	2.3	2.7	3.3
Jungfraujoch	6.3±0.3	2.9	3.1	6.6
Kerguelen Island	56.2±0.6	55.1	55.1	55.1
Khabarovsk	2.4±1.0	2.4	0.9	0.9
Kiel	18.4±0.7	18.0	11.3	18.2
Kiev	7.6±0.7	7.4	4.7	8.6
Leeds	21.2±0.7	21.0	12.7	20.4
Lomnicky Stit	8.9±0.3	6.7	4.1	8.2
Magadan	4.3±0.7	4.0	6.0	5.5
Mawson	15.4±2.7	14.8	10.4	14.8
Moscow	19.4±0.7	18.8	9.8	16.9
Mt. Washington	17.6±1.0	12.1	11.7	14.8
Mt. Wellington	5.9±0.7	5.0	7.5	6.8
Newark	9.1±0.9	9.1	10.4	7.0
Novosibirsk	5.8±0.8	5.7	5.3	5.8
Oulu	10.0±0.9	9.8	19.9	16.2
Rome	1.6±0.8	1.6	1.5	2.4
South Pole	24.5±0.3	13.5	4.9	7.0
Terre Adelie	11.7±0.8	11.1	5.1	5.3
Thule	27.1±0.8	26.8	20.4	27.3
Tixie Bay	1.8±0.8	1.8	1.1	1.3
Tsumeb	0.5±0.4	0.4	17.5	9.9
Σ variances from corrected %			1128.3	332.9

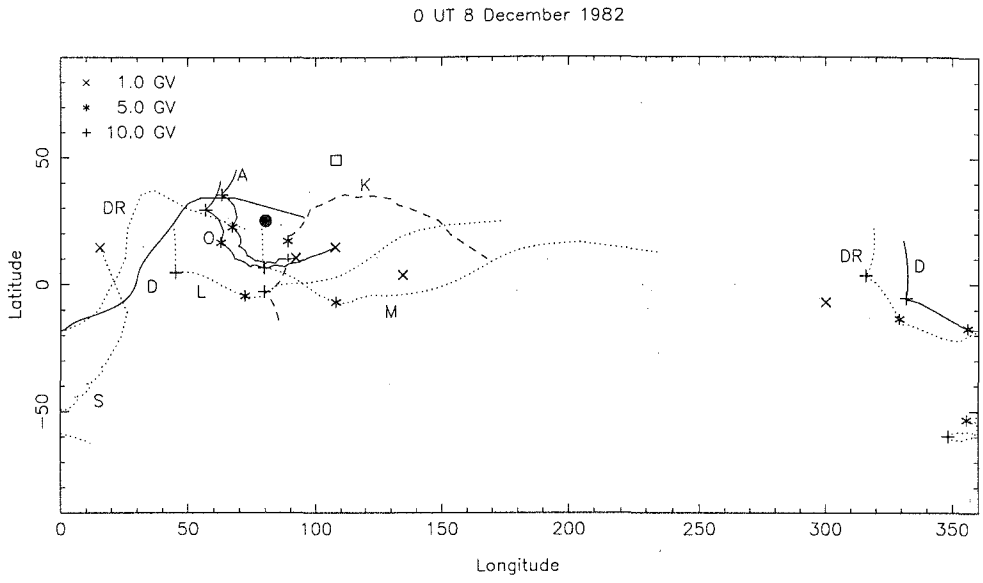

Figure 6.11: Viewing directions for Apatity (A), Deep River (DR), Durham (D), Kerguelen Island (K), Leeds (L), Moscow (M), Oulu (O) and South Pole (S) for 0000 UT on 8 December 1982. Viewing directions at 10, 5 and 1 GV are indicated. Stations whose response was over-estimated by the model are shown with solid lines, those which were under-estimated are shown with dotted lines and the normalisation station is shown with a dashed line. The measured IMF direction is marked with a solid circle and the fitted particle arrival direction with an open square.

It is clear from the data in Table 6.7 that the model substantially over-estimates the response at Apatity, Oulu, Durham and Tsumeb, while the response at stations such as Deep River, Kiel, Leeds, Moscow and South Pole is under-estimated. The viewing directions of some of these stations are shown in Figure 6.11 along with the measured interplanetary magnetic field direction and the fitted particle arrival direction. Different line styles have been used for those stations whose response was over- or under-estimated by the model (see figure caption for details). It can be seen that the fitted particle arrival direction has been moved to the north and east by the least squares routine to minimise the predicted response at Apatity and Oulu. This has resulted in low calculated responses for many other stations. The fitted pitch angle distribution is also much narrower than expected considering the turbulent magnetic fields surrounding the Earth.

It appears that if the particle arrival direction is to be aligned with the measured IMF direction, there must be a deficit cone in the region of space viewed by Apatity and Oulu. This has been modelled by suppressing the response in an ellipse of variable size and orientation. The centre, eccentricity, orientation and length of one axis of the ellipse were variable parameters in this modified model. A sixth parameter was the factor by which contributions from inside the ellipse were attenuated.

The fitted ellipse is shown in Figure 6.12 along with the apparent particle arrival direction and the viewing directions of selected stations. Note that the different line styles used in this figure are purely to enable the different traces to be distinguished and do not represent over- or under-estimates by the model (as

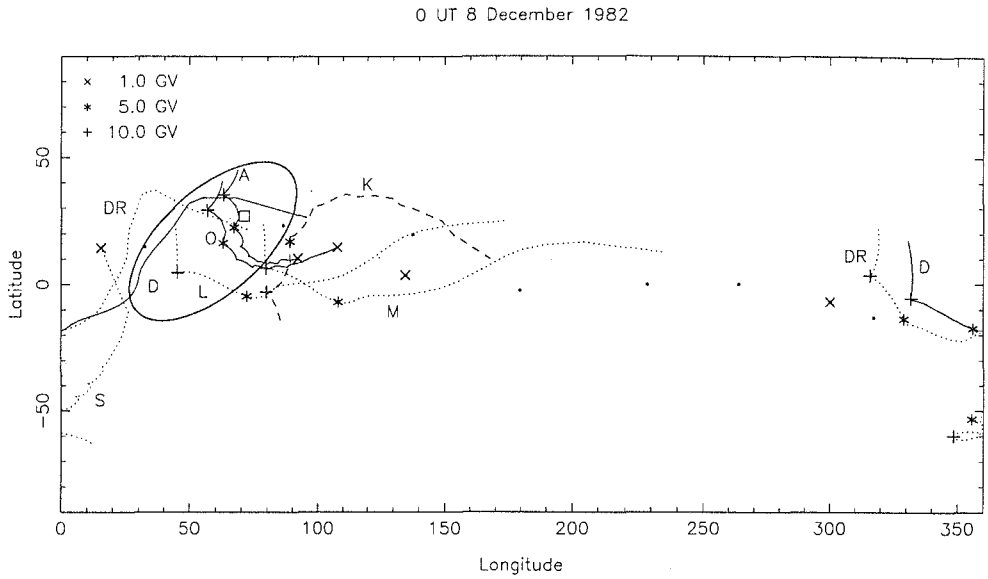

Figure 6.12: Viewing directions for Apatity (A), Deep River (DR), Durham (D), Kerguelen Island (K), Leeds (L), Moscow (M), Oulu (O) and South Pole (S) for 0000 UT on 8 December 1982 with fitted deficit region (ellipse) and particle arrival direction (square). Viewing directions at 10, 5 and 1 GV are marked. Different line styles have been used so that stations can be distinguished more easily. It should be noted that the line styles do not indicate the quality of the model fit to observed data (as in the previous figure).

in Figure 6.11). The multiplicative factor used inside the ellipse was 3.0×10^{-2}. The apparent particle arrival direction was N27°, E71° which is much closer to the measured IMF direction than that fitted in the previous model. The fitted pitch angle distribution is shown in Figure 6.13. The slope of the fitted power law spectrum was −5.1. The parallel and average fluxes cannot easily be calculated due to the effects of the deficit region. The calculated percentage increases for this model are shown in the final column of Table 6.7. The sum of variances for this fit indicates a great improvement from the previous model. Close examination shows that many of the poorly modelled responses are significantly improved by this model. Specifically, the calculated response at Apatity has been substantially reduced, while at Durham, Oulu and Tsumeb, smaller improvements have been made. The calculated responses at Deep River, Kiel, Leeds and Moscow are all much closer to the observed values and the response calculated for South Pole has increased a little.

The presence of the deficit cone must be associated with the magnetic cloud situated ~0.01 AU beyond the Earth early in the event. The local interplanetary magnetic field line suggested in Figure 6.7 passed very close to the cloud before reaching Earth. Particles gyrating around this field line with sufficiently large gyroradii interact with the cloud and therefore do not reach the Earth. This should produce a deficit region on the anti-sunward side of the particle arrival direction. Points on the boundary of the fitted ellipse have been converted to GSE coordinates and plotted in Figure 6.14 with the apparent particle arrival direction. This shows that a larger portion of the deficit region was located on the

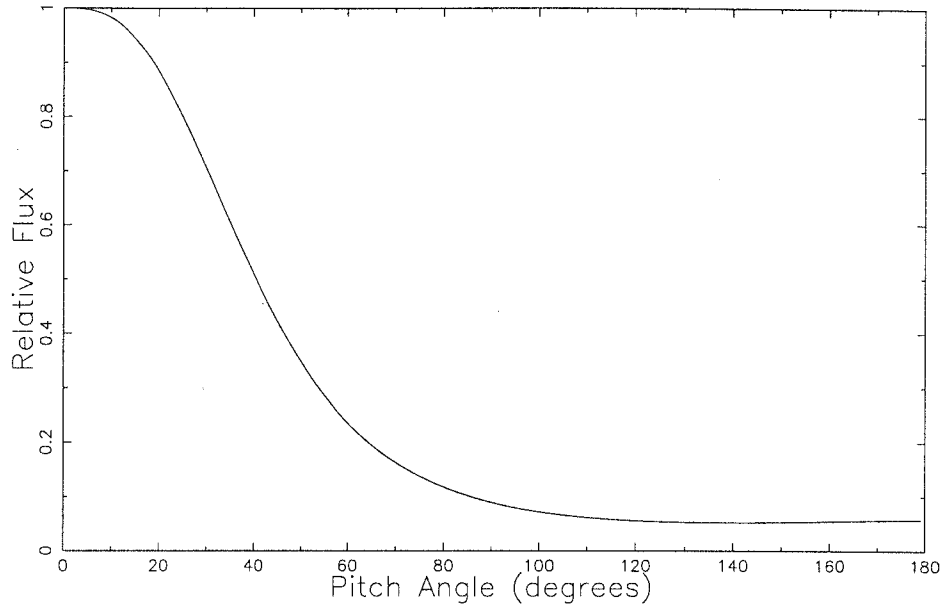

Figure 6.13: Fitted pitch angle distribution for 0000 UT, 8 December 1982 (Model 2).

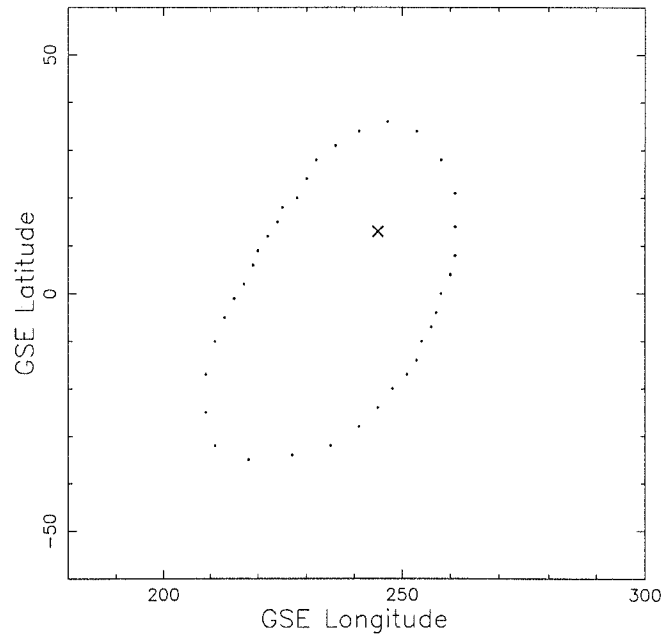

Figure 6.14: Points on the boundary of the deficit region plotted in GSE coordinates. The apparent particle arrival direction is indicated by the cross.

anti-sunward side of the arrival direction. The measured field direction was N14°, E253° in GSE coordinates which is a little closer to the edge of the deficit region.

The model described above is much simpler than the physical reality. Clearly the size and shape of the deficit region will depend on rigidity since it is, in part, the gyroradius of the particles which determines whether they pass close enough to the magnetic cloud to be deflected away from the Earth. It is probable that the deficit region would be smaller at low rigidities since these particles have smaller gyroradii and are therefore more likely to follow the field line to the Earth. In fact it is possible that at very low rigidities, the deficit region may be surrounded by a region where particles are scattered back towards the Earth. This has not been modelled and may account for the low calculated response at South Pole. The second major simplification is that the multiplicative factor applied inside the ellipse was constant over the whole region. This produces a 'well' with sharp edges which is not likely to occur in reality. Further elaboration of the model is not practicable given the number of extra parameters required and the small number of stations viewing the relevant region of space.

It may be expected that the effects of the magnetic cloud would still be evident at the later times for which results have been presented. By 0015 UT, the cloud had only moved a further ~0.002 AU away from the Earth. The strength of the field through which the particles were moving as they approached Earth was ~7–8 nT. The gyroradii of 1–3 GV particles in such a field is comparable to the distance through which the cloud has moved, so it is likely that fewer of these particles would interact with the magnetic cloud than at 0000 UT. Higher rigidity particles would still be affected, but to a lesser extent than before. It is possible that the steepening of the spectrum fitted for 0015 UT is a compensation for such a deficit at high rigidities. It should also be noted that a significant number of particles would be scattered back towards Earth from the vicinity of the cloud and these would rapidly fill the deficit cone.

6.3 16 February 1984

The 16 February 1984 GLE was not associated with any solar flare on the visible disc. During the preceding days the active regions 4408 and 4410 moved beyond the west limb and on 16 February were located approximately 40° and 10° respectively behind the limb. The presence of a flare was indicated by the observation of type III radio bursts followed by types II and IV. These have been associated with region 4408 (Chertok *et al.*, 1987). Microwave emission was also observed, but was much weaker than the microwave emission usually associated with events which produce GLEs. This is not surprising since the probable source region was located well behind the limb (Chertok *et al.*, 1987).

The type II emission began about 0900 UT and had a dynamic spectrum which exhibited an inverted U-shape indicative of shock wave propagation (Chertok *et al.*, 1987). The type IV emission began at 0858 UT, was delayed at low frequencies and was unpolarised. Both of these features can be explained by the location of the flare behind the limb (Zlobec *et al.*, 1987).

The onset of the GLE as determined by the 10-second South Pole data was at 0904 UT (Pomerantz *et al.*, 1984), only six minutes after the first observed radio emission. This indicates that there must have been an extremely rapid acceleration process near the start of the flare and the particles propagated to Earth within 14 minutes. This propagation time is extremely short for particles originating up to 70° from the nominal 'garden hose' footpoint. For this reason Filippov and Niskovskikh (1990) questioned the association of region 4408 with the GLE. They suggested that the particles may have been accelerated in region 4410, situated 5–10° behind the west limb. This would make the transport of particles to the Earth much easier as the footpoint of the 'garden hose' field line was about W88° (as determined by Bieber *et al.* from the solar wind speed). However it is thought that the characteristics of the radio emissions are more easily associated with region 4408 (Chertok *et al.*, 1987), so it is still necessary to investigate the possibility of particles propagating from this region. The geomagnetic field was relatively undisturbed with Kp values between 1 and 2 throughout the event.

The largest cosmic ray increase, of nearly 200% above background levels was observed at South Pole. The plots of cosmic ray profiles in Figure 6.15 show a short risetime (10–15 minutes) and a rapid decay. The short timescale over which the increase was observed is indicative of focused interplanetary transport as reflected by the large mean free path determined by several investigators (Bieber *et al.*, 1986; Debrunner *et al.*, 1988).

Belov *et al.* (1985) suggested a mechanism by which the particles accelerated near W140° may drift along the neutral sheet and gain access to the field line connected with the Earth. This involves the accelerated particles travelling along a field line which passed close to the neutral sheet, then drifting along the sheet until they pass close to the field line connected to Earth. From this point, they must propagate along the field line in order to be observed at Earth. The method of confinement to the neutral sheet is not explained. This must be considered in conjunction with information concerning the proximity of the field lines to the neutral sheet in order to justify this mechanism. Without further evidence it is difficult to evaluate the validity of this hypothesis.

Bieber *et al.* (1986) investigated the possibility of coronal diffusion of the particles away from the flare site. Their model used coronal diffusion and energy-dependent escape combined with focused interplanetary transport to reproduce the cosmic ray time profile. The derived pitch angle distribution in their analysis suggests a parallel scattering mean free path >2 AU. An impulsive injection of particles and such a large mean free path would result in a much narrower spike in the cosmic ray profile than is observed. This supports the coronal diffusion hypothesis.

Debrunner *et al.* (1988) also deduced that the scattering mean free path was >2 AU, however they proposed a different mechanism for the acceleration and release of the solar protons into the interplanetary magnetic field. They compared the arrival times of particles in different energy ranges and deduced that the 70 MeV – ~500 MeV particles arrived 4±2 minutes earlier than expected from fits to the arrival times of higher energy particles. This was interpreted to mean that the first low energy protons were accelerated earlier than the relativistic

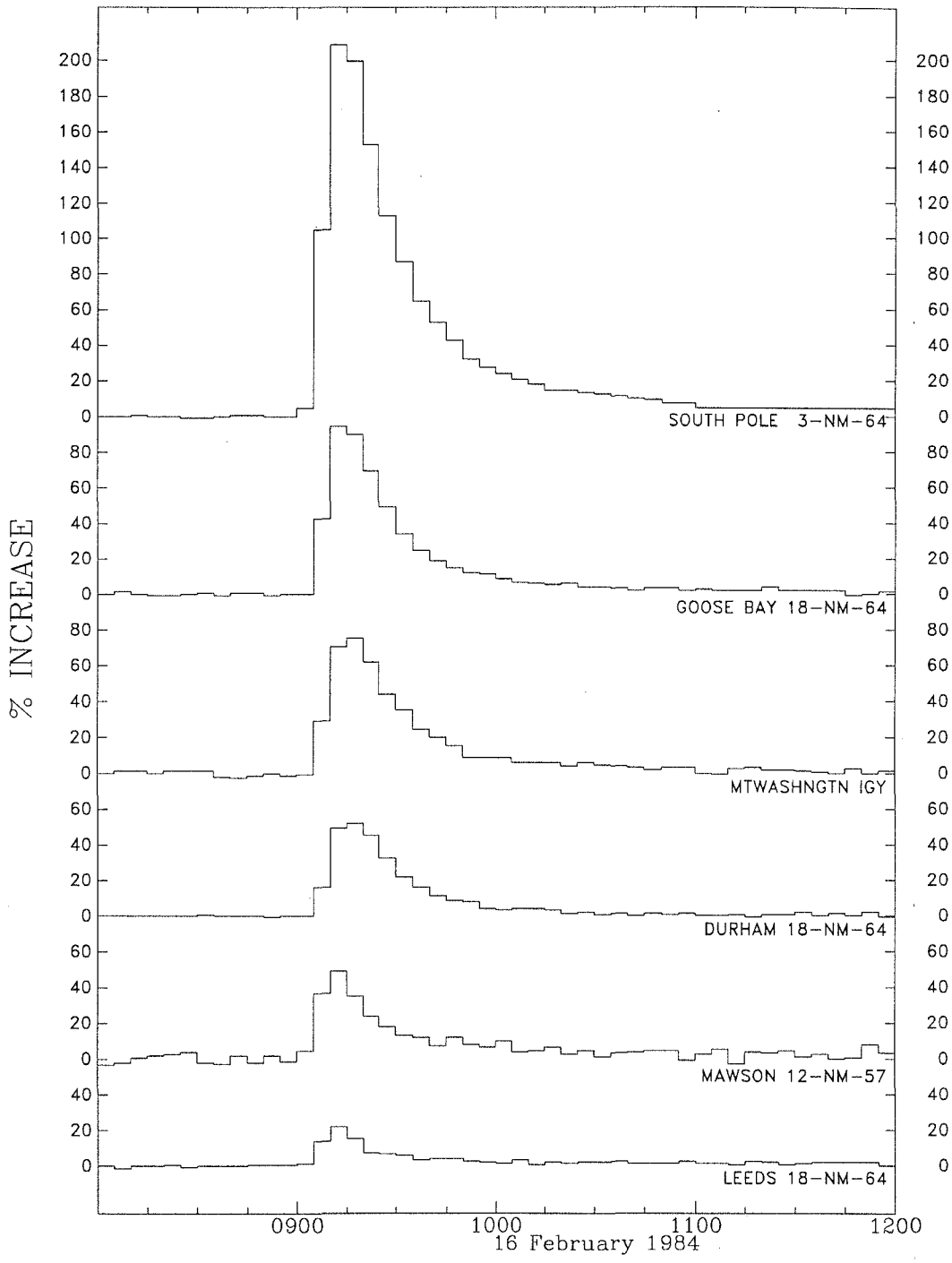

Figure 6.15: Cosmic ray increases at South Pole, Goose Bay, Mt. Washington, Durham, Mawson and Leeds neutron monitors between 0800 and 1200 UT on 16 February 1984.

protons. Thus the acceleration process must have been such that the time required to accelerate particles increased with energy. Debrunner *et al.* further observed that the duration of particle injection into the IMF was shorter at high energies. They attributed this to diffusive transport of particles near the acceleration region before release into the IMF.

Debrunner *et al.* concluded that the particle acceleration was not a δ-like process (as proposed by Bieber *et al.*), but that coronal shock acceleration was responsible. The presence of such a shock was indicated by the observation of type II radio emission. They proposed the following scenario to explain the observed features of the event: An explosive process at the flare site resulted in a shock wave which propagated radially outward through the corona. Expansion during propagation allowed the intersection of the shock with the footpoint of the IMF line connected to Earth ($\sim$40–50° from the flare site). Protons were accelerated by the shock, first to low energies, with the maximum energy increasing with time. As the shock continued to expand, it weakened and the diffusion coefficient in front of it increased. Thus the efficiency of the acceleration process decreased, producing energy dependence in the duration of particle injection. Debrunner *et al.* could not infer any specific model for the shock acceleration, however further investigations by Lockwood *et al.* (1990) indicated that the spectra were consistent with the diffusive shock acceleration model of Ellison and Ramaty (1985). The mechanism proposed by Debrunner *et al.* not only accounts for the observed particle spectra and energy dependent arrival times, but solves the problem of particle propagation from a flare site $\sim$40° beyond the west limb to the 'garden hose' field line.

6.3.1 Modelling the neutron monitor response

Analysis has been performed for two times near the maximum of the GLE (0910 and 0915 UT) and two times during the decay phase (0925 and 1000 UT). Each of these times is the start of a 5 minute period over which the cosmic ray data were averaged. The spectral form used in the model was a power law. An additional parameter to allow steepening of the spectrum with increasing rigidity was included, but found to be unnecessary. The pitch angle distribution function was of exponential form (as described in Section 3.4) without rigidity dependence.

The spectral slope and calculated particle fluxes are shown in Table 6.8. The slope of the spectrum did not change significantly through the event. Lockwood *et al.* (1990) fitted similar spectra for this GLE with a slope of –5.0 at 0917 UT and –5.2 at 0942 UT. They concluded that these spectra were consistent with those predicted by a diffusive shock acceleration model and indicate that stochastic acceleration of protons in the downstream region of the shock did not play a significant role.

The fitted pitch angle distributions are shown in Figure 6.16. These reveal a high degree of anisotropy superimposed on a small isotropic component. The axes of symmetry of these distributions are listed in Table 6.9 along with the measured interplanetary magnetic field directions from ISEE3 which was located $\sim$0.07 AU from the Earth at the time of this event. The discrepancy between the observed field direction and apparent particle arrival direction varies between $\sim$35° and

Table 6.8: Spectral parameters and calculated particle fluxes for the GLE of 16 February 1984. Fluxes in units of particles $(cm^2\ s\ ster\ GV)^{-1}$.

	γ	$J_{\|\|}$	J_{av}
0910 UT	–5.5	159.6	26.5
0915 UT	–5.5	154.5	25.7
0925 UT	–5.0	41.8	8.9
1000 UT	–5.5	15.5	4.8

$\sim$50° throughout the event. This is quite large and corresponds to intensities of less than half the peak in the pitch angle distribution. Debrunner *et al.* (1988) used a different modelling technique, but derived a very similar longitude (5° for 0907 UT) for the axis of symmetry of their pitch angle distributions to those derived in this analysis. The latitude derived by Debrunner *et al.* was –6° at 0907 UT, $\sim$30° further north than the latitude found to give the best fit in this model. The pitch angle distributions used by Debrunner *et al.* comprised four variable line segments, so were not very good representations of the physical situation. The distributions were extremely steep for pitch angles less than 7° throughout the event and much broader beyond 7°. Their method did not employ a least squares routine to determine the best fit parameters, but relied upon exploring parameter space 'by hand'. The chosen form of pitch angle distribution required six parameters. In addition to these, there were the latitude and longitude of the source direction and the spectral slope. Adjustment of nine parameters by hand is difficult and very time consuming, so it is quite possible that the derived solution was not optimal. These factors do not affect the general conclusions made by Debrunner *et al.* but are sufficient to explain the discrepancy found between the latitudes of the apparent particle arrival direction derived from the two models. The good agreement (within 5°) in the longitudes derived from the two different models suggests that the discrepancy between these and the measured field direction is not simply due to uncertainty in the parameters of the model. It is interesting to note that the derived particle arrival directions lie $\sim$40° west of the Sun-Earth line, close to the nominal 'garden hose' field direction, whereas the measured field direction was some 30–40° further west.

Table 6.9: Apparent particle arrival directions and measured field directions for the GLE of 16 February 1984.

	Fitted		Measured	
	Latitude	Longitude	Latitude	Longitude
0910 UT	–34	0	–13	326
0915 UT	–36	5	–9	318
0925 UT	–33	357	–9	341
1000 UT	–40	353	–14	326

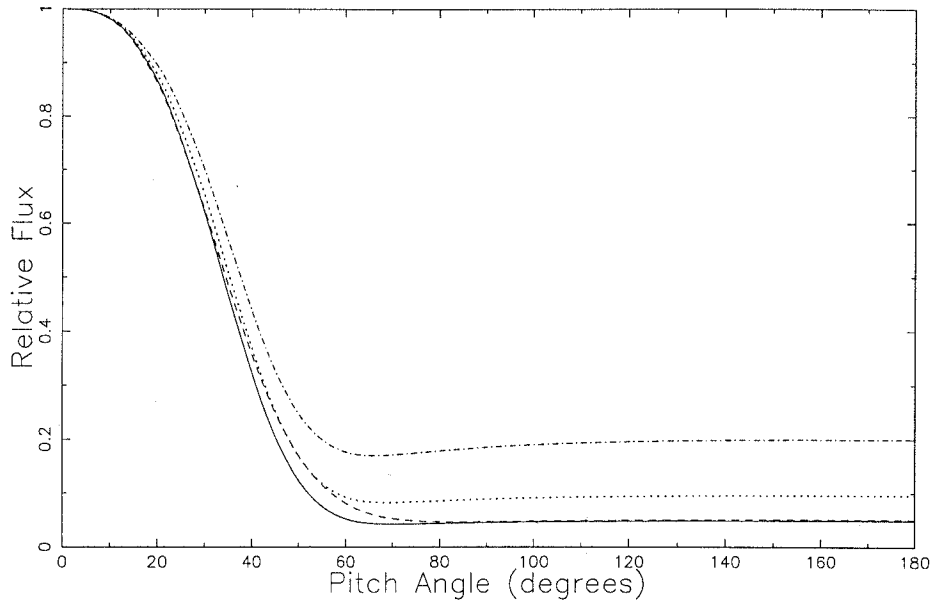

Figure 6.16: Pitch angle distributions at 0910 UT (solid line), 0915 UT(dashed line), 0925 UT (dotted line) and 1000 UT (dot-dash line) on 16 February 1984.

The calculated increases are shown in Tables 6.10 and 6.11 along with the observed increases (and Poisson errors) and the increases corrected to sea level pressure by the two attenuation length method. The flare attenuation length used in these corrections was 115 g cm^{-2}.

Bieber *et al.* (1986) derived a method of determining the scattering mean free path from the pitch angle distribution of particles arriving at the Earth. The method arises from the Boltzmann transport equation in the presence of isotropic pitch angle diffusion and adiabatic focusing. Bieber *et al.* derived an expression for the pitch angle distribution under steady state conditions which can be used as an approximation where steady state conditions do not apply. The equation, written as a function of μ (the cosine of the pitch angle) is

$$f = c_0 + c_1 B \exp\left(\frac{\lambda\mu}{\mathrm{L}}\right) \tag{6.1}$$

where c_0 and c_1 are constants, B is the magnetic field strength, L is the scale length of the interplanetary magnetic field and λ is the scattering mean free path. In a Parker spiral, at positions close to the ecliptic plane, L can be calculated from the angle, Ψ, between the magnetic field line and the radial direction (Bieber *et al.*, 1986). This expression is

$$\mathrm{L} = \frac{r}{\cos\Psi\,(1+\cos^2\Psi)} \tag{6.2}$$

where r is the radial distance from the Sun.

Bieber *et al.* (1986) and Debrunner *et al.* (1988) used Equation 6.1 to determine λ from their derived pitch angle distributions. Both papers report that λ was

Table 6.10: Increases at 0910 UT and 0915 UT, 16 February 1984, normalised to Goose Bay.

	0910 UT			0915 UT		
Station	Actual %	Corrected %	Calculated %	Actual %	Corrected %	Calculated %
Alert	0.3±0.6	0.3	8.4	2.5±0.6	2.5	8.7
Apatity	10.3±0.6	10.3	7.9	11.8±0.6	11.8	8.3
Deep River	71.9±0.4	71.9	85.8	65.4±0.4	65.4	81.7
Durham	49.0±0.7	49.0	55.0	51.9±0.7	51.9	49.4
Goose Bay	94.6±0.6	93.7	93.7	89.7±0.6	88.8	88.8
Hobart	11.1±3.4	11.0	10.7	15.6±3.4	15.4	10.6
Inuvik	1.5±0.6	1.5	8.5	4.3±0.6	4.3	8.9
Irkutsk	3.5±0.6	3.3	3.4	3.4±0.6	3.2	3.1
Kerguelen Island	11.0±0.6	11.0	8.6	10.8±0.6	10.8	9.4
Khabarovsk	0.1±1.1	0.1	1.1	0.6±1.1	0.6	1.0
Kiev	1.5±0.7	1.5	2.8	0.7±0.7	0.7	2.7
Leeds	21.7±0.6	21.7	6.5	15.4±0.6	15.4	6.8
Lomnicky Stit	3.7±0.3	3.0	2.8	3.0±0.3	2.5	2.1
Magadan	11.3±0.7	10.8	7.7	12.4±0.7	11.9	6.8
Mawson	49.4±2.5	46.9	47.1	35.6±2.5	33.8	29.5
McMurdo	0.8±0.5	0.8	13.5	3.5±0.5	3.3	10.6
Moscow	5.9±0.7	5.8	5.1	5.9±0.7	5.8	7.0
Mt. Washington	70.7±1.0	53.7	66.6	75.1±1.0	57.1	59.9
Mt. Wellington	16.0±0.7	14.1	10.8	16.9±0.7	14.9	11.0
Newark	45.5±0.9	45.5	37.1	42.8±0.9	42.8	32.4
Novosibirsk	3.6±1.4	3.6	5.2	6.7±1.4	6.6	6.6
Oulu	15.2±0.8	15.2	7.8	14.9±0.8	14.9	8.3
Potchefstroom	0.1±0.9	0.1	0.7	1.7±0.9	1.4	0.7
Rome	1.8±0.8	1.8	0.7	1.8±0.8	1.8	0.6
South Pole	208.8±0.3	131.5	125.7	199.1±0.3	125.4	120.2
Terre Adelie	5.0±0.8	4.8	7.7	6.0±0.8	5.8	8.1
Thule	8.6±0.8	8.5	8.2	17.6±0.8	17.4	8.6
Tixie Bay	0.0±0.9	0.0	8.6	16.3±0.9	0.6	8.9
Tsumeb	1.4±0.4	1.1	0.4	0.8±0.4	0.6	0.3
Turku	21.8±1.2	21.8	9.2	16.3±1.2	16.3	10.1
Σ variances from corrected %			1345.9			943.1

Table 6.11: Increases at 0925 UT and 1000 UT, 16 February 1984, normalised to Goose Bay.

	0925 UT			1000 UT		
Station	Actual %	Corrected %	Calculated %	Actual %	Corrected %	Calculated %
Alert	6.2±0.6	6.1	7.1	4.3±0.6	4.3	3.0
Apatity	10.3±0.6	10.3	6.8	3.3±0.6	3.3	2.9
Deep River	36.9±0.4	36.9	43.6	7.3±0.4	7.3	8.8
Durham	32.4±0.7	32.3	29.1	3.2±0.7	3.2	5.3
Goose Bay	44.7±0.6	44.3	44.3	8.7±0.6	8.6	8.6
Hobart	9.6±3.4	9.5	8.5	2.2±3.4	2.2	2.8
Inuvik	5.0±0.6	5.0	7.2	2.6±0.6	2.6	3.1
Irkutsk	1.4±0.6	1.3	3.5	0.6±0.6	0.6	0.8
Kerguelen Island	6.4±0.6	6.4	7.1	2.1±0.6	2.1	3.1
Khabarovsk	1.8±1.1	1.8	1.3	2.9±1.1	2.8	0.3
Kiev	0.8±0.7	0.8	3.4	0.0±0.7	0.0	0.8
Leeds	6.7±0.6	6.7	5.2	1.6±0.6	1.6	1.7
Lomnicky Stit	2.8±0.3	2.3	2.5	0.8±0.3	0.7	0.7
Magadan	7.7±0.7	7.4	6.6	2.6±0.7	2.5	2.2
Mawson	17.8±2.5	16.9	12.2	9.7±2.5	9.2	3.5
McMurdo	8.2±0.5	7.8	8.5	6.3±0.5	6.0	4.2
Moscow	4.1±0.7	4.0	5.6	2.0±0.7	2.0	1.7
Mt. Washington	44.2±1.0	33.6	34.3	8.9±1.0	6.8	6.2
Mt. Wellington	11.3±0.7	9.9	8.3	3.3±0.7	2.9	2.8
Newark	24.2±0.9	24.2	21.5	3.0±0.9	3.0	3.9
Novosibirsk	1.7±1.4	1.7	4.8	1.0±1.4	1.0	1.4
Oulu	8.9±0.8	8.9	6.7	2.8±0.8	2.8	2.9
Potchefstroom	3.0±0.9	2.4	0.9	0.0±0.9	0.0	0.2
Rome	0.0±0.8	0.0	0.9	0.5±0.8	0.5	0.2
South Pole	112.9±0.3	71.1	62.4	23.7±0.3	14.9	14.5
Terre Adelie	4.5±0.8	4.3	6.5	4.2±0.8	4.0	2.7
Thule	14.7±0.8	14.6	7.3	5.6±0.8	5.5	3.0
Tixie Bay	1.8±0.9	1.8	7.3	2.9±0.9	2.9	3.1
Tsumeb	0.8±0.4	0.6	0.5	0.7±0.4	0.5	0.1
Turku	14.6±1.2	14.6	7.0	4.5±1.2	4.5	2.9
Σ variances from corrected %			372.7			65.9

Table 6.12: Calculated scattering mean free paths (λ) based on the angle (Ψ) between the apparent particle arrival direction and the radial direction for the GLE of 16 February 1984.

	λ	Ψ
0910 UT	5.0	46
0915 UT	5.0	41
0925 UT	5.4	45
1000 UT	4.4	42

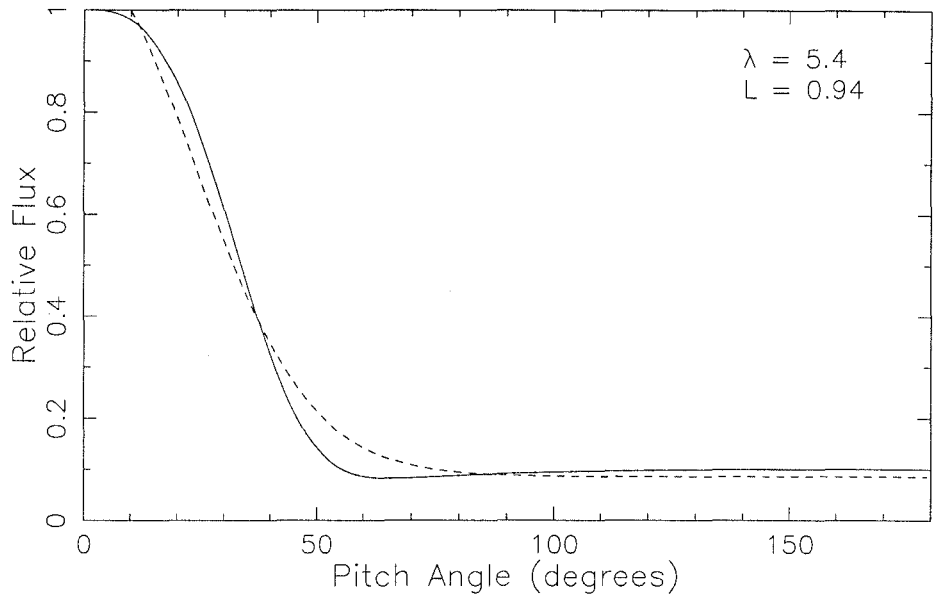

Figure 6.17: Derived pitch angle distribution for 0925 UT (solid line) and function (dashed line) fitted to determine the scattering mean free path for the GLE of 16 February 1984.

greater than 2 AU, however they note that steady state conditions were only marginally (at best) satisfied. Table 6.12 shows the values of λ determined by fitting Equation 6.1 to the pitch angle distributions shown in Figure 6.16. In each case the value of L was calculated using the angle between the radial direction and the apparent particle arrival direction. Figure 6.17 shows an example of the quality of the fit. The agreement is reasonable and possibly better than that shown by Debrunner *et al.* where the steep section of the distribution for pitch angles $<7°$ is not fitted at all well. The calculated values of λ are consistent with the findings of Bieber *et al.* and Debrunner *et al.*

The determination of λ from the derived pitch angle distributions is very sensitive to the choice of Ψ. If the Ψ values corresponding to the measured field direction are used, the value of λ increases by up to an order of magnitude. This is unreasonable and reflects the fact that the field must be significantly distorted from the nominal Parker spiral if the local field direction is up to 80° west of the Sun-Earth line. The equation for L is not valid under these conditions. The variation in λ through the event confirms that steady state conditions were not

satisfied, hence the calculated mean free paths are upper bounds on the actual value of λ.

6.4 Summary

The results presented in this chapter have revealed the importance of limiting the number of assumptions made in modelling so that unusual features can be studied. In each case, the interplanetary magnetic field directions measured at near-Earth satellites were available, however the particle arrival directions were not tied to these directions in the least squares analysis. Without these IMF data, satisfactory explanation of some features of the particle propagation in the first two events would not have been possible. The field data also reveal an as yet unexplained particle propagation direction for the third of the events discussed in this chapter. Without the field data, a nominal field would have been assumed and good agreement obtained with the derived particle arrival directions. These results underline the extreme importance of measured interplanetary magnetic field directions for full interpretation of particle propagation. These data have unfortunately become rather sparse in recent years, limiting the study of some events discussed earlier in this thesis.

The particle arrival directions and pitch angle distributions for the 12 October 1981 GLE reveal bi-directional flow. This is consistent with the conclusions of Richardson *et al.* (1991) who explained satellite observations by the presence of a looped field structure allowing propagation of particles from the eastern side of the Sun. The results presented in Section 6.1 show that their hypothesis is also consistent with higher energy particle data. The particles observed at ground level initially arrived from the west, but following the development of bi-directional flow, the primary arrival direction was from the east. This was earlier than the bi-directional flux observed with satellite instruments, but may be accounted for by consideration of the different propagation characteristics of the two energy regimes.

The GLE of 7-8 December 1982 had several distinct maxima observed at different stations. The later parts of the event can be satisfactorily modelled with a small degree of anisotropy and power law spectra. The particle arrival directions are consistent with the measured interplanetary magnetic field directions. At the time when the first stations reached maximum intensity, the observed increases cannot be reproduced by the usual model. The presence of a magnetic cloud $\sim$0.01 AU beyond the Earth results in a lower increase for stations viewing the region of space on the anti-sunward side of the interplanetary magnetic field line. This has been modelled using an elliptical deficit region near the particle arrival direction. The slow rise in intensity at Apatity and Oulu can only be modelled satisfactorily when the effects of the magnetic cloud are taken into account.

Finally, the 16 February 1984 GLE has been modelled with pitch angle distributions exhibiting a high degree of anisotropy and a small isotropic component. The derived particle arrival direction lies some 35°–50° from the measured interplanetary magnetic field direction. The reason for this is not understood, but

the results are consistent with those derived by Debrunner *et al.* (1988) using a different modelling technique.

The next chapter presents a discussion of the confidence limits on the derived parameters of the models presented in the Chapters 4, 5 and 6. The form of the derived spectra are also discussed and compared with the Ellison and Ramaty shock acceleration spectral form. Calculations of scattering mean free paths are presented for several of the events modelled. Further improvements to the model are discussed, including atmospheric depth corrections, yield functions and alternate forms for the pitch angle distribution.

Chapter 7

Discussion

This chapter presents a discussion of results, their significance and possible further work. The first section outlines the difficulties experienced with determining confidence limits on the derived parameters. These are due to the non-linearity of the model, combined with the strong dependence of some parameters on others.

Section 7.2 includes a discussion of spectral forms. The derived power law and modified power law spectra are compared with the Ellison and Ramaty (1985) shock acceleration spectral form. This form is preferable due to its basis in the theory of particle acceleration.

The Bieber *et al.* (1986) method for calculating the scattering mean free path discussed in Section 6.3 is again employed in the third section of this chapter. The calculation has been applied to the pitch angle distributions derived for events which occurred when interplanetary magnetic field conditions were close to nominal.

Atmospheric cutoffs are addressed in Section 7.4, in particular the lower cutoff at the South Pole neutron monitor due to its high altitude. This leads to a discussion of yield functions which is continued in the fifth section. Possible refinements to the pitch angle distribution are also considered along with the treatment of particles back-scattered from beyond the Earth.

7.1 Confidence limits on parameters

It is reasonable to expect that the use of a least squares technique to determine best fit parameters should also allow the determination of confidence limits on the derived parameters. In the case of a non-linear model (such as that used here), error analysis is more difficult. The individual confidence limits for each parameter determined in the least squares routine described in Section 3.3 are approximate 95% confidence limits based on a linear hypothesis (*i.e.* assuming the model to be linear) when all other parameters are ignored. In general the uncertainties obtained by this procedure were very large, in some cases as large as the parameter itself. Clearly the main assumptions in the error calculation are invalid. Firstly, the model is highly non-linear in all parameters. Secondly, ignoring all other parameters assumes that each parameter is independent of the others. This is also far from the truth. It is easy to see that the parameters

which define the shape of the pitch angle distribution will depend on the axis of symmetry (latitude and longitude) of the distribution. The spectral exponent is clearly dependent on any 'change of slope' parameter (in the case of the modified power law or the modified Ellison and Ramaty type spectral forms). The spectrum will also depend on the particle arrival direction and pitch angle distribution due to the rigidity dependence of viewing directions.

It may be possible to determine approximate confidence limits for the parameters by considering contours in χ^2 over a range of parameter values. If errors are distributed normally, a value, $\Delta\chi^2$, can be determined which is the difference between the minimum in χ^2 and the value of χ^2 at a chosen confidence level (*e.g.* 68%, 90% etc.) (Press *et al.*, 1989). There are two problems with this. Firstly it is not known whether the errors follow a normal distribution. If this is not so, the derived confidence limits may still be approximately correct. Secondly, the determination of $\Delta\chi^2$ requires the number of degrees of freedom of the problem. On the surface, this may not seem to present any difficulties as it is usual to define the degrees of freedom as the number of data points minus the number of fitted parameters. The data points used in this GLE model are the observed increases in count rate at each cosmic ray detector. It is important to recognise that the response at each instrument is made up of the sum of the responses at all rigidities, each of which represents a different viewing direction in space. While the contribution from individual rigidity ranges is not available, it still remains that the response at each instrument results from a range of viewing directions and rigidities, thus placing much more significant limits on the parameters than would be achieved from a single data point. For this reason, the true number of degrees of freedom is believed to be larger than the number of observations minus the number of fitted parameters, however it is unclear how to determine its value. Without this information it is not possible to calculate $\Delta\chi^2$ and hence determine confidence limits for the parameters.

It would appear that a rigorous error analysis is not possible, however some attempt to estimate the errors can be made by observing the significance of changing the parameter values in the model. It is only practical to consider one parameter at a time while fixing the values of all other parameters. Allowance must be made for this in the estimation, to account for improvements in the fit by re-evaluation of the other parameters for the new value of the parameter in question.

The errors in the derived latitude and longitude of the particle arrival direction are strongly dependent on the degree of anisotropy. Figure 7.1 shows two pitch angle distributions derived for models presented earlier (1805 UT on 22 October 1989 and 2010 UT on 24 October 1989). Clearly, a $\sim 10^\circ$ change in the axis of symmetry would make a large difference in the calculated response using the highly anisotropic distribution whereas such a change would be less significant for the other model. Table 7.1 shows the effect on the sum of squares of differences between calculated and actual increases for the two models when the latitude and longitude are varied. Example 1 is 1805 UT, 22 October 1989 and Example 2 is 2010 UT, 24 October 1989. The sum of squares is not comparable between the two models, however the change in its value for each model gives a measure of the significance of the change in the parameters. It is estimated that the errors in the

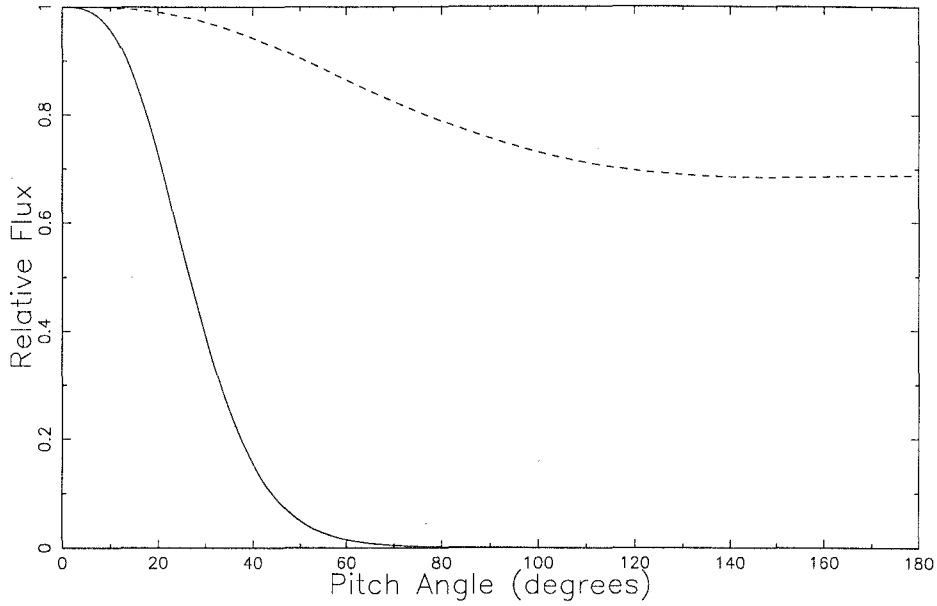

Figure 7.1: Pitch angle distributions determined for 1805 UT, 22 October 1989 (solid line) and 2010 UT, 24 October 1989 (dashed line).

Table 7.1: Sum of squares for different latitudes and longitudes in the two models (see text).

	Example 1	Example 2
Minimum sum	35	460
$\pm 3°$ in Latitude	290	500
$\pm 3°$ in Longitude	150	500
$\pm 30°$ in Latitude	50000	1100
$\pm 30°$ in Longitude	50000	900

derived latitude and longitude for 1805 UT on 22 October 1989 are approximately $\pm 3°$ while for 2010 UT on 24 October 1989 the errors may be as large as $\pm 30°$. The errors in the latitude and longitude of the particle arrival direction for most other models will lie between these values (with the exception of those events with almost isotropic distributions) depending on the degree of anisotropy.

The estimated errors in the parameters of the two example models are tabulated in Table 7.2. The pitch angle distributions in each of these models were defined by two parameters. While these are not completely independent, the first has most effect on the width of the distribution and the second on the height of any isotropic component. The error in the width of the pitch angle distribution for Example 1 was estimated at half the height of the curve. The pitch angle distribution in Example 2 had a significant isotropic component so the width was measured at the half height of the non-isotropic part (0.85). The error on the height of the isotropic component of this distribution was also estimated.

The spectrum in Example 1 was a power law in rigidity. This model is dominated by the degree of anisotropy in the pitch angle distribution which restricts

Table 7.2: Estimated error on parameters for 1805 UT, 22 October 1989 (Example 1) and 2010 UT, 24 October 1989 (Example 2).

		Example 1		Example 2	
Pitch Angle Distribution	Latitude	−50°	±3°	−33°	±30°
	Longitude	264°	±3°	175°	±30°
	Width	27°	±5°	63°	±20°
	Height			0.7	±0.05
Spectrum	Slope	−5.8	+1.3, −0.5	−4.2	±0.5
	Change of Slope			5.3	±1.0

the response to a small group of stations viewing the appropriate region of space. These stations all have similar cut-off rigidities (up to ~2 GV) so the spectrum is not well determined. The spectrum in Example 2 was of the modified Ellison and Ramaty form. The two parameters defining this spectrum are highly dependent upon each other, however the errors quoted in Table 7.2 for each of the parameters are based on the other parameter holding a fixed value. It should be noted that the validity of the derived rigidity spectrum is highly dependent on the choice of stations used in the model. One example of this is the model for the 12 October 1981 GLE. The inclusion of Jungfraujoch (which did not record a significant increase) was essential to correctly determine the spectrum. Without this station (cutoff ~5 GV), the derived spectral index for some of the times modelled was very close to zero. This emphasises the importance of including null observations in the analysis as the model should predict zero responses as well as reproducing the increases at other stations.

The two models discussed in this section represent extreme cases in the size of the estimated uncertainties in derived parameters. The high degree of anisotropy at 1805 UT on 22 October 1989 led to small errors in the latitude and longitude of the particle arrival direction, while the much broader distribution derived for 2010 UT on 24 October 1989 resulted in much larger errors. The error on the power law exponent of the rigidity spectrum for Example 1 is probably as large as any expected for other models, due to the dominance of the anisotropy. Most other models presented have included a sufficient range of geomagnetic cutoffs for the spectral slope to be well determined. It is expected that the spectra which include a change of slope parameter will result in parameters with larger uncertainties than those with a single parameter. This will occur because of the dependence of the two parameters on each other. The general form of these spectra and their average slope should be fairly accurate.

7.2 Spectral form

Various spectral forms have been used by different investigators when modelling GLEs. The most common are power laws and exponential functions in rigidity. Examples of exponential forms can be found in Smart *et al.* (1971; 1979) and

Shea and Smart (1982), while Duggal *et al.* (1971) employed a power law when analysing the same event as Shea and Smart.

Smart and Shea (1990) and Smart *et al.* (1987) found that a pure power law predicted too large a response at high cutoff stations, so modified the function to incorporate a steepening with increasing rigidity. This spectral form has been used in many of the analyses presented in this thesis. Humble *et al.* (1991) used an average of the modified power law and an exponential function in their analysis.

While these spectral forms are convenient to use, they do not have a clear basis in theory (although power law spectra can result from shock acceleration under some conditions). The shape of the particle spectrum should be determined by the acceleration process. Ellison and Ramaty (1985) investigated the effect of a shock of infinite size interacting with particles for an infinite time. The resulting spectrum can be approximated by a power law in rigidity with exponent $-\gamma - (1 - \beta^2)$, where β is the ratio of particle speed to the speed of light and γ is a variable parameter. A non-infinite shock interacting for a finite time will produce a particle spectrum which falls off more rapidly with increasing rigidity. One attempt to model this is a power law with exponent $-\gamma - (1 - \beta^2)(1 + \delta\gamma)$, where $\delta\gamma$ is an additional parameter (D.F. Smart, private communication). This form was found to give a good fit to the observed data for the 24 October 1989 GLE (see Section 5.3.1).

Most of the analyses presented in this thesis were completed before the introduction of the Ellison and Ramaty type spectra into the model. These events were modelled with either power law or modified power law spectra. A comparison of the derived spectra with the Ellison and Ramaty and modified Ellison and Ramaty forms has been made to investigate the validity of the shock acceleration spectrum in these events.

The modified Ellison and Ramaty spectral form was fitted to the derived spectra for each event, using a least squares routine. This also allows for the result to be a pure Ellison and Ramaty spectrum, as the modified form reduces to the pure form when $\delta\gamma \rightarrow 0$. Most of the power law spectra were well fitted over the rigidity range 1–$\sim$5 GV by the Ellison and Ramaty form with the same value of γ as the power law. The fit was better for steeper spectra. Examples are shown in Figure 7.2. The rigidity range over which there is good agreement between these spectral forms is the best determined part of the spectrum in the GLE model due to the large number of stations with geomagnetic cutoffs between 1 and 5 GV. This indicates that in many cases a satisfactory fit to the observed neutron monitor data could probably be obtained by replacing the power law spectrum with the Ellison and Ramaty spectrum. The most significant difference between the power law and the Ellison and Ramaty spectral forms will be at rigidities below 1 GV. In this rigidity range the Ellison and Ramaty spectrum is flatter than the power law. It is therefore necessary to consider lower energy particle data to assess the validity of the two spectral forms over the full range of energies present in these particle events.

The modified power law spectra were best fitted by the modified Ellison and Ramaty spectral form. Some of these gave excellent fits over the whole range of rigidities considered. Such examples are shown in Figure 7.3. These spectra could

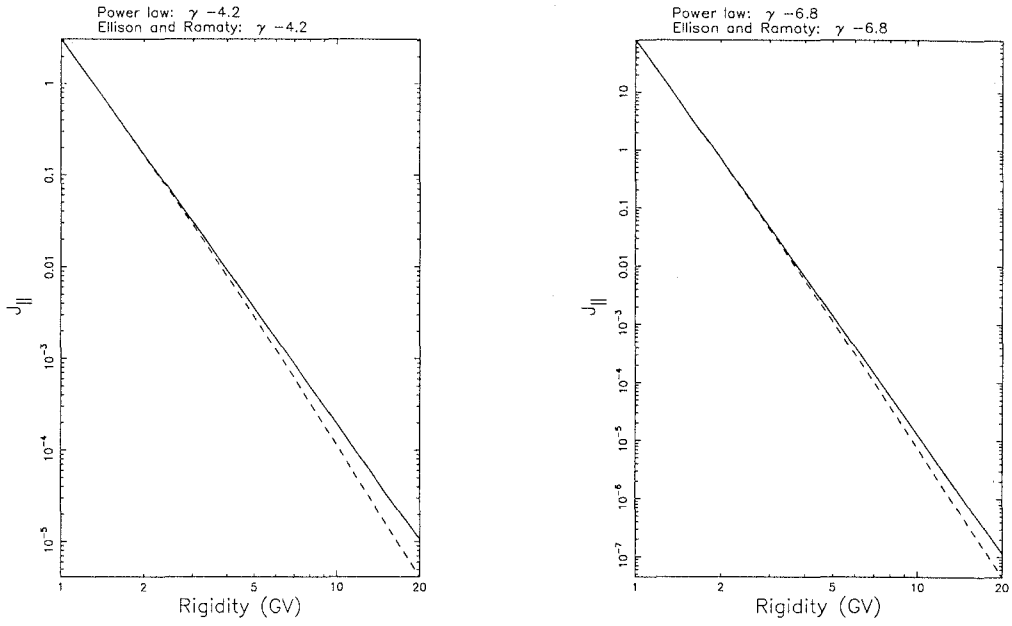

Figure 7.2: Comparison of derived power law spectra (solid lines) for 0715 UT, 12 October 1981 (left) and 1825 UT, 19 October 1989 (right) with Ellison and Ramaty shock acceleration spectra (dashed lines).

clearly be interchanged with very little effect on the neutron monitor increases predicted by the models. Two further examples are shown in Figure 7.4. In each case there is a serious discrepancy between the two spectral forms for rigidities between 1 and 2 GV. These modified power law spectra had the largest change of slope of any of the derived spectra. The spectrum on the left was determined for 0015 UT on 8 December 1982 when the arriving particles may have been affected by the presence of a magnetic cloud-like structure near the Earth. This may be the cause of the significant steepening of the derived spectrum (as discussed in Section 6.2.1). The power law spectra derived for later times in this event were in reasonable agreement with the Ellison and Ramaty spectral form between 1 and 5 GV. The spectrum on the right of Figure 7.4 is that derived for 1215 UT on 29 September 1989. The results presented in Section 4.3 indicate that the high rigidity particles may have had easier access to the 'garden hose' field line early in this event. This is probably responsible for the flattening of the spectrum at low rigidities. The spectra derived for later times in the event exhibited much less steepening with rigidity. The modified Ellison and Ramaty form provides excellent agreement with the spectrum at 1325 UT and the Ellison and Ramaty form is in reasonable agreement with the spectrum at 1600 UT.

The functional approximations of the Ellison and Ramaty type shock acceleration spectra allow convenient use of a spectral form which is based on a realistic theoretical understanding of particle acceleration. The derived spectra for most of the events presented in this thesis have been found to be consistent with these spectral forms. Further evaluation of these spectral forms should incorporate lower

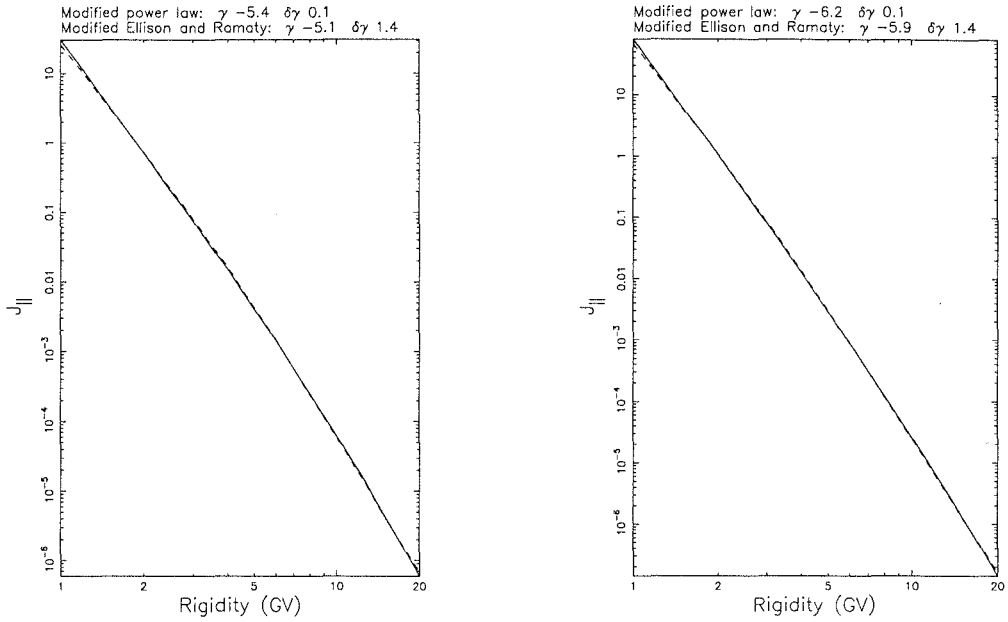

Figure 7.3: Comparison of derived modified power law spectra (solid lines) for 1820 UT (left) and 1840 UT (right) on 22 October 1989 with modified Ellison and Ramaty shock acceleration spectra (dashed lines).

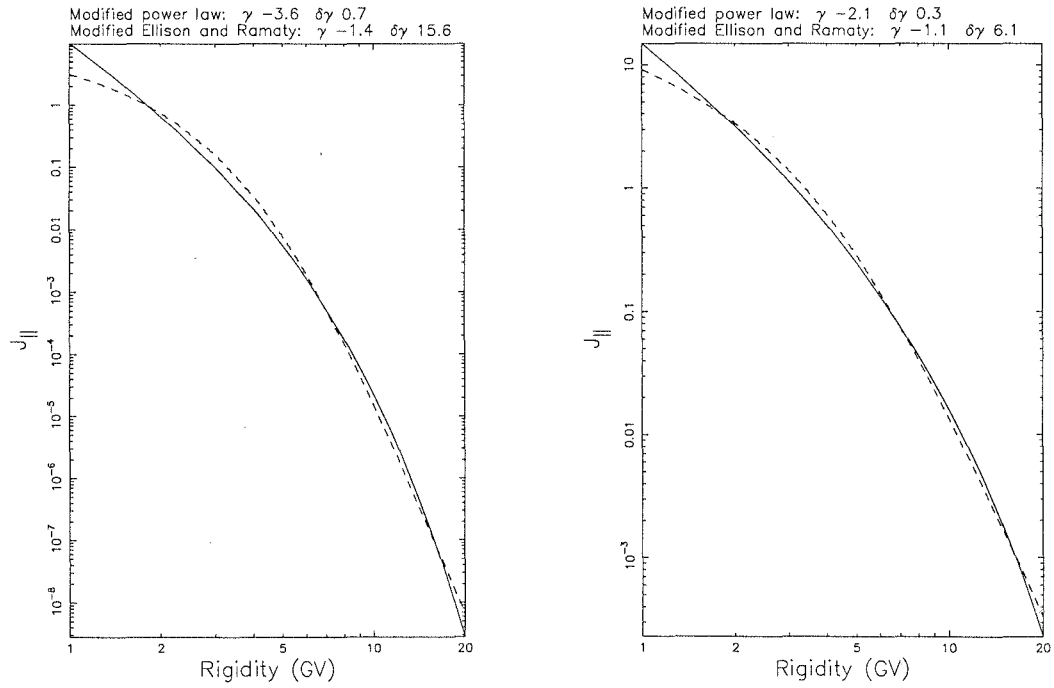

Figure 7.4: Comparison of derived modified power law spectra (solid lines) for 0015 UT on 8 December 1982 and 1215 UT on 29 September 1989 with modified Ellison and Ramaty shock acceleration spectra (dashed lines).

energy particle data as the change in slope is most significant below a few GeV.

7.3 Scattering mean free path

The method described in Section 6.3 for calculating the scattering mean free path, λ, only applies under steady state conditions. This means that in order for the calculation to be meaningful, the particle injection must continue long enough for the first particles to be scattered while other particles are still being injected (*i.e.* the time taken to travel ~two mean free path lengths). In the case of 16 February 1984, steady state conditions were perhaps only marginally achieved (Bieber *et al.*, 1986; Debrunner *et al.*, 1988). The calculated values of λ varied throughout the event and represent an upper bound to the true value. If steady state conditions are achieved, there should be a period where the degree of anisotropy is relatively constant. Prior to this, the calculated values of λ will be larger than the true value. After particle injection has ceased, isotropy will be approached and the calculated values of λ will be smaller.

Calculation of λ by this method also relies upon the interplanetary magnetic field configuration being the normal Archimedean spiral. This is assumed in the equation used to calculate L, the scale length of the magnetic field. Several of the GLEs discussed in this thesis occurred when the field was significantly distorted. In such cases the value of L cannot be calculated from Equation 6.2.

The interplanetary magnetic field configurations during the 12 October 1981 and 7–8 December 1982 GLEs were significantly distorted so no attempt has been made to determine the scattering mean free paths for these times. The results for 16 February 1984 were presented and discussed in Section 6.3. The 'garden hose' angle (inferred from the apparent particle arrival direction) at 1215 UT on 29 September 1989 was ~100°, so L could not be determined for this time. Later in the event, the particle arrival direction moved closer to the Sun-Earth line, however the estimated errors were quite large due to the broad pitch angle distributions. The particle anisotropies at 1325 and 1600 UT indicate $\lambda \simeq 0.5$ AU, however steady state conditions may not apply at these times. This is probably a lower limit on the true value of λ.

The scattering mean free path on 19 October 1989 cannot be determined for the particle population which arrived from east of the Sun-Earth line. An upper bound for λ can be calculated from the pitch angle distribution derived for 1305 UT which was centred on the local interplanetary magnetic field line. Clearly, steady state conditions do not apply at this time. A fit to this distribution results in $\lambda < 3.8$ AU for a 'garden hose' angle of 19° inferred from the axis of symmetry of the distribution.

The derived particle arrival directions for 1805 and 1820 UT on 22 October 1989 were slightly east of the Sun-Earth line, so L could not be calculated. The values of the 'garden hose' angle, Ψ, (inferred from the particle arrival direction) and calculated values of λ for later times in the event are shown in Table 7.3. The values of λ were based on the 'forward' section of the pitch angle distributions with the enhanced back-scatter ignored. The first few values are fairly constant at

Table 7.3: Inferred 'garden hose' angle, Ψ, and calculated scattering mean free paths for 22 October 1989.

	Ψ	λ (AU)
1830 UT	4°	1.1
1840 UT	6°	1.2
1850 UT	12°	1.2
1900 UT	12°	1.1
1910 UT	16°	1.0
1920 UT	20°	0.8

around 1.1 AU with later calculations indicating that particle injection had ceased and the distributions were approaching isotropy. These results indicate that the scattering mean free path was ~1.1 AU at the time of this event.

Values of Ψ and λ determined for 24 October 1989 are shown in Table 7.4. The determination of λ for 1910 UT was very sensitive to the size of Ψ. Clearly $\Psi = 82°$ indicates some distortion in the magnetic field structure so the calculation may not be valid. It is also important to consider the confidence limits on Ψ. The pitch angle distribution at this time was relatively broad, so the errors in the derived particle arrival direction may have been large. This introduces a fairly large uncertainty in the calculated λ and this also applies to the values determined for later times. Regardless of this, there is a significant change in λ between 2100 and 2130 UT indicating that this may be the point at which steady state conditions ceased to apply. The earlier values of λ indicate that the scattering mean free path was probably ~0.5–1.0 AU.

Table 7.4: Inferred 'garden hose' angle, Ψ, and calculated scattering mean free paths for 24 October 1989.

	Ψ	λ (AU)
1900 UT	82°	2.5
2010 UT	43°	0.9
2025 UT	45°	0.3
2100 UT	39°	0.6
2130 UT	14°	0.004

The method of Bieber *et al.* (1986) provides a convenient way to determine scattering mean free paths from derived particle pitch angle distributions, however it is reliant on the presence of a normal interplanetary magnetic field configuration and the existence of steady state conditions. The first of these conditions may be overcome by the determination of $\frac{1}{B}\frac{\delta B}{\delta z}$ (required for the calculation of L) for the particular field configuration, but this requires more information about the field than is usually available. It is often difficult to determine whether steady state conditions apply. It is probable that steady state conditions were achieved

during the 22 and 24 October 1989 GLEs. In these cases the value of λ can be determined with reasonable confidence, although the errors in the apparent particle arrival directions introduce some uncertainty. The results presented for other events serve only to place bounds on the size of λ.

7.4 Atmospheric cutoff

Throughout the analyses presented in this thesis, the atmospheric cutoff rigidity has been assumed to be 1 GV. The effective atmospheric cutoff for sea level stations can be estimated from a log-log plot of enhancement against effective geomagnetic cutoff rigidity for an isotropic particle distribution (McCracken, 1962). It has been shown that for the five minute interval beginning at 1825 UT on 19 October 1989, the particle distribution was isotropic (see Section 5.1). Figure 7.5 shows the recorded increases for this interval (corrected to sea level pressure by the two attenuation length method) plotted against the magnetic cutoff rigidity of the stations. It can be seen that there is an approximately linear turn-off of intensity for stations with cutoff above ~1 GV. A linear fit to these data is shown as well as the average of the data points for stations with cutoff below the atmospheric cutoff. The point at which these two lines intersect defines the effective atmospheric cutoff rigidity, P_{atm}. These results identify the value as 1.1 GV, so for stations at sea-level, the assumption of $P_{atm} = 1$ GV is adequate. For high altitude stations with low geomagnetic cutoff (such as South Pole) the atmospheric cutoff will be lower.

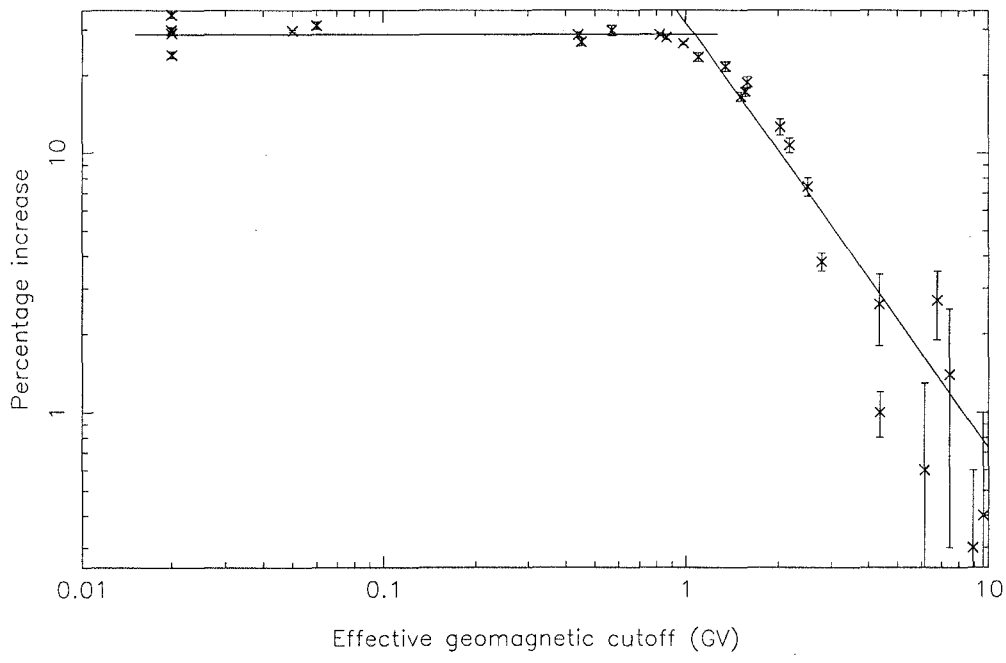

Figure 7.5: Percentage increase plotted against effective geomagnetic cutoff rigidity for 1825 UT on 19 October 1989. The rigidity at which the fitted lines intersect indicates the effective atmospheric cutoff.

It should be possible to determine P_{atm} at any atmospheric depth by considering the propagation of nucleons in the atmosphere, however most theoretical

Table 7.5: Investigation of the effect of atmospheric cutoff rigidity on the response of the South Pole neutron monitor (as described in the text). Fluxes in units of particles $(cm^2\ s\ ster\ GV)^{-1}$.

Arrival Direction		Spectral	Pitch Angle	$J_{\|\|}$	$J_{\|\|}$
Latitude	Longitude	Slope	Distribution	P_{atm}=1 GV	P_{atm}=0.7 GV
−20	350	−6	a	69.2	64.9
−20	350	−6	b	10.6	17.5
−20	350	−6	c	16.3	15.4
−20	350	−2	a	0.3	0.3
−20	350	−2	b	0.1	0.1
−20	350	−2	b	0.1	0.1
10	250	−6	b	385.7	367.3
10	250	−6	c	24.0	25.4

methods have significant uncertainties at low rigidity (Nagashima *et al.*, 1989). This is due to the incomplete representation of the effect of scattering of a nucleon with low kinetic energy compared with its rest mass and/or by neglecting the ionisation loss of protons. The effect of decreased atmospheric cutoff will be most significant at the South Pole neutron monitor, altitude 2820 m (and Vostok, although no data from this station were available for use in this thesis). The effect of including rigidities below 1 GV at South Pole has been investigated. Table 7.5 shows the flux required to generate a 10% response at South Pole for selected particle anisotropies and spectra using the viewing directions for 1805 UT on 22 October 1989 when the Kp level was 5. The fluxes listed in each row are the required flux at 1 GV over the forward steradian with the two assumptions P_{atm} = 1 GV and P_{atm} = 0.7 GV. The pitch angle distributions indicated as a, b and c in the table are shown in Figure 7.6. Power law spectra were used in all cases. Spectral indices of −6 and −2 were chosen respectively as softer and harder than most GLE spectra.

It can be seen from Table 7.5 that the choice of atmospheric cutoff made no difference in the cases where the spectrum was hard. For the soft spectrum, results are shown for two different arrival directions. The first (−20°, 350°) was chosen so that the South Pole viewing cone would be fully encompassed by pitch angle distribution c, but only the low rigidity viewing directions would lie within the other two distributions. The largest effect can be seen for distribution b where the change in required flux was ~40%. The second particle arrival direction (10°, 250°) was chosen to be well away from the South Pole viewing directions. The narrowest pitch angle distribution (a) could not be used in this case as it did not intersect the viewing cone. The change in flux for the other cases was insignificant. It is also unlikely that derived parameters for an event with an arrival direction so far from the South Pole viewing direction would be biased by inadequate representation of this station as larger responses would have been recorded at many other sites which would be more significant in the weighted least squares analysis.

In summary, these results show that the choice of atmospheric cutoff rigidity for the South Pole neutron monitor is only significant for soft particle spectra in

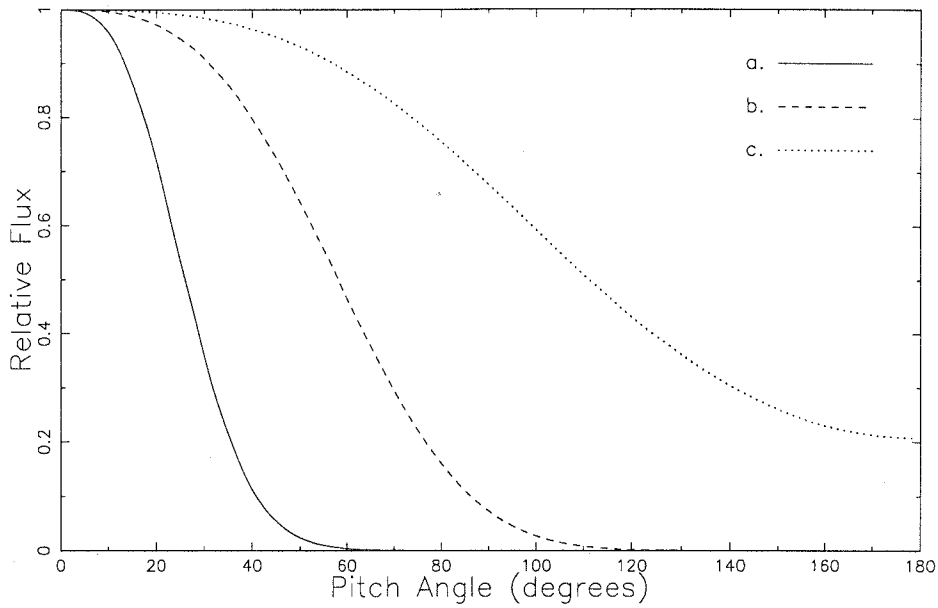

Figure 7.6: Pitch angle distributions a, b and c used for results presented in Table 7.5.

cases where the pitch angle distribution intersects only the low rigidity viewing directions. In such situations, South Pole would have one of the largest responses to the event and the derived spectral and particle distribution parameters may be affected by the choice of cutoff rigidity. It is not expected that any results presented in this thesis would be significantly changed by allowing contributions from lower rigidities at South Pole, however care should be taken in analysis of soft spectrum events with particle arrival directions in the vicinity of the low rigidity viewing directions of the South Pole neutron monitor.

The best way to eliminate this problem would be to use a yield function with a dependence on atmospheric depth. This would also eliminate the need for correction of recorded increases by the two attenuation length method. Nagashima *et al.* (1989) have developed yield functions for different atmospheric depths. These were determined by re-analysis of historical data sets from latitude and altitude surveys. The geomagnetic cutoff rigidities were re-computed as many were originally determined from a dipole representation of the geomagnetic field. Data from both IGY and IQSY monitors were included. The differences in the yield of the two types of monitor were ignored and must increase the uncertainty in the resulting yield functions. Nagashima *et al.* compared their derived functions with some theoretically determined functions. They found increasing discrepancy at smaller atmospheric depths. It is not known whether this is due to errors in the theoretically or experimentally determined functions, or both. No comparison was made for rigidities below ~10 GV, the rigidity range of most significance in the analysis of solar particle events. The validity of these yield functions should be investigated before inclusion in the modelling of ground level enhancements, however if they are found to be accurate, this would be the best approach to the problems of using data from stations at different atmospheric depths.

7.5 Further work

7.5.1 Modelling procedure

A complex GLE modelling procedure has been developed and modified to account for specific circumstances. There are still some areas which could be further refined. The Debrunner *et al.* (1982) yield function has been widely accepted for use with neutron monitor data, but this does not account for differences in atmospheric depth. If the Nagashima *et al.* (1989) yield functions described in the previous section are found to be satisfactory for use in GLE modelling, this problem would be solved. Such a function should also be used to account for the variation of atmospheric depth with zenith angle. This process should be used when incorporating contributions from non-vertical arrival directions, however it was not possible with the Debrunner *et al.* yield function.

The muon yield function used in modelling the 29 September 1989 GLE (see Section 4.2.2) is not well suited to low rigidity particles, however it does incorporate atmospheric depth dependence. Refinement of this function or development of another is required if muon telescope responses to solar particles are to be successfully modelled. The scaling of an appropriate yield function for simultaneous use with neutron monitor yield functions is also necessary.

The rigidity dependence of yield functions is very important for the accurate determination of particle rigidity spectra. The Ellison and Ramaty spectral form and the modified version of this have been found to give good agreement with most of the derived spectra presented in this thesis. These spectral forms should be used in preference to the modified power law in future modelling.

The pitch angle distributions used in this modelling procedure were cylindrically symmetric. This is a consequence of the original software in which the pitch angle is determined from the angular separation of the asymptotic viewing direction and the axis of symmetry of the pitch angle distribution. Morishita *et al.* (1991) used an elliptical distribution when modelling the 29 September 1989 GLE. Such a distribution could be incorporated into this modelling procedure with relatively minor changes to the software. This may prove to be a valuable extension of the model and lead to further insights into the dynamics of particle propagation in the interplanetary medium.

Several of the results presented in this thesis involved bi-directional particle flows, either along looped magnetic field lines or due to back-scattering. The rigidity spectrum of the particles propagating in both directions was assumed to be the same. In the case of particles arriving from opposite directions along a looped field line, the process by which access was gained to each of the two paths will determine whether the spectra are the same. The spectrum of particles reflected back towards the Earth by a scattering region beyond 1 AU may also differ from that of particles arriving directly from the Sun. This will depend on the rigidity dependence of the back-scattering efficiency which may well be other than unity. Modelling two distributions with different spectra should be possible if sufficient data are available to allow an increase in the number of fit parameters. In the case of 12 October 1981 where particles arrived along two

different paths from the Sun, spectral differences may give some insight into the acceleration processes involved at, or near, the flare site however the small amount of data available for this event may lead to inconclusive results. Investigation of spectral differences between 'forward' and 'reverse' propagating particles during the 22 October 1989 GLE may provide additional information about the region responsible for the back-scatter *e.g.* the rigidity dependence of the back-scatter efficiency may be related to the size of the region or the strength of the magnetic fields.

Another assumption built into the bi-directional pitch angle distributions is that the flow directions must be separated by 180° in pitch angle. This is reasonable if the flow is in two directions along the same field line as long as the curvature of the field line is not significant in the vicinity of the Earth. It is possible that the flow directions may not be separated by exactly 180°, in which case, additional parameters may be included in the model to define different axes of symmetry for the two distributions. This, combined with additional spectral parameters would slow the process of determining best fit parameters, but may be necessary in particular cases.

7.5.2 Other events

The current GLE database contains world-wide neutron monitor data for events of the 22nd solar cycle. Some surface muon data are also available. Expansion of this facility to include events from previous and subsequent solar cycles will open up new avenues for the study of GLEs and may allow statistical analysis of some features. It is important that the database be maintained and that data are submitted whether an increase was recorded or not. It is just as important for models to reproduce null observations as increases and these are valuable in determining the best fit parameters of the model.

It may be possible to apply a similar modelling method in the study of cosmic ray decreases. In this case the derived spectrum and particle distribution would be a deficit subtracted from the background galactic cosmic ray intensity. Such modelling may provide insights into the features of different classes of decreases. This would require a similar world-wide data sharing arrangement to that which resulted in the GLE database.

Conclusion

The ground level response to solar particle events can be successfully modelled using functional representations of particle pitch angle distributions and rigidity spectra, combined with calculated asymptotic viewing directions. The Tsyganenko (1989) representation of the geomagnetic field and software developed by Kobel (1989) allow the determination of viewing directions for appropriate levels of geomagnetic disturbance. A least squares method for finding the best fit parameters removes the trial and error of adjustment 'by hand', but steps must be taken to avoid finding local minima in parameter space.

An exponential function has been used for the pitch angle distributions, and different forms of the same function were employed to model bi-directional flow and rigidity dependence. The modified power law spectra used in the analyses presented in Chapters 4–6 have been found to be largely consistent with approximations of the Ellison and Ramaty shock acceleration spectral form.

The responses at both neutron monitors and surface muon telescopes were modelled during the 29 September 1989 GLE. Rigidity dependence of the pitch angle distribution early in this event is consistent with higher rigidity particles having access from a greater range of pitch angles. This is thought to be due to the larger gyroradii of these particles and the separation of the flare site from the footpoint of the 'garden hose' field line. It is probable that shock acceleration was responsible for the transport of particles from the flare site to the field line. The lack of rigidity dependence in the modelled pitch angle distributions later in the event confirms that the early dependence was probably related to particle access to the 'garden hose' field line rather than propagation characteristics of the interplanetary medium.

Initial anisotropic spikes observed by some stations on 19 and 22 October 1989 have been found to be consistent with scatter-free, focussed transport. The main event on 22 October continued to exhibit significant anisotropy in particles arriving along the 'garden hose' field line. Back-scattering from beyond the Earth resulted in increases at stations viewing in the anti-sun direction. This has been attributed to a high field strength disturbed plasma region which passed the Earth during 19 and 20 October. The 19 October GLE had an unusual eastern particle arrival direction with a broad pitch angle distribution due to diffusion of particles from nearby field lines. A later spike in the neutron monitor data can be explained by further focussed transport of shock accelerated particles.

The 24 October 1989 GLE was used as a 'test case' for different spectral forms. A modification of the Ellison and Ramaty shock acceleration spectrum gave the best results. This implies acceleration by a finite shock for a finite time. A rigidity

dependent pitch angle distribution resulted in a marginal improvement in the fit to the observed data, suggesting that the scattering mean free path may have been smaller for low rigidity particles.

The interplanetary magnetic field configuration during the 12 October 1981 and 7-8 December 1982 ground level enhancements was distorted from the nominal Archimedean spiral. The first of these events was modelled with a bi-directional pitch angle distribution. This is consistent with results at lower energies and is further evidence for the presence of a looped field structure. Interplanetary magnetic field and plasma data during 7 December 1982 were consistent with a magnetic cloud-like structure passing the Earth. This was situated just beyond the Earth during the GLE. The neutron monitor response to this event has been modelled with an elliptical deficit region to account for the scattering of solar particles which encountered this feature. The slow rise to maximum intensity at Apatity and Oulu can only be satisfactorily modelled if the effects of the magnetic cloud are taken into account.

The derived pitch angle distributions for 16 February 1984 suggest a scattering mean free path of greater than 2 AU. The axes of symmetry of these distributions were $\sim 40^{\circ}$ from the measured interplanetary magnetic field directions. This could not be explained, but is found to be consistent with the results of previous studies.

A possible improvement to this GLE model is the inclusion of an atmospheric depth dependent yield function. This would eliminate the necessity for the two attenuation length correction of observed increases and should also be used to account for the zenith angle dependence of atmospheric depth. Spectral differences between the two populations in bi-directional pitch angle distributions should also be explored as well as the possibility of elliptical pitch angle distributions.

Finally, analysis of other events should be undertaken so that a larger sample can be obtained for comparison of the features of different events. This will require expansion of the GLE database and cooperation between those responsible for data collection so that a comprehensive data set is available. The results of such a study would provide a valuable contribution to the understanding of the acceleration and propagation of solar energetic particles.

References

Ahluwalia, H. S., and K. G. McCracken, The influence of the magnetopause on cosmic ray particle trajectories, *Proceedings of the 9th International Cosmic Ray Conference, London 1*, 568–570, 1965

Badhwar, G. D., and P. M. O'Neill, Galactic cosmic radiation model and its applications, *Adv. Space Res. 17*, 7–17, 1995

Bavassano, B., N. Iucchi, R. Lepping, C. Signorini, E. Smith, and G. Volloresi, Galactic cosmic ray modulation and interplanetary medium perturbations due to a long-living active region during October 1989, *J. Geophys. Res. 99*, 4227–4234, 1994

Beeck, J., and G. Wibberenz, Pitch angle scattering of solar energetic particles and the local scattering properties of the interplanetary medium, *Astrophys. J. 311*, 437–450, 1986

Belov, A. V., Y. L. Blokh, E. A. Eroshenko, V. N. Ishkov and V. G. Yanke, Ground increase of cosmic ray intensity on February 16, 1984, *Proceedings of the 19th International Cosmic Ray Conference, La Jolla 4*, 118–121, 1985

Bieber, J. W., and P. Evenson, Determination of energy spectra for the large solar particle events of 1989, *Proceedings of the 22nd International Cosmic Ray Conference, Dublin 3*, 129–132, 1991

Bieber, J. W., P. Evenson, and M. A. Pomerantz, Focusing anisotropy of cosmic rays, *J. Geophys. Res. 91*, 8713–8724, 1986

Bieber, J. W., P. Evenson, and M. A. Pomerantz, Unusual cosmic ray spike, *Antarctic Journal of the U.S. 25*, 277–278, 1990

Burlaga, L. F. E. Magnetic clouds, in *Physics of the Inner Heliosphere*, Physics and Chemistry in Space 21; Space and Solar Physics, Chapt. 6, Springer-Verlag, Berlin, R. Schwenn and E. Marsch (eds.), 1991

Cain, J. C., S. J. Hendricks, R. A. Langel, and W. V. Hudson, A proposed model for the International Geomagnetic Reference Field-1965, *J. Geomag. Geoelec. 19*, 335–355, 1967

Cane, H. V., R. E. McGuire, and T. T. von Rosenvinge, Two classes of solar energetic particle events associated with impulsive and long-duration soft X-ray flares, *Astrophys. J. 301*, 448–459, 1986

Cane, H. V., and D. V. Reames, Soft X-ray emissions, meter-wavelength radio bursts, and particle acceleration in solar flares, *Astrophys. J. 325*, 895–900, 1988

Cane, H. V., D. V, Reames, and T. T. von Rosenvinge, The role of interplanetary shocks in the longitude distribution of solar energetic particle events, *J. Geophys. Res. 93*, 1–6, 1988

Cane, H. V., and I. G. Richardson, Cosmic ray decreases and solar wind disturbances during late October 1989, *J. Geophys. Res. 95*, 1755–1762, 1995

Cane, H. V., T. T. von Rosenvinge, and R. E. McGuire, Energetic particle observations at the Helios 1 spacecraft of shocks associated with coronal mass ejections, *J. Geophys. Res. 95*, 6575–6579, 1990

Chertok, I. M., V. V. Famichev, A. A. Gnezdilov, R. V. Gorgutsa, and A. K. Markeev, U-shaped type II burst connected with the flare on 16 February 1984 and preceding activity, *Report UAG-96, World Data Center A for solar-terrestrial physics* pp 49–51, 1987

Cliver, E. W., J. Feynman, and H. B. Garrett, An estimate of the maximum speed of the solar wind, 1938–1989, *J. Geophys. Res. 95*, 17103–17112, 1990

Cliver, E. W., S. W. Kahler, and W. T. Vestra, On the origin of gamma-ray emission from the behind the limb flare on 29 September 1989, *Proceedings of the 23nd International Cosmic Ray Conference, Calgary 3*, 91–94, 1993

Cooke, D. J., J. E. Humble, M. A. Shea, D. F. Smart, N. Lund, I. L. Rasmussen, B. Byrnak, P. Goret, and N. Petrou, On cosmic-ray cut-off terminology, *Il Nuovo Cimento 14C*, 213–234, 1991

Cramp, J. L., M. L. Duldig, and J. E. Humble, Neutron monitor responses during highly anisotropic ground level enhancements, *Proceedings of the 24th International Cosmic Ray Conference, Rome 4*, 248–251, 1995

Debrunner, H., E. 0. Flückiger, H. Grädel, J. A. Lockwood, and R. E. McGuire, Observations related to the acceleration, injection and interplanetary propagation of energetic particles during the solar cosmic ray event on February 16, 1984, *J. Geophys. Res. 93*, 7206–7216, 1988

Debrunner, H., E. O. Flückiger, and J. A. Lockwood, *Presented at the 8th European Cosmic Ray Symposium, Rome*, 1982

Duggal, S. P., I. Guidi, and M. A. Pomerantz, The unusual anisotropic solar particle event of November 18, 1968, *Sol. Phys. 19*, 234–246, 1971

Duldig, M. L., Cosmic ray transient variations observed from the Earth, *Pub. Astron. Soc. Aust. 11*, 110–125, 1994

Dulk, G. A., Radio emission from the sun and stars, *Ann. Rev. Astron. Astrophys. 23*, 169–224, 1985

Ellison, D. C., and R. Ramaty, Shock acceleration of electrons and ions in solar flares, *Astrophys. J. 298*, 400–408, 1985

Evenson, P., P. Meyer, S. Yanagita, and D. Forrest, Electron-rich particle events and the production of gamma-rays by solar flares, *Astrophys. J. 283*, 439–449, 1990

Fairfield, D. H., An evaluation of the Tsyganenko magnetic field model, *J. Geophys. Res. 96*, 1481–1494, 1991

Filippov, A. T., and A. S. Noskovskikh, Peculiarities of the February 16, 1984 cosmic-ray burst, *Geomag. Aeron. 30*, 612–614, 1990

Firor, J., Cosmic radiation intensity-time variations and their origin IV. Increases associated with solar flares, *Phys. Rev. 94*, 1017–1028, 1954

Flückiger, E. O., and E. Kobel, Aspects of combining models of the Earth's internal and external magnetic field, *J. Geomag. Geoelec. 42*, 1123–1136, 1990

Flückiger, E. O., E. Kobel, D. F. Smart, and M. A. Shea, On the significance of magnetospheric effects in the analysis of the ground-level solar cosmic ray event on 7 December 1982, *Proceedings of the 21st International Cosmic Ray Conference, Adelaide 7*, 22–25, 1990

Flückiger, E. 0., E. Kobel, D. F. Smart, M. A. Shea, J. E. Humble, J. L. Cramp, and M. L Duldig, On the unusual aspects of the 22 October 1989 anisotropic GLE, *EOS Transactions, (suppl)* p. 487, 1993, Abstract only

Forbush, S. E., Three unusual cosmic ray increases probably due to charged particles from the sun, *Phys. Rev. 70*, 771–772, 1946

Forbush, S. E., World-wide cosmic-ray variations 1937–1952, *J. Geophys. Res. 59*, 525–542, 1954

Forbush, S. E., T. B. Stinchcomb, and M. Schein, The extraordinary increase of cosmic ray intensity on November 19, 1949, *Phys. Rev. 79*, 501–504, 1950

Fujimoto, K., K. Murakami, I. Kondo, and K. Nagashima, Approximate formula for response function of cosmic ray hard component at various depths of the atmosphere and underground, *Proceedings of the 15th International Cosmic Ray Conference, Plovdiv 4*, 321–325, 1977

Gall, R., Daily variation of asymptotic directions of cosmic rays, *J. Geophys. Res. 73*, 4400–4403, 1968

Gall, R., J. Jiminez, and A. Orozco, Directions of approach of cosmic rays for high latitude stations, *J. Geophys. Res. 74*, 3529–3540, 1969

Hatton, C. J., The neutron monitor, in *Progress in elementary particles and cosmic ray physics*, Chapt. 1, North Holland, Amsterdam, 1971

Humble, J. E., M. L. Duldig, D. F. Smart, and M. A. Shea, Detection of 0.5–15 GeV solar protons on 29 September 1989 at Australian stations, *Geophys. Res. Lett. 18*, 737–740, 1991

Kahler, S. W., Coronal mass ejections and long risetimes of solar energetic particle events, *J. Geophys. Res. 98*, 5607–5615, 1993

Kahler, S. W., Injection profiles of solar energetic particles as functions of coronal mass ejection heights, *Astrophys. J. 428*, 837–842, 1994

Kobel, E., Determination of cut-off rigidities and asymptotic directions of cosmic rays for the solar proton event on 7-8 December 1982, allowing for the influence of the disturbed geomagnetosphere (in German), *Master's Thesis*, Physikalishces Institut der Universität Bern, 1989

Kodama, K. P., IGRF, 1991 revision, *EOS Transactions 73*, 182, 1992

Kosik, J. C., Quantitative magnetospheric field modelling with toroidal and poloidal vector fields, *Planet. Space Sci. 32*, 965–974, 1984

Lee, M. A., and J. M. Ryan, Time dependent coronal shock acceleration of energetic solar flare particles, *Astrophys. J. 303*, 829–842, 1986

Lockwood, J. A., H. Debrunner, E. O. Flückiger, and H. Grädel, Proton energy spectra at the sun during the May 7, 1978 and February 16, 1984 solar cosmic ray events, *Proceedings of the 21st International Cosmic Ray Conference, Adelaide 5*, 9–12, 1990

Lockwood, J. A., W. R. Webber, and L. Hsieh, Solar flare proton rigidity spectra deduced from cosmic ray neutron monitor observations, *J. Geophys. Res. 79*, 4149–4155, 1974

Lovell, B., The emergence of radio astronomy in the U.K. after World War II, *Quart. J. Roy. Astron. Soc. 28*, 1–9, 1987

Lüst, R., and J. A. Simpson, Initial stages in the propagation of cosmic rays produced by solar flares, *Phys. Rev. 108*, 1563–1576, 1957

Mandzhavidze, N., R. Ramaty, V. V. Akimov, and N. G. Leikov, Pion decay and nuclear line emission from the 1991 June 15 flare, *Proceedings of the 23nd International Cosmic Ray Conference, Calgary 3*, 119–122, 1993

McCracken, K. G., The cosmic ray flare effect. 1. Some new methods of analysis, *J. Geophys. Res. 67*, 423–434, 1962

McCracken, K. G., and R. A. R. Pelmeira, Comparison of solar cosmic rays injection including July 17, 1959 and May 4 1960, *J. Geophys. Res. 65*, 2673–2683, 1960

McCracken, K. G., U. R. Rao, and M. A. Shea, The trajectories of cosmic rays in a high degree simulation of the geomagnetic field, *Technical Report 77*, MIT, 1962

Mead, G. D., and D. H. Fairfield, A quantitative magnetospheric model derived from spacecraft magnetometer data, *J. Geophys. Res. 80*, 523–542, 1975

Menvielle, M., and A. Berthelier, The *K*-derived planetary indices: description and availability, *Reviews of Geophys. 29*, 415–432, 1991

Meyer, P., E. N. Parker, and J. A. Simpson, Solar cosmic rays of February, 1956 and their propagation through interplanetary space, *Phys. Rev. 104*, 768–783, 1956

Morishita, I., K. Nagashima, and S. Sakakibara, Space distribution and rigidity spectrum of solar particles of the GLE observed on 29 September 1989, *Proceedings of the 22nd International Cosmic Ray Conference, Dublin 3*, 121–124, 1991

Morrison, P., Solar origin of cosmic ray time variations, *Phys. Rev. 101*, 1397–1404, 1956

Murakami, K., K. Nagashima, S. Sagisaka, Y. Mishima, and A. Inoue, Response functions for cosmic-ray muons at various depths underground, *Il Nuovo Cimento 2C*, 635–651, 1979

Nagashima, K., S. Sakakibara, K. Murakami, and I. Morishita, Response and yield functions of neutron monitor, galactic cosmic-ray spectrum and its solar modulation, derived from all the available world-wide surveys, *Il Nuovo Cimento 12C*, 173–209, 1989

Nemzek, R. J,, R. D. Belian, T. E. Cayton, and G. D. Reeves, The 22 October 1989 cosmic ray event measured at geosynchronous orbit, *J. Geophys. Res. 99*, 4221–4226, 1994

Ness, N. F., C. S. Scearce, and J. B. Seek, Initial results of the IMP 1 magnetic field experiment, *J. Geophys. Res. 69*, 3531–3569, 1964

Palmer, I. D., Transport coefficients of low-energy cosmic rays in interplanetary space, *Rev. Geophys. Space Phys. 20*, 335–351, 1982

Parker, E. N., Sudden expansion of the corona following a large solar flare and the attendant magnetic field and cosmic ray effects, *Astrophys. J. 133*, 1014–1033, 1961

Parker, E. N., *Interplanetary Dynamical Processes*, Interscience Publishers, first Edition, 1963

Parker, E. N. The passage of energetic charged particles through interplanetary space, *Planet. Space Sci. 13*, 9–49, 1965

Peredo, M., D. P. Stern, and N. A. Tsyganenko, Are existing magnetospheric models excessively stretched?, *J. Geophys. Res. 98*, 15343–15354, 1993

Phillips, J., and N. R. Parsons, Some experiments with a mobile neutron monitor, *J. Phys. Soc. Japan 17(Suppl. AII)*, 519–523, 1962

Piddington, J. H., Interplanetary magnetic field and its control of cosmic-ray variations, *Phys. Rev. 112*, 598–596, 1958

Piddington, J. H., The cis-lunar magnetic field, *Planet. Space Sci. 9*, 305–318, 1962

Pomerantz, M. A., J. W. Bieber, and P. A Evenson, The remarkable anisotropic relativistic solar particle event of 16 February 1984, *Proceedings of the International Symposium on Cosmic Ray Modulation in the Heliosphere, Iwate University, Morioka, Japan* pp 437–443, 1984

Potemra, T. A. (Ed.) in *Magnetospheric Currents*, Geophys. Monogr. Ser. 28, 8, AGU, Washington, 1984

Press, W. H., B. P. Flannery, S. A. Teukolsky, and W. T. Vetterling, *Numerical Recipes. The art of scientific computing. (FORTRAN version)*, Cambridge University Press, 1989

Rao, U. R., K. G. McCracken, and D. Venkatesan, Asymptotic cones of acceptance and their use in the study of the daily variation of cosmic radiation, *J. Geophys. Res. 68*, 345–369, 1963

Reid, G. C., A diffusive model for the initial phase of a solar proton event, *J. Geophys. Res. 69*, 2659–2667, 1964

Richardson, I. G., H. V. Cane, and T. T. von Rosenvinge, Prompt arrival of solar energetic particles from far eastern events: The role of large-scale interplanetary magnetic field structure, *J. Geophys. Res. 96*, 7853–7860, 1991

Rieger, E., D. J. Forrest, G. Bazilevskaya, E. L Chupp, G. Kanbach, C. Reppin, and G. H. Share, Gamma ray emission from a solar flare observed also as a ground level event, *Proceedings of the 20th International Cosmic Ray Conference, Moscow 3*, 65–68, 1987

Shea, M. A., Solar cosmic rays, 1960–1989, *Proceedings of the 21st International Cosmic Ray Conference, Adelaide 12*, 196–204, 1990

Shea, M. A., and D. F. Smart, Possible evidence for a rigidity-dependent release of relativistic protons from the solar corona, *Space Sci. Rev. 32*, 251–271, 1982

Shea, M. A., D. F. Smart, and E. O. Flückiger, The evolution of the anisotropy of solar neutron decay protons during the 19 October 1989 solar cosmic ray event, *Proceedings of the 22nd International Cosmic Ray Conference, Dublin 3*, 41–44, 1991b

Shea, M. A., D. F. Smart, M. D. Wilson, and E. O. Flückiger, Possible ground-level measurements of solar neutron decay protons during the 19 October 1989 solar cosmic ray event, *Geophys. Res. Lett. 18*, 829–832, 1991a

Smart, D. F., and M. A. Shea, Probable pitch angle distribution and spectra of the 23 February 1956 solar cosmic ray event, *Proceedings of the 21st International Cosmic Ray Conference, Adelaide 5*, 257–260, 1990

Smart, D. F., M. A. Shea, and E. O. Flückiger, Unusual aspects of the ground-level cosmic ray event of 7/8 December 1982, *Proceedings of the 20th International Cosmic Ray Conference, Moscow 3*, 135–138, 1987

Smart, D. F., M. A. Shea, J. E. Humble, and P. J. Tanskanen, A model of the 7 May 1978 solar cosmic ray event, *Proceedings of the 16th International Cosmic Ray Conference, Kyoto 5*, 238–243, 1979

Smart, D. F., M. A. Shea, and P. J. Tanskanen, A determination of the spectra, spatial anisotropy and propagation characteristics of the relativistic solar cosmic ray flux on November 18, 1968, *Proceedings of the 12th International Cosmic Ray Conference, Hobart 2*, 483–488, 1971

Steljes, J. F., H. Carmichael, and K. G. McCracken, Characteristics and fine structure of the large cosmic-ray fluctuations in November 1960, *J. Geophys. Res. 66*, 1363–1377, 1961

Stewart, R.T., Moving type IV bursts, in *Solar radiophysics*, Chapt. 14, Cambridge University Press, D. J. McLean and N. R. Labrum (eds.), 1985

Stoer, J. and R. Bulirsch, *Introduction to Numerical Analysis*, Springer Verlag, New York, 1980

Sullivan, J. D., Geometrical factor and directional response of single and multi-element particle telescopes, *Nuclear Instruments and Methods 95*, 5–11, 1971

Swinson, D. B. and M. A. Shea, The 29 September, 1989 ground-level event observed at high rigidity, *Geophys. Res. Lett. 17*, 1073–1075, 1990

Tsyganenko, N. A., Global quantitative models of the geomagnetic field in the cislunar magnetosphere for different disturbance levels, *Planet. Space Sci. 35*, 1347–1358, 1987

Tsyganenko, N. A., A magnetospheric magnetic field model with a warped tail current sheet, *Planet. Space Sci. 37*, 5–20, 1989

Tsyganenko, N. A., Quantitative models of the magnetospheric magnetic field: methods and results, *Space Sci. Rev. 54*, 75–186, 1990

Tsyganenko, N. A., and A. Usmanov, Determination of the magnetospheric current system parameters and development of experimental geomagnetic field models based on data from IMP and HEOS satellites, *Planet. Space Sci. 30*, 985–998, 1982

Voigt, G., The shape and position of the plasma sheet in Earth's magnetotail, *J. Geophys. Res. 89*, 2169–2179, 1984

Wainio, K. M., T. H. Colvin, K. A. More, and O. L. Tiffany, Calculated specific yield functions for neutron monitors, *Can. J. Phys. 46*, S1048–S1051, 1968

Webber, W. R., and J. J. Quenby, On the derivation of cosmic ray specific yield functions, *Phil. Mag. 4*, 654–664, 1959

Wilcox, J. M., J. T. Hoeksema, and P. H. Scherrer, Origin of the warped heliospheric current sheet, *Science 209*, 603–604, 1980

Wilson, B. G., T. Mathews, and R. H. Johnson, Intercomparison of neutron monitors during solar-flare increases, *Phys. Rev. Lett. 18*, 675–676, 1967

Zlobec, P., M. Monino, M. Messerotti, M. Comari, and L. Fornasari, The proton flare of 16 February 1984 radiopolarimeter aspects at meter wavelengths, *Report UAG-96, World Data Center A for solar-terrestrial physics* p. 52, 1987